NTNU

Norwegian University of
Science and Technology

Integrating Laboratory Data in a Rock Physics Model to Characterise the Effects of Exhumation on P-wave Velocities

Sondre Torset

Petroleum Geoscience and Engineering
Submission date: June 2018
Supervisor: Rune Martin Holt, IGP

Norwegian University of Science and Technology
Department of Geoscience and Petroleum

Summary

Rocks have memory. The characteristics measured by seismic, wireline or in laboratory tests on cores depend on the history that brought the rock to its current state. The burial history is also a controlling factor on elements such as the maturation of hydrocarbons and reservoir quality. Identification, quantification and characterisation of any uplift a rock has been subjected to in order to reach its current depth is therefore an important aspect in interpretation and risking in the oil and gas industry.

Several methodologies exist to accomplish the goal of characterisation of uplift. The focus of this thesis is sandstone modelling. Currently applied procedures for the estimation of uplift from such a strategy is based on the assumption that as the rock is uplifted out of the cementation domain, the properties are unchanged during continued exhumation.

Experimental data from SINTEF showed that whilst the assumption of no change might be good for porosity, for a relatively weakly cemented synthetic sandstone formed under simulated in-situ stress, there was a dramatic increase in stress dependence of the velocity upon simulated uplift under uniaxial strain conditions. In addition to this increased stress dependence, the P-wave anisotropy was reversed upon sufficient simulated uplift. The main goal of this work was to incorporate these observations into an updated rock physics model for characterising the effects of uplift.

In previous work (Torset, 2017) one interpretation of the observations regarding velocity and P-wave anisotropy was the formation of microcracks as a result of broken cement bonds, with normals preferentially oriented parallel to the axial direction. The uplift interval has therefore been modelled with the crack model presented in Fjær (2006).

To implement a full burial history calibrated to the experimental data, models capable of recreating the experimental data down to the onset of uplift are also needed. Before cementation, the model provided in Walton (1987) is used. Instead of using the explicit expressions given in Walton (1987), the general equations for strain and stiffness have been solved for a particular triaxial strain state, namely that the horizontal strains are equal.

The experimental data displayed both anisotropy and stress dependence after cementation. To account for this, a modified version of the patchy cement model presented in Avseth et al. (2016) has been utilised. The modification came from using an anisotropic granular media with an anisotropic formulation of the Hashin-Shtrikman bounds, as opposed to the isotropic varieties implemented in Avseth et al. (2016).

Sowing together the three models enabled for a very good recreation of the experimental P-wave velocities as function of the simulated burial history. After calibration to the experimental data the model is implemented in combination with a cement estimation model (Walderhaug, 1996) to produce a model capable of taking in a real burial history.

The ability of the model to fit the data is not taken as validity of the model. The final rock physics model developed for characterising the uplift is dependent on the assumptions of the underlying models, the method of implementation and a wide variety of parameters that are available to facilitate fitting to the experimental data. The quantitative nature of the final model is therefore uncertain. This statement is however not unique to the model in this work, as most rock physics models aiming to characterise velocity as function of burial history suffer generalisations and depend on the choice of parameters such as the elastic parameters of the grain material.

Analysis of additional experimental data suggests that the effects of the uplift might be reduced in the case of a very stiff rock (corresponding to a lot of cement). In such a scenario, uplift modelling by assuming no change in parameters might be more appropriate.

The effect of fluids were modelled by the isotropic Biot-Gassmann equation. The effects of increased stress dependence on the velocities and P-wave anisotropy were reduced, but under sufficient unloading a reversal in the P-wave anisotropy was still observed.

Sammendrag

Bergarter har minne. Egenskapene målt av seismikk, i brønn eller i laboratorietester på kjerner, avhenger av historien som brakte bergarten til sin nåværende tilstand. Begravelseshistorien er også en kontrollerende faktor på elementer som modning av hydrokarboner og reservoarkvalitet. Identifikasjon, kvantifisering og karakterisering av oppløft som en bergart har blitt eksponert til for å nå dens nåværende dybde er derfor et viktig aspekt i tolkningsstrategi og beslutningstaking i olje- og gassindustrien.

Flere metoder eksisterer for å oppnå målet om karakterisering av oppløft. Fokuset i denne oppgaven er modellering av sandsteiner. Nåværende prosedyrer for estimering av oppløft fra slik modellering er basert på antagelsen om at når bergarten løftes ut av sementeringsdomenet, vil egenskaper som porøsitet og hastighet forbli uendret under videre oppløft.

Eksperimentelle data fra SINTEF viste at mens antakelsen om ingen endring kan være bra for porøsitet, for en relativt svakt sementert syntetisk sandstein, var det en dramatisk økning i spenningsavhengighet av hastigheten ved simulert oppløft under enaksiell ekstensjon. I tillegg til denne økte spenningsavhengigheten ble P-bølgeanisotropien reversert ved tilstrekkelig simulert oppløft. Hovedmålet med dette arbeidet er å inkorporere disse observasjonene i en oppdatert bergartsfysisk modell, for å predikere effektene av oppløft.

I tidligere arbeid var en tolkning av observasjonene angående hastighet og P-bølgeanisotropi dannelsen av mikrosprekker som følge av brutte sementbindinger, med normaler fortrinnsvis orientert parallelt med aksialretningen (Torset, 2017). Oppløftingsintervallet er derfor modellert med sprekkmodellen presentert i Fjær (2006).

For å modellere en fullstendig begravelseshistorie som er kalibrert til de eksperimentelle dataene, er det også nødvendig med modeller som kan gjenskape de eksperimentelle dataene ned til starten av oppløft. Før sementering brukes modellen som er gitt i Walton (1987). I stedet for å bruke de eksplisitte uttrykkene gitt i Walton (1987), har de generelle ligningene for belastning og stivhet blitt løst for en mer generell belastningstilstand.

De eksperimentelle dataene viste både anisotropi og stressavhengighet etter sementering. For å ta hensyn til dette, har en modifisert versjon av "patchy cement" modellen, presentert i Avseth et al. (2016), blitt benyttet. Modifikasjonen kom fra å bruke et anisotropt granulært medium med en anisotrop formulering av Hashin-Shtrikman-grensene, i motsetning til de isotrope variantene implementert i Avseth et al. (2016).

Sydd sammen resulterte de tre modellene i en god gjenskapelse av de eksperimentelle P-bølgehastighetene som funksjon av den simulerte begravelseshistorien. Etter kalibrering til eksperimentelle data, ble modellen implementert i kombinasjon med en sementestimeringsmodell for sementvolum (Walderhaug, 1996) for å produsere modeller som kan simulere prosesser i en ekte begravelseshistorie.

Modellenes evne til å gjenskape dataene er ikke tatt som bevis på modellens gyldighet. Den endelige bergartsfysiske modellen utviklet for å karakterisere oppløft er avhengig av antagelsene i de underliggende modellene, metoden for implementering og et bredt utvalg av parametere. Den endelige modellenes kvantitative karakter er derfor usikker. Dette er imidlertid ikke unikt for modellen i dette arbeidet, da de fleste bergarstfysiske modeller som karakteriserer hastighet som funksjon av begravelseshistorie lider av generaliseringer og valg av parametere, som for eksempel de elastiske parametrene til kornmaterialet.

Analyse av ytterligere eksperimentelle data antyder at effekten av oppløft kan bli redusert i meget stive bergarter (tilsvarende mye sement). I et slikt scenario kan oppløftsmodellering ved å anta ingen endring i parametere være gyldig.

Effekten av væsker ble modellert av den isotrope Biot-Gassmann-ligningen. Effektene av økt spenningsavhengighet for hastighetene og P-bølgeanisotropien ble redusert, men under tilstrekkelig avlastning ble det fortsatt observert en reversering i anisotropien.

Preface

This thesis has been carried out at the Department of Geoscience and Petroleum at the Norwegian University of Science and Technology (NTNU). The thesis is completed as the final part of a specialisation in Petroleum Geophysics in the 5 year masters programme *Petroleum Geosciences and Engineering*.

First of all I would like to extend my gratitude to my supervisor, Professor Rune Martin Holt, for guiding me through the final year of my study. The feedback and discussions have been essential for the completion of this work. I would also like to thank Associate Professor Kenneth Duffaut for fruitful conversations over the last year. Furthermore SINTEF and ENI are thanked for the permission to use and reproduce the experimental data.

In thriving as a student, the social aspect of life is perhaps just as important as the academic part. To that extent I would like to thank all my friends in Trondheim, as well as the student organisation *Bergstuderendes Forening* for facilitating what has been five truly fantastic years.

Finally I would like to thank my family for providing limitless support throughout not only the years at university, but throughout my education as a whole.

11.06.2018
Sondre Torset

True knowledge exists in knowing that you know nothing - Socrates

In loving memory of my grandmother Brit Torset, who passed away 28.05.2018.

Table of Contents

List of Tables

List of Figures

Part I

Thesis Introduction

Chapter 1

Background

Why does a rock body have the properties that are observed by seismic, wireline or in the lab? The elastic properties of the rock, and consequently the velocities are functions of composition and history. Modelling how rocks are affected by processes occurring throughout geological history can help shed light on its observed properties. This information can also used to characterise any uplift that a rock has been subjected to, as shall be demonstrated in the next chapter. Being able to predict parameters such as velocity by modelling can help reduce the potential for misinterpretation caused by the interplay of lithology and fluid in defining seismic parameters. Knowledge of how the rock properties have developed through time will help contextualise the seismic and well data in terms of the fluids contained. How elastic velocities of grain assemblages and cemented rocks are affected by burial history is thus the key challenge addressed in this work.

This work is based on laboratory data, and the information that can be extracted from a simulated burial history applied to a synthetic sandstone. By employing the laboratory data, a rock physics model is calibrated based on various underlying models to describe the development of the axial and radial P-wave velocities through this simulated burial history.

This thesis is split in 6 parts in an attempt to focus the discussion around one topic at a time. Part I will provide some insight into geological processes that may or may not take place during the burial history of a rock, although the discussion will by no means be exhaustive. This is done because the potential complexity of the burial history is important to keep in mind when the later assumptions in the models are presented. The discussion in this chapter is not limited only to sandstones, as much of the later parts of this work, but aims to give a slightly broader overview of geological processes. A discussion into some of the reasons why being able to extract information regarding the history of rocks is of interest is also included in this part.
Some of the methods used in uplift quantification are also introduced. Finally, some fundamental theory necessary in several aspects of this work is depicted. Instead of collecting all the theory in one long chapter, more topic specific theory has been put in the parts where it is utilised.

Part II aims to give an insight into the experimental procedure, and the necessary laboratory data used to develop the model produced in this work. These laboratory data have been discussed in detail in previous work, and this part thus aims to provide a bridge to that work, and demonstrate how the laboratory data impact the models presented in part I.

Parts III through to V attempt to develop a model that can recreate the experimental data over three distinct phases of the experiment: Pre-cementation loading, Post-cementation loading and Post-cementation unloading.

Part VI will discuss the applicability of the developed model on the field scale. The wide range of limitations that is introduced due to the underlying models that form the building blocks of the final model as well as other necessary assumptions are also presented. Factors such as cement volume, stress path and the effects of fluids are also mentioned in this extended discussion.

1.1 Processes Defining the Properties of a Rock

The velocities and density of a rock can be seen as a result of its burial history. The burial history describes the depth of a sediment as a function of time. As sediments are buried they are subjected to diagenetic processes. *Diagensis* is the term commonly given to those mechanisms who affect the sediments after deposition, but in a temperature regime lower than that of metamorphism (Worden and Burley, 2003). This comprises a host of physical and chemical changes, only a few of which will be included in modelling of velocity as a function of burial history in the present work.

1.1.1 Mechanical Compaction

After deposition, as sediments are buried deeper, the vertical component of stress increases, and is at any a depth a function of the weight of the overlying sediments (Worden and Burley, 2003). This increase in compressive stress can cause the

porosity to decrease because of grain rearrangement, plastic deformation of components that are ductile and brittle fracturing (Worden and Burley, 2003).

Variability in the mineralogical composition and depositional properties such as grain size and sorting of the sediments leads to variable porosity/depth curves. Cleavage planes in feldspars and plastic deformation in micas are, among others, processes that could lead to the porosity loss being different than for a pure quartz assemblage (Worden and Burley, 2003).

The reduction in porosity increases the density of the sediments. Increased effective stress on grain contacts will cause the stiffness of the rock to increase (Mavko et al., 2009) and the interplay between stiffness and density subsequently defines the velocity development.

If compaction is rapid in relation to the permeability of the sediment the fluid pressure gradient will deviate from that of normal hydrostatic pressure, causing overpressure (Osborne and Swarbrick, 1997). This means the effective stress is lower, which inhibits mechanical compaction and thus manifests itself in higher porosities than expected. Overpressure and the effect of fluids on the stiffness of sediments is discussed in slightly more detail in appendix B.

1.1.2 Cementation and Chemical Compaction

Chemical compaction and cementation are by some[1] used interchangeably, to depict porosity loss in deeply buried rocks. This is not particularly precise. Chemical compaction refers to a loss of rock volume to chemical processes such as dissolution (Worden and Burley, 2003). Cementation is the precipitation of minerals in the pore space. Indeed, the two processes may have a degree of interconnectedness as material dissolved in one area may be reprecipitated elsewhere as cement.

In the modelling of the quantities of cement in a sandstone, cementation is in this work taken to mean quartz cementation. Choosing quartz makes sense as it is the most common cement in sandstones (Worden and Burley, 2003). Rocks may however be cemented by carbonate, clay minerals, anhydrite, pyrite, feldspars and zeolites (Worden and Burley, 2003) which would complicate the description of the rock throughout the burial history.

Cement at grain contacts significantly increases the stiffness of the rock (Dvorkin et al., 1994), whilst reducing the porosity. Excessive exposure to cementation can completely destroy porosity and permeability. Knowledge of the depositional setting and burial history of rocks can help predict the amount of cement, and thus the extent to which it affects velocities and reservoir properties (Dvorkin and Nur (1996), Walderhaug (1996)).

[1]Particularly in literature regarding quartz cementation on the Norwegian continental shelf.

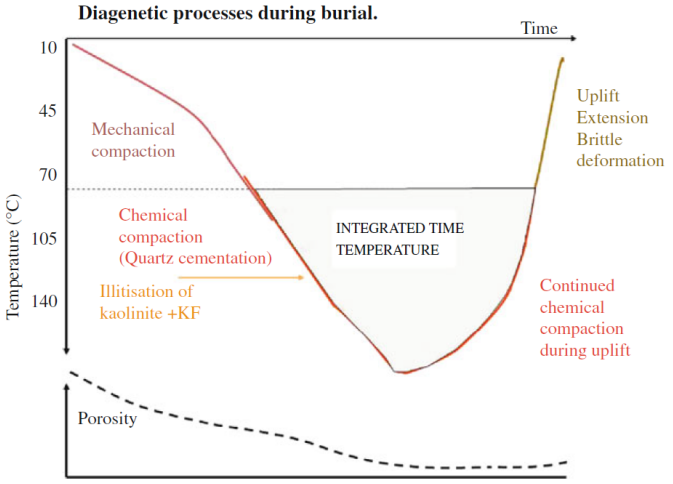

Figure 1.1: An illustrative figure from Bjørlykke and Jahren (2010) summarising some of the important processes affecting a sediment as it goes through deposition, burial and subsequent uplift and the effect they have on porosity

1.1.3 Uplift

Although uplift is a commonly used term, "the geological literature is much confused by an inconsistent definition of the word uplift" (Molnar and England, 1990). England and Molnar (1990) define the word uplift as "displacement in the direction opposite to the gravity vector", and three kinds of displacements to which uplift and uplift rate can be applied are presented. "Exhumation" is the displacement of rocks with respect to the surface, and the rate of exhumation is then the rate of erosion, or the rate at which overburden is removed by tectonic forces (England and Molnar, 1990). This is the characterisation of uplift that will be used throughout this work. This means that rocks buried deeper down are brought closer to the surface, which causes unloading, as the weight of overlying overburden is reduced. This stress release might cause brittle deformation (Bjørlykke and Jahren, 2010), and the extensional behaviour causes extensional fractures (Bjørlykke, 2010). This brittle deformation is not likely to cause major changes in the porosity.

Figure 1.1 summarises some of the most important changes happening to sediments as they progress through time and temperature, and how the porosity is impacted as a result of the various mechanisms[2]. The present day properties are a consequence of the history that brought it there, in other words, *rocks have memory*.

1.2 Why is Burial History Important?

Several processes that happen during burial are of interest in hydrocarbon exploration. These processes impact both the amount of producible hydrocarbons and may also influence interpretation and drilling. Some of these processes are not

[2]Note that quartz cementation is "lumped together" with chemical compaction.

reversible upon uplift and exhumation. This means that in uplifted rocks, some features that are characteristic of deeper buried sediments and rocks are observed.

Further, factors occurring in the eogenetic regime, in other words under the influence of the original depositional environment are not considered in the modelling in this work. It is however noted that these reaction may influence which reactions take placer during deep burial by altering the mineral assemblage prior to burial (Worden and Burley (2003), Bjørlykke and Jahren (2010)).

1.2.1 Quartz Cementation

Quartz cementation is a major porosity reducing factor. As figure 1.1 suggests, quartz cementation is a function of both time and temperature, and starts at around 70-80 $^{\circ}C$. Knowing the maximum burial depth provides information of the maximum temperature. Factors favourable for extensive quartz cementation are slow burial and high geothermal gradients (Bjørlykke and Jahren, 2010), and as illustrated by figure 1.1 quartz cementation may severely reduce the pore space available for hydrocarbons to be stored.

A reduction in porosity by cementation would be expected to come with an accompanying reduction in permeability, as some pore throats are cemented shut.

The link to uplift is that the quartz cement is not removed after the rock is brought to temperatures below 70-80 $^{\circ}C$ where the cementation stops. This means that the rock porosity at shallower depths than the onset of cement can have reduced reservoir quality as a result of previous burial into the cementation realm.

1.2.2 Clay Mineral Reactions

The conversion of smectite to illite, occurring at around 70-90 $^{\circ}C$ in mudstones with potassium rich pore waters can release ions that could reprecipitate as chlorite and quartz in adjacent sandstone formation, but the effects of this transformation as a source for quartz cement "remains conjectural" (Eslinger and Pevear, 1988).

In addition, the conversion of smectite to illite might alter the compressibility of the sediment, which can facilitate further compaction by the overburden (Osborne and Swarbrick, 1997). This increased compaction in unison with the potential for reduced permeability might facilitate overpressure development, which can be a drilling hazard (Osborne and Swarbrick, 1997). Overpressure is however a transient phenomenon, and so it is not necessarily preserved through an uplift phase as fracturing might occur.

The transformation from smectite to illite has also been observed to cause a sharp increase in density and velocity, (Marcussen et al. (2009), Bjørlykke and Jahren (2010)). In horizontal sedimentary packages where temperature and conditions are relatively constant laterally this might cause a horizontal reflector, that could be mistaken for a fluid contact (Bjørlykke and Jahren, 2010).

In sandstones containing K-feldspar and kaolinite, illite might also be precipitated accompanied by dissolved silica. According to Worden and Burley (2003) K-feldspar and kaolinite are "universally unstable together". Kaolinite and K-feldspar may however be found together at low temperatures. Worden and Burley (2003) attributes this to the fact that the reaction is only prevalent at temperatures exceeding around $70^{\circ}C$ and pervasive at $130^{\circ}C$ due to a kinetic reaction barrier or slow rate of reaction at lower temperatures. Bjørlykke and Jahren (2010) claims that the reaction happens at $130^{\circ}C$, where the "two minerals are no longer thermodynamically stable together".
Authigenic (formed in situ) illite can have a detrimental effect on reservoir properties by reducing permeability (Bjørlykke and Jahren, 2010). This permeability reduction can come from its tendency to grow as masses of long, hair-like crystals (Almon and Davies, 1981).

1.2.3 Source Rock Maturation

The maturation of source rocks to produce hydrocarbons is, as cementation, a function of time and temperature. One relatively simple quantification of this is Lopatin's "Time Temperature Index", a review of which can be found in Waples (1980). The key is that the organic rich shale must be subjected to a high enough temperature for a sufficient period of time. Exposure to high temperatures for significant periods of time will however cause gas formation and eventually the source rock will become overmature.

Knowing when the source rock was active in generating oil is important when put into context with other principal events such as trap formation. If the source rock produced oil before a trap geometry was formed, the hydrocarbons may have leaked off (Allen and Allen, 2013).

1.3 Techniques for Characterising Burial History

The main focus in this work is modelling the properties of a quartoze grain assemblage through compaction, cementation and uplift. In this section, a very simple conceptual sketch of how this process may be conducted to characterise burial and uplift history is shown. There exist other methods to characterise the temperature history of rocks and sediments, and some of these are presented in brief.

1.3.1 Diagenetic Sandstone Modelling

As an introductory example, a conceptual sketch of how sandstone diagenetic model can be conducted will be considered. All the models that enter into creating this will be discussed at length at later stages in this work. The inclusion of this before all the models are discussed is simply to provide overview of the current methodology. Prior to cementation, the only processes considered are mechanical compaction and increased

stress on grain contacts. Upon the onset of cementation, it is assumed that the only porosity lost is due to the formation of cement.

Consider a sandstone with a dry velocity of 2776 m/s found at a burial depth of 600 m. By combining compaction modelling of porosity, such as that in Lander and Walderhaug (1999), together with granular media models and cement models, such as the friable sand and contact cement models, describe in Dvorkin and Nur (1996) the velocity as a function of burial history can be modelled. The amount of cement is a function of several parameters, and can be estimated using the model in Walderhaug (1996). The effect of increased stress on uncemented granular media is discussed in more detail in part 3, whereas the effects of cementation are discussed in part 4.

During uplift, as long as the sandstone is within the quartz cementation realm cementation continues. The onset of quartz cement is in this work taken to be $70°C$. This is from Bjørlykke and Jahren (2010) who seems to suggest "70-80 °C". The exact temperature at the onset of cement might be slightly higher, but this is easily changed in the models, and so the exact temperature at the onset of cement is not discussed in any further detail. After the rock is uplifted past depths corresponding to these temperatures the cementation ceases. During subsequent uplift, common practice in sandstone diagenetic modelling is to assume that the sandstone retains the properties it possessed at the exit point for cementation (see for example Avseth et al. (2014b) or Avseth and Lehocki (2016)). This will then manifest itself as a vertical line upon uplift past the 70° C mark.

Figure 1.2 shows the result of such as modelling sequence, predicting an uplift of 2200 m (2800 → 600). The corresponding burial history is shown in figure 1.3. The porosity loss is illustrated in figure 1.4. The value of Lopatin's TTI is in this case 6.65, which is outside the oil window. The models implemented here are limited to isotropic stress states, and stress insensitivity during cementation.

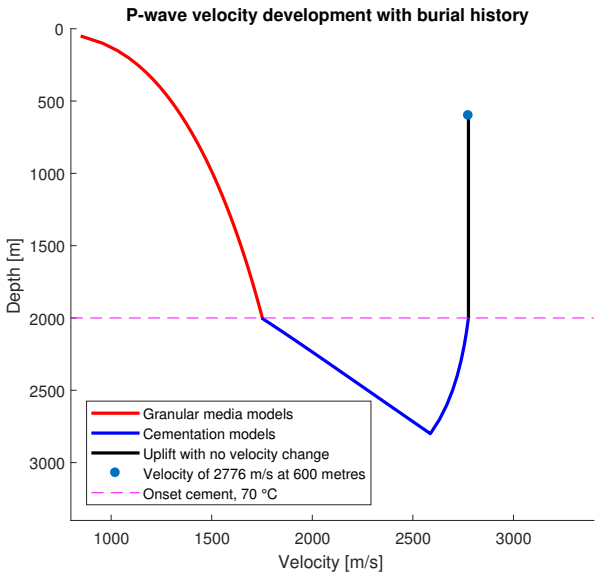

Figure 1.2: Conceptual model of P-wave velocity development with burial history. The pre-cementation interval is modelled using the friable sand model in Dvorkin and Nur (1996). The volume and effect of quartz cementation interval is modelled using a combination of the models in Walderhaug (1996) and Dvorkin and Nur (1996). The velocity is assumed to be constant during uplift. Onset cement is set at $70°C$, corresponding to a geothermal gradient of $35\frac{°C}{km}$, with a surface temperature of $0°C$

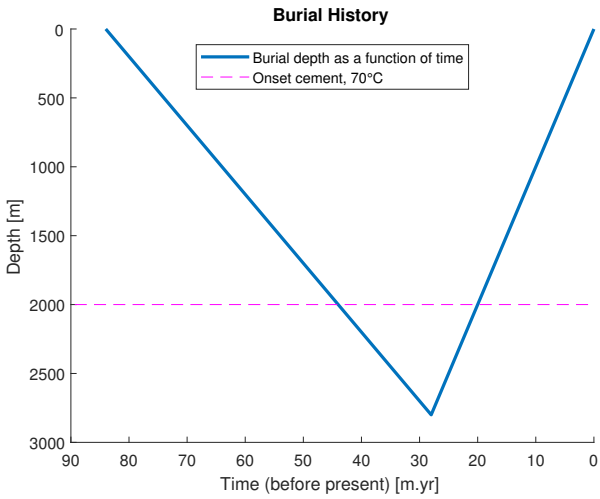

Figure 1.3: Burial depth as a function of time for the rock whose velocity is modelled in figure 1.2.

1.3.2 Vitrinite Reflectance

Vitrinite reflectance (often denote $\%R_0$) measures how much of incident light is reflected off vitrinite particles in sedimentary rocks. Vitrinite is something referred to as a maceral, which are organic particles that are microscopically detectable in kerogen (Cardott, 2012). Used as a thermal maturity indicator, the value of the vitrinite reflectance is much more sensitive to the maximum burial temperature than time (Japsen and Bidstrup, 1999).

Therefore, although vitrinite reflectance can be used as a measure for quantifying the maximum burial depth, it will have to be combined with other geological evidence to recreate the burial history.

1.3.3 Interval Velocities in Shale

Richardsen et al. (1993) models uplift based on interval veloci-

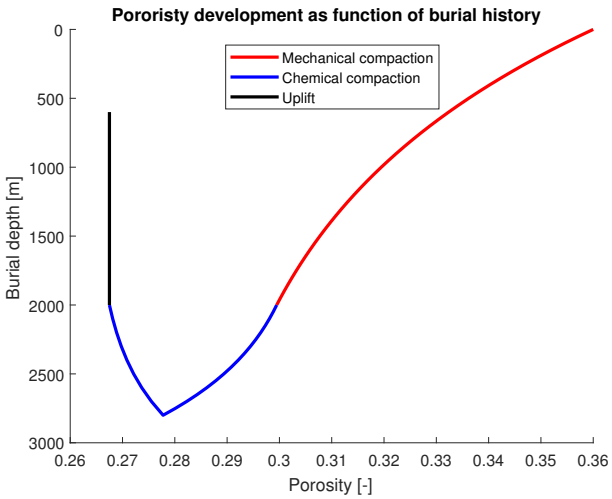

Figure 1.4: Porosity loss as a function of burial depth for the burial history shown in figure 1.3. The mechanical compaction is modelled with the model from Lander and Walderhaug (1999), and the amount of cement is modelled with the model in Walderhaug (1996). Porosity is assumed to remain unchanged as a result of the uplift.

ties in shale. The methodology is rooted in two assumptions:

1. Velocity increase in shales due to compaction is caused by a reduction in porosity

2. There exists a linear relationship between the porosity and interval velocities

Under these assumptions, the present day properties of the shale reflects the maximum burial depth of the shale. This is somewhat similar to the assumption that there is no change in the sandstone after it is uplifted out of the cementation domain.

1.3.4 The Smectite to Illite Transformation

Smectite and illite commonly occur in mixed layer clays (Eslinger and Pevear, 1988). The amount of illite, and the ordering of the smectite/illite is directly related to temperature in the presence of sufficient initial potassium (Eslinger and Pevear, 1988). The ordering of smectite and illite in the mixture is not discussed in detail (see Eslinger and Pevear (1988) for a detailed description), apart from the notable fact that the ordering is related to the amount of smectite and temperature.

Eslinger and Pevear (1988) and Abid et al. (2004) thus suggest that the composition of mixed layer clays may be used as a paleotemperature indicator. It is however important to note that the transition from smectite to illite is also dependent on the original composition of the clay, and the availability of potassium, and so should not be used alone (Eslinger and Pevear, 1988). In terms of hydrocarbon exploration, it is interesting that the zone of abrupt transformation of smectite to illite coincides roughly with temperatures ideal for intense oil generation (Eslinger and Pevear, 1988). A way to identify smectite is by recognition of a 17Å peak in X-ray diffraction, and presence of such a peak might thus indicate that source rocks are immature, or only marginally mature (Eslinger and Pevear, 1988). Furthermore, in Abid et al. (2004) the occurrence of so-called “R1” ordered mixed layer clay at lower temperatures than expected is taken to be a possible indication of uplift.

Chapter 2

Introductory Theory

This chapter aims to provide some of the general theory utilised in several aspects of this work. More detailed theory is provided in the individual parts.

2.1 Stress, Strain and Elasticity

2.1.1 Stress and Strain

Stress is defined as the force acting through a cross-sectional area, divided by that cross sectional area (Fjær et al., 2008).

$$\sigma = \frac{F}{A} \tag{2.1}$$

Strain is a way to quantify deformation caused by applying stress to a body (Fjær et al., 2008).

2.1.2 Elasticity

An elastic material is one that is able to recover from a deformation induced by the application of a force (Fjær et al., 2008). The relationship between stress and strain in an elastic material need not be linear, the key being that the material returns to its original state upon removal of the force (Wood, 1990).

The generalised Hooke's law provides the relationship between stresses and strains in a material that is linearly elastic

$$\sigma_{ij} = \sum_{k=1}^{3}\sum_{l=1}^{3} c_{ijkl}\epsilon_{kl} \tag{2.2}$$

Isotropic materials are materials in which the properties are independent of orientation, and in that case Hooke's law can be written as (Fjær et al., 2008)

$$\begin{bmatrix}\sigma_x\\ \sigma_y\\ \sigma_z\\ \tau_{yz}\\ \tau_{xz}\\ \tau_{xy}\end{bmatrix} = \begin{bmatrix}\lambda+2G & \lambda & \lambda & 0 & 0 & 0\\ \lambda & \lambda+2G & \lambda & 0 & 0 & 0\\ \lambda & \lambda & \lambda+2G & 0 & 0 & 0\\ 0 & 0 & 0 & 2G & 0 & 0\\ 0 & 0 & 0 & 0 & 2G & 0\\ 0 & 0 & 0 & 0 & 0 & 2G\end{bmatrix}\begin{bmatrix}\epsilon_x\\ \epsilon_y\\ \epsilon_z\\ \Gamma_{yz}\\ \Gamma_{xz}\\ \Gamma_{xy}\end{bmatrix} \tag{2.3}$$

In the above equation, σ_i and ϵ_i are those stresses and strains which are parallel to the principal axes in a coordinate system where $x = 1$, $y = 2$ and $z = 3$, so called "normal" stresses and strains. The shear stress and strains are represented by τ and γ respectively.

λ and G are the Lamé parameters. G is the shear modulus and quantifies the materials ability withstand shear deformation, λ does not have a simple physical interpretation (Shearer, 2009). There exists three more parameters that are commonly used to describe isotropic materials.

- Young's modulus, E, is the ratio between the extensional stress, and subsequent strain in a cylinder where both ends are pulled (Shearer, 2009).
- The ratio between a hydrostatic change in stress and the volumetric strain caused by this is called bulk modulus, and is denoted K (Shearer, 2009).
- Poisson's ratio, ν is a measure of the lateral contraction in relation to a longitudinal extension when a cylinder is pulled at both ends (Shearer, 2009)

Under macroscopic changes in stress, porous materials generally exhibit non-linear behaviour, such that the application of stress leads to irrecoverable damage. One potential cause of this is changes to the grain packing (Gassmann, 1951). For stress variations that are small enough however, deformation might be reversible. Propagation of waves induce only small strains, and thus the porous media might behave "differentially elastic" (Gassmann, 1951).

2.2 Overburden Stress and Pore Pressure

Vertical stress in the subsurface can be calculated, if the properties of the overburden are known (Bjørlykke et al., 2015)

$$\sigma_v = \int_0^z \rho(z) g dz \tag{2.4}$$

where ρ is the depth-dependent density, and g is the acceleration due to gravity.

If the rock is saturated with water that is unable to escape, the fluid will carry some of the load. This reduces the "effective stress" according to the equation

$$\sigma' = \sigma - \alpha P_p \tag{2.5}$$

Where σ' is an effective stress, σ is the total stress, and P_p is the pore pressure. α is a parameter known as Biot's alpha, given by $\alpha = \frac{C}{M}$, where C and M are extra elastic moduli needed to fully describe the two-phase system (Biot (1962), Fjær et al. (2008)). By subtracting the load carried by the fluid, the remaining load is carried by the framework of the porous system[1].

2.3 Anisotropy

If the response of a material to deformation is dependent on the orientation and direction, it is called anisotropic (Fjær et al., 2008).

Some sources of anisotropy include

1. Intrinsic,such as from clay platelet orientation
2. Stress induced
3. Layering

Deformation of anisotropic media is governed by the generalised Hooke's law, given in equation (2.2). At the lowest symmetry (triclinic), there are 21 independent elastic parameters. By making assumptions regarding symmetries, the number of elastic parameters can be brought down. A common assumption is "Vertical Transverse Isotropy (VTI)" referring to a material with a vertical symmetry axis, and a horizontal symmetry plane (Fjær et al., 2008).

2.4 Elastic Wave Velocities

For an isotropic, linearly elastic and homogeneous material, the P- and S wave velocities can be given as Fjær et al. (2008)

$$V_p = \sqrt{\frac{K + \frac{4}{3}G}{\rho}} \tag{2.6}$$

$$V_s = \sqrt{\frac{\rho}{G}} \tag{2.7}$$

From these equations, it is clear that the velocities are functions of the elastic moduli and the density of the rock.

In anisotropic media, the case is naturally a little more complex. The propagation velocities can be related to the parameters in equation (2.2), propagation direction and particle displacement through the Christoffel equation (Fjær et al., 2008)

$$\sum_{i,j}(C_{ijkl}l_j l_l - \rho v^2 \delta_{ik})u_k^0 = 0 \tag{2.8}$$

This will not be discussed in any great detail, for a thorough discussion, see for example Fjær et al. (2008).

[1] Some additional comments regarding the presence of pore fluids in the pore network is discussed in appendix B.

For a VTI media, the stiffness matrix, after introduction of Voigt notation[2] (Voigt, 1910) can be written

$$\mathbf{C} = \begin{bmatrix} C_{11} & C_{11}-2C_{66} & C_{13} & 0 & 0 & 0 \\ C_{11}-2C_{66} & C_{11} & C_{13} & 0 & 0 & 0 \\ C_{13} & C_{13} & C_{33} & 0 & 0 & 0 \\ 0 & 0 & 0 & C_{44} & 0 & 0 \\ 0 & 0 & 0 & 0 & C_{44} & 0 \\ 0 & 0 & 0 & 0 & 0 & C_{66} \end{bmatrix} \tag{2.9}$$

The velocity of a wave with propagation and particle displacement parallel to the axis of symmetry (A vertically propagating P-wave) is given as (where z is the vertical axis)

$$V_{p,z} = \sqrt{\frac{C_{33}}{\rho}} \tag{2.10}$$

A P-wave travelling perpendicular to the axis of symmetry would have velocity given by

$$V_{p,(x,y)} = \sqrt{\frac{C_{11}}{\rho}} \tag{2.11}$$

A S-wave travelling parallel to the axis of symmetry (particle displacement does not matter, as it will be in the symmetry plane) has velocity given by

$$V_{s,z} = \sqrt{\frac{C_{44}}{\rho}} \tag{2.12}$$

2.5 Hashin-Shtrikhman Bounds

The Hashin-Shtrikhman bounds are a way of constraining the value of a mixture of two phases with different elastic properties, based on their individual elastic properties and volume fractions (Mavko et al., 2009).

2.5.1 Isotropic Formulation

To compute the bounds for an assemblage of potentially more than two phases Berryman (1995) introduces three equations

$$\Lambda(x) = \left(\sum_{i=1}^{N} \frac{f_i}{K_i + \frac{4x}{3}}\right)^{-1} - \frac{4}{3}x \tag{2.13}$$

$$\Gamma(y) = \left(\sum_{i=1}^{N} \frac{f_i}{\mu_i + y}\right)^{-1} - y \tag{2.14}$$

$$F(x,z) = \frac{x}{6}\left(\frac{9z+8x}{z+2x}\right) \tag{2.15}$$

Where K_i and μ_i represent the bulk and shear moduli for the i'th component. The proportion of each component is given by f_i.
If the maximum values of K and μ are denoted K_+, μ_+ and the

[2] A way to represent a symmetric tensor by reducing its order; 11 22 33 23 13 12 → 1 2 3 4 5 6.

minimum values K_-, μ_-, the Hashin Shtrikhman bounds are defined as (Berryman, 1995)

$$K_{HS}^{\pm} = \Lambda(\mu_{\pm}) \tag{2.16}$$
$$\mu_{HS}^{\pm} = \Gamma[F(\mu_{\pm}, K_{\pm})] \tag{2.17}$$

2.5.2 Anisotropic Hashin-Shtrikman Bounds

Throughout this work anisotropy is a major factor, and the need to mix anisotropic phases will become apparent. In anisotropic media, a reformulation of the Hashin-Shtrikman bounds is needed, due to rock no longer having a well defined bulk or shear modulus. This can be found in Parnell and Calvo-Jurado (2015), and is reviewed below. The rendition here does not delve deep into the mathematical and physical considerations found in Parnell and Calvo-Jurado (2015), but aims to provide the parts necessary for implementation.

Consider two phases with symmetric TI elastic modulus tensor (written in the shorthand notation adopted in Parnell and Calvo-Jurado (2015))

$$\mathbf{C^r} = (2k_r, l_r, l_r, n_r, 2m_r, 2p_r), \quad r = 0, 1 \tag{2.18}$$

The components are related to the stiffness parameters through the following relations[3]:

$$k = \frac{C_{11} + C_{12}}{2} \tag{2.19a}$$
$$m = \frac{C_{11} - C_{12}}{2} \tag{2.19b}$$
$$l = C_{13} \tag{2.19c}$$
$$n = C_{33} \tag{2.19d}$$
$$p = C_{44} \tag{2.19e}$$

Define two functions, "Contraction" (con) and "Inversion" (inv). The contraction function acts on two 6-vectors

$$\mathbf{H^1} = (2k_1, l_1, l_1', n_1, 2m_1.2p_1)$$
$$\mathbf{H^0} = (2k_1, l_0, l_0', n_0, 2m_0, 2p_0)$$

in the following manner:

$$\begin{aligned} con(\mathbf{H^1}, \mathbf{H^0}) =& (4k_1k_0 + 2l_1l_0', 2k_1l_0 + l_1n_0, 2k_0l_1' + l_0n_1, \\ & n_1n_0 + 2l_1'l_0, 4m_1m_0, 4p_1p_0) \end{aligned} \tag{2.20}$$

the inversion function has the following result

$$\begin{aligned} inv(\mathbf{H^1}) =& \left(\frac{n_1}{2\Delta}, \frac{-l_1}{2\Delta}, \frac{l_1}{2\Delta}, \frac{k_1}{\Delta}, \frac{1}{2m_1}, \frac{1}{2p_1}\right) \\ & \Delta = k_1n_1 - l_1l_1' \end{aligned} \tag{2.21}$$

Now consider two phases, with stiffness parameters contained in $\mathbf{C^1}$ and $\mathbf{C^0}$. First let the so called comparison face be given by $\mathbf{C^0} = \mathbf{C^c}$. The bound is then given by

$$\mathbf{C^B} = \mathbf{C^0} + \phi_1\mathbf{M^0} \tag{2.22}$$

This is a lower bound if $\mathbf{C^1} - \mathbf{C^0}$ is positive semi-definite and a upper bound if $\mathbf{C^1} - \mathbf{C^0}$ is negative semi-definite. Switching $\mathbf{C^1}$ and $\mathbf{C^0}$ in the two phase compositions to be considered in this work should then produce the opposite bound, although it is important to remain consistent in the proportion definitions[4].

$\mathbf{M^0}$ is given as

$$\mathbf{M^0} = inv(\mathbf{N} + \mathbf{P_s} - \phi_1\mathbf{P_d}) \tag{2.23}$$

where

$$\mathbf{N} = inv(\mathbf{C^1} - \mathbf{C^0}) \tag{2.24}$$

It remains to define the $\mathbf{P}$-tensor. Parnell and Calvo-Jurado (2015) defines it as

$$\mathbf{P}^{\delta} = con(\mathbf{S}^{\delta}, (\mathbf{C^c})^{-1}) \tag{2.25}$$

Where $\mathbf{S}^{\delta}$ is the TI Eshelby tensor.

The resulting Eshelby tensor in the case of "a spheroidal inclusion with semi-axes $a_1 = a_2 \neq a_3$, embedded inside a TI comparison phase with axis of symmetry along x_3 and with elastic modulus tensor may be written" (Parnell and Calvo-Jurado, 2015):

$$\mathbf{S_s} = (2k_\delta, l_\delta, l_\delta', n_\delta, 2m_\delta, 2p_\delta) \tag{2.26}$$

The δ parameter is used to describe the shape of the inclusions. $\delta = 1$ is spherical. To describe the distributions of the inclusions, ϵ is used. The subscript "s" is thus to highlight "Shape" rather than "Distribution". A "d" would incite the use of ϵ.

The relationship of ϵ and δ puts a limit of how much of an inclusion can fit into a security spheroid, and consequently a limit on the amount of the inclusion phase, if the values of ϵ and δ are fixed. The relations are given in Parnell and Calvo-Jurado (2015) as

$$0 \leq \phi \leq \frac{\epsilon^2}{\delta^2}, \quad \delta > \epsilon \tag{2.27}$$
$$0 \leq \phi \leq \frac{\delta}{\epsilon}, \quad \epsilon > \delta \tag{2.28}$$

Throughout this work they are assumed to be equal, such that the inclusion phase can vary from 0 to 1 in proportion, and also implies $\mathbf{P_s} = \mathbf{P_d}$.

[3] Note that in this work Voigt notation has been adopted.

[4] In this work, the phases are limited to scenarios where $\mathbf{C^1}$ is componentwise larger than $\mathbf{C^0}$, so having $\mathbf{C^0}$ as the comparison phase produces a lower bound, and having $\mathbf{C^1}$ as the comparison phase produces the upper bound.

Further, define:

$$v_1 = \left(\frac{(\hat{l_c} - l_c)(\hat{l_c} + l_c + 2p_c)}{4n_c p_c}\right)^{1/2} + \left(\frac{(\hat{l_c} + l_c)(\hat{l_c} - l_c - 2p_c)}{4n_c p_c}\right)^{1/2} \tag{2.29a}$$

$$v_2 = \left(\frac{(\hat{l_c} - l_c)(\hat{l_c} + l_c + 2p_c)}{4n_c p_c}\right)^{1/2} - \left(\frac{(\hat{l_c} + l_c)(\hat{l_c} - l_c - 2p_c)}{4n_c p_c}\right)^{1/2} \tag{2.29b}$$

$$v_3 = \left(\frac{m_c}{p_c}\right)^{1/2} \tag{2.29c}$$

Where

$$\hat{l_c} = (n_c(k_c + m_c))^{1/2} \tag{2.30}$$

It is noted in Parnell and Calvo-Jurado (2015) that generally $v_1, v_2 \in \mathbb{C}$ with one the complex conjugate of the other.
for $v_i \in \mathbb{R}$ define:

$$I_1(v_i) = \frac{2\pi\delta}{(1 - v_i^2\delta^2)} \cdot \begin{cases} \left(\frac{cos^{-1}(v_i\delta)}{(1-v_i^2\delta^2)^{1/2}} - v_i\delta\right), & v_i\delta < 1 \\ \left(\frac{cosh^{-1}(v_i\delta)}{(v_i^2\delta^2-1)^{1/2}} - v_i\delta\right), & v_i\delta > 1 \end{cases} \tag{2.31}$$

if $v_i \in \mathbb{C}$ either of the cases of equation (2.31) can be used.

2.5.2.1 Isotropic Comparison Phase

For an isotropic comparison phase the following relations are true, based on the elastic descriptions of isotropic media (Parnell and Calvo-Jurado, 2015)

$$l_c = \lambda_c = l'_c \tag{2.32}$$

$$p_c = m_c = \mu_c \tag{2.33}$$

$$k_c + m_c = n_c = \lambda_c + 2\mu_c \tag{2.34}$$

The relation in equation (2.32) comes from the fact that $C_{13} = \lambda$, where λ is the aforementioned Lamè parameter. The relation in equation (2.33) is from the fact that $C_{44} = C_{66} = \mu_c$ and finally, equation (2.34) is from the fact that $k_c + m_c = C_{11} = C_{33} = n$.

Inserting equation (2.34) into equation (2.30) yields

$$\hat{l_c^{iso}} = n_c = k_c + m_c \tag{2.35}$$

Further insertion of equations (2.32) to (2.35) into equations (2.29a) to (2.29c) yields $v_1 = v_2 = v_3 = 1$.

For an isotropic comparison phase the components of the Eshelby Tensor becomes (Parnell and Calvo-Jurado, 2015)

$$S_{11} = 3AI_{11} + BI_1 \tag{2.36a}$$

$$S_{33} = 3AI_{33} + BI_3 \tag{2.36b}$$

$$S_{12} = AI_{11} - BI_1 \tag{2.36c}$$

$$S_{13} = AI_{13} - BI_1 \tag{2.36d}$$

$$S_{31} = \frac{A}{\delta^2}I_{13} - BI_3 \tag{2.36e}$$

$$S_{44} = \frac{\delta^2 + 1}{2\delta^2}AI_{13} + \frac{B}{2}(I_1 + I_3) \tag{2.36f}$$

Where

$$A = \frac{1}{8\pi(1 - \nu_c)} \tag{2.37a}$$

$$B = (1 - 2\nu_c)A \tag{2.37b}$$

ν_c is the Poisson's ratio of the isotropic comparison medium. Further

$$I_3 = 4\pi - 2I_1 \tag{2.38a}$$

$$I_{33} = \frac{4\pi}{3} - \frac{2}{3}I_{13} \tag{2.38b}$$

$$I_{11} = \pi - \frac{I_1 - I_3}{4(\delta^2 - 1)} \tag{2.38c}$$

$$I_{13} = \frac{\delta^2(I_1 - I_3)}{\delta^2 - 1} \tag{2.38d}$$

In the case of $\delta = 1$ there is division by zero in equation (2.31).

Parnell and Calvo-Jurado (2015) gives this limit as $I_1 = \frac{4\pi}{3}$. What happens to all the remaining divide by zero terms is not explicitly given, but still of interest, as isotropic comparison phases are to be used.

I_3 is relatively simple and is given as

$$I_3^{\delta=1,iso} = 4\pi - 2\frac{4\pi}{3} = \frac{4\pi}{3} \tag{2.39}$$

where the superscript $\delta = 1, iso$ refers to the case of isotropic inclusion with $\delta = 1$. The limit of the remaining terms has been found as:

$$I_{13}^{\delta=1,iso} = I_{11}^{\delta=1,iso} = I_{33}^{\delta=1,iso} = \frac{4\pi}{5} \tag{2.40}$$

Formal proof is omitted, but visual representation of the limit is given in appendix A

2.5.2.2 Anisotropic Comparison Phase

For a TI comparison phase:

$$S_{11} = \sum_{i=1}^{2}[2p_c(1+K_i)v_i^2 - m_c]L_i v_i I_1(v_i) + \frac{1}{2}Dm_c I_1(v_3) \quad (2.41a)$$

$$S_{12} = \sum_{i=1}^{2}[2p_c(1+K_i)v_i^2 - 3m_c]L_i v_i I_1(v_i) - \frac{1}{2}Dm_c I_1(v_3) \quad (2.41b)$$

$$S_{33} = 2\sum_{i=1}^{2}[l_c - n_c K_i v_i^2]v_i^3 K_i L_i I_3(v_i) \quad (2.41c)$$

$$S_{13} = 2\sum_{i=1}^{2}[l_c - n_c K_i v_i^2]v_i L_i I_1(v_i) \quad (2.41d)$$

$$S_{31} = 2\sum_{i=1}^{2}[p_c v_i^2(1+K_i) - m_c]K_i L_i v_i^3 I_3(v_i) \quad (2.41e)$$

$$S_{44} = 0.5p_c\sum_{i=1}^{2} L_i v_i^3(1+K_i)(I_3(v_i) - 2K_i I_1(v_i)) + \frac{1}{4}Dp_c I_3(v_3)v_3^2 \quad (2.41f)$$

where

$$D = \frac{1}{4\pi p_c v_3} \quad (2.42a)$$

$$K_i = \frac{(k_c + m_c)/v_i^2 - p_c}{l_c + p_c} \quad (2.42b)$$

$$L_i = (-1)^i \frac{p_c - n_c v_i^2}{8\pi n_c p_c (v_1^2 - v_2^2)v_i^2} \quad (2.42c)$$

Parnell and Calvo-Jurado (2015) uses in these equations the notation $I_3(v_i) = \frac{4\pi}{v_i} - 2I_1(v_i)$. These results can then be used to create the short-hand notation through

$$k_\delta = \frac{1}{2}(S_{11} + S_{12}) \quad (2.43a)$$

$$l_\delta = S_{13} \quad (2.43b)$$

$$l'_\delta = S_{31} \quad (2.43c)$$

$$n_\delta = S_{33} \quad (2.43d)$$

$$m_\delta = \frac{1}{2}(S_{11} - S_{12}) \quad (2.43e)$$

$$p_\delta = S_{44} \quad (2.43f)$$

The final step is then to utilise equation (2.25) to calculate $\mathbf{P}$.

2.5.2.3 Comparison of the Isotropic and Anisotropic Methods

Setting $\delta = \epsilon = 1$ means that mixing of two isotropic phases should yield an isotropic result, identical to the isotropic Hashin-Shtrikhman bound. Figure 2.1 and 2.2 demonstrates this for two phases with elastic parameters given in table 2.1, an indeed the bounds overlap.

Table 2.1: Elastic parameters of the two phases used to demonstrate the equivalence of the anisotropic and isotropic Hashin-Shtrikman bounds in the limit of isotropic phases with $\delta = \epsilon = 1$. The values are taken from Parnell and Calvo-Jurado (2015), and k, l, m, n, p refer to the parameters used in the anisotropic formulation.

Phase 1	
C_{11} (k+m)	6.73 GPa
C_{12} (k-m)	4.19 GPa
C_{13} (l)	4.19 GPa
C_{33} (n)	6.73 GPa
C_{44} (p)	1.27 GPa
$K = C_{11} - \frac{4C_{44}}{3}$ (Bulk modulus)	5.04 GPa
$G = C_{44}$ (Shear modulus)	1.27 GPa

Phase 2	
C_{11} (k+m)	77.77 GPa
C_{12} (k-m)	25.77 GPa
C_{13} (l)	25.77 GPa
C_{33} (n)	77.77 GPa
C_{44} (p)	26 GPa
$K = C_{11} - \frac{4C_{44}}{3}$ (Bulk modulus)	43.1 GPa
$G = C_{44}$ (Shear modulus)	26 GPa

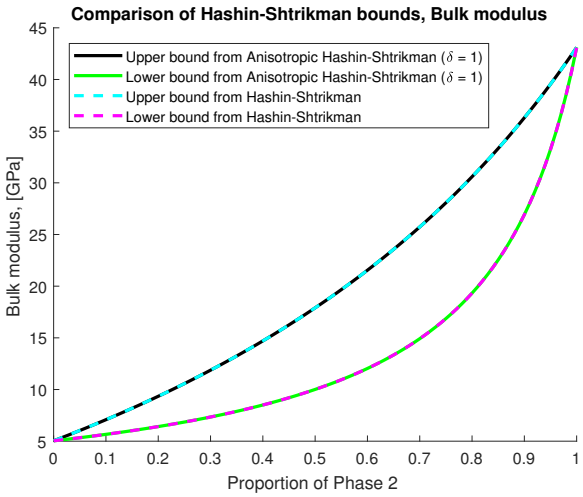

Figure 2.1: Comparison of the upper and lower bounds of the bulk modulus estimated from the isotropic Hashin-Shtrikman bounds presented in Mavko et al. (2009), and the anisotropic Hashin-Shtrikman formulations in the limit of isotropic phases and $\delta = \epsilon = 1$. The input parameters are given in table 2.1, and are taken from Parnell and Calvo-Jurado (2015). Note that the figures in Parnell and Calvo-Jurado (2015) are normalised against the lowest elastic parameter, which is not done here, as it seems unnecessary. The bounds overlap as expected.

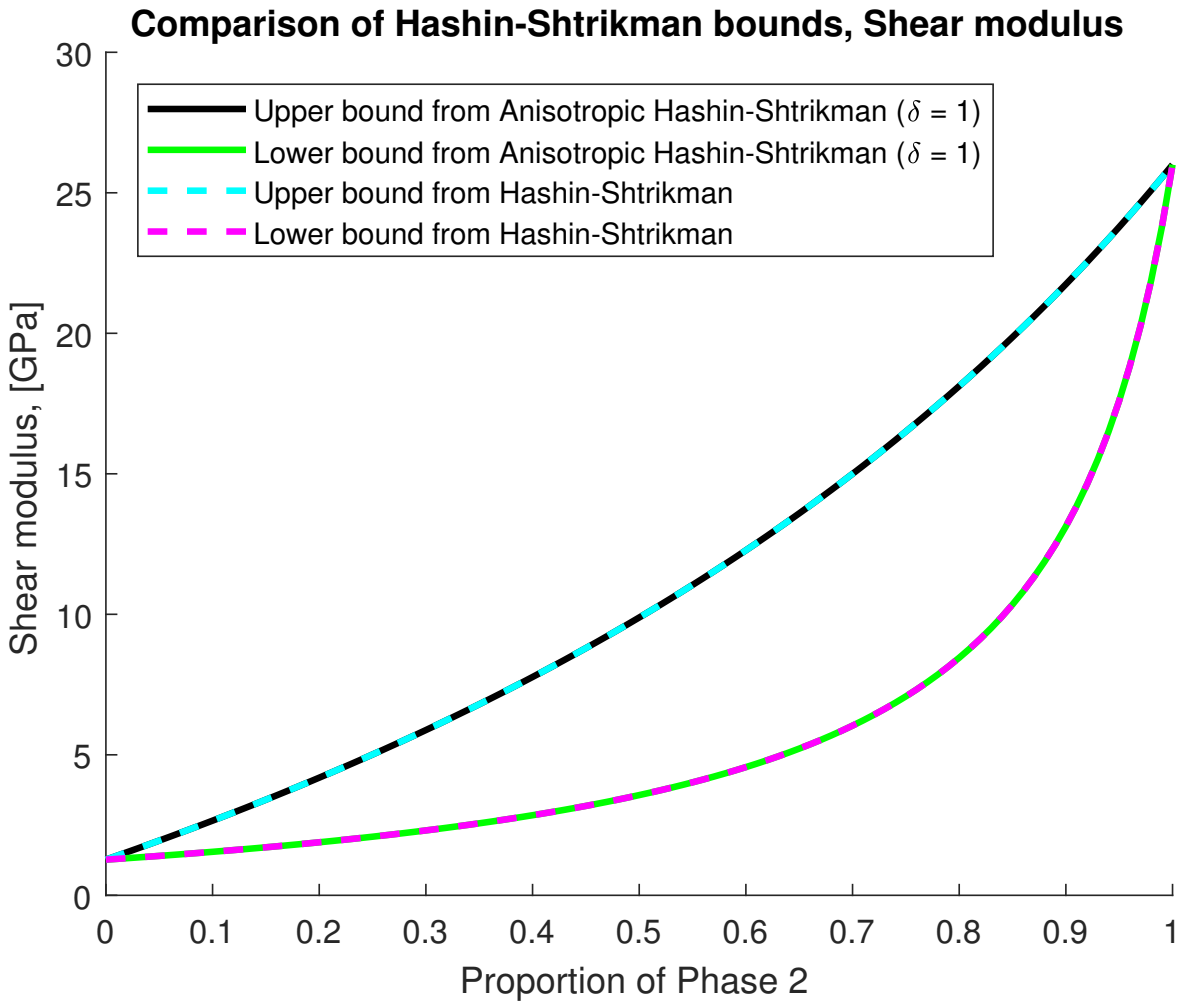

Figure 2.2: Comparison of the upper and lower bounds of the shear modulus estimated from the isotropic Hashin-Shtrikman bounds presented in Mavko et al. (2009), and the anisotropic Hashin-Shtrikman formulations in the limit of isotropic phases and $\delta = \epsilon = 1$. The input parameters are given in table 2.1, and are taken from Parnell and Calvo-Jurado (2015). Note that the figures in Parnell and Calvo-Jurado (2015) are normalised against the lowest elastic parameter, which is not done here, as it seems unnecessary. The bounds overlap as expected.

Part II

Laboratory Experiments Simulating Burial and Uplift - A Bridge From Previous Work

Chapter 3

Overview of Experimental Procedure and Interpretation

3.1 Introduction to Part II

This part includes a rendition of prior work. The work in Torset (2017)[1] investigated the consequences that simulated uplift has on a synthetic sandstone. This part will demonstrate some observations in the experimental data that are not included in the diagenetic sandstone modelling used to create the conceptual model seen in figure 1.2. In the next chapter, an investigation into how modelling might improve the conceptual model in terms of incorporating the experimental observations is presented.

3.2 Experimental Background

The data used in Torset (2017) were from experiments done by SINTEF in 2013. SINTEF's motivation was to investigate how coring damaged the rock, and how subsequent laboratory tests were not directly adequate in predicting reservoir compaction. According to SINTEF, the aim was to "to improve best practices for correction of core compaction data for stress-release induced data" (Holt et al., 2013).

The motivation was thus not directly linked to uplift estimates, and the effect of uplift on sandstones. As part of the experiment, there was however one "reference" stress path which was not subjected to the simulated coring. This is the stress path that will serve as the basis for the discussion in this work.

3.3 Experimental Procedure

The synthetic sandstones were formed by mixing sodium silicate and a representative grain size. After being precompacted, the sample was flushed with CO_2, which reacts with the silicate to form quartz, which precipitates as a synthetic cement. This happens according to the reaction (Kiesel and van Oene, 1982):

$$Na_2Si_3O_7 + 2H_2O + 2CO_2 \rightarrow 3SiO_2xH_2O + 2NaHCO_3$$

This silicate is less brittle than naturally occurring cement according to Holt et al. (2000), who utilised the same procedure.

As a "measure of representativeness" between the synthetic and real sandstones, Holt et al. (2000) provide four criteria:

- The mechanical behaviour of the synthetic sample should be the same as a target natural rock.
- Key petrophysical properties such as permeability, elastic wave velocity and porosity should be close to that of the target rock.
- The visual characteristics of the real and synthetic rocks should be the same.
- Real and synthetic rocks should possess comparable microstructure.

Varying the amounts of sodium silicate in the samples allows for the creation of sandstones of variable stiffness. For the purpose of this work, the primary focus will be on the sample labelled "stiff"[2]. Some additional samples are discussed in part VI and in appendix C.

3.3.1 "Burial History"

Figure 3.1 shows the stress path[3] of the synthetic sandstone. Prior to cementation the sample is loaded along a stress path defined by $\sigma_z = 2\sigma_r$. After the sample is flushed with CO_2 it is left for two hours to settle. Following this, the sample is loaded (simulated burial) under uniaxial strain conditions, before being unloaded (simulated uplift) under uniaxial strain conditions. Stress paths that involve loading after cementation are referred to as "A"[4].

[1] Torset (2017) was a specialisation project conducted at NTNU. It is not published, so this part will give insight into what aspects of this thesis that originates from previous work.

[2] Which is actually quite soft, just stiff in relation to the other samples.

[3] Taken to be analogous with burial history.

[4] Experiments simulating coring involve unloading right after cementation and their stress paths are identified by "B".

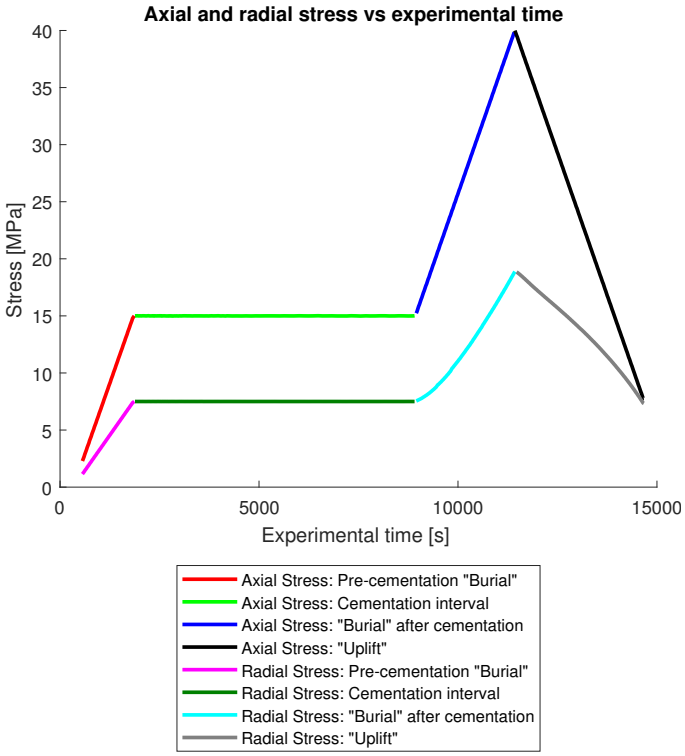

Figure 3.1: The axial and radial stress paths over the experimental time interval utilised in this work. The experiment did have another loading/unloading phase which was discussed in Torset (2017), but in relation to the modelling in this work the time interval displayed in this figure is sufficient. During pre-cementation loading and the cementation interval it can be observed that $\sigma_z = 2\sigma_r$. During loading and unloading after cementation the criteria is uniaxial strain.

3.4 Results

In Torset (2017), a significant number of experimental parameters are plotted against each other to give a broad overview of the processes occurring. In this chapter however, only a small number of those results are displayed. These are the ones deemed necessary for the subsequent work. Some additional experimental results are given in appendix C together with a more detailed discussion. In addition to this, some experimental data are given in the extended discussion in part VI in relation to the effect of cement volume and unloading right after cementation (as opposed to unloading after first loading as done here). The reason for segregating the experimental results is that the model developed will be implemented on one cement volume with one stress path, which is the sample discussed in the present chapter.

Figure 3.2 shows the axial P-wave velocity plotted against axial stress for the simulated burial history. Since these samples are left to cement over a constant stress, the velocity increase due to cementation naturally happens at that stress, which can be seen at 15MPa.

During loading after cementation the axial P-wave velocity is still seemingly stress dependent. The cementation has however made the sample less dependent to the further increase in stress. The most important observation in relation to uplift is that the velocity during unloading acts distinctly different than during the loading after cementation, even though both paths are defined by uniaxial strain. At 15MPa, the velocity is around 200m/s lower during simulated uplift than right after cementation, and the stress dependence keeps increasing. At the end of the unloading the total change in axial P-wave velocity is around 500 m/s compared to maximum burial.

The P-wave anisotropy is shown against the axial stress development in figure 3.3. During loading prior to cementation the P-wave anisotropy becomes slightly more negative. Cementation brings the anisotropy towards isotropy. The main observation from this figure is the large variation in P-wave anisotropy during loading and unloading after cementation. The loading conditions (uniaxial strain) are the same, but the P-wave anisotropy is actually reversed upon simulated uplift.

The stress versus strain is shown in figure 3.4. It can be seen that during the uplift there is less strain, as compared to the burial, conforming well with the prediction that porosity change during uplift is relatively small. Upon reversal of the stress, it would be expected that the strain is also reversed, causing extension in the core. It can be observed however that over the first few MPa's of unloading, the sample keeps compacting (i.e., axial strain increases). This is known as creep (Fjær et al., 2015).

3.5 Interpretation

The stress release during uplift can result in brittle deformation, leading to the formation of, and/or reactivation of microcracks

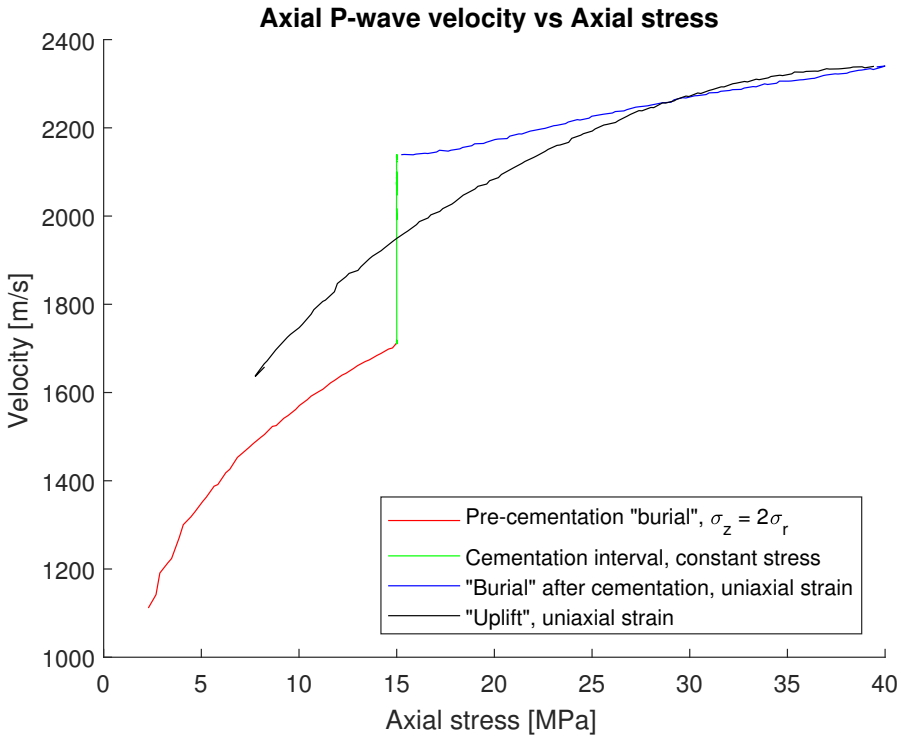

Figure 3.2: Measured axial P-wave velocity visualised against the axial stress. The measured data are discrete, but are joined by lines to form the observed trends, and this will be adopted for all figures showing experimental data. Three things to note: Large increase in velocity during cementation at constant stress, some stress dependence upon continued loading, but a much high stress dependence upon subsequent unloading

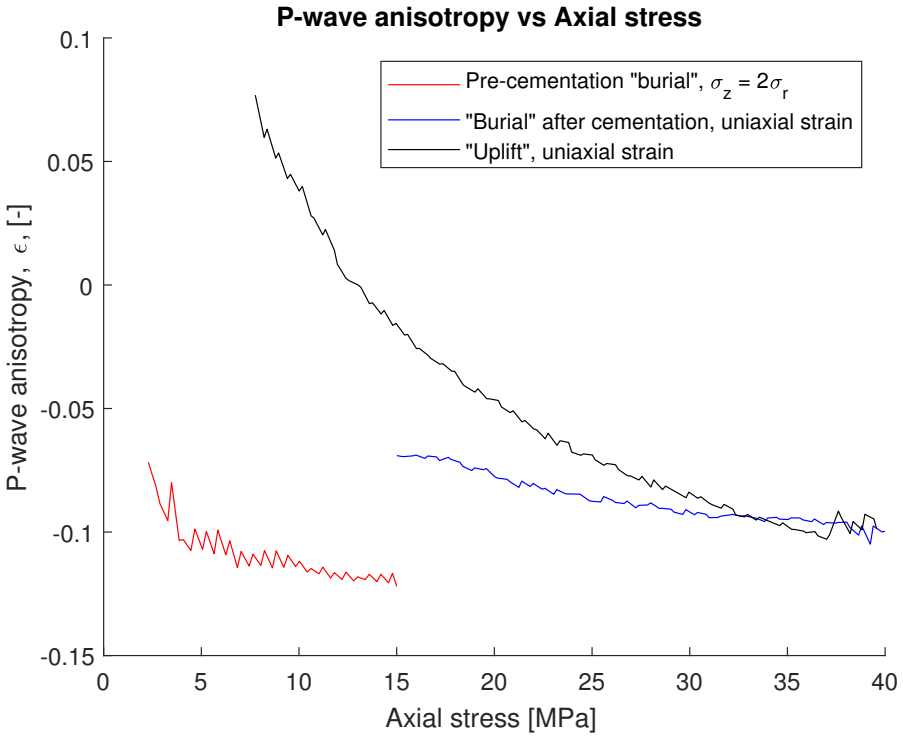

Figure 3.3: Measured P-wave anisotropy visualised against the axial stress. The measured data are discrete, but are joined by lines to form the observed trends, and this will be adopted for all figures showing experimental data. In figures showing anisotropy this occasionally causes a "zig-zag" pattern due to the indexing of the data containing radial and axial P-wave velocities. Three things to note: The P-wave anisotropy becomes more negative as the sample is loaded prior to cementation, the cementation brings the rock closer to isotropy, before a reversal of the P-wave anisotropy is seen during simulated uplift.

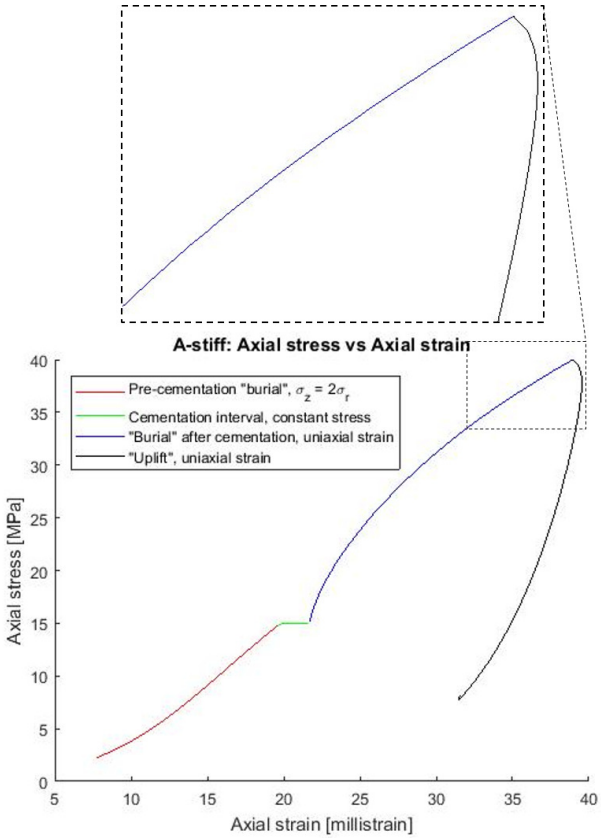

Figure 3.4: Measured axial strain visualised against the axial stress. The measured data are discrete, but are joined by lines to form the observed trends, and this will be adopted for all figures showing experimental data. During uplift the strain does not return to its pre-burial values, indicating permanent deformation and reduction in porosity. Inset: Upon reversal of the stress, there is a creep effect, whereby the strain keeps increasing, even though the stress has been reversed

and fractures (Bredesen, 2017). According to Holt et al. (1997), opening and closing of microcracks, as the stress is varied facilitates variations in stress dependence. The term "crack" is used loosely in the following discussion, to also include grain contacts that are failing, or poorly cemented. Open cracks that are oriented with normals parallel to either wave propagation direction, or the particle displacement direction reduce the velocity of propagating waves (Fjær et al., 2008, Chapter 5). If these cracks then have a preferred direction, velocity development would be expected to be affected in an anisotropic way.

Holt et al. (2004) conducted numerical simulations to investigate the effect of unloading on cemented grain contacts. It is discussed how these cement bonds may break through tension as well as shear. The cement in Holt et al. (2004) is formed at the max stress level, which is different from the present discussion, and thus may alter the processes. Furthermore, the results in Holt et al. (2004) are dependent on parameters provided to the cement bonds.
One way to explain these observations is thus microcracks with normals preferentially oriented in the axial direction upon simulated uplift. This would reduce the axial P-wave velocity to a greater extent than the radial P-wave velocity. The P-wave anisotropy is thus reversed when the sample is subjected to sufficient amounts of simulated uplift. These microcracks could be broken cement bonds. As the sample is subjected to uniaxial strain during unloading, the only extension is in the axial direction. This means tensional axial stress might develop at grain contacts, causing breakage mainly oriented in the axial direction.

3.6 Summarising Remarks

Simulated uplift in the laboratory yielded an increased stress dependence in the observed P-wave velocity, with the uplift affecting the axial velocity to a larger degree than the radial P-wave velocity, leading to a reversal in the P-wave anisotropy.

The exact mechanisms causing the increased stress dependence are not exactly known, although the interpretation made in Torset (2017) revolves around brittle deformation in the core, leading to the formation of microcracks, possibly from the breakage of cement bonds.

Chapter 4

Uplift Modelling With the Crack Model

4.1 Introduction to Uplift Modelling

It was an objective in Torset (2017) to investigate models that were able to explain the observed P-wave velocities during simulated uplift. In "explain", fitting the observed data was of course an important aspect. It was also desirable that the model should also carry some physical interpretation concomitant with reported potential effects, such as microcracks.

In Torset (2017), three models were tested to model the measured velocities, namely the models in Prioul et al. (2004), Fjær (2006) and Ciz and Shapiro (2008). Based on the interpretation of the microcrack formation, as well as the fact that there is not a lot of cement, the crack model presented in Fjær (2006) was deemed to be appropriate.

4.2 The Crack Model (Fjær 2006)

A model to describe the stress dependence of the elastic wave velocities in weak rocks is depicted in Fjær (2006). The starting point for the model is that the rock can be considered as a solid, containing flat cracks, and spherical pores, remembering the definition of cracks to include poorly or failing cemented grain contacts. The cracks are assumed to be contained in three sets, with orientations normal to the principal stresses, as illustrated in figure 4.1.

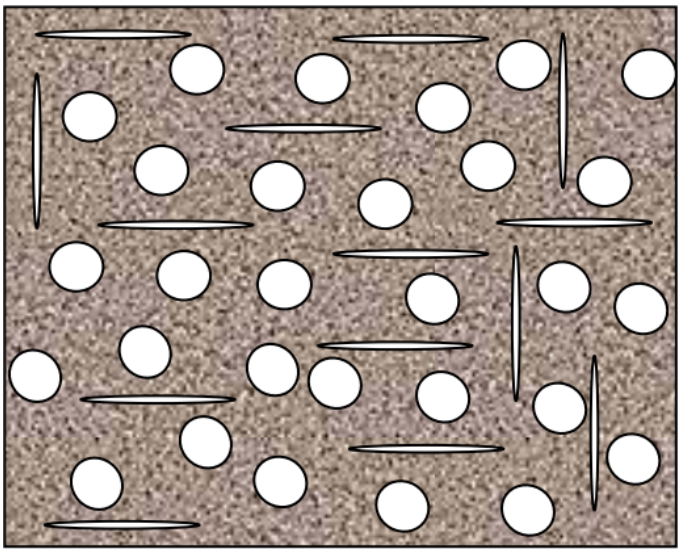

Figure 4.1: Taken from Fjær (2006), this figure depicts the three sets of cracks with normals oriented perpendicular to each other that are are present in the crack model.

If the cracks and pores are assumed to be non-interacting, the elements of the elastic stiffness tensor are given as (Fjær, 2006)

$$C_{11} = C^0_{11}[1 - Q^p_{11}\phi - Q_{33}\zeta_x - Q_{11}(\zeta_y + \zeta_z)] \quad (4.1)$$
$$C_{22} = C^0_{22}[1 - Q^p_{11}\phi - Q_{33}\zeta_y - Q_{11}(\zeta_y + \zeta_x)] \quad (4.2)$$
$$C_{33} = C^0_{33}[1 - Q^p_{33}\phi - Q_{33}\zeta_z - Q_{11}(\zeta_y + \zeta_x)] \quad (4.3)$$
$$C_{12} = C^0_{12}[1 - Q^p_{13}\phi - Q_{12}\zeta_z - Q_{13}(\zeta_y + \zeta_x)] \quad (4.4)$$
$$C_{13} = C^0_{13}[1 - Q^p_{13}\phi - Q_{12}\zeta_y - Q_{13}(\zeta_z + \zeta_x)] \quad (4.5)$$
$$C_{23} = C^0_{23}[1 - Q^p_{13}\phi - Q_{12}\zeta_x - Q_{13}(\zeta_y + \zeta_z)] \quad (4.6)$$
$$C_{44} = C^0_{44}[1 - Q^p_{44}\phi - Q_{44}(\zeta_y + \zeta_z) - Q_{66}\zeta_x] \quad (4.7)$$
$$C_{55} = C^0_{55}[1 - Q^p_{44}\phi - Q_{44}(\zeta_x + \zeta_z) - Q_{66}\zeta_z] \quad (4.8)$$
$$C_{66} = C^0_{66}[1 - Q^p_{66}\phi - Q_{44}(\zeta_y + \zeta_x) - Q_{66}\zeta_z] \quad (4.9)$$

In a rock without cracks or pores, the C^0_{ij}s represent the stiffness of the rock. In the absence of anisotropy prior to crack formation C_{11}, C_{22} and C_{33} are equivalent to the P-wave modulus of the solid material, given as $M = K + \frac{4G}{3}$. C_{44}, C_{55} and C_{66} are equivalent to the shear modulus G of the solid material. ϕ is the porosity and the ζ's represent the crack densities.

The Q's are given as (Fjær et al., 2008, p. 233-235)

$$Q_{11} = \frac{16}{3}\frac{\nu^2}{1-2\nu}D \tag{4.10a}$$

$$Q_{33} = \frac{16}{3}\frac{(1-\nu)^2}{1-2\nu}D \tag{4.10b}$$

$$Q_{44} = \frac{16}{3}\frac{1-\nu}{2-\nu} \tag{4.10c}$$

$$Q_{66} = 0 \tag{4.10d}$$

$$Q^p_{11} = Q^p_{33} = \frac{1}{2}\left(\frac{1+\nu}{1-2\nu} + 10\frac{1-2\nu}{7-5\nu}\right) \tag{4.10e}$$

$$Q^p_{44} = Q^p_{66} = 15\frac{1-\nu}{7-5\nu} \tag{4.10f}$$

Selecting a Poisson's ratio of 0.076 it can be seen that[1]

$$Q_{11} = 0.036, \;\; Q_{33} = 5.37, \;\; Q_{44} = 2.56 \tag{4.11}$$

Looking at equations (4.1), (4.3) and (4.7) it can be seen that C_{11} in this scenario is in terms of crack densities nearly only dependent on ζ_x, C_{33} is primarily dependent on ζ_z and C_{44} is dependent on both ζ_y and ζ_z. This makes sense when considering the way in which the waves propagate, as one would expect a P-wave to be primarily effect by cracks with normals parallel to the propagation direction, as is the case in the equations above. The shear wave has a more biaxial dependence, as the propagation and polarisation directions of the wave are perpendicular.

The crack densities are expressed as

$$\zeta_x = \zeta^0_x\left(\frac{\sigma^0_x + T_0}{\sigma_x + T_0}\right)^n e^{-\beta(2\epsilon_x - \epsilon_y - \epsilon_z) + \eta\Gamma^2} \tag{4.12}$$

$$\zeta_y = \zeta^0_y\left(\frac{\sigma^0_y + T_0}{\sigma_y + T_0}\right)^n e^{-\beta(2\epsilon_y - \epsilon_x - \epsilon_z) + \eta\Gamma^2} \tag{4.13}$$

$$\zeta_z = \zeta^0_z\left(\frac{\sigma^0_z + T_0}{\sigma_z + T_0}\right)^n e^{-\beta(2\epsilon_z - \epsilon_y - \epsilon_x) + \eta\Gamma^2} \tag{4.14}$$

At some reference point $\sigma_i = \sigma^0_i$ the strain is set to zero, and the crack densities denoted ζ^0_i are the crack densities at this point. T_0 is a parameter that Fjær (2006) describe as a parameter with some relation to the tensile strength. The remaining parameters are defined in Fjær (2006) as

- n: "Key parameter for stress sensitivity related to normal stress"
- β: "A key parameter for stress sensitivity due to shear deformation"
- η: A term related to the maximum shear strain, Γ
- In TI media $\Gamma = \epsilon_z - \epsilon_r$

Under triaxial stress applied to a circular core, with a radial confining stress[2] where $\sigma_x = \sigma_y = \sigma_r \neq \sigma_z$, and $\epsilon_x = \epsilon_y = \epsilon_r \neq \epsilon_z$, then $\zeta_x = \zeta_y = \zeta_r$. Returning to equations (4.1), (4.3) and (4.7) with the previous information of the Q's, it is clear that the crack model will predict an axial P-wave velocity that in terms of stress is dependent primarily on the axial stress, and a radial P-wave which is dependent on the radial stress. The axial shear wave velocity will have a more biaxial stress dependence, consistent with results from triaxial experiments conducted by Dillen et al. (1999).

In Fjær (2006), porosity is calculated as

$$\phi = \frac{\phi_0 - \epsilon_{vol}}{1 - \epsilon_{vol}} \tag{4.15}$$

where ϕ_0 is the initial porosity.

The P-wave modulus in Fjær (2006) is chosen "somewhat arbitrarily", and suitable values for the shear modulus and crack densities are chosen to match the stiffnesses in the reference point. The Poisson's ratio is set to 0.2, which Fjær (2006) describes as "typical for rock constituting solids". Fjær (2006) also allows the Poisson's ratio to vary independently of the values of H_0 and G_0. This introduces an additional degree of freedom, but according to Fjær (2006) "given the level of approximations used in this model, the potential physical contribution from this degree of freedom is minor".

4.2.1 Implementation of the Crack Model in Torset (2017)

Implementation of the crack model in Torset (2017) was done by letting the maximum "burial" serve as the reference point. The crack densities ζ^0_x and ζ^0_z were calibrated to the measured velocities, and predicted porosity and densities.

This starting point was fed into a Levenberg-Marquardt algorithm[3] which calculated the optimal choice of n, β and η. These parameters were thus estimated based on the measured velocities as well as estimated porosity and density for the measured stress and strain values. In addition to the measurements, grain parameters are needed.

The porosity and therefore density estimations introduces some degree of uncertainty, as the porosity is never measured, but only estimated. Deviations in the porosity from the actual values would naturally change the observed model, but the fitting algorithm would likely change the optimal parameters in response to this. If the porosity deviates from the estimated value, this can be compensated in other parameters used for the fitting of the data.

4.2.2 Sensitivity to Solid Parameters in the Crack Model

Torset (2017) discussed the effect of the solid parameters on the models ability to recreate the observed velocities. In terms of P-wave anisotropy, the choice of different parameters does not

[1] D = 1 in dry rocks

[2] r for radial

[3] Levenberg-Marquardt is a standard technique for solving non-linear least squares problems (Gavin, 2011). In *Matlab* it is easily implemented through a built in function.

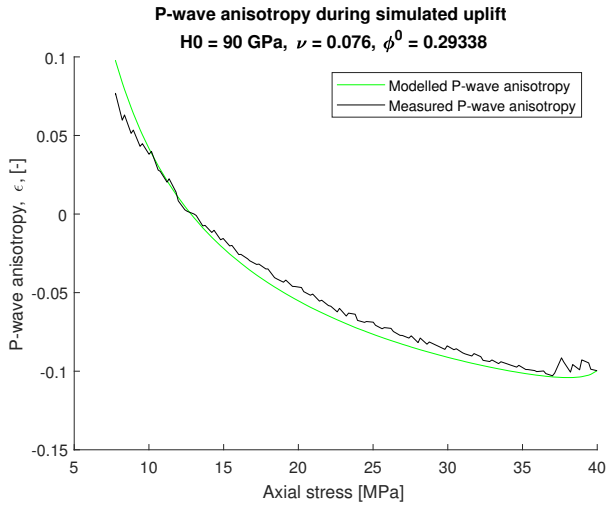

Figure 4.2: Modelled P-wave anisotropy during uplift, with solid parameters $H^0 = 90$ GPa, $\nu = 0.076$ and porosity $\phi = 0.293$. The modelled anisotropy provides a relatively good fit

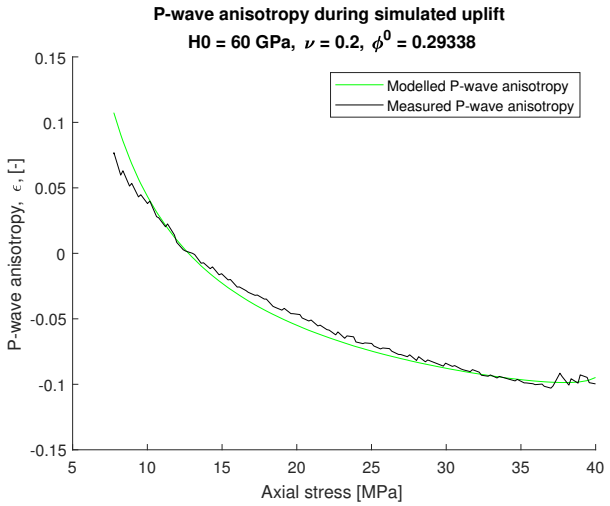

Figure 4.3: Modelled P-wave anisotropy during uplift, with solid parameters $H^0 = 60$ GPa, $\nu = 0.2$ and porosity $\phi = 0.293$. The modelled anisotropy fits quite well, and is not too different from that in figure 4.2

seem not impact the model a great deal, as seen in figures 4.2 and 4.3. Both sets of parameters produce reasonable recreations of the measured experimental data. The reason for why both sets of parameters can yield relatively good fits is because the difference is grain parameters is compensated by the values of the crack densities.

The axial shear wave velocity is however greatly affected, as can be seen from figure 4.4 and 4.5. The value of $\nu = 0.2$ is what Fjær (2006) suggests should be used, and can be seen to give a much better prediction of the axial shear wave velocities.

The underlying reason for why the crack densities are not able to compensate for variable grain parameters when describing the axial shear wave velocity can be found by returning to the defining equations for C_{11}, C_{33} and C_{44}. Fjær (2006) allows the shear modulus to vary independently of the Poisson's ratio and bulk modulus of the material, and so these equations form, in the reference point, a system of three equations, and three unknowns (G^0, ζ_x and ζ_z). This is because in the experimental data only these three stiffnesses are available.

C_{11} and C_{33} are completely given by ζ_z and ζ_x, and so these equations can be solved for ζ_x and ζ_z yielding: (Torset, 2017)

$$\zeta_x = \frac{H^0(Q_{11} - Q_{33})(1 - Q_{11}^p\phi) + C_{11}Q_{33} - C_{33}Q_{11}}{H^0(2Q_{11} + Q_{33})(Q_{11} - Q_{33})} \tag{4.16}$$

and

$$\zeta_z = \frac{Q_{11}(C_{33} + H^0 - H^0\phi Q_{11}^p - 2C_{11})}{H^0(2 \cdot Q_{11} + Q_{33})(Q_{11} - Q_{33})} + \frac{Q_{33}((Q_{11}^p\phi - 1) \cdot H^0 + C_{33})}{H^0(2 \cdot Q_{11} + Q_{33})(Q_{11} - Q_{33})} \tag{4.17}$$

Looking at equation (4.7), given that $C_{44} > 0$, the criteria for

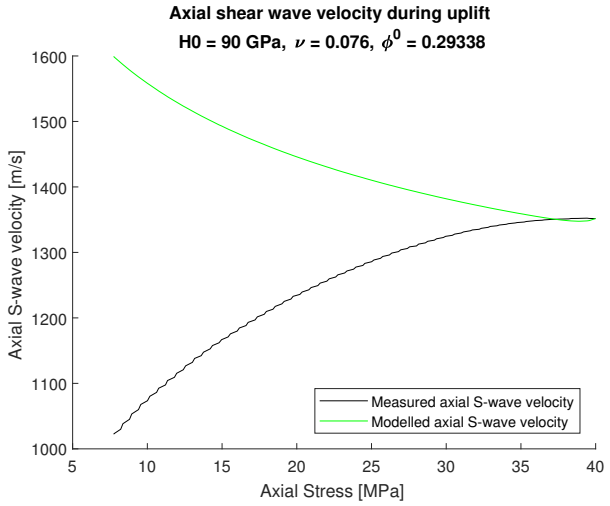

Figure 4.4: Modelled axial shear wave velocity with a starting material with solid properties $H^0 = 90$ GPa, $\nu = 0.076$, and porosity $\phi = 0.293$. The crack-model is not able to model the observed shear wave velocity for this set of grain parameters/porosity.

$C_{44}^0 > 0$ is that

$$\begin{aligned} &1 - Q_{44}^p\phi - Q_{44}(\zeta_x^0 + \zeta_z^0) > 0 \rightarrow \\ &Q_{44}^p\phi + Q_{44}(\zeta_x + \zeta_z) < 1 \end{aligned} \tag{4.18}$$

Defining

$$\Lambda = Q_{44}^p\phi + Q_{44}(\zeta_x + \zeta_z) \tag{4.19}$$

such that

$$C_{44}^0 = \frac{C_{44}}{1 - \Lambda} \tag{4.20}$$

it can further be seen that in the limit $\Lambda \rightarrow 1, C_{44}^0 \rightarrow \infty$.

Assuming that the solid shear modulus of quartz should be somewhere between $30 - 50$ corresponds to having $0.892 <$

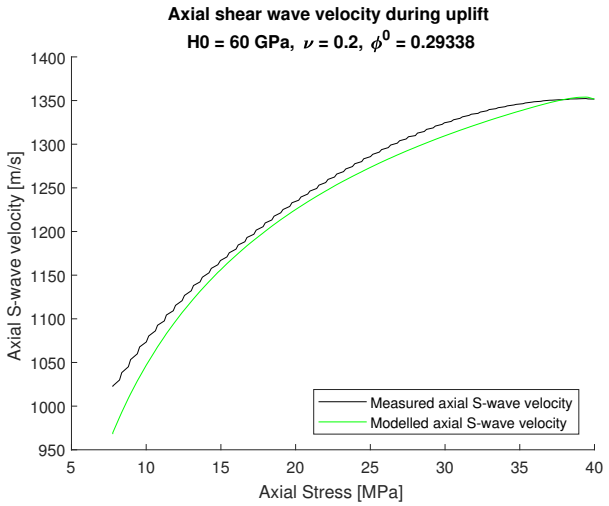

Figure 4.5: Modelled axial shear wave velocity, given a starting material with solid properties: $H^0 = 60$ GPa, $\nu = 0.2$, and porosity $\phi = 0.293$. The shear wave velocity modelling is significantly improved compared of that in figure 4.4

$\Lambda < 0.935$ based on the estimated value of C_{44} at maximum burial[4].

Inserting the expressions for ζ_z and ζ_x from equations (4.16) and (4.17) into equation (4.19), it is obtained that

$$\Lambda = Q^p_{44}\phi + Q_{44}\cdot \left(\frac{Q_{33}(2H^0Q^p_{11} + C_{11} + C_{33} - 2H^0)}{H^0(2Q_{11} + Q_{33})(Q_{11} - Q_{33})} + \frac{2Q_{11}((1 - Q^p_{11})H^0 - C_{11})}{H^0(2Q_{11} + Q_{33})(Q_{11} - Q_{33})}\right) \tag{4.21}$$

The $Q's$ are all functions of Poisson's ratio, such that Λ is a function of H^0, ν and ϕ [(5)].

Using equation (4.21), the sensitivity to H^0, ν and ϕ can be investigated. Two cross sections, with constant ϕ and H^0 are shown in figure 4.6 and 4.7 respectively.

The "Domain with no physical meaning in the model" corresponds to $\Lambda > 1 \rightarrow C^0_{44} < 0$. The "Unwanted domain" are values of Λ producing $C_{44} < 30$ GPa & $C_{44} > 50$ GPa. The value of Λ can be seen to be relatively independent of H^0. For a porosity of 0.3[(6)] however, it is observed that a Poisson's ratio of 0.076 falls in the unphysical domain, explaining why the shear wave velocity is not well modelled at all in figure 4.4. A Poisson's ratio of 0.2 however, as utilised in Fjær (2006) falls within the "useful domain".

Modelling only P-wave anisotropy can thus be done with a Poisson's ratio of 0.076, but to include modelling of the shear wave velocity, the Poisson's ratio must be higher, such that C^0_{44}

[4]In other words, although the solid shear modulus is a free parameter, it is not allowed to be "too free". For a P-wave modulus of 100, the value of G in a material with Poisson's ratio 0 would be 50

[5]Recall that although H^0 and ν are linked through $C_{44}(= G)$ Fjær (2006) allows them to vary independently

[6]Close to the estimated to be the porosity at the start of uplift, which is 0.29

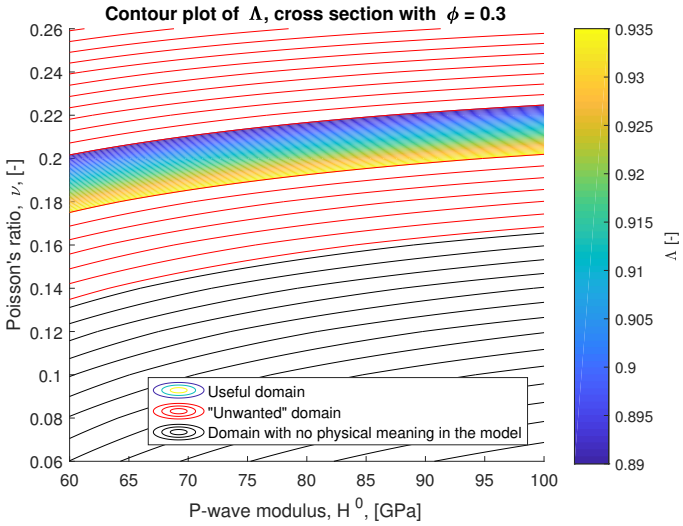

Figure 4.6: Values of Λ for a cross section with a porosity of 30% at the start of modelling. It can be observed that Λ (and so C^0_{44}) is relatively independent of the the P-wave modulus in the range of 70-100GPa, as indicated by the close to horizontal contour-lines. The "unwanted domain" is defined based on the assumption that the shear modulus of the solid material is not allowed to lie outside the 30-50 GPa range. The "domain of no physical meaning" is where $\Lambda > 1$.

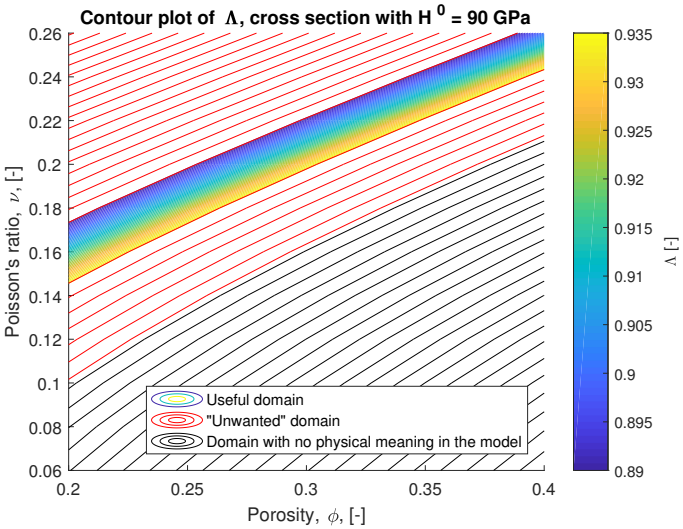

Figure 4.7: Values of Λ for a cross section with a P-wave modulus of 90 GPa. It can be observed that Λ is quite sensitive to both Poisson's ratio and porosity. For all porosities in the given range, a Poisson's ratio of 0.076 would yield a negative shear modulus for the solid material, as indicated by $\Lambda > 1$. A Poisson's ratio of 0.2, with a porosity of 0.29 is however seen to fall within the defined "Useful domain". The "unwanted domain" is defined based on the assumption that the shear modulus of the solid material is not allowed to lie outside the 30-50 GPa range.

does not become negative. Note, that if a fixed value of C_{44}^0 was used, the consequence would be to make the shear wave velocity imaginary (as C_{44} would then be predicted as negative). The exact values of the elastic parameters of solid quartz is reported differently in different sources, and seems to be the subject of some debate. This is discussed in slightly more detail in part III. For now it is noted that some report the Poisson's ratio of pure quartz as low as 0.07 (Dvorkin et al., 2002), a value which if used would clearly not be able to model the shear wave velocity in the experimental data according to figure 4.6. The P-wave velocities will be modelled in other parts with a solid Poisson's ratio of around 0.08, and so if this is carried into the crack model, the shear wave velocities will not be modelled well, and the uplift modelling will thus focus on the stress sensitivity of the P-wave velocities and subsequently P-wave anisotropy.

4.3 Updating the Conceptual Model

The results in figures 3.4 suggests that the assumption of small porosity changes during uplift might be quite reasonable. Over the uplift interval, the rock only regains the porosity (if the porosity is assumed to be directly given by the strain) compacted over the last 5-6 MPa of loading. The assumption that the velocity does not change during uplift is however put into question. Returning to the conceptual model discussed in relation to figure 1.2, a reduction in velocity as the rock is uplifted would have to be included for the conceptual model to match the velocity decrease observed in the experimental data.

To incorporate the observation of decreased velocity during uplift as seen in the lab, the crack model is implemented in parallel with the other models to model the velocity as a function of burial history. For the purpose of this example, the crack model is calibrated to give roughly the same velocity decrease over similar stress unloading as observed for the axial P-wave velocity in the experiment.

The result of implementing this in the diagenetic modelling is seen in figure 4.8. To observe a velocity of 2776 m/s at 600 m would now require a deeper maximum burial according to the sandstone diagenetic modelling. This follows directly from the fact that the uplift acts to reduce the velocities, as observed in the experimental data. Prior to cementation the two grain assemblages would behave exactly the same. The effects of cementation would also, until the onset of uplift be identical.

During uplift, as long as the rock is within the cementation domain, the velocities are assumed to be changed as a combination of increase from cementation, and decrease from crack formation. This is represented by the cyan curve. In this illustration the contribution from cementation and crack formation are assumed to independent, i.e., $\Delta V_p = \Delta V_{p,cem} + \Delta V_{p,crack}$. For reference, the effect of cementation with no velocity loss during uplift is shown by the continuation of the blue curve. Once the rock is out of the cementation domain, the only factors acting to reduce the velocity is the crack model.

In both of these samples, the processes acting on the sediments during burial is limited to mechanical compaction and quartz cementation. By comparing the green curve to the new burial history, it is clear that the initial methodology would underpredict the uplift by 400m.

The processes in the subsurface will not proceed in exactly the same way as in the laboratory, such that the velocities will not be exactly the same for similar stress levels in the laboratory and subsurface. One major difference is the fact that in the subsurface cementation continue over a multitude of stress levels, whereas in the lab it is limited to one stress level. Regardless, if the experimental data is taken to be a fair representation of processes also occurring in the subsurface, standard diagenetic modelling of sandstones will underpredict the uplift. By fair representation it is meant that even though the velocity vs stress curves will not look exactly identical, the processes causing the increased stress dependence during simulated uplift in the laboratory also occur to some extent in the subsurface.

In relation to the source rock maturation, a source rock with a similar burial history to that incorporating uplift would have a TTI of 19.5, which would be in the oil window, but only barely. A sandstone reservoir would have larger amounts of cement, and thus lower porosity.

4.4 Linking the Experimental Results to Uplift Prediction

The crack model in Fjær (2006) was considered appropriate to model the effects of uplift on the P-wave velocities, with some restrictions regarding solid grain parameters limiting the modelling of shear wave velocities.

However, put into context of uplift prediction, the "history" of the rock down to the uplift starts also has to be modelled. Prior to cementation that constitutes a granular media subjected to a stress state where $\sigma_z = 2\sigma_r$. After cementation, some model describing the effects of cementation on a granular assemblage would be required. Furthermore, the strain, which is a parameter utilised in Torset (2017) is generally not readily available, which means that the crack model will have to be modified slightly.

In addition to the decrease in the velocity, the anisotropy appears to show interesting potential as an attribute for uplift (whilst remembering that the experiments are conducted under uniaxial strain). Therefore, incorporating the ability to model P-wave anisotropy as a function of the simulated burial history would be desirable.

The following parts addresses these problems in turn, starting with the modelling of granular media (part III), followed by a discussion of cementation (part IV), and finally these are combined with a slightly altered implementation of the crack model to describe the entire "burial history" of the synthetic sandstone in part V.

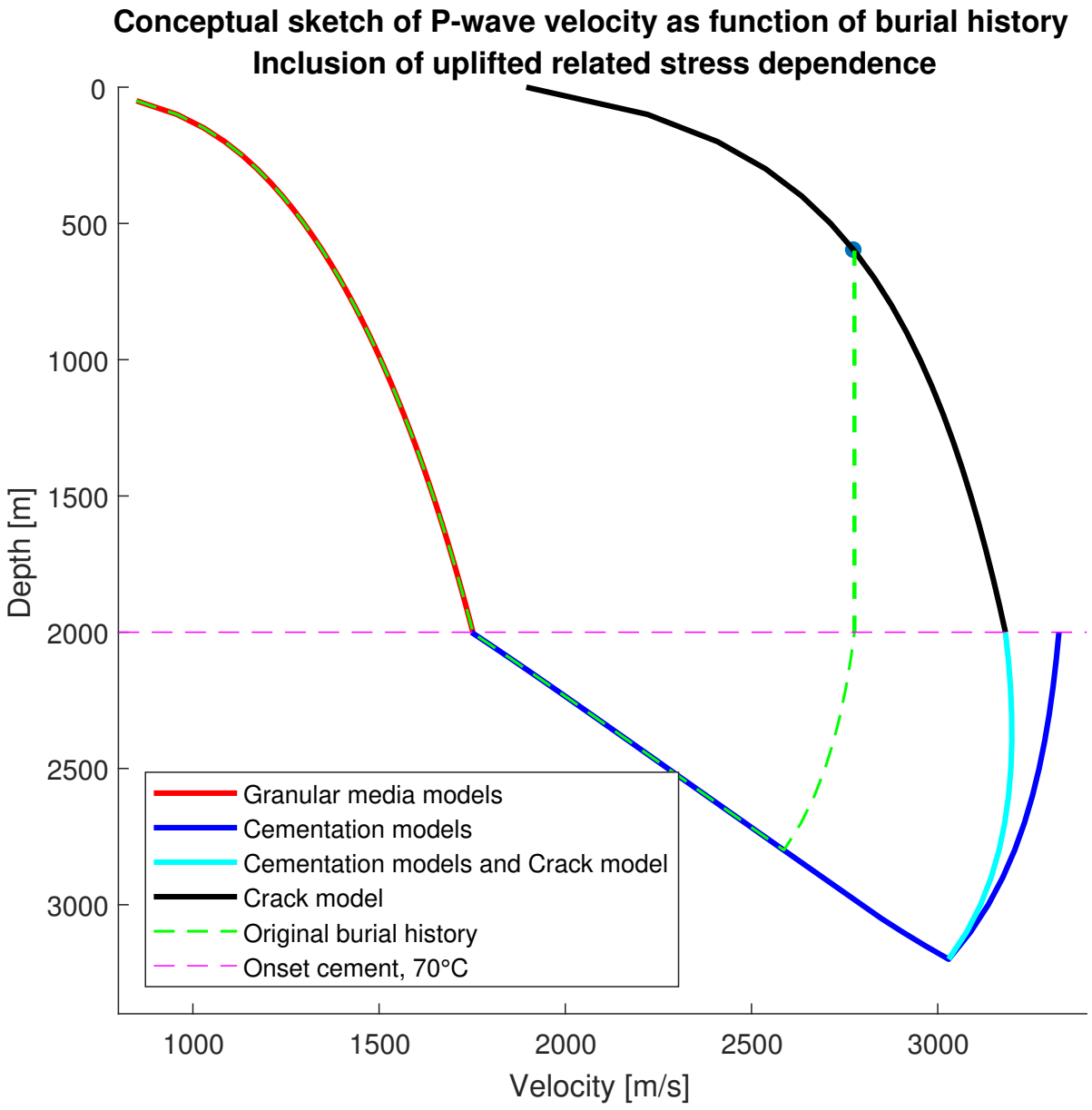

Figure 4.8: Updated conceptual model with the inclusion of some uplift related increase in stress dependence. The modelling methodology of granular media and cementation is the same as for figure 1.2. The input parameters in the crack model in this illustrative scenario is calibrated to yield roughly the same velocity decrease over similar stress intervals as the experimental data. After the onset of uplift, but within the cementation domain, the effects of the crack model are superposed with those from increased cement in the cementation models.

Part III

Stiffness of Unconsolidated Granular Media

Chapter 5

Introduction and Background to Part III

5.1 Introduction to Part III

Modelling the stiffness parameters of granular media is one technique for estimating velocities as functions of depth in the subsurface. This chapter provides the necessary background for the discussion in subsequent chapters in this part. Firstly, the Hertz-Mindlin model used to create the conceptual model in the earlier parts of this work will be reviewed. Following this, the results of Walton (1987) are presented. Walton (1987) provides explicit expressions for the stiffness parameters in terms of strain in two limiting strain cases: Uniaxial strain and hydrostatic strain. Although these might be good approximations in many situations, in the experimental data described in part II the stress during loading prior to cementation was a triaxial stress state with $\sigma_z = 2\sigma_r$. In this configuration the strain is neither uniaxial nor hydrostatic. Furthermore, the concept of "slip" and "no-slip" contacts are discussed, and why a mixture of these limits might be appropriate to describe the rock as a whole.

Deriving triaxial strain and stress expressions for a particular triaxial scenario (where the horizontal strains are equal) is attempted in Bandyopadhyay (2009). The results of this paper will be reviewed in the second chapter of this part. Potential errors and shortcomings are pointed out. Following this, expressions for a triaxial strain case under the same assumption of equal horizontal strains, but without the limitation on the relationship between the axial and the horizontal strain imposed in Bandyopadhyay (2009) are derived directly from Walton (1987). Additionally, since in the field, stress is generally more available than strain, expressions for the strain in terms of the stress are also presented.

The fourth chapter in this part will focus on the implementation of the model derived throughout the first three chapter to the experimental data presented in part II.

5.2 Hertz-Mindlin

The normal compliance of a contact between two identical spheres is given as: (Mindlin, 1949)

$$C_z = \frac{d\alpha}{dP_z} \tag{5.1}$$

where α is the normal displacement of the spheres relative to each other, corresponding to a shortening of the sphere radius. Stiffness in this case is given as $\frac{1}{C_z}$, and together with the results from Digby (1981), the normal stiffness of a contact can be written

$$S_n = \frac{4G_s a}{1-\nu_s} \tag{5.2}$$

Where G and ν represent the shear modulus and Poisson's ratio of the sphere material, and a if the radius of the contact area.

Furthermore Mindlin (1949) gives the tangential compliance with no slip as

$$C_t = \frac{2-\nu_s}{8G_s a} \tag{5.3}$$

In the notation of Digby (1981), the tangential stiffness is given as

$$S_t = \frac{8G_s b}{2-\nu_s} \tag{5.4}$$

Where b is what Digby (1981) calls "bonding radius". The limit $b = 0$ corresponds to slip, and $b = a$ corresponds to no-slip (Norris and Johnson, 1997).

When two identical spheres are compressed normally, they have a contact area, a given by (Mavko et al., 2009)

$$a = \Big[\frac{3FR}{8G_s}(1-\nu_s)\Big]^{\frac{1}{3}} \tag{5.5}$$

Under hydrostatic loading by confining pressure P, on a random, identical sphere packing the confining force of two particles is given as (Mavko et al., 2009)

$$F = \frac{4\pi R^2 P}{n(1-\phi)} \tag{5.6}$$

where R is the grain radius, ϕ is the porosity and n is the coordination number.
Following the derivation in Mavko et al. (2009), equation (5.6) can be inserted into equation (5.5), which subsequently can be inserted into equation (5.2) to yield the normal stiffness. Assuming no-slip this can also be inserted into equation (5.4) to yield the tangential stiffness.

The effective bulk and shear modulus are given in terms of S_n and S_t as (Mavko et al., 2009)

$$\begin{aligned} K &= \frac{n(1-\phi)}{12\pi R} S_n \rightarrow \\ K &= \Big[\frac{n^2(1-\phi)^2 G_s^2 P}{18\pi^2(1-\nu_s)^2}\Big]^{1/3} \end{aligned} \tag{5.7}$$

$$\begin{aligned} G &= \frac{n(1-\phi)}{20\pi R}(S_n + 1.5S_t) \rightarrow \\ G &= \frac{5-4\nu_s}{5(2-\nu_s)}\Big[\frac{3n^2(1-\phi)^2 G_s^2 P}{2\pi^2(1-\nu_s)^2}\Big]^{1/3} \end{aligned} \tag{5.8}$$

The slip limit is obtained by setting $S_t = 0$. The equations above can then be used to calculate the P- and S-wave velocities as a function of stress during burial.

5.3 Walton (1987)

Walton (1987) develops a model to determine the elastic parameters of a random packing of spheres which are homogeneous and elastically isotropic. Walton (1987) provides explicit relations for the elastic parameters in two strain states; isotropic and uniaxial. Furthermore, the spherical grains are either infinitely rough, or infinitely smooth[1].

The general expression for average stress in terms of average strain for the rough contacts is[2], [3], [4]:

$$\sigma_{ij}^r = \frac{(1-\phi)n}{\pi^2 B(2B+C)}\Big[B\Big\langle(-E_{pq}n_p n_q)^{0.5}[E_{ik}n_k n_j + E_{jk}n_k n_i]\Big\rangle - C\Big\langle(-E_{pq}n_p n_q)^{3/2} n_i n_j\Big\rangle\Big] \tag{5.9}$$

Here ϕ is the porosity, n is the coordination number, E_{ij} are values of the strain[5], and n_i are the directional cosines[6] . B and C are given as (Walton, 1987):

$$B = \frac{1}{4\pi}\left(\frac{1}{G_s} + \frac{1}{\lambda_s + G_s}\right) \tag{5.10}$$

$$C = \frac{1}{4\pi}\left(\frac{1}{G_s} - \frac{1}{\lambda_s + G_s}\right) \tag{5.11}$$

λ and G are the Lamé parameters of the sphere material.

The general expression for stiffness for the rough contacts is given as

$$\begin{aligned} C_{ijkl} = \frac{3(1-\phi)N}{4\pi^2 B(2B+C)}\Big\{B\big[&\langle(-E_{pq}n_p n_q)^{1/2} n_j n_k\rangle\delta_{il} + \\ &\langle(-E_{pq}n_p n_q)^{1/2} n_i n_k\rangle\delta_{jl} + \langle(-E_{pq}n_j n_l)^{1/2}\rangle\delta_{ik} + \\ &\langle(-E_{pq}n_i n_l)^{1/2}\rangle\delta_{jk}\big] + 2C\langle(-E_{pq}n_p n_q)^{1/2} n_i n_j n_k n_l\rangle\Big\} \end{aligned} \tag{5.12}$$

The general expression for average stress in terms of average strain for smooth contacts is

$$\sigma_{ij}^s = \frac{(1-\phi)N}{\pi^2 B}\langle(-E_{pq}n_p n_q)^{3/2} n_i n_j\rangle \tag{5.13}$$

The general expression for stiffness for the smooth contacts is given as[7]

$$C_{ijkl}^s = \frac{3(1-\phi)N}{4\pi^2 B}\big[2\langle(-E_{pq}n_p n_q)^{1/2} n_i n_j n_k n_l\rangle\big] \tag{5.14}$$

According to Bandyopadhyay (2009)[8]

$$n_1 = sin(\theta)cos(\phi) \tag{5.15a}$$

$$n_2 = sin(\theta)sin(\phi) \tag{5.15b}$$

$$n_3 = cos(\theta) \tag{5.15c}$$

$$\langle x\rangle = \frac{1}{4\pi}\int_0^{2\pi}\int_0^{\pi} x\sin(\theta)d\theta d\phi \tag{5.15d}$$

5.3.1 Explicit Expressions Given in Walton (1987) for Hydrostatic Strain

The stress expressions for rough and smooth contacts in the case of a hydrostatic strain E are given as

$$\sigma_{ij}^r = -\frac{(1-\phi)n\cdot(-E)^{3/2}}{3\pi^2 B} \tag{5.16}$$

$$\sigma_{ij}^s = \sigma_{ij}^r \tag{5.17}$$

For an isotropic strain field with infinitely rough grains, the effective Lamé parameters are given as (Walton, 1987):

$$\lambda^r = \frac{C}{10(2B+C)}\left(\frac{3(1-\phi)^2 n^2 p}{\pi^4 B^2}\right)^{\frac{1}{3}} \tag{5.18}$$

$$G^r = \frac{5B+C}{10(2B+C)}\left(\frac{3(1-\phi)^2 n^2 p}{\pi^4 B^2}\right)^{\frac{1}{3}} \tag{5.19}$$

where p refers to a hydrostatic confining pressure.

The effective moduli for smooth grain contacts are given as[9]

$$\lambda^s = G^s = \frac{1}{10}\left(\frac{3(1-\phi)^2 n^2 p}{\pi^4 B^2}\right)^{1/3} \tag{5.20}$$

[1] In Walton (1987) strains are negative in compaction and stresses are negative in compression.

[2] Note that the strain notation of Bandyopadhyay (2009) is used throughout, this is to ease the transition to the more in depth discussion of that paper. The results of Walton (1987) will serve mainly as reference points in the limits of hydrostatic and uniaxial strain.

[3] The superscript r indicates rough limit.

[4] Note: Walton (1987) uses ϕ as the fraction of solid grains. Throughout this analysis, ϕ will be used as porosity. 1-porosity = solid fraction.

[5] Defined as e_i in Walton (1987).

[6] Defined as I_i in Walton (1987).

[7] This is not actually given in Walton (1987), but it is provided in Bandyopadhyay (2009).

[8] This is not explicitly written in Walton (1987).

[9] Do not confuse the superscript s, denoting "smooth" with the subscript s denoting "sphere material".

5.3.2 Explicit Expressions Given in Walton (1987) for Uniaxial Strain

The rough and smooth grain limits of stress are given in Walton (1987) as

$$\sigma_{11}^r = -\frac{(1-\phi)nC(-E_3)^{3/2}}{24\pi^2 B(2B+C)} \tag{5.21}$$

$$\sigma_{33}^r = -\frac{(1-\phi)n(3B+C)(-E_3)^{3/2}}{6\pi^2 B(2B+C)} \tag{5.22}$$

$$\sigma_{11}^s = -\frac{(1-\phi)n(-E_3)^{3/2}}{24\pi^2 B} \tag{5.23}$$

$$\sigma_{33}^s = -\frac{(1-\phi)n(-E_3)^{3/2}}{6\pi^2 B} \tag{5.24}$$

where E_3 is uniaxial strain in this case in the $3(z)$ direction.

For the infinitely rough, uniaxial strain situation, the elastic moduli of the granular media are given as (Walton, 1987)[10]:

$$C_{11}^r = 3(\alpha + 2\beta) \tag{5.25a}$$
$$C_{12}^r = \alpha - 2\beta \tag{5.25b}$$
$$C_{13}^r = 2C_{12}^r \tag{5.25c}$$
$$C_{33}^r = 8(\alpha + \beta) \tag{5.25d}$$
$$C_{44}^r = 2\alpha + 5\beta \tag{5.25e}$$

where

$$\alpha = \frac{(1-\phi)n(-E_3)^{\frac{1}{2}}}{32\pi^2 B} \tag{5.26}$$

$$\beta = \frac{(1-\phi)n(-E_3)^{\frac{1}{2}}}{32\pi^2(2B+C)} \tag{5.27}$$

E_3 is the axial strain.

The P-wave anisotropy predicted in this limit can be found from

$$\begin{aligned} \epsilon &= \frac{C_{11}^r - C_{33}^r}{2C_{33}^r} \rightarrow \\ \epsilon &= \frac{3\alpha + 6\beta - 8\alpha - 8\beta}{16\alpha + 16\beta} \rightarrow \\ \epsilon &= -\frac{12B + 5C}{48B + 16C} \end{aligned} \tag{5.28}$$

This is clearly only dependent on the grain parameters, through equations (5.10) and (5.11).

For the smooth limit the anisotropic parameters are given as

$$C_{11}^s = 3\alpha \tag{5.29a}$$
$$C_{12}^s = \alpha \tag{5.29b}$$
$$C_{13}^s = 2C_{12}^s \tag{5.29c}$$
$$C_{33}^s = 8\alpha \tag{5.29d}$$
$$C_{44}^s = 2\alpha \tag{5.29e}$$

[10]Note that C_{44}^r is modified from Walton (1987) to account for a misprint, as pointed out in Holt et al. (2007).

The anisotropy in this limit is given through

$$\begin{aligned} \epsilon &= \frac{C_{11}^r - C_{33}^r}{2C_{33}^r} \rightarrow \\ \epsilon &= \frac{3\alpha - 8\alpha}{16\alpha} \rightarrow \\ \epsilon &= \frac{-5}{16} \end{aligned} \tag{5.30}$$

5.4 Mixing of Infinitely Rough and Smooth Contacts - a Pragmatic Solution to a Difficult Problem

Not all contacts are infinitely rough or infinitely smooth. In a sense the concept of infinitely rough (also referred to as no-slip) and infinitely smooth (also referred as slip) describe limits.

Bachrach and Avseth (2008) suggest a binary mixing model, where the effective stiffness is given as a fraction of rough and smooth grains. The binary mixing is presented in equation 14 in Bachrach and Avseth (2008)

$$\sigma_{ij} = (f_s C_{ijkl}^*(S_n, S_t = 0) + f_t C_{ijkl}^*(S_n, S_t \neq 0))e_{kl} \tag{5.31}$$

and "tries to account for the heterogeneities in stress chains as observed in laboratory measurements and numerical simulations" (Bachrach and Avseth, 2008).

Note that Bachrach and Avseth (2008) suggest the stiffnesses be functions of S_n and S_t. This is consistent with the Hertz-Mindlin formulation, but Walton's model is a function of grain-constants B and C. The expressions in Walton (1987) can however be expressed in terms of S_n and S_t.

5.4.1 Equivalence of Hertz-Mindlin and Walton in the Isotropic Compaction Limit

Assuming that the sphere material is isotropic and lineraly elastic, λ is given as

$$\lambda_s = 2\,\frac{\nu_s\, G_s}{1 - 2\,\nu_s} \tag{5.32}$$

Inserting this in the equations for B and C given in equations (5.10) and (5.11) yields

$$B = \frac{1}{2}\frac{1-\nu_s}{G_s\pi} \tag{5.33}$$

$$C = \frac{1}{2}\frac{\nu_s}{G_s\pi} \tag{5.34}$$

$$\tag{5.35}$$

From which it can further be shown that

$$\frac{5B + C}{10(2B + C)} = \frac{1}{2}\frac{5 - 4\nu_s}{5(1 - 2\nu_s)} \tag{5.36}$$

Furthermore

$$B = \frac{1}{4\pi}\Big(\frac{1}{G_s} + \frac{1}{\lambda_s + G_s}\Big) \rightarrow$$
$$B = \frac{1}{4\pi}\Big(\frac{\lambda_s + 2G_s}{G_s(\lambda_s + G_s)}\Big) \tag{5.37}$$

$$\nu_s = \frac{\lambda_s}{2(\lambda_s + G_s)} \rightarrow$$
$$1 - \nu = \frac{2(\lambda_s + G_s)}{2(\lambda_s + G_s)} - \frac{\lambda_s}{2(\lambda_s + G_s)} \rightarrow \tag{5.38}$$
$$1 - \nu = \frac{\lambda_s + 2G_S}{2(\lambda_s + G_s)} \rightarrow$$
$$B^2 = \frac{1}{4\pi^2}\frac{(1-\nu_s)^2}{G_s^2} \tag{5.39}$$

Inserting the results from equations (5.36) and (5.39) into equation (5.19) yields the Hertz-Mindlin result in equation (5.8).

Since the rough bulk modulus is given as

$$K = \frac{5(2-\nu_s)}{3(5-4\nu_s)}G \tag{5.40}$$

it follows that the bulk modulus is also consistent.

For the smooth limit, the value of G in Hertz-Mindlin is given as (Mavko et al., 2009)

$$G = \frac{3K}{5} \tag{5.41}$$

The bulk modulus does not change in either Hertz-Mindlin or Walton (1987) as it is not affected by $S_t \rightarrow 0$. The bulk modulus in Walton (1987) is given as

$$K = \frac{1}{6}\left(\frac{3(1-\phi)^2 P n^2}{\pi^4 B^2}\right) \rightarrow \tag{5.42}$$
$$K = \frac{1}{6}\left(\frac{3(1-\phi)^2 P n^2}{\pi^4(\frac{1}{4\pi^2}\frac{(1-\nu_s)^2}{G_s^2})}\right) \rightarrow \tag{5.43}$$
$$K = \left(\frac{(1-\phi)^2 P n^2 G_s^2}{18\pi^2(1-\nu_s)^2}\right) \tag{5.44}$$

which can be recognised as the bulk modulus given in equation (5.7).

5.4.2 Expressing the Uniaxial Results from Walton (1987) in Terms of S_n and S_t

Hertz-Mindlin is limited in its current formulation to isotropic loading, but the stiffnesses in Walton (1987) can still be extended to S_n and S_t under uniaxial compaction. This is done in Duffaut (2011). For no-slip[11] contacts

$$C_{11}^r = \frac{3(1-\phi)n}{64\pi R}(S_n + S_t) \tag{5.45a}$$
$$C_{33}^r = \frac{(1-\phi)n}{16\pi R}(2S_n + S_t) \tag{5.45b}$$
$$C_{13}^r = \frac{(1-\phi)n}{32\pi R}(S_n - S_t) \tag{5.45c}$$
$$C_{44}^r = \frac{(1-\phi)n}{128\pi R}(4S_n + 5S_t) \tag{5.45d}$$
$$C_{66}^r = \frac{(1-\phi)n}{64\pi R}(S_n + 2S_t) \tag{5.45e}$$

and for slip contacts[12]

$$C_{11}^s = \frac{3(1-\phi)n}{64\pi R}S_n \tag{5.46a}$$
$$C_{33}^s = \frac{(1-\phi)n}{16\pi R}2S_n \tag{5.46b}$$
$$C_{13}^s = \frac{1(1-\phi)n}{32\pi R}S_n \tag{5.46c}$$
$$C_{44}^s = \frac{(1-\phi)n}{128\pi R}4S_n \tag{5.46d}$$
$$C_{66}^s = \frac{(1-\phi)n}{64\pi R}S_n \tag{5.46e}$$

In these definitions, the contacts radius, a, used to define S_t and S_n is given as (Duffaut, 2011)

$$a = R\sqrt{E_{33}} \tag{5.47}$$

It is on the basis of this argued that mixing of the rough and smooth limits in Walton (1987) is consistent with the binary mixing model, and that the B and C parameters in Walton (1987) can be used instead of S_n and S_t to accomplish this.

5.4.3 The Concept of Friction

Duffaut et al. (2010) uses results from isotropic loading experiments on glass beads in order to investigate the effects of a friction parameter based in Mindlin's theory. This is done in attempt to characterise observations that fall between the slip and no-slip limits. The idea of finite frictions on the grain contacts is a somewhat contrasting concept to the simple mixing of slip and no slip contacts.

The friction idea is however mathematically similar to an arithmetic average of slip and non-slip contacts. This can be demonstrated for, as an example, the anisotropic elastic stiffnesses C_{11} under uniaxial compaction.

With the introduction of the friction parameter, the equation for C_{11} is (Duffaut, 2011)

$$C_{11}^{dry} = \frac{3(1-\phi)n}{64\pi R}[S_n + S_t f(\mu)] \tag{5.48}$$

[11] Denoted by the superscript r.
[12] Denoted by the superscript s.

n corresponds to the coordination number. R is the grain radius.

$$f(\mu) = \Big(1 - \frac{F_t}{F_n \mu}\Big)^{1/3} \tag{5.49}$$

is the function describing the friction component (Duffaut, 2011, chapter 4). $f(\mu) = 0$ corresponds to the slip limit, whereas $f(\mu) = 1$ corresponds to the non-slip limit.

The no-slip and slip limits were given in equations (5.45a) and (5.46a). Following this, mix f rough contacts with $1 - f$ smooth contacts:

$$\begin{aligned} C_{11}^{dry} &= fC_{11}^{r} + (1-f)C_{11}^{s} \rightarrow \\ C_{11}^{dry} &= fX[S_n + S_t]X + (1-f)XS_n \rightarrow \\ C_{11}^{dry} &= X[S_n + fS_t] \end{aligned} \tag{5.50}$$

Where

$$X = \frac{3(1-\phi)n}{64\pi R} \tag{5.51}$$

Equations (5.48) and (5.50) can be seen to have an extremely similar form, such that the fraction of rough grains can numerically describe the same as the partial slip suggested in Duffaut et al. (2010). That is, a value of $f(\mu) = 0.6$ will give the same result as 60% non-slip and 40% slip contacts.

The derivation is not done for all the stiffness parameters in (Duffaut, 2011, Chapter 4), but the result is the same for all the stiffness parameters. Each stiffness parameter has the same friction function.

Although numerically the methods in Duffaut et al. (2010) and Bachrach and Avseth (2008) provide the same answer, the phenomena they are trying to describe are slightly different. Bachrach and Avseth (2008) aims to explain that in a force chain, some grain contacts act as slip, whereas some act as non-slip contacts. Duffaut et al. (2010) on the other hand extends the theory of Mindlin (1949) to describe an assemblage where all contacts have finite friction.

It is suggested here that in fact both of these proposals might provide insight into the processes that occur to produce the observed experimental data. In Duffaut et al. (2010) it is observed that during loading, the moduli seem to migrate to a higher value for the friction coefficient $f(\mu)$, which would correspond to a higher fraction of no-slip contacts.

Duffaut et al. (2010) gives the radius of the no-slip fraction of the grain contact as

$$c = a\Big(1 - \frac{F_t}{\mu F_n}\Big)^{1/3} \tag{5.52}$$

from which it is clear that if $F_t = \mu F_t$ then $c = 0$ meaning that there will be slip, and if $\mu F_n >> F_t$ then $c = a$, indicating no-slip.

In a thought experiment, letting the normal force imposed on the contact with a constant tangential force, would thus increase the radius of the no-slip contact area, leading to an increase in the tangential stiffness, given in Duffaut et al. (2010) as

$$S_t = \frac{8Ga}{2-\nu}\Big(1 - \frac{F_t}{\mu F_n}\Big)^{1/3} \tag{5.53}$$

The normal stiffness would also increase across a contact when the normal stress is increased.
In the case of an isotropic compressive stress, this effect of increasing normal and shear stiffness would be expected to be the same in all directions. This corresponds to having the same friction function across all the elastic parameters, as well as the same normal and tangential stiffnesses. What about if the stress field is anisotropic? It is argued that if the stress field is anisotropic the effect across the range of orientations of grain contacts could also be anisotropic and this anisotropy effect could be stress dependent. This would introduce an anisotropy effect that would not be captured by the assumptions in Walton (1987).

The P-wave anisotropy in Walton (1987) was shown to be constant in the rough and smooth limits. In the case where the friction effect is assumed to be the same across all elastic parameters, Duffaut (2011) shows that the P-wave anisotropy is purely dependent on the Poisson's ratio and value of the friction coefficient:

$$\epsilon = -\frac{5 + 2\frac{1-\nu}{2-\nu} f(\mu)}{16(1 + \frac{1-\nu}{2-\nu}) f(\mu)} \tag{5.54}$$

This is similar to the result in Walton (1987) in that the anisotropy is constant, provided that the friction coefficient is constant. If the friction coefficient varies during loading, as the experimental results depicted in Duffaut et al. (2010) might suggest, the anisotropy would also change.

By differentiating equation (5.54) with respect to f it is obtained that

$$\frac{d\epsilon}{df} = \frac{3}{16}\frac{(1-\nu_s)(2-\nu_s)}{(f\nu - f + \nu - 2)^2} \tag{5.55}$$

Since $\nu_s < 0.5$, and $f, \nu \in \mathbb{R}$ the derivative is always positive, i.e., $d\epsilon/df > 0$ meaning that an increase in f yields a positive change in P-wave anisotropy (towards isotropy in the case of $V_{pz} > V_{pr}$).

5.4.4 Force Chains Under Anisotropic Loading

Force chain refers to the inhomogenous contact network carrying most of the external load when an external stress is applied to a granular media (Majmudar and Behringer, 2005). In Majmudar and Behringer (2005) such force chains are investigated for loading under isotropic and pure shear (uniaxial compression) states. Although the pure shear state used in Majmudar and Behringer (2005) constitutes a rather extreme form of strain anisotropy, it is assumed that the effects of the stress induced anisotropy for weaker forms of strain anisotropy is similar, although not as pronounced as in Majmudar and Behringer (2005).

The force chain network in an isotropically loaded sample is correlated over only short distances, and with no preferred direction (Majmudar and Behringer, 2005). During isotropic loading then, it can be justified claiming that the force chains will be roughly isotropically distributed, such that the effect of some load bearing, and some non-load bearing contacts is isotropic (warranting the use of the same scalar to describe the relationship in all directions).

During anisotropic loading, the anisotropy created by the load, is reported to have two effects. First, it creates anisotropy in the contact network, and secondly it develops an anisotropic force chain network and alters the stress distribution in the system (Majmudar and Behringer, 2005). In these anisotropic force chains, forces have correlations over long ranges, in the direction of the force chains.

In other words, it might be expected that such a force chain network would orient itself to have a larger number of load bearing contacts in the direction parallel to the maximum applied stress. In the binary mixing model, this could be numerically compensated for by having anisotropic no-slip/slip fractions.

5.4.5 Overestimation of the Shear Modulus

Jenkins et al. (2005) discusses how the methods of Digby (1981) and Walton (1987) tend to overestimate the shear modulus. The idea in Jenkins et al. (2005) is that under non-hydrostatic strain, the motion of a sphere in relation to its adjacent grains is allowed to be different from the mean strain field of a homogeneous effective media (Mavko et al., 2009). The considerations in Jenkins et al. (2005) are done in the slip limit. In the binary mixing method under non-hydrostatic strain, incorporating the observation of Jenkins et al. (2005) would correspond to shifting the slip limit of the shear wave moduli down. This would be mathematically similar to letting the shear wave moduli have a lower no-slip/slip fraction than the P-wave moduli, whilst keeping the no-slip and slip limits of Walton (1987). This method of compensation is however limited by scenarios where the observed velocities fall below the slip limit.

5.4.6 Mixing of Rough and Smooth Contacts - Summarising Remarks

As pointed out in the last few sections, not all contacts are likely to be infinitely rough, or infinitely smooth. The relationship between rough and smooth contacts is possibly anisotropic based on force chain network work done in Majmudar and Behringer (2005). Furthermore, the normal and tangential stiffnesses on grain contacts might be on average anisotropic in a manner not captured by Walton (1987) due to friction considerations. These effects, together with incorporation of the effects observed in Jenkins et al. (2005) can be compensated for pragmatically by letting the no-slip/slip factor applied to each stiffness in the binary mixing model be anisotropic and stress dependent.

Although giving each stiffness a separate, potentially stress dependent slip/no slip relationship allows for freedom when modelling, this freedom comes at a cost. Most things can be modelled given enough free parameters, and it puts a large degree of ambiguity into the forward modelling process.

5.5 Porosity Considerations

The granular media models are typically derived for “random dense packings”, with porosities of 36%. Thus, instead of inputting the porosities directly in the granular media models, a porosity of 36% is used, and then other porosities are interpolated using a Hashin-Shtrikman lower bound, as described in Dvorkin and Nur (1996), Mavko et al. (2009) and Avseth et al. (2010). The “friable sand model” as it is termed in Avseth et al. (2010) is implemented to deal with sorting effects on porosity, but in this work it will be implemented to model all effects of porosity change on stiffness. This is based on the implementation of the friable sand model in Dvorkin and Nur (1996). The model is compared to measured porosities, which are likely a combination of sorting and compaction effects.

Chapter 6

Extension to Triaxial Strain - Bandyopadhyay 2009

In this chapter the extension of the theory in Walton (1987) to triaxial strain by Bandyopadhyay (2009) is reviewed, and some limitations are pointed out[1].

6.1 Review of Bandyopadhayay (2009)

Bandyopadhyay (2009) extends the work of Walton (1987) to provide explicit expressions for triaxial strain, but limited to the scenario where the horizontal strains are equal. In other words strain of the form

$$E_{ij} = E_{11}\delta_{i1}\delta_{j1} + E_{11}\delta_{i2}\delta_{j2} + E_{33}\delta_{i3}\delta_{j3} \tag{6.1}$$

In the following discussion, any strain state referred to as triaxial, will be limited by this condition.

Note that in Bandyopadhyay (2009), the discussion on triaxial strain is conducted with a definition of strain as positive in compaction, which is the opposite to that of Walton (1987). This is evident from the terms inside square roots in Bandyopadhyay (2009).

Bandyopadhyay (2009) still keeps the stress as negative in compression however. The notation in Bandyopadhyay (2009) introduces some differences regarding signs when compared to the expressions in Walton (1987).

Bandyopadhyay (2009) presents the following elastic moduli for the rough scenario in the case where the strain can be described as $E_{33} \neq E_{11} = E_{22}$,

$$C^r_{11} = \frac{2}{5}X\sqrt{E_{33}}\left[C + \frac{10B}{3} + \left(\frac{6C}{7} + \frac{8B}{3}\right)E_r\right] \tag{6.2a}$$

$$C^r_{33} = \frac{2}{5}X\sqrt{E_{33}}\left[C + \frac{10B}{3} + \left(\frac{2C}{7} + \frac{4B}{3}\right)E_r\right] \tag{6.2b}$$

$$C^r_{13} = \frac{2}{15}X\sqrt{E_{33}}\left[C + \frac{4CE_r}{7}\right] \tag{6.2c}$$

$$C^r_{44} = \frac{2}{15}X\sqrt{E_{33}}\left[C + 5B + \left(\frac{4C}{7} + 3B\right)E_r\right] \tag{6.2d}$$

$$C^r_{66} = \frac{2}{15}X\sqrt{E_{33}}\left[C + 5B + \left(\frac{6C}{7} + 4B\right)E_r\right] \tag{6.2e}$$

Where

$$X = \frac{3(1-\phi)N}{4\pi^2 B(2B+C)} \tag{6.3}$$

$$E_r = \frac{E_{11} - E_{33}}{2E_{33}} \tag{6.4}$$

B and C are the same as defined earlier.

These expressions are based on the assumption that

$$\left|\frac{E_{11} - E_{33}}{E_{33}}\right| << 1 \tag{6.5}$$

The assumption in (6.5) puts a limitation on how big the strain anisotropy, E_r, can be.

For smooth contacts, the stiffness parameters are given in Bandyopadhyay (2009) as:

$$C^s_{11} = \frac{2}{35}Y\sqrt{E_{33}}(7 + 6E_r) \tag{6.6a}$$

$$C^s_{33} = \frac{2}{35}Y\sqrt{E_{33}}(7 + 2E_r) \tag{6.6b}$$

$$C^s_{13} = \frac{2}{105}Y\sqrt{E_{33}}(7 + 4E_r) \tag{6.6c}$$

$$C^s_{44} = C^s_{13} \tag{6.6d}$$

$$C^s_{66} = \frac{2}{105}Y\sqrt{E_{33}}(7 + 6E_r) \tag{6.6e}$$

Where

$$Y = \frac{3(1-\phi)N}{4\pi^2 B} \tag{6.7}$$

[1] An additional extension to triaxial strain, shown in Johnson et al. (1998) is briefly discussed in appendix D.

As aptly pointed out in Bandyopadhyay (2009), stresses are generally more available than strains in the field, and are defined in Bandyopadhyay (2009) as[2]:

$$\sigma_{11}^r = -\frac{Z}{15}(E_{33}^{3/2})(5C + 10B + 16BE_r^2 + 12CE_r + 28BE_r) \tag{6.8}$$

$$\sigma_{33}^r = -\frac{Z}{15}E_{33}^{3/2}(5C + 10B + (6C + 8B)E_r) \tag{6.9}$$

$$Z = \frac{(1-\phi)N)}{\pi^2 B(2B + C)} \tag{6.10}$$

These expressions can then be solved for strain in terms of stress, and Bandyopadhyay (2009) present the following equations[3]:

$$E_r = \frac{1}{16B\sigma_{33}}[\sigma_{11}(2B + 3C) - 2\sigma_{33}(7B + 3C) - P] \tag{6.11}$$

Where

$$\begin{aligned} S_1 &= \sigma_{11}^2 - 4\sigma_{11}\sigma_{33} + 4\sigma_{33}^2 \\ S_2 &= 3\sigma_{11}^2 - 7\sigma_{11}\sigma_{33} + 22\sigma_{33}^2 \\ S_3 &= \sigma_{11}^2 + 26\sigma_{11}\sigma_{33} + 9\sigma_{33}^2 \\ P &= 9C^2S_1 + 4BCS_2 + 4B^2S_3 \end{aligned} \tag{6.12}$$

Further,

$$\begin{aligned} &E_{33} = \\ &\left[\frac{12B^2(\sigma_{11} + 13\sigma_{33}) + 27C^2(\sigma_{11} - 2\sigma_{33}) +}{2Z(9C^3 + 40C^2B + 28CB^2 - 32B^2)}\right. \\ &\left.\frac{(9C + 6B)P + 6BC(6\sigma_{11} - 7\sigma_{33})}{2Z(9C^3 + 40C^2B + 28CB^2 - 32B^2)}\right]^{2/3} \end{aligned} \tag{6.13}$$

6.2 Potential Errors in Bandyopadhyay (2009)

The first problem in Bandyopadhyay (2009) starts with the integral equations presented (equations 3.38 to 3.47 in Bandyopadhyay (2009))

$$I_1 = \langle (E_{pq}n_pn_q)^{0.5}n_1^4\rangle \approx \frac{1}{35}\sqrt{E_{33}}(7 + 6E_r) \tag{6.14a}$$

$$I_2 = \langle (E_{pq}n_pn_q)^{0.5}n_3^4\rangle \approx \frac{1}{35}\sqrt{E_{33}}(7 + 2E_r) \tag{6.14b}$$

$$I_3 = \langle (E_{pq}n_pn_q)^{0.5}n_1^2\rangle \approx \frac{1}{15}\sqrt{E_{33}}(5 + 4E_r) \tag{6.14c}$$

$$I_4 = \langle (E_{pq}n_pn_q)^{1/2}n_3^2\rangle \approx \frac{1}{15}\sqrt{E_{33}}(5 + 2E_r) \tag{6.14d}$$

$$I_5 = \langle (E_{pq}n_pn_q)^{1/2}n_3^2\rangle \approx \frac{1}{15}\sqrt{E_{33}}(5 + 4E_r) \tag{6.14e}$$

$$I_6 = \langle (E_{pq}n_pn_q)^{0.5}n_1^2n_3^2\rangle \approx \frac{1}{105}\sqrt{E_{33}}(7 + 4E_r) \tag{6.14f}$$

$$I_7 = \langle (E_{pq}n_pn_q)^{0.5}n_2^2n_3^2\rangle \approx \frac{1}{105}\sqrt{E_{33}}(7 + 4E_r) \tag{6.14g}$$

$$I_8 = \langle (E_{pq}n_pn_q)^{0.5}n_1^2n_2^2\rangle \approx \frac{1}{105}\sqrt{E_{33}}(7 + 4E_r) \tag{6.14h}$$

$$I_9 = \langle (E_{pq}n_pn_q)^{1.5}n_1^2\rangle \approx \frac{1}{15}E_{33}^{1.5}(5 + 12E_r) \tag{6.14i}$$

$$I_{10} = \langle (E_{pq}n_pn_q)^{1.5}n_3^2\rangle \approx \frac{1}{15}E_{33}^{1.5}(5 + 6E_r) \tag{6.14j}$$

Note that there are two integrals, I_4, I_5 which apparently have the same expression $\langle (E_{pq}n_pn_q)^{1/2}n_3^2\rangle$, but different approximations[4]:

In Bandyopadhyay (2009) it is stated that[5]

$$(E_{pq}n_pn_q)^{0.5} = (E_{11}n_1n_1 + E_{22}n_2n_2 + E_{33}n_3n_3)^{0.5} \tag{6.15a}$$

$$\approx \sqrt{E_{33}}\left[1 + \frac{E_{11} - E_{33}}{2E_{33}}sin^2(\theta)\right] \tag{6.15b}$$

Where the approximation is limited by the condition in equation (6.5)[6].

This can be inserted into the expressions for I_4 and I_5. Using equation (5.15d) it can be seen from figures 6.1 and 6.2 that I_4 is correct, whereas I_5 should be for n_2^2 [7].

This oversight did not need evolve into a problem, but it appears as if Bandyopadhyay (2009) uses I_5 when creating explicit expressions for stress. This can be discovered by returning to equation (5.9) with the results from above[8]:

[2]The expression for σ_{33}^r provided in Bandyopadhyay (2009) is likely wrong, but is written as presented in Bandyopadhyay (2009) for reference.

[3]The starting point is wrong, as σ_{33}^r is wrong, but the expression for E_{33} would wrong even if σ_{33}^r was correct.

[4]I_4 corresponds to equation 3.41, and I_5 to equation 3.42 in Bandyopadhyay (2009)

[5]$(E_{pq}n_pn_q)^{0.5}$ should in principle as far as Einstein summation convention goes equal $(E_{11}n_1n_1 + E_{12}n_1n_2 + E_{13}n_1n_3 + E_{21}n_2n_1 + E_{22}n_2n_2 + E_{23}n_2n_3 + E_{31}n_3n_1 + E_{32}n_3n_2 + E_{33}n_3n_3)^{0.5}$ but due to the definition of strain as $E_{ij} = E_{11}\delta_{i1}\delta_{j1} + E_{11}\delta_{i2}\delta_{j2} + E_{33}\delta_{i3}\delta_{j3}$ a lot of these terms are 0 ($i \neq j \rightarrow E_{ij} = 0$).

[6]This approximation will be analysed in more detail later.

[7]The software utilised is *maple*.

[8]Compared to expression (5.9) $-E_{pq}n_pn_q \rightarrow E_{pq}n_pn_q$ and $E_{33} \rightarrow -E_{33}$ due to the switch from negative to positive in compaction.

$r := \text{sqrt}(E_{33})\ (1 + E_r \sin(\text{theta})^2)$

$$\sqrt{E_{33}}\ \left(1 + E_r \sin(\theta)^2\right)$$

$n_3 := \cos(\text{theta})$

$t := r \cdot n_3^{\,2} \cdot \sin(\text{theta})$

$$\sqrt{E_{33}}\ \left(1 + E_r \sin(\theta)^2\right) \cos(\theta)^2 \sin(\theta)$$

$u := integrate(t, \text{theta} = 0 \ldots \text{Pi})$

$$\frac{4}{15}\sqrt{E_{33}}\ E_r + \frac{2}{3}\sqrt{E_{33}}$$

$v := integrate(u, \text{phi} = 0 \ldots 2 \cdot \text{Pi})$

$$\frac{8}{15}\sqrt{E_{33}}\ E_r \pi + \frac{4}{3}\sqrt{E_{33}}\ \pi$$

$f := \frac{v}{4\,\text{Pi}}$

$$\frac{1}{4}\ \frac{\frac{8}{15}\sqrt{E_{33}}\ E_r \pi + \frac{4}{3}\sqrt{E_{33}}\ \pi}{\pi}$$

simplify

$$\frac{1}{15}\sqrt{E_{33}}\ (2E_r + 5)$$

Figure 6.1: Solving the integrals with n_3, which can be seen to correspond to I_4 as seen in equation (6.14d) .

$r := \text{sqrt}(E_{33})\ (1 + E_r \sin(\text{theta})^2)$

$$\sqrt{E_{33}}\ \left(1 + E_r \sin(\theta)^2\right)$$

$n_2 := \sin(\text{theta}) \cdot \sin(\text{phi})$

$$\sin(\theta)\ \sin(\phi)$$

$t := r \cdot n_2^{\,2} \cdot \sin(\text{theta})$

$$\sqrt{E_{33}}\ \left(1 + E_r \sin(\theta)^2\right) \sin(\theta)^3 \sin(\phi)^2$$

$u := integrate(t, \text{theta} = 0 \ldots \text{Pi})$

$$\frac{16}{15}\sqrt{E_{33}}\ \sin(\phi)^2 E_r + \frac{4}{3}\sqrt{E_{33}}\ \sin(\phi)^2$$

$v := integrate(u, \text{phi} = 0 \ldots 2 \cdot \text{Pi})$

$$\frac{16}{15} E_r \sqrt{E_{33}}\ \pi + \frac{4}{3}\sqrt{E_{33}}\ \pi$$

$f := \frac{v}{4\,\text{Pi}}$

$$\frac{1}{4}\ \frac{\frac{16}{15} E_r \sqrt{E_{33}}\ \pi + \frac{4}{3}\sqrt{E_{33}}\ \pi}{\pi}$$

simplify

$$\frac{1}{15}\sqrt{E_{33}}\ (4E_r + 5)$$

Figure 6.2: Solving the integrals with n_2, which can be seen to correspond to I_5, suggesting that the expression for I_5 presented in Bandyopadhyay (2009) given in equation (6.14e) should be for n_2

$$\sigma_{33}^r = \frac{(1-\phi)B}{\pi^2 B(2B+C)}\{B\langle(E_{pq}n_p n_q)^{1/2}[-E_{33}n_3n_3 - E_{33}n_3n_3]\rangle -$$
$$C\langle(E_{pq}n_p n_q)^{3/2}n_3n_3\rangle\} \rightarrow$$
$$\sigma_{33}^r = \frac{(1-\phi)B}{\pi^2 B(2B+C)}\{-2E_{33}B\frac{1}{15}\sqrt{E_{33}}(2E_r+5) -$$
$$C\frac{1}{15}E_{33}^{3/2}(5+6E_r)\} \rightarrow$$
$$\sigma_{33}^r = -\frac{Z}{15}E_{33}^{3/2}(5C + 10B + E_r(6C+4B)) \tag{6.16}$$

Where it has been used from Bandyopadhyay (2009) that

$$\langle(E_{pq}n_p n_q)^{3/2}n_3n_3\rangle \approx \frac{1}{15}E_{33}^{3/2}(5+6E_r) \tag{6.17}$$

Equation (6.16) does not correspond to (6.9), the difference being 4B rather than 8B in the final bracket. If the expression for I_5 is used (seemingly corresponding to n_2) the expression in equation (6.9) is obtained. This might be an indicator that Bandyopadhyay (2009) utilised the expressions which corresponding to n_2 rather than n_3. It is uncertain how much of an error this would actually introduce, since the condition in equation (6.5) means that the term multiplied by E_r will have a small contribution.

Given that the error introduced by the first mistake might be minor, it is relevant to investigate to what extend the expressions for strain in terms of stress given in Bandyopadhyay (2009) are correct. Presumably, the equations for stress in equations (6.8) and (6.9) are solved to yield the explicit expressions for strain given in equations (6.13) and (6.11) (Bandyopadhyay, 2009).

A good way to check if a solution to such a system of equations is correct is by simply by inserting some numbers. This is done for a set of parameters, and an implementation sequence in *maple* is given in appendix A[9]. It is observed that the proposed solutions does not work with back substitution and might therefore be wrong. Recall however that the starting point is likely wrong due to the mistake in σ_{33}^r.

The expressions presented in Bandyopadhyay (2009) should thus be treated with care. A further problem with the claim of having developed triaxial expressions, as is done in Bandyopadhyay (2009) is the limitation of equation (6.5). This limitation means that not all strain states satisfying equation (6.1) are covered by the expressions.

6.2.1 Understanding the Approximation

The first step in investigating the possibility of removing the assumption of equation (6.5) is to investigate what the approximation accomplishes.

[9] Recall that even though the strains are now positive in compaction, the stress is negative in compression in Bandyopadhyay (2009).

Recall from Bandyopadhyay (2009)

$$(E_{pq}n_pn_q)^{0.5} = (E_{11}n_1n_1 + E_{22}n_2n_2 + E_{33}n_3n_3)^{0.5} \tag{6.18a}$$

$$\approx \sqrt{E_{33}}\left[1 + \frac{E_{11} - E_{33}}{2E_{33}} sin^2(\theta)\right] \tag{6.18b}$$

$$n_1 = sin(\theta)cos(\phi) \tag{6.18c}$$

$$n_2 = sin(\theta)sin(\phi) \tag{6.18d}$$

$$n_3 = cos(\theta) \tag{6.18e}$$

By inserting the expressions for n_i and the condition that the horizontal strains are equal, $E_{11} = E_{22}$, the right hand side of equation (6.18a) can be written

$$(E_{11} sin^2(\theta)(\sin^2(\phi) + \cos^2(\phi)) + E_{33}\cos^2(\theta))^{0.5} = \tag{6.19a}$$

$$(E_{11}\sin^2(\theta) + E_{33}\cos^2(\theta))^{0.5} = \tag{6.19b}$$

$$\sqrt{E_{33}}\Big(\frac{E_{11}}{E_{33}}\sin^2(\theta) + \cos^2(\theta)\Big)^{0.5} = \tag{6.19c}$$

$$\sqrt{E_{33}}\Big(\frac{E_{11}}{E_{33}}\sin^2(\theta) + \frac{E_{33}}{E_{33}}(1 - \sin^2(\theta)\Big)^{0.5} = \tag{6.19d}$$

$$\sqrt{E_{33}}\Big(1 + \frac{E_{11} - E_{33}}{E_{33}}\sin^2(\theta)\Big)^{0.5} \tag{6.19e}$$

- To get to equation (6.19b) it has been used that $\sin^2(\phi) + \cos^2(\phi) = 1$.
- To get to equation (6.19c) E_{33} has simply been pulled out of the brackets.
- To get to equation (6.19d) it has been used that $\cos^2(\theta) = 1 - \sin^2(\theta) = \frac{E_{33}}{E_{33}}(1 - \sin^2(\theta))$.
- To get to equation (6.19e) the terms are simply collected.

Let $x = \frac{E_{11} - E_{33}}{E_{33}}\sin^2(\theta)$ such that equation (6.19e) can be written

$$\sqrt{E_{33}}\sqrt{1 + x} \tag{6.20}$$

By introducing the assumption in (6.5) a reasonable approximation of the square root term is the first two terms of the Taylor expansion (see (Adams and Essex, 2009, Chapter 9.6)). The fact that $\sin^2(\theta) \leq 1$ means that the value of x is small, such that higher order terms approach 0.

$$\sqrt{1 + x} = 1 + \frac{x}{2} - \frac{x^2}{8} + \frac{x^3}{8} - \frac{5x^4}{128}... \rightarrow \tag{6.21}$$

$$\sqrt{1 + x} \approx 1 + \frac{x}{2} \rightarrow \tag{6.22}$$

$$\sqrt{E_{33}}\Big(1 + \frac{E_{11} - E_{33}}{E_{33}}\sin^2(\theta)\Big)^{0.5} \approx \tag{6.23}$$

$$\sqrt{E_{33}}\Big(1 + \frac{E_{11} - E_{33}}{2E_{33}}\sin^2(\theta)\Big) = \tag{6.24}$$

$$\sqrt{E_{33}}\Big(1 + E_r\sin^2(\theta)\Big)^{0.5} \tag{6.25}$$

One more approximation was utilised in Bandyopadhyay (2009)

$$(E_{pq}n_pn_q)^{3/2} \approx E_{33}^{3/2}(1 + 3E_r\sin^2(\theta)) \tag{6.26}$$

This has its root in

$$(1 + x)^{3/2} = 1 + \frac{3x}{2} + \frac{3x^2}{8} - \frac{x^3}{16} + ... \tag{6.27}$$

By choosing $x = \frac{E_{11} - E_{33}}{E_{33}}\sin^2(\theta)$ and choosing two terms:

$$E_{33}^{3/2}\Big(1 + \frac{E_{11} - E_{33}}{E_{33}}\sin^2(\theta)\Big)^{3/2} \approx \tag{6.28a}$$

$$E_{33}^{3/2}\Big(1 + 3\frac{E_{11} - E_{33}}{2E_{33}}\sin^2(\theta)\Big) = \tag{6.28b}$$

$$E_{33}^{3/2}(1 + 3E_r\sin^2(\theta)) \tag{6.28c}$$

The purpose of the approximations is therefore to remove the square root and $()^{3/2}$ terms containing variables that enter into the integral equations $I_1 \rightarrow I_{10}$. This simplifies the integrals, such that the final expressions are easier to implement.

The approximations are better for the square root terms than the 1.5 terms, but when approaching the uniaxial compaction limit ($E_r = -0.5$) there is expected to be significant deviation also in the square root term.

One consequence is that the model does not reduce to Walton's model in the limit of $E_r \rightarrow -0.5$ (uniaxial compaction).

As an example, consider the smooth model. From Walton (1987)

$$\sigma_{11}^s = -\frac{(1 - \phi)n}{\pi^2 B}\langle(E_{pq}n_pn_q)n_1^2\rangle \tag{6.29}$$

$$\sigma_{33}^s = -\frac{(1 - \phi)n}{\pi^2 B}\langle(E_{pq}n_pn_q)n_3^2\rangle \tag{6.30}$$

$$\frac{\sigma_{33}^s}{\sigma_{11}^s} = \frac{I_{10}}{I_9} \tag{6.31}$$

In the limit of uniaxial compaction, it can further be shown from Walton (1987)

$$\sigma_{11}^s = -\frac{(1 - \phi)nE_{33}^{3/2}}{24\pi^2 B} \tag{6.32a}$$

$$\sigma_{33}^s = -\frac{(1 - \phi)nE_{33}^{3/2}}{6\pi^2 B} \rightarrow \tag{6.32b}$$

$$\frac{\sigma_{33}^s}{\sigma_{11}^s} = 4 \tag{6.32c}$$

Figure 6.3 shows plots of I_{10} and I_9 as functions of E_r. The interesting thing to note is that the approximation causes the value of I_9 to cross 0. This means that $\frac{I_{10}}{I_9}$ at some point is infinite, before it becomes negative, clearly not approaching the expected value of 4. The exact values are dependent on E_{33}, but the zero crossing is always at $E_r = -\frac{5}{12}$.

The expressions by Bandyopadhyay (2009) are not appropriate for all triaxial stress states, even if the horizontal stresses are equal, and so to implement the theory from Walton (1987) a new set of equations are needed.

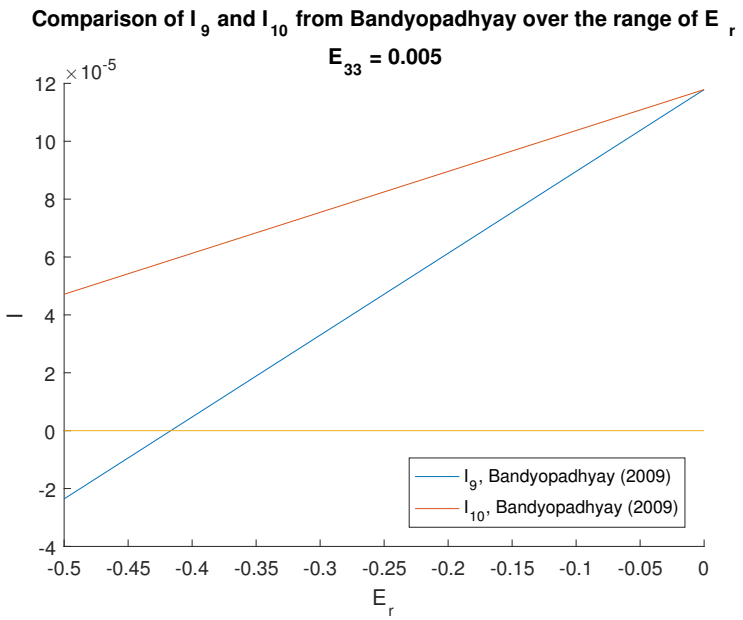

Figure 6.3: Comparison of I_9 and I_{10} from Bandyopadhyay (2009). Note how I_9 crosses zero for a strain anisotropy of $E_r = -5/12$

Chapter 7

Creating Triaxial Expressions From Walton (1987)

The previous chapter describe the extension to triaxial strain from Walton (1987) in Bandyopadhyay (2009), which was limited to the scenario where the horizontal strains are equal. By assuming small strain anisotropy, relatively simple expressions can be created[1]. The assumption however means that the expressions are not applicable over all strain states covered by equation (6.1).

It is of interest to derive the expressions from Walton (1987) for a triaxial strain state, still under the condition in equation (6.1), but without the strain anisotropy limitations imposed by Bandyopadhyay (2009).

7.1 Rewriting the Integral Equations

The approximation was implemented to simplify the integral equations, and so to remove the approximation, these must be re-evaluated. Keeping with the notation of Bandyopadhyay (2009) the integral equations are solved to yield[2]:

$$I_1 = \langle (E_{pq} n_p n_q)^{0.5} n_1^4 \rangle = \frac{1}{4096} \frac{\sqrt{E_{33}}}{(-E_r)^{5/2}} \big[480(-E_r)^{5/2} - 64(-E_r)^{5/2} - 24\sqrt{-E_r} + V \cdot (240\sqrt{2}E_r^3 + 72\sqrt{2}E_r^2 - 12\sqrt{2}E_r + 6\sqrt{2})\big] \tag{7.1}$$

$$I_2 = \langle (E_{pq} n_p n_q)^{0.5} n_3^4 \rangle = \frac{1}{1536} \frac{\sqrt{E_{33}}}{(-E_r)^{5/2}} \big[96(-E_r)^{5/2} + 128(-E_r)^{5/2} - 24\sqrt{-E_r} + V \cdot (48\sqrt{2}E_r^3 + 72\sqrt{2}E_r^2 + 36\sqrt{2}E_r + 6\sqrt{2})\big] \tag{7.2}$$

$$I_3 = \langle (E_{pq} n_p n_q)^{0.5} n_1^2 \rangle = \frac{-1}{128} \frac{\sqrt{E_{33}}}{(-E_r)^{3/2}} \big[-24(-E_r)^{3/2} + 4\sqrt{-E_r} + V \cdot (12\sqrt{2}E_r^2 + 4\sqrt{2}E_r - \sqrt{2})\big] \tag{7.3}$$

$$I_4 = \langle (E_{pq} n_p n_q)^{0.5} n_3^2 \rangle = \frac{-1}{64} \frac{\sqrt{E_{33}}}{(-E_r)^{3/2}} \big[-8(-E_r)^{3/2} - 4\sqrt{-E_r} + V \cdot (4\sqrt{2}E_r^2 + 4\sqrt{2}E_r + \sqrt{2})\big] \tag{7.4}$$

$$I_5 = \langle (E_{pq} n_p n_q)^{0.5} n_2^2 \rangle = \frac{-1}{128} \frac{\sqrt{E_{33}}}{(-E_r)^{3/2}} \big[-24(-E_r)^{3/2} + 4\sqrt{-E_r} + V \cdot (12\sqrt{2}E_r^2 + 4\sqrt{2}E_r - \sqrt{2})\big] \tag{7.5}$$

$$I_6 = \langle (E_{pq} n_p n_q)^{0.5} n_1^2 n_3^2 \rangle = \frac{1}{3072} \frac{\sqrt{E_{33}}}{(-E_r)^{5/2}} \big[96(-E_r)^{5/2} - 32(-E_r)^{5/2} + 24\sqrt{-E_r} + V \cdot (48\sqrt{2}E_r^3 + 24\sqrt{2}E_r^2 - 12\sqrt{2}E_r - 6\sqrt{2})\big] \tag{7.6}$$

$$I_7 = \langle (E_{pq} n_p n_q)^{0.5} n_2^2 n_3^2 \rangle = \frac{1}{3072} \frac{\sqrt{E_{33}}}{(-E_r)^{5/2}} \big[96(-E_r)^{5/2} - 32(-E_r)^{5/2} + 24\sqrt{-E_r} + V \cdot (48\sqrt{2}E_r^3 + 24\sqrt{2}E_r^2 - 12\sqrt{2}E_r - 6\sqrt{2})\big] \tag{7.7}$$

$$I_8 = \langle (E_{pq} n_p n_q)^{0.5} n_1^2 n_2^2 \rangle = \frac{1}{12288} \frac{\sqrt{E_{33}}}{(-E_r)^{5/2}} \big[480(-E_r)^{5/2} - 64(-E_r)^{5/2} - 24\sqrt{-E_r} + V \cdot (240\sqrt{2}E_r^3 + 72\sqrt{2}E_r^2 - 12\sqrt{2}E_r + 6\sqrt{2})\big] \tag{7.8}$$

$$I_9 = \langle (E_{pq} n_p n_q)^{1.5} n_1^2 \rangle = -\frac{1}{1536} \frac{E_{33}^{3/2}}{(-E_r)^{3/2}} (480(-E_r)^{5/2} - 352(-E_r)^{3/2} + 24\sqrt{-E_r} + V \cdot (240\sqrt{2}E_r^3 + 216\sqrt{2}E_r^2 + 36\sqrt{2}E_r - 6\sqrt{2})) \tag{7.9}$$

$$I_{10} = \langle (E_{pq} n_p n_q)^{1.5} n_3^2 \rangle = -\frac{1}{768} \frac{E_{33}^{3/2}}{(-E_r)^{3/2}} (96(-E_r)^{5/2} - 128(-E_r)^{3/2} - 24\sqrt{-E_r} + V \cdot (48\sqrt{2}E_r^3 + 72\sqrt{2}E_r^2 + 36\sqrt{2}E_r + 6\sqrt{2})) \tag{7.10}$$

[1] Figures 6.1 and 6.2 demonstrate how one set of these simple expressions are created.

[2] Due to the fact that $E_{11} = E_{22}$ it can be observed that $I_3 = I_5$ and $I_6 = I_7$.

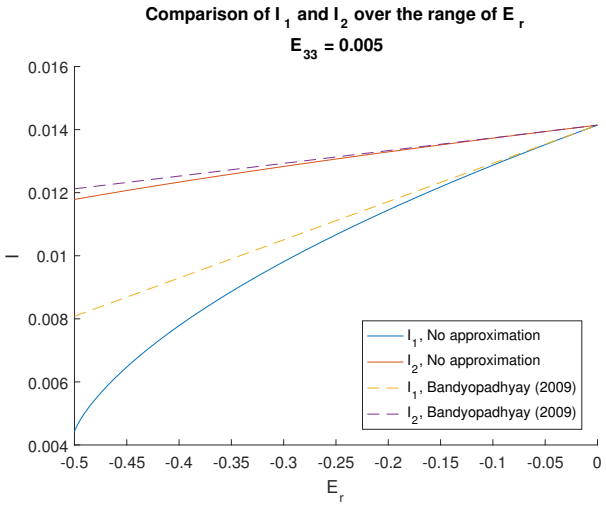

Figure 7.1: Comparison of the values of I_1 and I_2 as functions of strain anisotropy derived in this work, and those presented in Bandyopadhyay (2009)

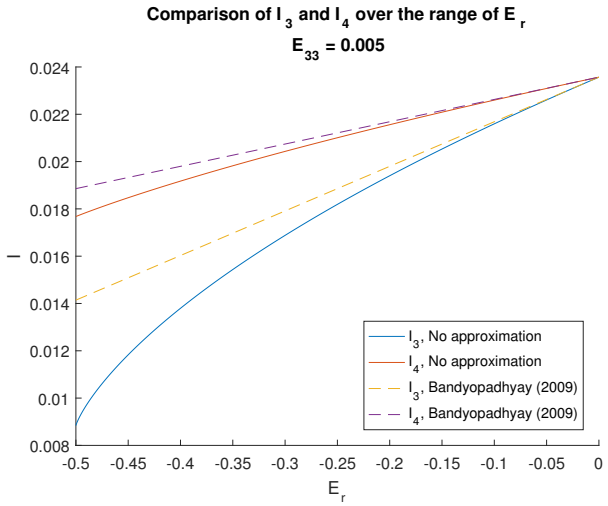

Figure 7.2: Comparison of the values of I_3 and I_4 as functions of strain anisotropy derived in this work, and those presented in Bandyopadhyay (2009)

Where

$$V = \ln\left(\frac{1+\sqrt{2}\sqrt{-E_r}}{1-\sqrt{2}\sqrt{-E_r}}\right) \tag{7.11}$$

A detailed rendition of the process of solving these integral equations is given in appendix A for I_9.

7.2 Comparison of the Updated Integral Equations With Those From Bandyopadhyay (2009)

The expressions for $I_1 \rightarrow I_{10}$ can now be compared to those given in Bandyopadhyay (2009) and this is displayed in figures 7.1 to 7.4. It can be observed that down to a strain ansiotropy of around $E_r = -0.15$ the approximated values seem to match the actual values quite well. As the strain anisotropy becomes stronger, the deviation between the integral equations increases. The exact values of these curves are dependent on the value of E_{33}, but the observed trends are not affected by a change in E_{33}.

7.3 The Limits of Uniaxial and Isotropic Compaction

The cases of $E_r = 0$ and $E_r = -0.5$ correspond to isotropic and uniaxial strain respectively. Inserting these limits directly into equations $I_1 \rightarrow I_{10}$ involves division by zero and also creates a term with $\ln 0$. Both of these are undefined, and so the limits have to be calculated. This can be done using for example l'Hôpitals rule. The methodology and an example of how the limits can be calculated is discussed in appendix A, and the

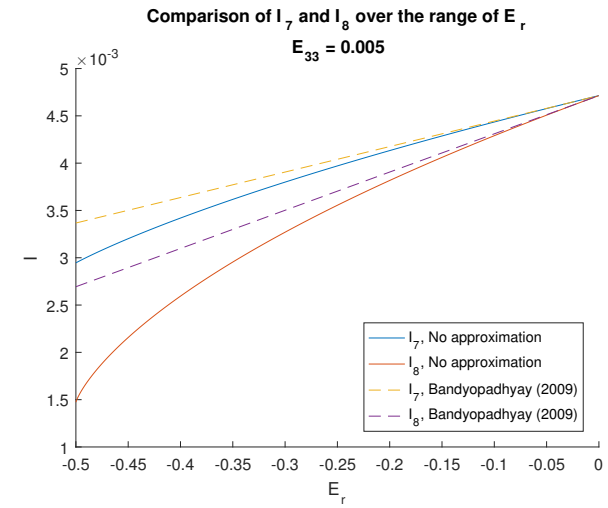

Figure 7.3: Comparison of the values of I_7 and I_8 as functions of strain anisotropy derived in this work, and those presented in Bandyopadhyay (2009)

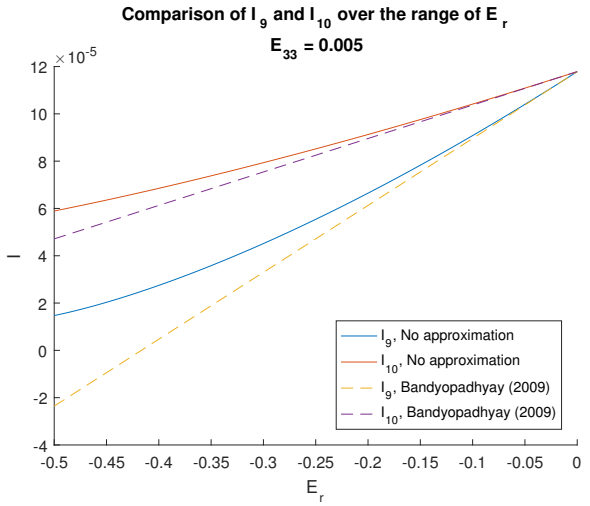

Figure 7.4: Comparison of the values for I_9 and I_10 as functions of strain anisotropy derived in this work, and those presented in Bandyopadhyay (2009)

following limits are obtained[3]:

$$I_1(E_r \to -0.5) = \frac{\sqrt{E_{33}}}{16} \tag{7.12a}$$

$$I_1(E_r \to 0) = \frac{\sqrt{E_{33}}}{5} \tag{7.12b}$$

$$I_2(E_r \to -0.5) = \frac{\sqrt{E_{33}}}{6} \tag{7.13a}$$

$$I_2(E_r \to 0) = \frac{\sqrt{E_{33}}}{5} \tag{7.13b}$$

$$I_3(E_r \to -0.5) = \frac{\sqrt{E_{33}}}{8} \tag{7.14a}$$

$$I_3(E_r \to 0) = \frac{\sqrt{E_{33}}}{3} \tag{7.14b}$$

$$I_4(E_r \to -0.5) = \frac{\sqrt{E_{33}}}{4} \tag{7.15a}$$

$$I_4(E_r \to 0) = \frac{\sqrt{E_{33}}}{3} \tag{7.15b}$$

$$I_6(E_r \to -0.5) = \frac{\sqrt{E_{33}}}{24} \tag{7.16a}$$

$$I_6(E_r \to 0) = \frac{\sqrt{E_{33}}}{15} \tag{7.16b}$$

$$I_8(E_r \to -0.5) = \frac{\sqrt{E_{33}}}{48} \tag{7.17a}$$

$$I_8(E_r \to 0) = \frac{\sqrt{E_{33}}}{15} \tag{7.17b}$$

[3]Recall $I_3 = I_5$, $I_6 = I_7$.

$$I_9(E_r \to -0.5) = \frac{E_{33}^{3/2}}{24} \tag{7.18a}$$

$$I_9(E_r \to 0) = \frac{E_{33}^{3/2}}{3} \tag{7.18b}$$

$$I_{10}(E_r \to -0.5) = \frac{E_{33}^{3/2}}{6} \tag{7.19a}$$

$$I_{10}(E_r \to 0) = \frac{E_{33}^{3/2}}{3} \tag{7.19b}$$

7.4 Stress and Stiffness - Rough Contacts

To utilise equations (7.1) to (7.10) the expressions for stress and stiffness are rewritten from equations (5.9) and (5.12) in terms of $I_1 \to I_{10}$[4], [5]

$$\sigma_{11}^r = Z \cdot (-2BE_{11}I_3 - C \cdot I_9) = Z \cdot (-4BE_{33}(E_r + 0.5)I_3 - C \cdot I_9) \tag{7.20}$$

$$\sigma_{33}^r = Z \cdot (-2BE_{33}I_4 - C \cdot I_{10}) = \tag{7.21}$$

Where

$$Z = \frac{(1-\phi)n}{\pi^2 B(2B+C)} \tag{7.22}$$

$$C_{11}^r = X \cdot (4BI_3 + 2CI_1) \tag{7.23}$$

$$C_{33}^r = X \cdot (4BI_4 + 2CI_2) \tag{7.24}$$

$$C_{13}^r = X \cdot (2CI_6) \tag{7.25}$$

$$C_{44}^r = X \cdot (BI_4 + BI_5 + 2CI_7) \tag{7.26}$$

$$C_{66}^r = X \cdot (BI_3 + BI_5 + 2CI_8) \tag{7.27}$$

Where

$$X = \frac{3(1-\phi)N}{4\pi^2 B(2B+C)} \tag{7.28}$$

The P-wave anisotropy can be seen to be given as

[4]Sign deviations come from the aforementioned fact that the strain is now *positive* in compaction, whereas it in Walton (1987) is *negative* in compaction.

[5]In equation (7.20) it is utilised that $E_{11} = E_{33}(2E_r + 1)$.

$$\epsilon = \frac{C_{11}^r - C_{33}^r}{2C_{33}^r} = \frac{2B(I_3 - I_4) + C(I_1 - I_2)}{4BI_4 + 2CI_2} \tag{7.29}$$

From figures 7.1 and 7.2 it is observed that $I_4 > I_3$ and $I_2 > I_1$, such that $\epsilon < 0$. Although the full expressions with insertion of the expression for I_j is not done, it is clear from equations (7.1) to (7.4) that $\sqrt{E_{33}}$ would cancel from the expression for anisotropy, leaving the P-wave anisotropy dependent on grain parameters and strain anisotropy.

As pointed out in Bandyopadhyay (2009) having equations dependent on stress rather than strain are desired, as stress is generally a more available parameter. Equations (7.20) and (7.21) are dependent on E_r and E_{33} and so in theory it is possible to derive expressions for the strain parameters in terms of the stress. These strain values can then be used to calculate the value of $I_1 \rightarrow I_{10}$ and thus the stiffness parameters.

Due to the complexity of the expressions, creating explicit expressions (as presented in Bandyopadhyay (2009), although these were wrong) is complicated. Dividing equation (7.21) by (7.20) leaves an equation only dependent on E_r. The stress is known, and so this can easily be rearranged and put equal to zero. By differentiating the expression, Newton's method can be used to solve for E_r numerically[6].

The function in terms of E_r to be set equal to zero is given in equation (7.30). The derivative is given in equation (7.31). The full expressions[7] can be seen in figures 7.5 and 7.6 and are easily copied into *matlab* where the iteration process is run.

$$\begin{aligned} f(E_r) = &\Big[(-192\,B - 128\,C)(-E_r)^{3/2} + 96\,C(-E_r)^{5/2} \\ &- (96\,B + 24\,C)\sqrt{-E_r} \\ &+ 96\,((\frac{E_r}{2} + \frac{1}{4})C + B)V\sqrt{2}(E_r + 1/2)^2\Big]/ \\ &\Big[(-384\,B - 176\,C)(-E_r)^{3/2} + (576\,B + 240\,C)(-E_r)^{5/2} + \\ &(48\,B + 12\,C)\sqrt{-E_r} + \\ &288\,((\frac{5\,E_r}{12} - \frac{1}{24})C + B(E_r - \frac{1}{6}))V\sqrt{2}(E_r + \frac{1}{2})^2\Big] \\ &- \frac{\sigma_{33}}{\sigma_{11}} = 0 \end{aligned} \tag{7.30}$$

[6] See for example (Kreyszig, 2010, Chapter 19.2) for a description of using Newton's method.

[7] I.e., with the expression for V inserted. Since V is a function of E_r as well it is instructive to view these expressions. The expression in equation (7.31) has been calculated by first differentiating the expression in figure 7.5, which is illustrated in figure 7.6 and then re-inserting V to make the expression more "clean".

$$\begin{aligned} 0 = &\left(96\left(E_r + \frac{1}{2}\right)^2\sqrt{2}\left(\left(\frac{1}{2}E_r + \frac{1}{4}\right)C\right.\right. \\ &\left. + B\right)\ln\left(\frac{-\sqrt{2}\sqrt{-E_r} - 1}{\sqrt{2}\sqrt{-E_r} - 1}\right) + (-192\,B - 128\,C)\left(-E_r\right)^{3/2} \\ &+ 96\,C\left(-E_r\right)^{5/2} - 96\left(B + \frac{1}{4}C\right)\sqrt{-E_r}\Bigg) \Bigg/ \Bigg(288\left(E_r\right. \\ &+ \frac{1}{2}\Big)^2\sqrt{2}\left(\left(\frac{5}{12}E_r - \frac{1}{24}\right)C + B\left(E_r\right.\right. \\ &\left.\left. - \frac{1}{6}\right)\right)\ln\left(\frac{-\sqrt{2}\sqrt{-E_r} - 1}{\sqrt{2}\sqrt{-E_r} - 1}\right) + (-384\,B - 176\,C)\left(-E_r\right)^{3/2} \\ &+ (576\,B + 240\,C)\left(-E_r\right)^{5/2} + 48\left(B + \frac{1}{4}C\right)\sqrt{-E_r}\Bigg) - \frac{\sigma_{33}}{\sigma_{11}} \end{aligned}$$

Figure 7.5: The full expression for the expression with $\frac{\sigma_{33}}{\sigma_{11}}$ set equal to 0, taken directly from *maple*. The expression corresponds to that seen in equation (7.30), with the expression for V inserted.

$$\begin{aligned} \frac{df(E_r)}{dE_r} = &\frac{-2}{3}\frac{(B + \frac{C}{4})(B + \frac{C}{2})}{\sqrt{-E_r}}\Big[\Big((-E_r)^{9/2} + \frac{\sqrt{-E_r}}{16} \\ &\frac{-1}{2}(-E_r)^{3/2} + \frac{3}{2}(-E_r)^{5/2} - 2\,(-E_r)^{7/2}\Big)V^2 \\ &- 2\sqrt{2}(E_r + \frac{1}{2})E_r\,({E_r}^2 - \frac{E_r}{3} + \frac{1}{4})V \\ &- \frac{3(-E_r)^{3/2}}{2} + \frac{10(-E_r)^{5/2}}{3} + 2(-E_r)^{7/2}\Big]/ \\ &\Big[\sqrt{2}\Big((\frac{5\,C}{12} + B)E_r - \frac{B}{6} - \frac{C}{24}\Big)(E_r + \frac{1}{2})^2V \\ &- (\frac{4}{3}B + \frac{11\,C}{18})(-E_r)^{3/2} + (2\,B + \frac{5}{6}C)(-E_r)^{5/2} \\ &+ \frac{1}{6}(B + \frac{C}{4})\sqrt{-E_r}\Big]^2 \end{aligned} \tag{7.31}$$

Following the calculation of E_r, E_{33} can be calculated:

$$\begin{aligned} E_{33} = &\Big([\sigma_{33}\,(-E_r)^{3/2}]/ \\ &[Z\{\frac{C{E_r}^3\sqrt{2}V}{16} + \frac{C(-E_r)^{5/2}}{8} + \frac{B{E_r}^2\sqrt{2}V}{8} + \\ &\frac{3\,C{E_r}^2\sqrt{2}V}{32} + \frac{BE_r\sqrt{2}V}{8} - \frac{B(-E_r)^{3/2}}{4} + \\ &\frac{3\,CE_r\sqrt{2}V}{64} - \frac{C(-E_r)^{3/2}}{6} + \frac{B\sqrt{2}V}{32} + \\ &\frac{C\sqrt{2}V}{128} - 1/8\,B\sqrt{-E_r} - 1/32\,C\sqrt{-E_r}\}^{-1}]\Big)^{2/3} \end{aligned} \tag{7.32}$$

The values for E_r and E_{33} are then inserted into equations (7.1) to (7.10) which yields the stiffnesses.

$$\text{derivative} = -\frac{2}{3}\left(\left(\left(-E_r\right)^{9/2}+\frac{1}{16}\sqrt{-E_r}-\frac{1}{2}\left(-E_r\right)^{3/2}+\frac{3}{2}\left(-E_r\right)^{5/2}-2\left(-E_r\right)^{7/2}\right)\ln\left(\frac{-\sqrt{2}\sqrt{-E_r}-1}{\sqrt{2}\sqrt{-E_r}-1}\right)^2-2\sqrt{2}\left(E_r+\frac{1}{2}\right)E_r\left(E_r^2-\frac{1}{3}E_r+\frac{1}{4}\right)\ln\left(\frac{-\sqrt{2}\sqrt{-E_r}-1}{\sqrt{2}\sqrt{-E_r}-1}\right)-\frac{3}{2}\left(-E_r\right)^{3/2}+\frac{10}{3}\left(-E_r\right)^{5/2}+2\left(-E_r\right)^{7/2}\right)\left(B+\frac{1}{4}C\right)\left(B+\frac{1}{2}C\right)\Bigg)\Bigg/\left(\sqrt{-E_r}\left(\sqrt{2}\left(\left(\frac{5}{12}C+B\right)E_r-\frac{1}{6}B-\frac{1}{24}C\right)\left(E_r+\frac{1}{2}\right)^2\ln\left(\frac{-\sqrt{2}\sqrt{-E_r}-1}{\sqrt{2}\sqrt{-E_r}-1}\right)+\left(-\frac{4}{3}B-\frac{11}{18}C\right)\left(-E_r\right)^{3/2}+\left(2B+\frac{5}{6}C\right)\left(-E_r\right)^{5/2}+\frac{1}{6}\left(B+\frac{1}{4}C\right)\sqrt{-E_r}\right)^2\right)$$

Figure 7.6: Expression for the derivative of equation (7.30) to be used in Newton's method. Taken directly from *maple*, with the expression for V inserted.

7.4.1 The Limits of Uniaxial and Isotropic Compaction

It is imperative that the equations for stress and stiffness reduce to the expressions in Walton (1987) for the limits of uniaxial and isotropic compaction. The limits for the integrals have been provided earlier, and these can be inserted into the equations for stress and stiffness in the limits.

The stress in the limit of isotropic compaction is also isotropic, and the expression from Walton (1987) was given in equation (5.16). Inserting the limits for $I_3(E_r \to 0)$ and $I_9(E_r \to 0)$ into equation (7.20) together with $E_{11} = E_{33}$ gives

$$\begin{aligned}\sigma_{11}^r &= -\frac{ZE_{33}^{3/2}}{3}(2B+C) \to \\ \sigma_{11}^r &= -\frac{E_{33}^{3/2}(1-\phi)n}{3\pi^2 B} = \sigma_{33}^r\end{aligned} \tag{7.33}$$

Equation (7.33) is thus consistent with the results from Walton (1987) in the limit of hydrostatic compaction of rough spheres, given in equation (5.16).

In the limit of uniaxial compaction the limits of $I_9(E_r \to -0.5)$ is inserted into equation (7.20) together with $E_{11} = 0$ to yield

$$\begin{aligned}\sigma_{11} &= \frac{-ZCE_{33}^{3/2}}{24} \to \\ \sigma_{11} &= \frac{-CE_{33}^{3/2}(1-\phi)n}{24\pi^2 B(2B+C)}\end{aligned} \tag{7.34}$$

Which corresponds to the limit given in Walton (1987), as shown in equation (5.21).

Further, the limits of $I_4(E_r \to -0.5)$ and $I_{10}(E_r \to -0.5)$ are inserted into equation (7.21) to yield

$$\begin{aligned}\sigma_{33} &= -\frac{ZE_{33}^{3/2}(3B+C)}{6} \to \\ \sigma_{33} &= -\frac{E_{33}^{3/2}(3B+C)(1-\phi)N}{6\pi^2 B(2B+C)} \to\end{aligned} \tag{7.35}$$

This corresponds to equations (5.22), and so the limits are consistent.

7.5 Stress and Stiffness - Smooth Contacts

The methodology is repeated for the smooth contacts to give

$$\sigma_{11}^s = -\frac{(1-\phi)nI_9}{\pi^2 B} \tag{7.36}$$

$$\sigma_{33}^s = -\frac{(1-\phi)nI_{10}}{\pi^2 B} \tag{7.37}$$

Thus

$$\frac{\sigma_{33}^s}{\sigma_{11}^s} = \frac{I_{10}}{I_9} \tag{7.38}$$

The stiffness parameters are given as

$$C_{11}^s = Y \cdot 2I_1 \tag{7.39}$$

$$C_{33}^s = Y \cdot 2I_2 \tag{7.40}$$

$$C_{13}^s = Y \cdot 2I_6 \tag{7.41}$$

$$C_{44}^s = Y \cdot 2I_7 \tag{7.42}$$

$$C_{66}^s = Y \cdot 2I_8 \tag{7.43}$$

Where

$$Y = \frac{3(1-\phi)N}{4\pi^2 B} \tag{7.44}$$

The P-wave anisotropy is then given as

$$\epsilon = \frac{I_1 - I_2}{2I_2} \tag{7.45}$$

The equation to be solved by Newton's method is in the smooth case given as

$$
\begin{aligned}
&g(E_r) = 2\big[96\,(-E_r)^{5/2} - 128\,(-E_r)^{3/2} - 24\,\sqrt{-E_r} + \\
&V(48\,\sqrt{2}{E_r}^3 + 72\,\sqrt{2}{E_r}^2 + 36\,\sqrt{2}E_r + 6\,\sqrt{2})\big]/ \\
&\big[480\,(-E_r)^{5/2} - 352\,(-E_r)^{3/2} + 24\,\sqrt{-E_r} + \\
&V(240\,\sqrt{2}{E_r}^3 + 216\,\sqrt{2}{E_r}^2 + 36\,\sqrt{2}E_r - 6\,\sqrt{2})\big] \\
&-\frac{\sigma_{33}}{\sigma_{11}} = 0
\end{aligned}
\tag{7.46}
$$

with corresponding derivative

$$
\begin{aligned}
&\frac{dg(E_r)}{dE_r} = 144\big[-48\,V^2(-E_r)^{9/2} + 96\,V{E_r}^4\sqrt{2} + \\
&96\,V^2(-E_r)^{7/2} + 16\,V{E_r}^3\sqrt{2} - 72\,V^2(-E_r)^{5/2} - \\
&96\,(-E_r)^{7/2} + 8\,V{E_r}^2\sqrt{2} + 24\,V^2(-E_r)^{3/2} - 160\,(-E_r)^{5/2} + \\
&12\,VE_r\,\sqrt{2} - 3\,V^2\sqrt{-E_r} + 72\,(-E_r)^{3/2}\big]/ \\
&\big[\sqrt{-E_r}(120\,V{E_r}^3\sqrt{2} + 240\,(-E_r)^{5/2} + 108\,V{E_r}^2\sqrt{2} + \\
&18\,VE_r\,\sqrt{2} - 176\,(-E_r)^{3/2} - 3\,V\sqrt{2} + 12\,\sqrt{-E_r})^2\big]
\end{aligned}
\tag{7.47}
$$

The equation for E_{33} is given as

$$
\begin{aligned}
&E_{33} = \Bigg(\big[-768\sigma_{33}^{3/2}\big]/ \\
&\big[Q(96\,(-E_r^{5/2} - 128(-E_r)^{3/2} - 24\,\sqrt{-E_r} + \\
&E(48\,\sqrt{2}{E_r}^3 + 72\,\sqrt{2}{E_r}^2 + 36\,\sqrt{2}E_r + 6\,\sqrt{2})\big]\Bigg)^{2/3}
\end{aligned}
\tag{7.48}
$$

7.5.1 The Limits of Uniaxial and Isotropic Compaction

Inserting the limit of $I_9(E_r \to 0)$ given in equation (7.18b) into equation (7.36) and $I_{10}(E_r \to 0)$, given in equation (7.19b) into equation (7.37) yields

$$
\sigma_{11}^s(E_r \to 0) = \sigma_{33}^s(E_r \to 0) = -\frac{(1-\phi)nE_{33}^{3/2}}{3\pi^2 B} \tag{7.49}
$$

which is consistent with that of Walton (1987), as illustrated by equations (5.16) and (5.17). Note that the sign convention reversal of the strain is evident by the fact that the equation (5.16) has a minus in front of the term that is raised to the power 1.5.

In the case of uniaxial compaction the limit of $I_9(E_r \to -0.5)$ given in equation (7.18a) is inserted into equation (7.36) to yield

$$
\sigma_{11}^s(E_r \to -0.5) = -\frac{(1-\phi)nE_{33}^{3/2}}{24\pi^2 B} \tag{7.50}
$$

which is consistent with the value given in Walton (1987) presented in equation (5.23). Finally, $I_{10}(E_r \to -0.5)$ which is given in equation (7.19a) is inserted into equation (7.37) to yield:

$$
\sigma_{33}^s(E_r \to -0.5) = -\frac{(1-\phi)nE_{33}^{3/2}}{6\pi^2 B} \tag{7.51}
$$

This coincides with equation (5.24). Thus the equations for stress all reduce to those of Walton (1987) in the limits of hydrostatic and uniaxial compaction.

Chapter 8

Implementation of the Equations for Triaxial Strain

This chapter presents the implementation of the equations derived in the previous chapter for a triaxial strain state where the horizontal strains are equal. In the continuation of this work, this will be taken as analogous for having an axial stress and a radial stress. In case of the experimental data, this radial stress is a confining stress around the core.

8.1 Stress Anisotropy as a Function of Strain Anisotropy

The rough uniaxial compaction limit presented in Walton (1987) predicts very low radial stress for a given axial stress.
This can be seen by dividing the equations for stress for rough contacts[1] given in equations (5.21) and (5.22)

$$\frac{\sigma_z^{rw}}{\sigma_r^{rw}} = \frac{4(3B+C)}{C} \tag{8.1}$$

Using the expressions for B, C and λ given in equations (5.10), (5.11) (5.32) together with grain values such as $G = 41GPa, \nu_s = 0.076$ it can be calculated that the stress anisotropy in this case is 149.9 i.e., $\sigma_z \approx 150\sigma_r$. This is not likely to be a stress state found in nature. The end limit of the stress fraction is sensitive to the Poisson's ratio. A value of 0.08 yields $\sigma_z = 142\sigma_r$ and $\nu_s = 0.2$ yields $\sigma_z = 52\sigma_r$.

Concluding that most stress states in nature should approach a hydrostatic strain for rough contacts, such that the approximation in Bandyopadhyay (2009) becomes valid based on this is too simplistic. Figure 8.1 shows a plot of $\frac{\sigma_z}{\sigma_r}$ against the strain anisotropy parameter, E_r with $G_s = 41GPa$ and $\nu_s = 0.076$. It can be seen that the large value at uniaxial strain is an edge effect. Figure 8.2 shows only down to values of $E_r = -0.4$. The strong dependence on the limit of the Poisson's ratio has not yet manifested itself as strongly at this level of strain anisotropy. Whereas a change of Poisson's ratio from $0.2 \rightarrow 0.076$ causes the stress fraction to be multiplied by nearly 3 in the limit of uniaxial compaction, at $E_r = -0.5$ the shift would only be from $6 \rightarrow 6.5$.

The stress relationship is plotted for smooth contacts in figure 8.3. The figure shows how the value approaches a value of 4 at

[1] superscript 'rw' refers to rough from Walton (Walton, 1987).

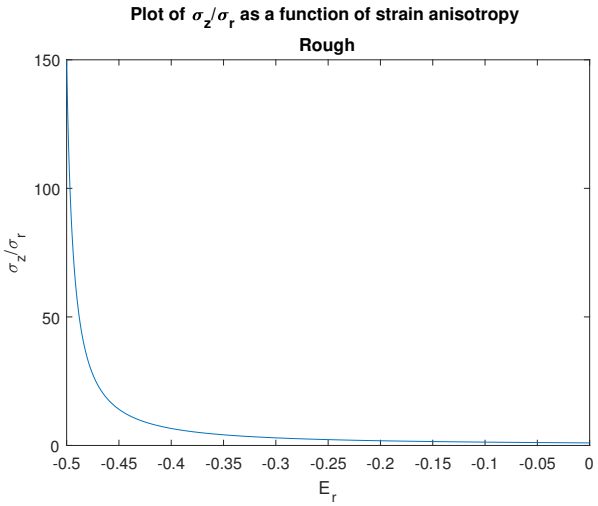

Figure 8.1: $\frac{\sigma_z}{\sigma_r}$ plotted against strain anisotropy. This figure illustrates how the very large stress anisotropy at uniaxial strain ($E_r = -0.5$) is an edge effect. Rough (no-slip) contacts.

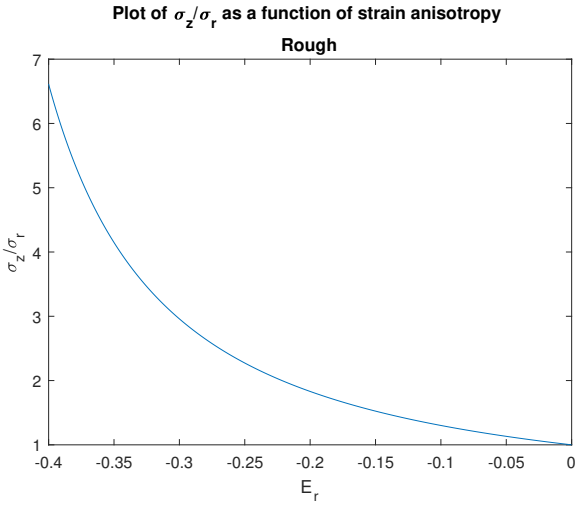

Figure 8.2: $\frac{\sigma_z}{\sigma_r}$ plotted against strain anisotropy, with a limited range on the strain anisotropy, to give a better illustration of the trends at stress levels more likely to exist in the subsurface. Rough (no-slip) contacts.

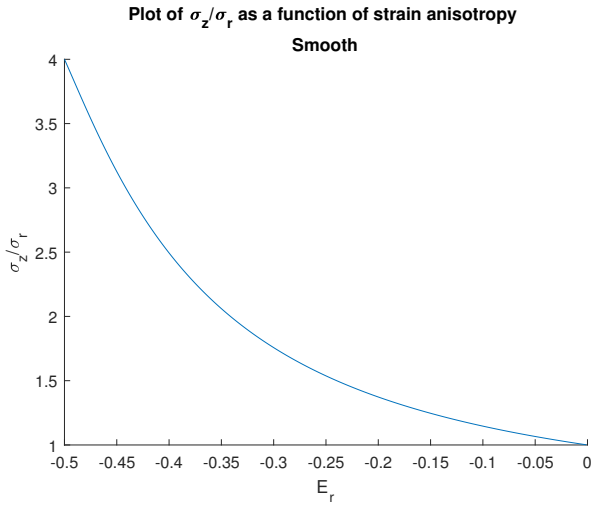

Figure 8.3: $\frac{\sigma_z}{\sigma_r}$ plotted against strain anisotropy for smooth (slip) contacts. Note how the curve approaches the value of 4, as predicted from Walton (1987) in the limit $E_r \to -0.5$

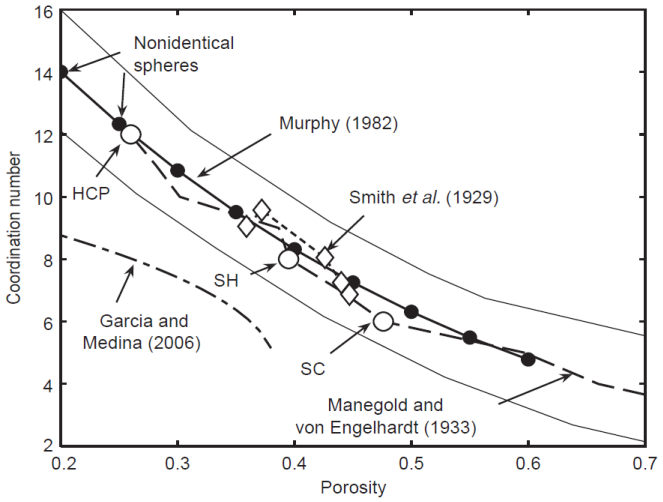

Figure 8.4: From Mavko et al. (2009) summarising the relationships between coordination number and porosity found in Smith et al. (1929), Manegold and von Engelhardt (1933), Murphy (1982) and García and Medina (2006) for random sphere packs. One standard deviation from Smith et al. (1929) is represented by the thin lines (Mavko et al., 2009). Mavko et al. (2009) also provide a discussion on this relationship

uniaxial compaction, consistent with Walton (1987).

8.2 Application on Experimental Data

Turning to the experimental data, the model can now be implemented to attempt to model the observed velocities.

The model, as in Walton, also requires the grain materials elastic parameters. These are subject to further discussion, but are initially set to $\nu_s = 0.08, G_s = 41GPa$ where ν_s is Poisson's ratio, and G_s is the shear modulus.

Furthermore the coordination number is needed. This is a slightly elusive parameter that describes on average, how many grains a grain is in contact with. Some authors relate the coordination number to the porosity, which then makes the coordination number stress dependent. This makes sense as one would expect more grains to come into contact with each other as the stress is increased. However, one of the assumptions in Walton (1987) is that no new contacts are made, and no contacts are lost. This means that the coordination number in Walton (1987) should remain constant. Different values of the relation between coordination number and porosity are present in literature. Mavko et al. (2009) summarises some of these, and this is is seen in figure 8.4. The effect of changing the coordination number is primarily to shift the curves up and down, and so it is in some scenarios used as a fitting parameter, initially a value of 9 will be used. The point of figure 8.4 is mainly to show that it is a parameter subject to debate. It is assumed that the effect of a stress dependence of the coordination number can be picked up by the stress dependent no-slip/slip fractions[2].

[2]This would however be limited by the case where the change in coordination number changes the velocity to such an extent that the observed velocities falls outside the predefined no-slip limit.

The implementation is conducted at a critical porosity of 36%, and other porosities are interpolated using the Hashin-Shtrikman lower bound, a methodology described in Dvorkin and Nur (1996). The reasoning for this is because the derivations in Walton (1987) are done under the assumption of random dense packing of grains, which, for equal spheres constitutes a porosity of 36% (Mavko et al., 2009).

The porosity is estimated based on the volumetric strain, by a formula given in Fjær (2006), which assumes grain incompressibility:

$$\phi = \frac{\phi_0 - \epsilon_{vol}}{1 - \epsilon_{vol}} \tag{8.2}$$

The starting porosity is calculated based on an assumption that the density of quartz is $2650\frac{kg}{m^3}$, together with the known weight and dimensions of the core. This yielded a starting porosity of 32.8%.

The porosity and subsequent density do of course affect the modelled velocities. The fact that they are not measured, but merely estimated is not ideal. It is argued that this does not completely inhibit the ability of the model to model the observed data. This is because an error in the porosity and density could be compensated in other parameters. Although two wrongs don't make a right physically, the fractions of no-slip/slip contacts can numerically compensate for the deviations. If the porosity and density are known to a larger degree of certainty, this would allow for better constraining of the remaining parameters in the model.

Figure 8.5 to 8.7 show the slip and no-slip limits predicted by the derivations above, for the axial P-wave, radial P-wave and axial S-wave velocities respectively. Starting with the axial P-wave velocity, it can be seen how the measured values falls

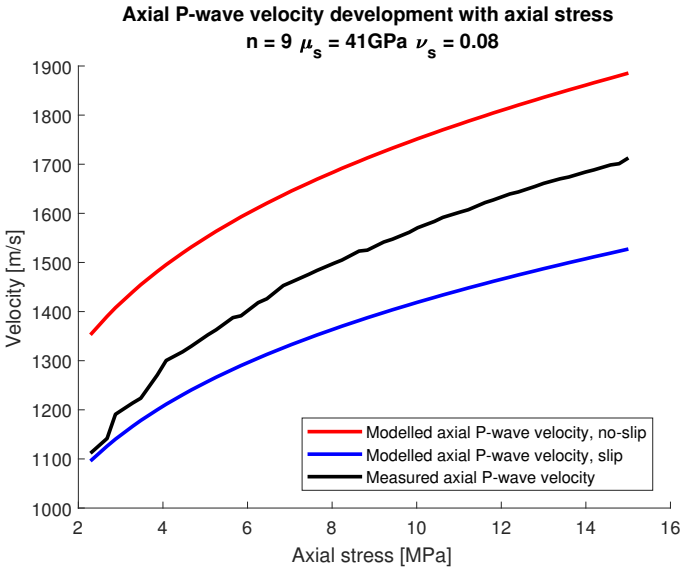

Figure 8.5: Axial P-wave velocity development as a function of axial stress, in the limits of slip (smooth) and no-slip (rough). Note how the measured data seems to move between the two extremes

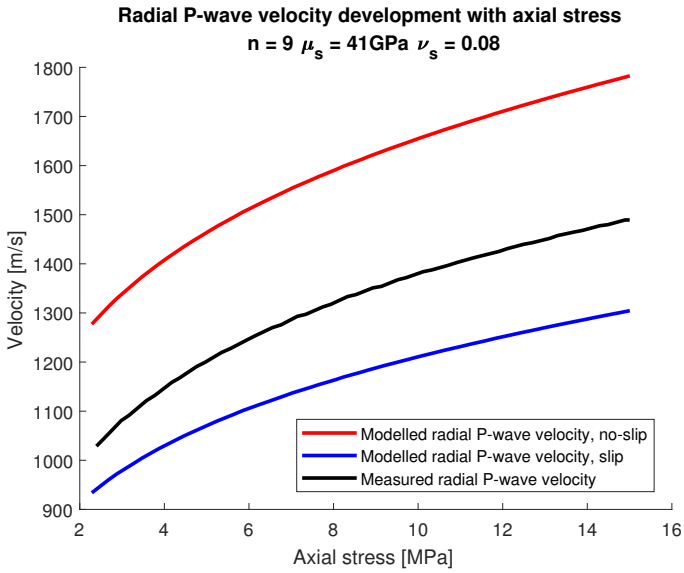

Figure 8.6: Radial P-wave velocity development as a function of axial stress, in the limits of slip (smooth) and no-slip (rough). A potential rough/smooth fraction appears lower than for the axial velocity at high stress levels. Note how the measured data seems to move between the two extremes, but the magnitude of the shifts seems less than for the axial velocity, perhaps indicating the effects of the loading affects the axial P-wave to a larger extent than predicted by purely the strain considerations in Walton (1987). Furthermore, the position between the two limits seems to stabilise towards the maximum stress

between the two "extremes". The position however shifts from being closest to the slip limit, before shifting towards the no-slip limit as loading progresses. A rough/smooth relationship would therefore have to be stress dependent to be able to capture this over the entire loading interval. This is in accordance with the observation in Duffaut et al. (2010), with the "correct" friction parameter varying over the loading interval.

For the radial P-wave velocity, the story is similar, with a move towards a larger proportion of rough contacts. The position between the rough and smooth limits however does not shift as much as for the axial P-wave velocity.

Finally, the axial S-wave velocity can be seen to require a lower rough/smooth relationship than for the P-wave velocities. It also shifts only slightly between the rough and smooth limit. The reason why the measured data starts so late is due to data availability.

In the limit of uniaxial compaction the P-wave anisotropy was in Walton (1987) seen to be independent of the amount of loading. Furthermore, in the discussion around the results in Duffaut (2011) in chapter 5 it was shown that an increase in a uniform no-slip fraction will yield a positive change in the P-wave anisotropy in the uniaxial compaction limit. This means that in the case of $V_{pz} > V_{pr}$ the sample would be brought towards isotropy.

The explicit expressions for P-wave anisotropy were given in equations (7.29) and (7.45) for the rough and smooth cases respectively. These equations, if the expression for the $I's$ are inserted are naturally not as simple as those in Duffaut (2011), and so visual inspection of the equations is less fruitful in terms of "what if" scenarios. It is however noted that they would be dependent on E_r. By mixing of rough and smooth contacts,

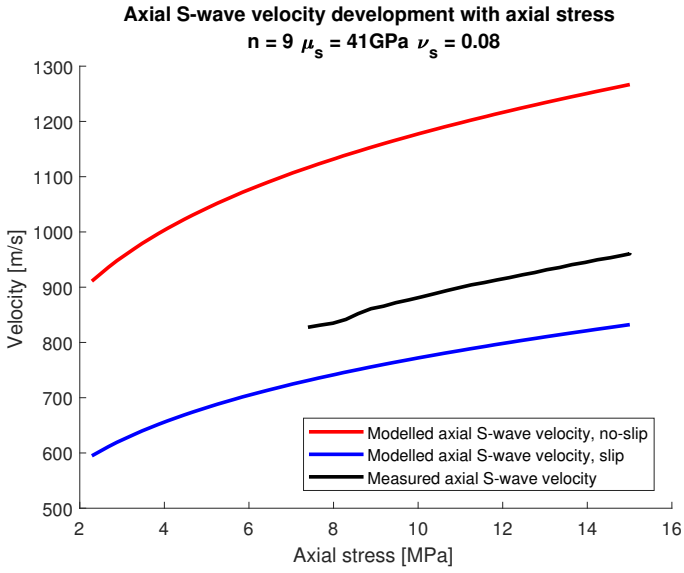

Figure 8.7: Axial S-wave velocity development as a function of axial stress, in the limits of slip (smooth) and no-slip (rough). Note how movement between the two extremes is small. It is important to remember that for the axial S-wave data is limited, and so the data starts at the stress level around which the radial P-wave velocity starts to equilibrate. A potential rough/smooth relationship would have to be lower to explain the observed data, when compared to the P-wave velocities.

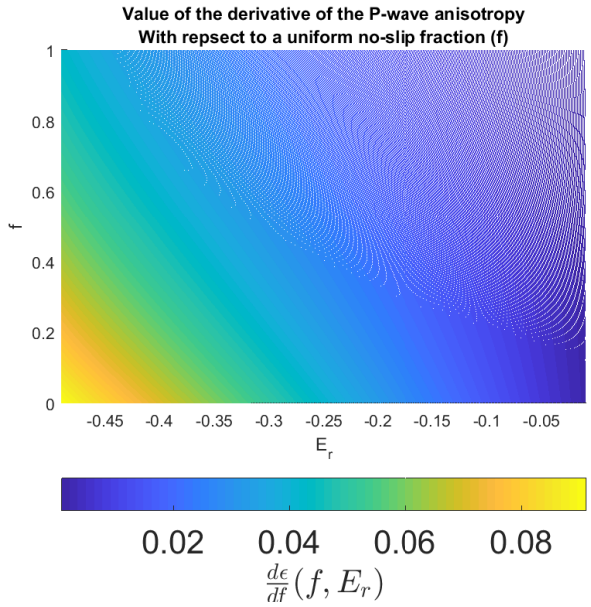

Figure 8.8: Contour plot of the derivative of the P-wave anisotropy with respect to a uniform no-slip/slip fraction, depicted over the range of strain anisotropy from hydrostatic to uniaxial. For all strain anisotropies, the effect of an increased fraction of a uniform no-slip compared to slip contacts would lead to a positive change in the P-wave anisotropy. This is the opposite trend to what is seen in figure 8.9, if an isotropic increase in the rough/smooth relationship is imposed on the model.

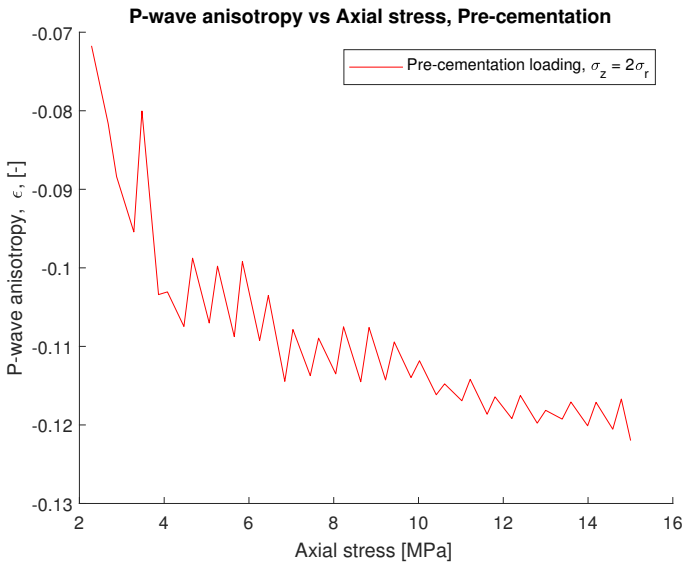

Figure 8.9: P-wave anisotropy prior to cementation. Note that the anisotropy trend is negative. The "zigzag" pattern is due to the uneven time indexing in the measurements of axial and radial P-wave velocity. In a scenario where the no-slip/slip relationship is uniform and constant, the anisotropy should be constant (apart from small changes possible due to the Hashin-Shtrikman interpolation). In a scenario where it is uniform and increasing, the P-wave anisotropy would become more positive (see figure 8.8). Uniform refers to the mixing proportion being equal for the elastic stiffnesses C_{11} and C_{33}.

the P-wave anisotropy would be dependent on the rough fraction and the strain anisotropy. The derivative of the P-wave anisotropy with respect to a uniform no-slip fraction as function of the no-slip fraction and E_r is contoured in figure 8.8 for a set of parameters

- $G_s = 41GPa$
- $\nu_s = 0.076$
- $\phi = 0.36$
- $n = 9$

From figure 8.8 it is clear that in a mixture of rough and smooth contacts with the same no-slip fraction on C_{11} and C_{33}, an increase in the no-slip proportion would cause a positive change in the P-wave anisotropy.

Figure 8.9 shows the P-wave anisotropy of the loading interval. It can be seen that it becomes *more negative* as loading progresses. This is in contrast with a scenario of constant rough/smooth relationship, in which it would be expected to remain constant (with minute variations possible due to the Hashin-Shtrikman interpolation, this is discussed in part VI). It was discussed in relation to the individual velocities that to fit the velocities, a no-slip/slip fraction would have to *increase*. A uniform increase would however cause a *positive* change in the anisotropy, as discussed in relation to figure 8.8.

Based on these observations, to fit the data, an anisotropic and stress dependent set of no-slip/slip parameters could be used, as discussed in the introduction chapter of this part.

8.3 Mixing Rough and Smooth Contacts

To model the observed data, mixing of the stiffnesses predicted for slip (smooth) and no-slip (rough) is utilised, with different no-slip fractions for the different stiffnesses. This is implemented to try to model the data in an as simple way as possible, whilst remembering the multitude of plausible causes the anisotropic and stress dependent no-slip fraction is trying to explain.

Furthermore, the exact value of grain parameters is subject to some debate. The main effect of G_s and n is to shift the curves for the slip and no slip up and down. Instead of choosing values for the grain parameters, they are assumed to be normally distributed around some mean. The mean and standard distribution of the parameters is chosen somewhat arbitrarily, and are as follows.

- n: mean = 9, Standard deviation = 1.5
- G_s: Mean = 42Gpa, standard deviation = 3 GPa
- ν_s: Mean = 0.08, standard deviation = 0.02

Undoubtedly some readers will strongly feel that "Oh no, it should be this or that", but that depends on which door on which one knocks, or which reference is cited.

The coordination number are reported by some as stress dependent, i.e., Duffaut et al. (2010). A case could probably be made for it being anisotropic as well. It is assumed that the effects of the increase in coordination number with decreasing porosity can be modelled as a factor in the rough/smooth relationship, as the main effect is upward and downward shifting of the curves.

The rough/smooth relationships are defined through a lower and an upper value, reported as [min max]. These values represent mean values of a normal distribution with standard deviation 0.05. Based on the observed measurements, the values were chosen as follows

- C_{11}: [0.25 0.35]
- C_{33}: [0.2 0.5]
- C_{44}: [0.18 0.23]

These values bear a dependence on the choice of mean for the grain parameters. Note that the implementation here assumes that the relationship of the no-slip/slip parameters varies lineraly over the loading interval. This might not be true, and it might be that for example the rise would be most accelerated during the first few MPa's of loading.

The point of the distributions is that by running an iterative script that picks random values each time, and checks the resulting curve fit against the measured data, the process of finding "good" values can be somewhat automated. The "measure of fit" so to speak, is in this case simply done by defining an upper value of the sum of the absolute value of the errors at each point, which must be smaller than the cut-off for all the velocities, simultaneously.

An "accepted" solution is one in which the sum of errors is smaller than an average of 10 m/s for a set of measurement points, for all the velocities

$$\frac{\sum_{i=1}^{M}|v_m(i) - v_e(i)|}{M} < 10m/s \tag{8.3}$$

M is the number of measurements of a given velocity, v_m is the modelled velocity and v_e is the measured experimental velocity. The shape of the graphs are always similar due to the nature of the underlying granular media model, so no additional constraints are put on the variance. These acceptance criteria are based solely on the observation that as long as that criteria is fulfilled, the curves reproduce the experimental data well.

The correlation coefficient, ρ is the Pearson correlation coefficient. Different sources subdivide the intervals differently, but the subdivision implemented here is:

- $\rho = \pm 1$: Perfect positive/negative
- $\rho = \pm(0.75 - 1)$: Strong positive/negative
- $\rho = \pm(0.5 - 0.75$: Moderate positive/negative
- $\rho = \pm(0.25 - 0.5)$: Weak positive/negative

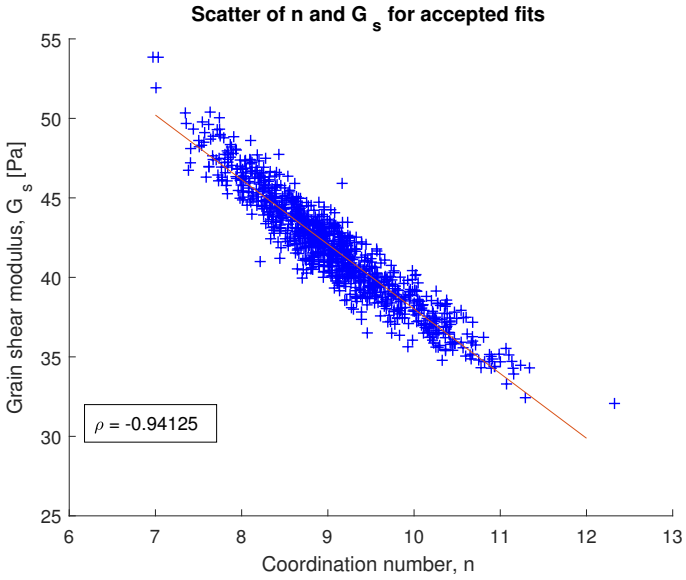

Figure 8.10: Cross plot of coordination number, n, and grain shear modulus G_s for 1000 accepted solutions to the velocities. There is a strong negative correlation between these two variables. The equations for triaxial strain are somewhat complicated, but using Hertz-Mindlin and equation (5.7) as an analogy it is not unreasonable that these are negatively correlated.

- $\rho = \pm(0 - 0.25$: Very weak/no correlation

Figure 8.10 shows a scatter plot of the coordination number and shear modulus for 1000 accepted fits. As expected, the two parameters show a strong negative correlation, where increasing one leads to a decrease in the other. The triaxial strain equations are somewhat complicated and this is perhaps not obvious. The equivalence of Walton (1987) and Hertz-Mindlin has been shown in the hydrostatic limit, and so the equation in (5.7) is used as an illustration. If K is to be the same if the grain shear modulus is increased, the coordination number must be decreased.

Figures 8.11 and 8.12 show the scatter of the Poisson's ratio vs the coordination number and shear modulus respectively. These show only very weak correlations. This is not unexpected, as it is the product between n and G that appear in the equations. Plotting then the Poisson's ratio versus the product of the coordination number and grain shear modulus reveals a moderate, approaching strong negative correlation, as seen in figure 8.13. Turning again to the equation in (5.7), increasing the Poisson's ratio decreases the value of the denominator, causing a decrease in the numerator.

The [min max] relationships of the stiffness, gives an idea of the effects not captured by the granular media model. It can be seen from figure 8.14 that for the no-slip/slip relationship describing C_{33} there is a strong correlation between the start and end values of the no-slip/slip relationship. In other words, the fraction at the highest stress seems to be correlated with the value at the start of compaction.

For C_{11} however, there is only a very weak correlation between the starting and ending slip/no-slip fraction, as displayed

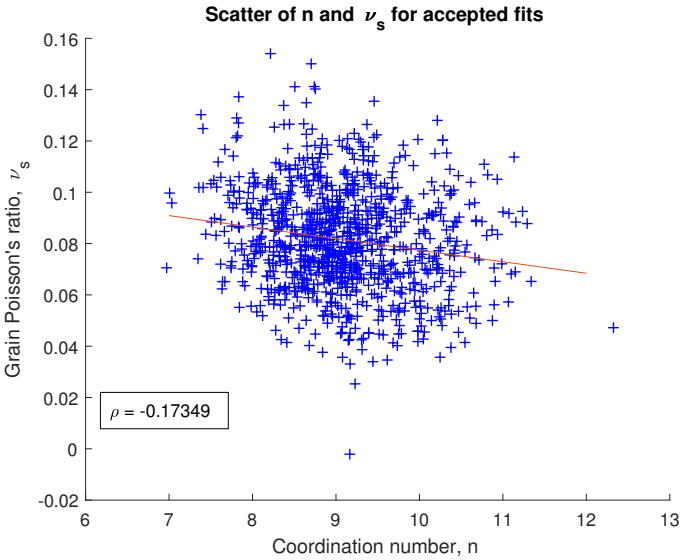

Figure 8.11: Cross plot of coordination number, n, and Poisson's ratio ν_s for 1000 accepted solutions to the velocities. There is a only a very weak correlation.

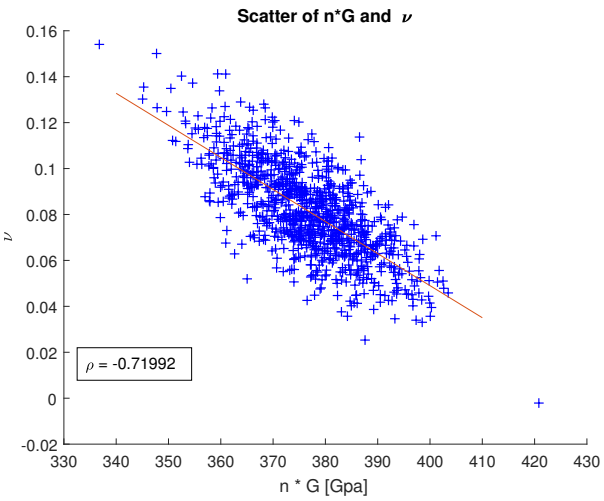

Figure 8.13: Cross plot of the product of coordination number, n, and grain shear modulus G_s with Poisson's ratio ν_s for 1000 accepted solutions to the velocities. There is a moderate-strong negative correlation between these values. The equations for triaxial strain are somewhat complicated, but using Hertz-Mindlin and equation (5.7) as an analogy it is not unreasonable that these are negatively correlated.

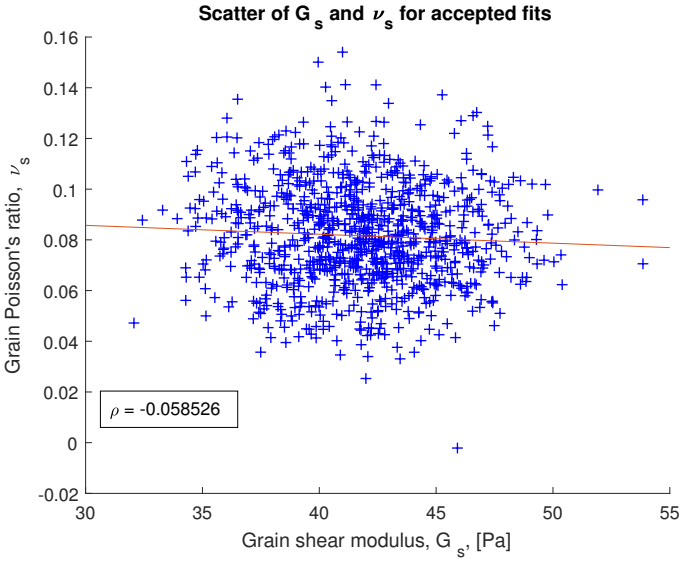

Figure 8.12: Cross plot of grain shear modulus, G_s, and Poisson's ν_s for 1000 accepted solutions to the velocities. There is a only a very weak correlation.

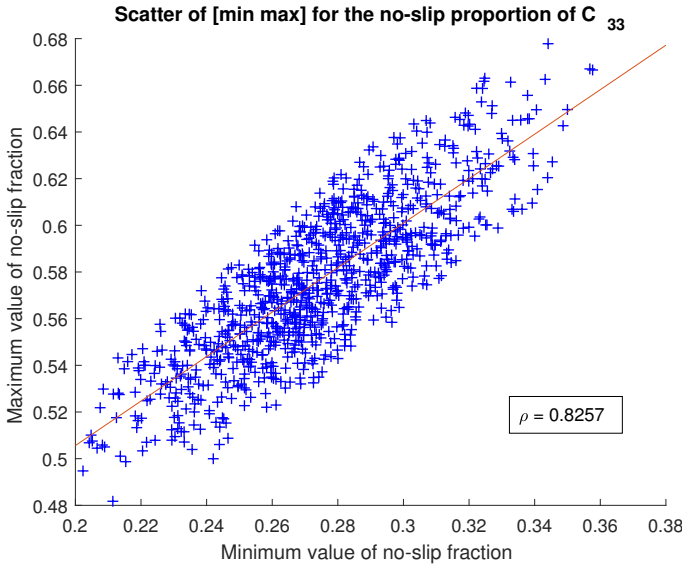

Figure 8.14: [min max] values for the no-slip fraction defining C_{33}. A strong positive correlation is seen, indicating that the max value is related to the min value.

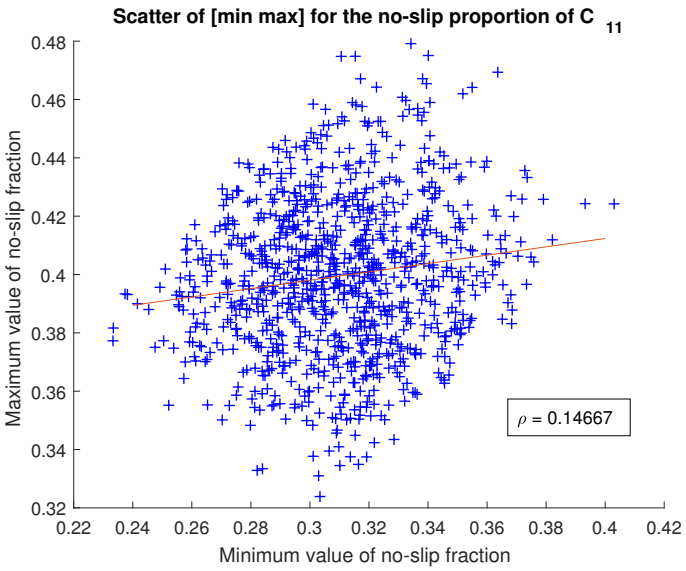

Figure 8.15: [min max] values for the no-slip fraction defining C_{11}. Only a very weak positive correlation is seen, perhaps suggesting that other factors to a larger extent control the shape of the graph than the difference between [min max].

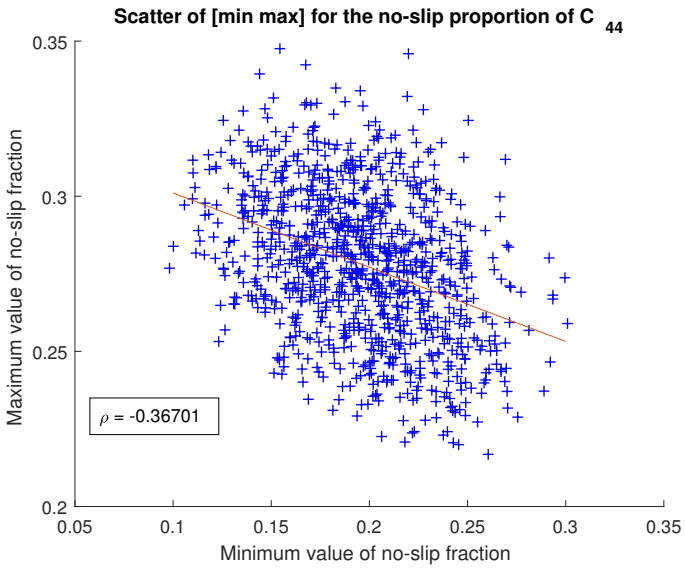

Figure 8.16: [min max] values for the no-slip fraction defining C_{44}. A weak negative correlation is seen. Some of the points actually plot with $min > max$. This would indicate that an accepted solution requires downshifting compared to the stress dependence provided by the granular media model. The fact that only data from the flattened out part of the curve is available means that the methodology might give incomplete answers. This is because most solution flatten out in this stress interval, and fitting the data in the more linear part is not necessarily a testament to a good fit in the more curved parts of the curve.

in figure 8.15. This might be a testament that other parameters are more important in determining the shape of the curve for C_{11}. This in agreement with the observations that the shift of the radial P-wave velocity towards the no-slip limit is less pronounced when compared to the axial P-wave velocity.

The relationship for the axial shear wave velocity is even more interesting. Shown in figure 8.16, this shows a weak *negative* correlation between the starting value and ending values. Some of the points actually plot such that the ending no-slip fraction is lower than the starting value. The experimental data for the shear wave velocity is limited to stress levels where the curves have flattened out, and the measured shear wave velocity data is increasing close to linearly over the entire stress interval where data is available. As most solutions flatten out towards the maximum burial, this methodology might be unsuitable for the shear wave velocity given the range of data available.

Taking the mean of all the parameters yields the curves for axial P-wave velocity, radial P-wave velocity and axial S-wave velocity seen in figure 8.17 to 8.19 respectively. These figures reveal that the model has the *ability* to model the observed data well. Whilst the observation that the model is able to fit the data is not up for debate, the fact that the model in the current formulation has several parameters available to be used as fitting parameters means that the model would be able to fit a large number of curves. This freedom permits the model to account for some natural variability in real rocks, but this freedom also means that the predictive power of the model in the case of sparse data is in question, as the parameters require calibration. Although the implementation of the anisotropic stress dependent elastic no slip proportions has been attempted to be justified, the utilisation is pragmatic. This means that the fact that the model fits the data should not be taken as direct evidence for the models validity.

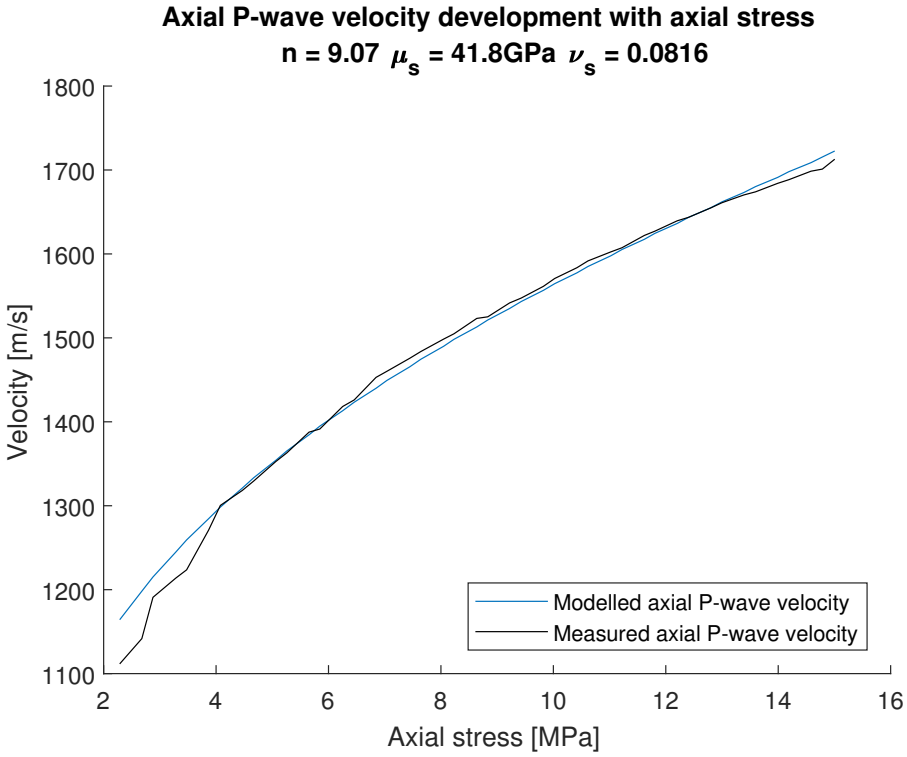

Figure 8.17: Modelled axial P-wave velocity created from the mean values of the 1000 accepted fits. This can be seen to correspond well with the measured velocity

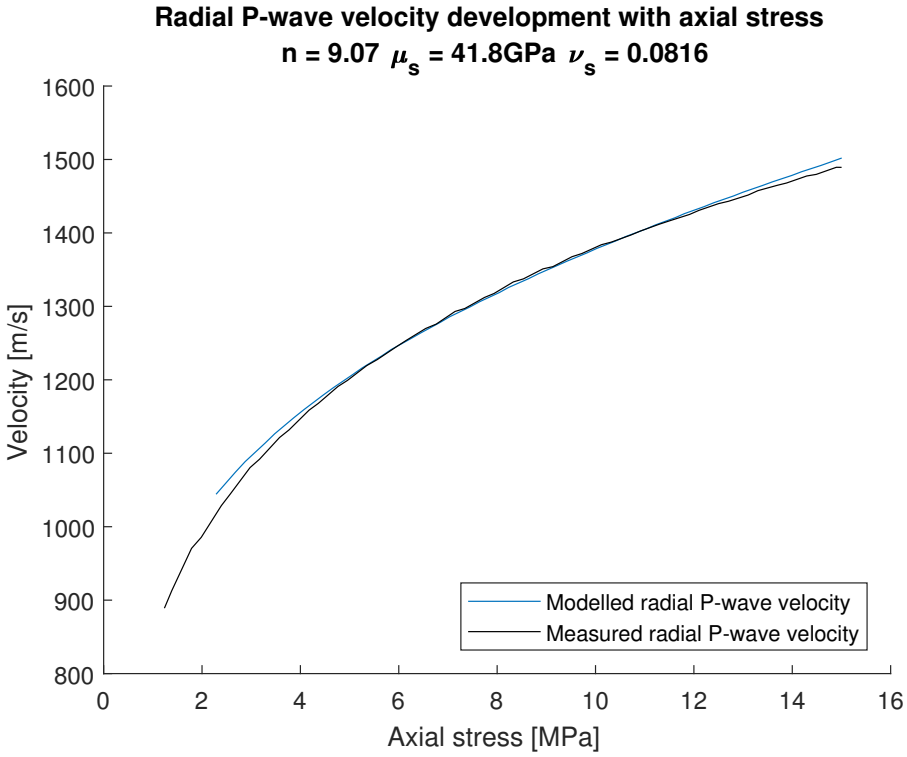

Figure 8.18: Modelled radial P-wave velocity created from the mean values of the 1000 accepted fits. This can be seen to correspond well with the measured velocity

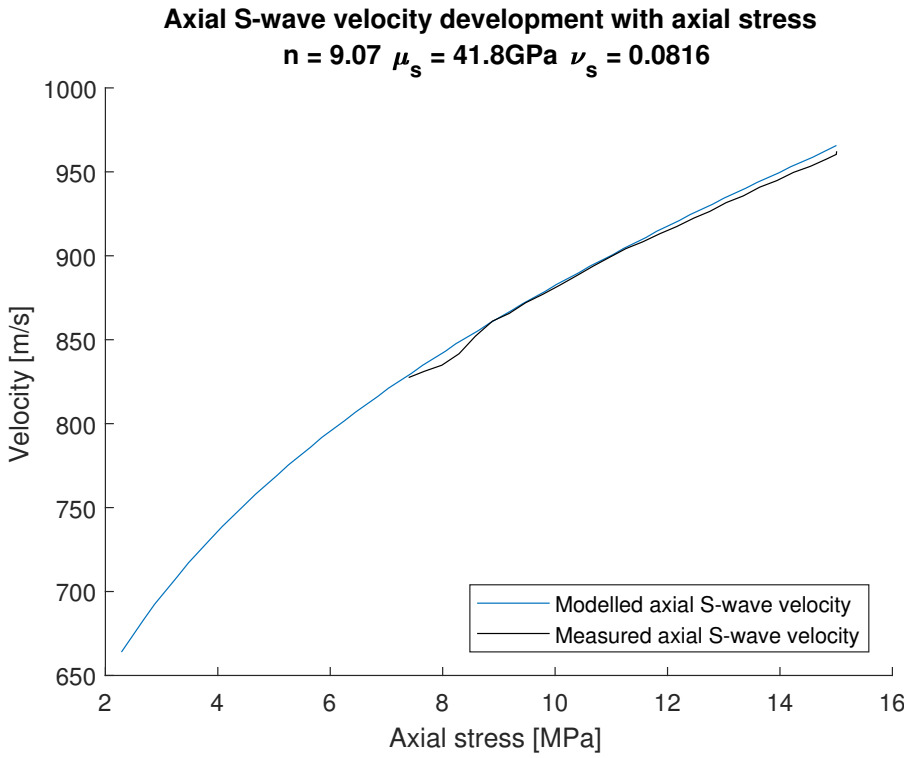

Figure 8.19: Modelled axial S-wave velocity created from the mean values of the 1000 accepted fits. This can be seen to correspond well with the measured velocity

Part IV

Cementation of Granular Media

Chapter 9

Estimation of the Amount and Effects of Quartz Cementation

9.1 Introduction to Quartz Cementation

The effect of quartz cementation on porosity and elastic wave velocities is of importance in exploration settings, both in terms of reservoir quality and interpretation. A brief discussion regarding this was presented in part I. In this part, models that predict the amount and effect of cementation are reviewed, before being implemented to the experimental data presented in part II.

Quartz cementation is a diagenetic processes, which is assumed to start between 70-80 $^{\circ}C$ (Bjørlykke and Jahren, 2010). The source of the quartz cement has however been a somewhat controversial topic in the diagenetic community. McBride (1989) provides an exhaustive list of no less than 23 reported sources of quartz cement, some of which have received more credit than others.

A discussion of all 23 is excessive, but three prominent sources are: (Bjørlykke and Egeberg, 1993)

- Silica phases that are more soluble, for example opal CT and amorphous silica from biogenic and volcanic source
- Dissolution of quartz, commonly from stylolites formed as a result of pressure solution
- Release of silica from reaction involving silicate minerals

Oelkers et al. (1996) support a stylolite model, with the quartz cement forming by dissolution at mica and illite interfaces in contact with the stylolites. This conclusion was based on petrographic data.

9.2 Walderhaug's Cement Model

This is the model that was used to model the cement volume in the introductory conceptual model in figure 1.2.

9.2.1 Background

Walderhaug's cement model, (Walderhaug, 1996), sources the quartz from stylolites within the sandstone being cemented, or from somewhat thicker zones of clay- or mica-catalysed quartz dissolution. In practice there may be several factors affecting porosity acting alongside cementation, such as mechanical compaction and volume loss due to pressure solution. The model however considers the precipitation of cement to be the only porosity reducing factor.

This is accomplished by modelling volumes of sandstone that do not include stylolites (but rather places the volumes in between stylolites). Mechanical compaction is assumed to be stopped by the formation of cement as it stabilises the rock's framework (Walderhaug, 1996). Furthermore, the cementation is modelled as a continuous phenomenon, as opposed to being a series of sporadic events separated by periods of non-cementation.

The lack of obvious gradients in the amount of cement away from stylolites on the Norwegian shelf supports an assumption that quartz precipitation is the rate-controlling i.e., slowest process in quartz cementation (Walderhaug, 1996). If the diffusion was rate controlling, only a small amount of silica would be common significant distances from the stylolites. This would likely lead to a gradient of cement outward from the stylolites. Work done in Oelkers et al. (1996) indicate that at higher temperatures and larger stylolite spacing a heterogeneous distribution of quartz cement away from stylolites is observed (figure 5 in Oelkers et al. (1996)). Oelkers et al. (1996) includes the observation that silica cementation is a function of distance from stylolites at higher temperatures, with sparse stylolite frequency as an observation that should be considered. Models do exist to incorporate the observation regarding stylolite spacing in the, see in addition to Oelkers et al. (1996) for example Bjørkum et al. (1998). These models are however not as simple to that presented in Walderhaug (1996), which is thus favoured, and valid at lower temperatures with high stylolite frequency.

Temperature is identified as a more important factor than pressure in Walderhaug (1996)[1]. This is because at diagenetic conditions, quartz precipitation rates depend exponentially upon temperature, but not pressure. Bjørkum (1996) suggests that effective stress at large burial depths have only minor effect on quartz dissolution at stylolites and grain contacts. This entices the exclusion of pore pressure and effective stress at grain contacts as a factor in the model present in Walderhaug (1996). Following the words of Walderhaug (1996) "Because precipitation rate is rate controlling, it is logically possible to regard the model as a precipitation model that does not really take issue with the source of quartz cement, but is simply based on the observation that there seems to exist a logarithmic relationship between quartz precipitation rate and temperature; However it is very difficult to find viable sources of quartz cement other than dissolution at stylolites and grain contacts containing clay or mica".

9.2.2 Modelling the Cement Volume

The volume of cement, V_{cem}, that is precipitated in a 1 cm^3 volume of sandstone possessing a quartz surface area A during time t can be given as (Walderhaug, 1996):

$$V_{cem} = \frac{MrAt}{\rho} \tag{9.1}$$

where M is the molar mass of quartz ($= 60.09 \frac{g}{mole}$), r is the rate of quartz precipitation in $\frac{moles}{cm^2 s}$ and ρ is the density of quartz.
The rate is expressible as (Walderhaug (1994), Walderhaug (1996)):

$$r = a10^{bT} \tag{9.2}$$

Where T is the temperature in $^\circ C$ and a and b are constants, estimated in Walderhaug (1994) to be $1.98 \cdot 10^{-22} \frac{moles}{cm^2 s}$ and $0.022 \frac{1}{^\circ C}$. Further, it is noted in Walderhaug et al. (2000) that in theory, the value of the a and b parameters should be essentially constant for all quartoze sandstones. This will however only be the case if the temperature histories are accurate. One method to overcome this, suggested in Walderhaug et al. (2000) is to allow the b parameter to vary between wells (but remain constant *within* a given well).
In a scenario where the temperature increases linearly with time, it can be understood that the temperature can be replaced with a linear function such that the rate for an area with such a linear trend can be written

$$r = a10^{ct+d} \tag{9.3}$$

c is now the gradient of the temperature/time graph, and d is the intercept, or, "initial temperature".

Introducing differentials in equation (9.1) to allow for varying temperature with time

$$dV_{cem} = \frac{MrA}{\rho} dt \tag{9.4}$$

the total volume of cement can be written as a sum of integrals over several time steps from a starting time, t_0 to an end time t_m (Walderhaug, 1996)

$$V_{cem} = \frac{MA_0 a}{\rho} \int_{t_0}^{t_1} 10^{b(c_1 t + d_1)} + \frac{MA_1 a}{\rho} \int_{t_1}^{t_2} 10^{b(c_2 t + d_2)} + ... + \frac{MA_{m-1} a}{\rho} \int_{t_{m-1}}^{t_m} 10^{b(c_m t + d_m)} \tag{9.5}$$

or alternatively

$$V_{cem} = \frac{Ma}{\rho} \sum_{n=1}^{n=m} A_{n-1} \int_{t_{n-1}}^{t_n} 10^{b(c_n t + d_n)} dt \tag{9.6}$$

Looking at the integral

$$\int_{t_{n-1}}^{t_n} 10^{b(c_n t + d_n)} dt \tag{9.7}$$

Since $e^{ln(x)} = x$ the 10 in the integral can be rewritten

$$\int_{t_{n-1}}^{t_n} (e^{ln(10)})^{b(c_n t + d_n)} dt = \tag{9.8}$$

$$\int_{t_{n-1}}^{t_n} e^{ln(10) b(c_n t + d_n)} dt \tag{9.9}$$

Where the identity follows from the fact that $(e^a)^b = e^{ab}$. Letting $u = ln(10)b(c_n t + d_n)$ it obtained that

$$du = ln(10) b c_n dt \rightarrow \tag{9.10}$$

$$dt = \frac{du}{ln(10) b c_n} \tag{9.11}$$

Equation (9.9) can then be rewritten

$$\frac{1}{bc_n ln(10)} \int_{u_{n-1}}^{u_n} e^u du = \tag{9.12}$$

$$\frac{1}{bc_n ln(10)} [e^u]_{u_{n-1}}^{u_n} = \tag{9.13}$$

$$\frac{1}{bc_n ln(10)} [e^{ln(10) b(c_n t + d_n)}]_{t_{n-1}}^{t_n} = \tag{9.14}$$

$$\frac{1}{bc_n ln(10)} [10^{b(c_n t + d_n)}]_{t_{n-1}}^{t_n} \tag{9.15}$$

This result can then be inserted into equation (9.6) to reveal the result obtained in equation 5 in Walderhaug (1996)

$$V_{cem} = \frac{Ma}{\rho bc ln(10)} \sum_{n=1}^{n=m} A_{n-1} [10^{b(c_n t + d_n)}]_{t_{n-1}}^{t_n} \tag{9.16}$$

The sum of integrals can incorporate two factors: (Walderhaug, 1996)

- Slope variations in the time/temperature relationship
- As quartz cement is precipitated, the area available for cementation will change, thus inciting alterations of the amount of cement for subsequent time steps.

[1] And other works regarding quartz cementation on the Norwegian shelf. See for example Bjørkum (1996), Oelkers et al. (1996), Bjørkum et al. (1998). Some additional discussion into the stylolite model and its validity can be found in Sheldon et al. (2003) and Walderhaug et al. (2004).

Further alterations can be made to equation (9.16) by introducing expressions for the A_n parameter.
The initial area available for cementation is given as (Walderhaug, 1996)

$$A_0 = \frac{6fV}{D} \tag{9.17}$$

Which is the cumulative surface area of spheres with diameter D (grain size) and with volume fraction given by f. If there is a variable grain size, each grain size is calculated with the equation above and their contributions added.

In the model, the change in surface area caused by the precipitation of quartz is considered proportional to the porosity loss caused by quartz precipitation, i.e.,

$$A = A_0(1 - \frac{V_{cem}}{\phi_0}) \tag{9.18}$$

where ϕ_0 is the porosity at the onset of cementation.

Implementing the result for A and having a constant rate of change of temperature, Walderhaug (1996) claims that equation (9.16) can be solved analytically to give

$$V_{cem_2} = \phi_0 - (\phi_0 - V_{cem_1})exp\Big(\frac{-MaA_0}{\rho\phi_0 bcln(10)}(10^{bT_2} - 10^{bT_1})\Big) \tag{9.19}$$

where T_2 and T_1 refer to time according to Walderhaug (1996), but looking at the units of b [1/°C], it is likely that this is a typo, and that the T's indeed refer to temperature, which would be consistent with previously used notation. Equation (9.19) is simple to implement in programming software such as *Matlab*.

9.3 Stiffness of Cemented Granular Media - Contact Cement Model

When cement is precipitated across grain contacts, the stiffness of the rock can be significantly increased, even with small amounts of cement (Dvorkin et al., 1994).

The model used to quantify this effect in the introductory example, was that developed over a series of papers (Dvorkin et al. (1991), Dvorkin et al. (1994), Dvorkin and Nur (1996))

9.3.1 Background

The theory developed by Dvorkin and Nur considers two schemes, one where the cement is precipitated at the grain contacts (scheme "A") and one where the cement is precipitated evenly across the grains (scheme "B"). The two schemes are illustrated in figure 9.1 together with the concept of non-contact cement. According to McBride (1989) a situation where rims of quartz cement form around grains is the most common.

This model is also referred to as the "contact-cement" model, and is applicable for high porosity sands, as the initial stage of the diagenetic trend. During more severe cementation when the cement starts to fill up the pore space the model breaks down. In this scenario, modifications, such as appending a modified upper Hashin Shtrikman bound ("increasing cement model") should be used (Avseth et al., 2010).

9.3.2 The Contact Cement Model

Figure 9.2 from Dvorkin and Nur (1996) illustrates the contact cement model by plotting porosity versus velocities, together with experimental data. It is observed how the model predicts that small amounts of cement can cause large changes in the velocities.

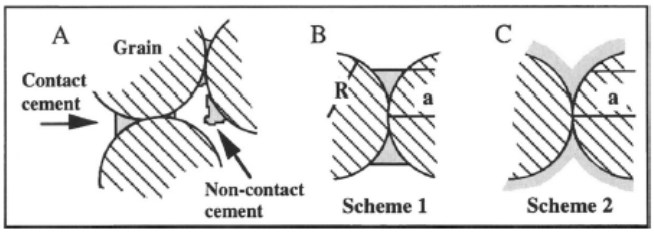

Figure 9.1: A: Contact and non-contact cement. B: Scheme 1. C: Scheme 2. From Dvorkin and Nur (1996).

The effective Bulk modulus and Shear modulus are given as (Dvorkin and Nur, 1996)

$$\begin{aligned} K_{eff} &= \frac{1}{6}n(1-\phi_0)M_cS_n \\ G_{eff} &= \frac{3}{5}K_{eff} + \frac{3}{20}n(1-\phi_0)G_cS_\tau \end{aligned} \tag{9.20}$$

M_c is the P-wave modulus of the cement, and G_c is the shear modulus of the cement, and they are given as:

$$\begin{aligned} M_c &= \rho_c V_{p_c}^2 \\ G_c &= \rho_c V_{s_c}^2 \end{aligned}$$

ρ_c is the density of the cement and $V_{p_c}\&V_{s_c}$ are the P- and S-wave velocities of the cement.

The S_n parameter is proportional to the normal stiffness of a cemented two-grain combination, and is given as

$$S_n = A_n(\Lambda_n)\alpha^2 + B_n(\Lambda_n)\alpha + C_n(\Lambda_n)$$

Where

$$\begin{aligned} A_n(\Lambda_n) &= -0.024153\Lambda_n^{-1.3646} \\ B_n(\Lambda_n) &= 0.20405\Lambda_n^{-0.89008} \\ C_n(\lambda_n) &= 0.00024649\Lambda_n^{-1.9846} \\ \Lambda_n &= \frac{2\cdot G_c}{\pi G}\frac{(2-\nu)(1-\nu_c)}{1-2\nu_c} \end{aligned}$$

The S_τ parameter is proportional to the shear stiffness of a cemented two-grain combination, and is given as

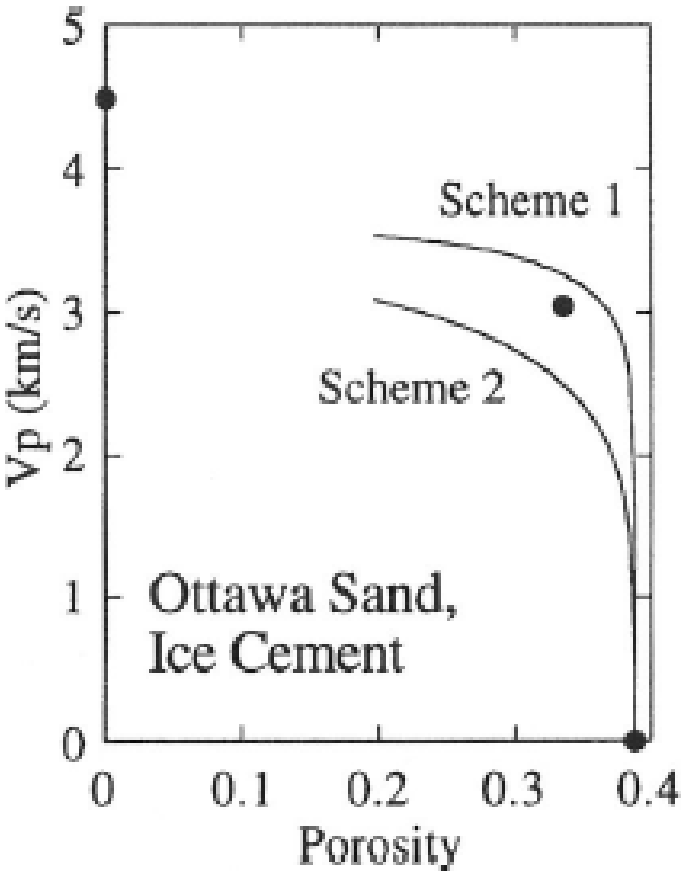

Figure 9.2: Effect of P-wave velocity from cementation from the two schemes in figure 9.1, taken from Dvorkin and Nur (1996). Note the very large increase in velocity over the first increments of cement (corresponding to the first increments of decreased porosity).

$$S_\tau = A_\tau(\Lambda_\tau, \nu)\alpha^2 + B_\tau(\Lambda_\tau, \nu)\alpha + C_\tau(\Lambda_\tau, \nu)$$

Where

$$A_\tau(\Lambda_\tau, \nu) = 10^{-2} \cdot (2.26\nu^2 + 2.07\nu + 2.3) \cdot \Lambda_\tau^{0.079\nu^2 + 0.1754\nu - 1.342}$$

$$B_\tau(\Lambda_\tau, \nu) = (0.0573\nu^2 + 0.0937\nu + 0.202) \cdot \Lambda_\tau^{0.0274\nu^2 + 0.0529\nu - 0.8765}$$

$$C_\tau(\lambda_\tau, \nu) = 10^{-4} \cdot (9.654\nu^2 + 4.945\nu + 3.1) \cdot \Lambda_\tau^{0.01867\nu^2 + 0.4011\nu - 1.8186}$$

$$\Lambda_\tau = s\frac{G_c}{\pi G}$$

G & ν represent the shear modulus and Poisson's ratio of the grain[2], whereas G_c & ν_c represent the same parameters for the cement.

The α parameter is used to express the amount of contact cement, and is the ratio of the cement layer, a, to the radius of the grain, R.

$$\alpha = \frac{a}{R}$$

Through the assumption that porosity loss is only due to cementation and by adopting the schemes presented earlier for cement deposition, the α parameter can be expressed in terms of the current porosity of the sandstone. For scheme 1, where all the cement is deposited is at the grain contacts

$$\alpha = 2\left[\frac{S\phi_0}{3n(1-\phi_0)}\right]^{0.25} \tag{9.21}$$

For scheme 2:

$$\alpha = \left[\frac{2S\phi_0}{3(1-\phi_0)}\right]^{0.5} \tag{9.22}$$

S is the cement saturation of the pore space, defined as the fraction of the pore space of the uncemented sand occupied by cement.

9.4 Modifications to Model Lower Porosities

As pointed out in Avseth et al. (2010), the contact cement model as presented in Dvorkin and Nur (1996) is a high porosity model.

For unconsolidated granular media, the friable sand model has been described previously. This is also mentioned in Dvorkin and Nur (1996) to extrapolate stiffnesses to lower porosities. Instead of letting the lower limit be defined by a granular media, the "constant cement model" takes the lower limit in the Hashin-Shtrikman lower bound from the contact cement model (Avseth et al., 2010). This is then a way to compensate for porosity effects for a given cement volume.

[2]The notation of Dvorkin and Nur (1996) was used, which deviates slightly from the notation used in the previous part to denote grain parameters.

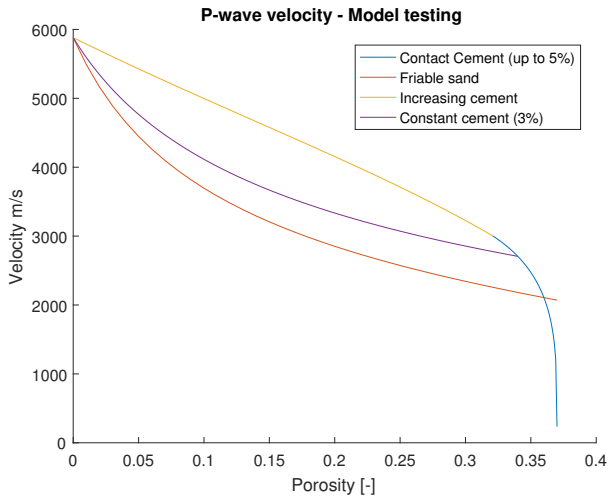

Figure 9.3: Illustration of the different models described in this section. The "critical" porosity for the contact cement model is in this case set at 5%. In this figure the different models and extrapolations are named as they are in literature. In the continuation of this work however, any model originating from Dvorkin and Nur (1996) will be referred to as "contact cement" to highlight and distinguish the origin of any estimated stiffnesses from that of "patchy cement".

When the cement volume increases to such an extent that the contact cement model is no longer valid, something called the "increasing cement model" can be used. This is described in Avseth et al. (2010) and appends a Hashin-Shtrikman upper-bound to maximum cement volume in the contact cement model.

An illustration of how the different models describe velocity as function of porosity is given in figure 9.3. The term "Contact Cement" will be used in the remainder of this work to mean any stiffness originating from the model of Dvorkin and Nur (1996). That is, even though the results from Dvorkin and Nur (1996) may have been extrapolated using a Hashin-Shtrikman lower-bound (constant), upper-bound (increasing), or both an upper and a lower-bound (increasing then constant) they will will referred to as "Contact Cement" so that the origin can be attributed to the model from Dvorkin and Nur (1996). This might seem counterintuitive, but it is the contact cement model (CCM) that is the actual cement model. The modifications are just extrapolations of the contact cement model.

9.5 Limitations of the Model from Dvorkin and Nur (1996)

9.5.1 The Boundary Between Mechanical Compaction and Cementation

From Dvorkin et al. (1994) "The process of cementation starts at the critical porosity point at which both bulk and shear moduli are zero in an unconsolidated granular media". In the Hertz-Mindlin model (see equations (5.7) and (5.8)) this would be equivalent to having no stress on grain contacts prior to cementation. This would mean that they have a velocity close to zero[3] which is of course not true for sediments entering the cementation domain at burial depths greater than 2-3km.

To illustrate this, consider now a situation where a rock is deposited at 36% porosity, and buried down to 2km of depth before the onset of cement. Utilising the compaction model in Lander and Walderhaug (1999) yields a porosity of around 0.3[(4)] at the onset of cement. Hertz-Mindlin is implemented at 36% and the friable sand model is used to extrapolate the elastic moduli down to 30% porosity yielding P- and a S-wave velocities corresponding to the scattered circles in figure 9.4. To implement the effect of cement volume the following procedure is used:

- Calculate the stiffness from the CCM at 36% starting porosity
- For each increment of cement extrapolate to the actual porosity using a Hashin-Shtrikman lower bound
- When the cement volume increases past the limit of the CCM append a Hashin-Shtrikman upper bound to account for higher cement volumes
- At these higher cement volumes, the Hashin-Shtrikman lower bound has its lower limit in the appended Hashin-Shtrikman upper bound.

The result of this for the P-wave and S-wave velocities is displayed together with the pre-cementation velocities in figure 9.4. It is clear how these models do not coincide at the porosity boundary between mechanical compaction and cementation. The same effect is also seen in figure 9.3, where at 36% porosity the end-point of the friable sand model, corresponding to Hertz-Mindlin is not zero. Figure 9.5 shows an illustration of the implementation given in a textbook (Avseth et al., 2010). In this example the cement model passes through the elastic moduli of the initial sand pack, but with no discussion as to how the models are modified to facilitate this joining.

Two pragmatic alterations seem possible. Either, the contact cement model can be added on top of the stiffness of the granular media. In this methodology, it would be assumed that the absolute change in stiffness is independent of the fact that the granular media has some stiffness to begin with for a given amount of cement. The other way to pragmatically alter these methods such that they "communicate" is to shift the cement model to the right, so that it passes through the granular media point. This is illustrated in figure 9.6. This would be equivalent to saying that the stiffness increase caused by an increase in stress on the unconsolidated granular media is equivalent to a tiny amount of cement (in this example, the necessary shift corresponds to 0.5% cement). In the shifting methodology, the first percent of actual cement, so the first porosity point lost along the black or magenta curves in figure 9.6 correspond to a smaller absolute increase in velocity than the CCM, shown in blue and red. The "excluded" parts in figure 9.6 are meant to

[3] Not actually zero in figure 9.3 because of the statistical work done to make the equations in Dvorkin and Nur (1996), but observed in Dvorkin et al. (1994).

[4] with $\beta = 0.06$.

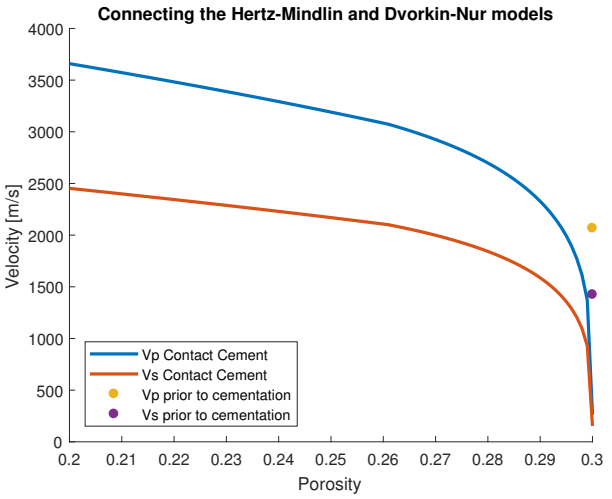

Figure 9.4: This figure illustrates how the contact cement model "misses" the velocity of a pre-compacted unconsolidated granular assemblage. Implementing the contact cement model from 36% and extrapolating down to the estimated porosities will naturally not coincide with that predicted from the friable sand model, unless the stress is so low prior to cementation that the velocity is close to 0 (see equations (5.7) and (5.8))

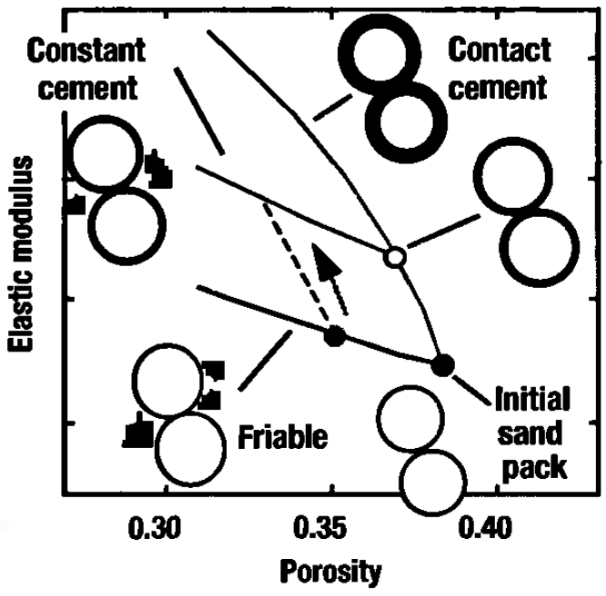

Figure 9.5: Conceptual illustration of how the elastic parameters of the contact cement model compare to the initial grain pack and the friable sand model from Avseth et al. (2010). Note that in this figure the contact cement model seems to "start" from the non-zero stiffness of the initial grain pack, which does not follow directly from the result presented in Dvorkin and Nur (1996).

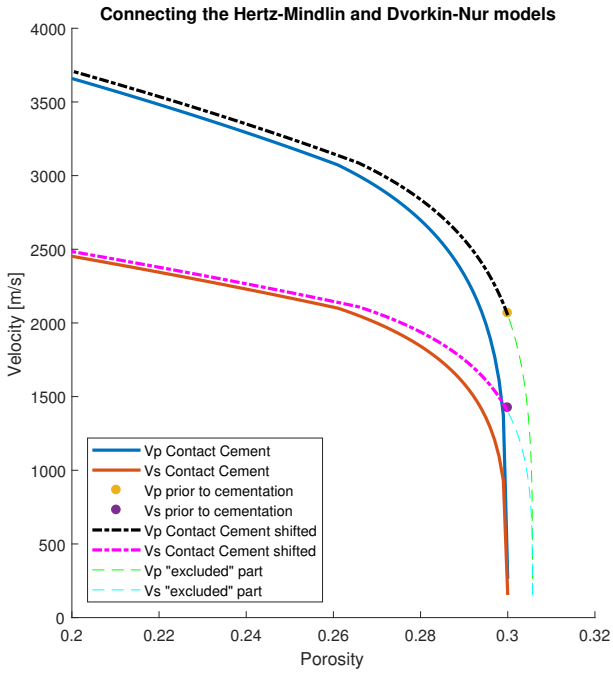

Figure 9.6: The contact-cement model, together with a pragmatic shift of the contact-cement model. Without shifting the modelled velocities to the right, it can be seen that the contact cement model is not able to coincide with the predicted velocities from granular media models, in this case Hertz-Mindlin, as was pointed out in relation to figure 9.4. The shift is numerically the same as treating the velocity increase for increased stress at the grain contacts as a small amount of cement. This is represented by the curves named "excluded" in the figure, which are not included in the stiffness estimations as function of cement volume. This means that the effect of a small amount of cement is smaller for the pre-compacted media than the original contact cement model. This can be seen by comparing for example the velocity change created by reducing the porosity 0.01 from 0.3 in the black curve (corresponding to the shifted velocities) and the blue curve (corresponding to the original contact cement model).

demonstrate the parts of the contact cement curve that would be excluded from the model in figure 9.5 if it is the shifting that is utilised. In the introductory conceptual sketch, the shifting methodology was used. This was done based on a perhaps overly simplistic argument: As the stress increases, the contact area between grains increases. This reduces the increased stiffness effect of a rim of cement with predefined thickness.

9.5.2 Isotropy and Stress Independence

The model of Dvorkin and Nur (1996) gives isotropic parameters. This makes sense as the granular media is assumed to be unstressed as the start, and the spheres are isotropic. Furthermore, the model demands that the the grain assemblage is stress independent (Dvorkin and Nur, 1996).

This is thus clearly not adequate to describe the experimental data observed, as the rock after cementation is both stress

dependent and isotropic.

9.6 The Patchy Cement Model

To deal with the observation of stress dependence in cemented rocks, Avseth et al. (2016) describes a model where the rock consists of some cemented, and some uncemented parts. In other words, the microstructure is considered as an effective medium with a mixture of cemented sandstone and unconsolidated sandstone.

The unconsolidated sandstone is allowed to be stress dependent through applying some effective granular media theory. In Avseth et al. (2016), Hertz-Mindlin is used to model the unconsolidated sand.
The cemented sandstone was modelled using the model in Dvorkin and Nur (1996). The cemented sandstone is assumed to be stress insensitive, but the level of cement that is needed for a sandstone volume to be insensitive is subjective. Avseth et al. (2016) suggests a level of 10%. This means that when the bulk cement volume reaches 10% the rock is stress insensitive.

To obtain the stiffnesses, Avseth et al. (2016) utilise what is referred to as "nested Hashin-Shtrikman". The implementation is summarised as follows:

- Calculate the stiffness of the stress sensitive and cemented sandstone end-members. As per usual, the stiffness of the granular media is calculated at the critical porosity. If 10% is chosen as the "critical" cement limit, the increasing cement model can be used in addition to the contact cement model.

- When the uncemented and cemented end-members are calculated, they are mixed with a Hashin-Shtrikman bound. The proportions of the cemented material in the Hashin Shtrikman bounds is taken as 0 for only uncemented grains and 1 for only the 10% cemented rock.
  An upper bound represents a situation where the stiff material coats the softer material, and is interpreted in Avseth et al. (2010) as "connected patchy cement". The lower bound is the oppsite and represents "disconnected patchy cement".

- After the high-porosity end-member is calculated with the Hashin-Shtrikman step above, a Hashin-Shtrikman lower bound connects that point to the mineral point, equivalent with the constant cement model.

Although pragmatic in nature, the patchy cement model also solves the issue of having to pragmatically shift the contact cement model to match the observed stiffness at the onset of cement. Figure 9.7 illustrates the implementation of the patchy cement model, and compares it to that obtained from the contact cement model. The initial impact of the cement in the patchy cement model is smaller than that obtained in the contact cement model.

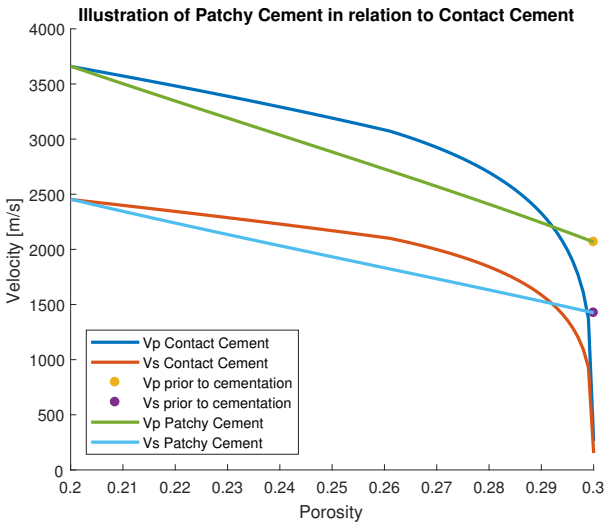

Figure 9.7: Illustration of how the Patchy Cement model compares with the contact cement model (with the increasing cement model appended at 4% cement). The Patchy Cement model is able to "overlap" with the predicted velocities of Hertz-Mindlin, but has a different development before becoming equal to the contact-cement model at 10% cement volume. In this figure, the upper bound is used to mix cemented and uncemented rock, corresponding to the interpretation of "connected patchy cement".

9.6.1 Extension to Anisotropy

The experimental data could be seen to preserve some of the anisotropy after cementation. The anisotropy is brought towards isotropy. Changes in P-wave anisotropy according to changes in velocities can be shown to be dependent on the relative changes of the two velocities:

$$\epsilon = \frac{V_r^2 - V_z^2}{2 \cdot V_z^2} \tag{9.23}$$

Taking the total differential yields

$$d\epsilon = \frac{V_r \cdot dV_r}{V_z^2} - \frac{V_r^2 \cdot dV_z}{V_z^3} \rightarrow \tag{9.24}$$

$$d\epsilon = \frac{V_r}{V_z^2}\left(dV_r - \frac{dV_z \cdot V_r}{V_z}\right) \tag{9.25}$$

The sign of the change in ϵ is therefore dependent on the term in the bracket in the equation above. Considering a change where both the axial and radial P-wave velocity increases thus yields two possibilities

$$dV_r \ \& \ dV_z > 0, \quad dV_r > \frac{dV_z \cdot V_r}{V_z} \rightarrow d\epsilon > 0 \tag{9.26a}$$

$$dV_r \ \& \ dV_z > 0, \quad dV_r < \frac{dV_z \cdot V_r}{V_z} \rightarrow d\epsilon < 0 \tag{9.26b}$$

From these equations it is clear that if the radial velocity is initially less than the axial velocity, a smaller increase in the radial velocity compared to the axial velocity can still bring the rock towards isotropy.

In the experimental data from part II, the radial velocity increase due to cementation was in fact greater than the axial velocity increase, which would bring the rock closer to isotropy, the absolute value of the anisotropy is roughly halved.

A potential way to explain the preferential increase in radial P-wave velocity could be by considering unevenly deformed grain contacts in the axial and radial directions, causing a rim of cement to affect the radial P-wave velocity to a slightly larger degree.

Using Hertz-Mindlin in the patchy cement model will naturally not be able to account for these factors. Instead of using Hertz-Mindlin, the granular media model based on the work in Walton (1987) is used for the stresses in the experiment. This means that at zero cement the patchy cement reduces to an anisotropic, stress dependent granular media model, whereas at the cutoff limit it approaches an isotropic media.

Chapter 10

Implementation of Cementation Models on the Experimental Data

10.1 Modelling Methodology

To be able to account for both the stress dependence and anisotropy observed in the experimental data, the patchy cement model described in Avseth et al. (2016) is utilised. The methodology implemented here can be summarised as

- Calculate the granular media stiffness based on the stress level, at 36% porosity.
- Calculate the cemented media stiffness at the isotropic limit
- Mix these using the Hashin-Shtrikman upper bound
- Extrapolate between the mixture of cemented and uncemented media down to the estimated porosities

To account for the anisotropy, the granular media model described in part III is used instead of Hertz-Mindlin. The granular media is treated independently of the strain condition on the cemented core, and is modelled only based on the measured stresses. The no-slip/slip fraction of the axial P-wave is increased as the loading progresses, based on the loose argument that it does not appear to have "flattened out" between the limits at the maximum loading prior to cementation. The radial P-wave velocity was observed to have "flattened out" to a larger degree, and so the no-slip/slip ratio is kept constant. At the start of the loading after cementation, the no-slip/slip fraction is the same as the [max] values from the previous part for C_{11}, C_{33} and C_{44}. The other moduli (C_{12} and C_{13}) also enter into the anisotropic Hashin-Shtrikman formulation, and so will for the last iteration need a no-slip/slip fraction. This is set equal to that of C_{44}, but the value does not yield significant changes in the estimated moduli C_{11} and C_{33}, if allowed to vary. The cement volume in the core is not measured. This is a weakness in the results, as it allows the cement volume to be a free parameter, although the cement volume should be relatively small. The porosities are estimated as before, using the equation from Fjær (2006) given in equation (4.15).

Based on previous comments regarding the uncertainties in the shear wave velocities, the modelling is limited to the P-waves.

10.2 Modelling Results

Figure 10.1 and 10.2 show the axial and radial P-wave velocities respectively in the interval of loading after cementation. The cement volume is taken as 1.6%, with an isotropic limit of 6%. In the figures, both the final anisotropic patchy cement result, as well as the velocity estimated prior to the final Hashin-Shtrikman implementation in the patchy cement model are shown. The stress sensitivity of the final result of the anisotropic patchy cement model can be seen to overpredict the stress dependence of the velocities, especially the radial P-wave velocity. The reason for this is however not the granular media model, but the effect of decreasing porosity with increased loading.

10.3 Discussion of the Results from Cementation Modelling

This argument for claiming that the porosity change creates the exaggerated stress dependence comes from the fact that the stress dependence introduced by the granular media model is contained in the velocity curves obtained prior to the final Hashin-Shtrikman bound. Another way to visualise this is to plot the results from using constant porosity in the second Hashin-Shtrikman bound. This is shown in figures 10.3 and 10.4 where the lower curves represent a constant porosity, equal to the estimated porosity at the end of cementation (15MPa). The upper curve represents a constant porosity, with the estimated porosity at max burial (40MPa). The anisotropic patchy cement model can be seen to move from the lower to the upper curve, representing the stress dependence caused by the decreased porosity.

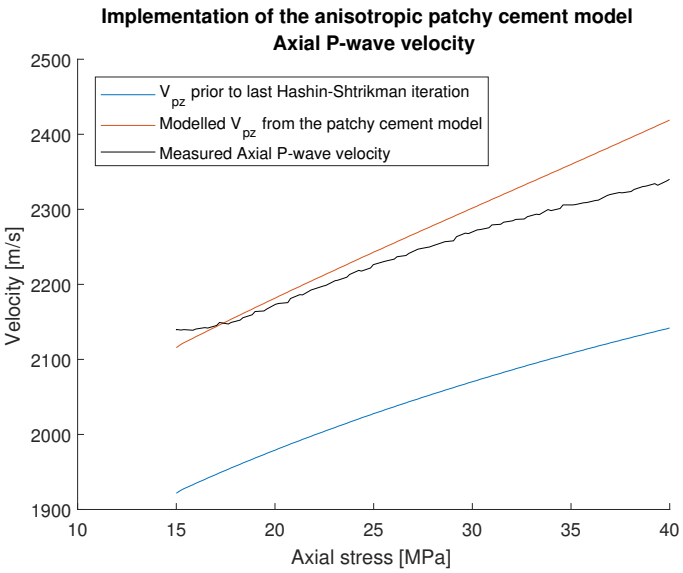

Figure 10.1: Axial P-wave velocity modelled by the anisotropic patchy cement (APC) model, with a cement volume of 1.6%. The blue line represents the velocity modelled prior to conducting the final Hashin-Shtrikman iteration in the patchy cement model. It is observed how the APC model as formulated overpredicts the stress dependence of the axial P-wave velocity. The stress dependence of the underlying granular media model is however given by the blue curve i.e., prior to the final Hashin-Shtrikman iteration. In the blue curve the stress dependence appears to be reasonable in comparison to the measured data

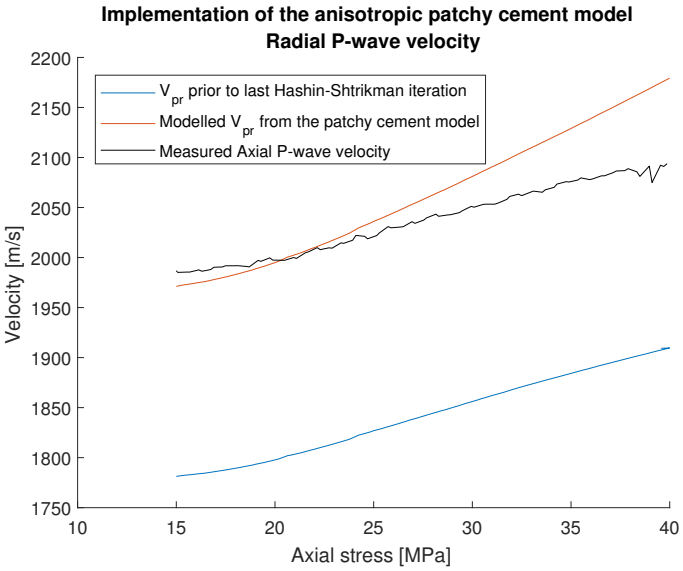

Figure 10.2: Radial P-wave velocity modelled by the anisotropic patchy cement model (APC), with a cement volume of 1.6%. The blue line represents the velocity modelled prior to conducting the final Hashin-Shtrikman iteration in the patchy cement model. It is observed how the APC model as formulated overpredicts the stress dependence of the radial P-wave velocity. The stress dependence of the underlying granular media model is however given by the blue curve i.e., prior to the final Hashin-Shtrikman iteration. In the blue curve the stress dependence appears to be reasonable in comparison to the measured data

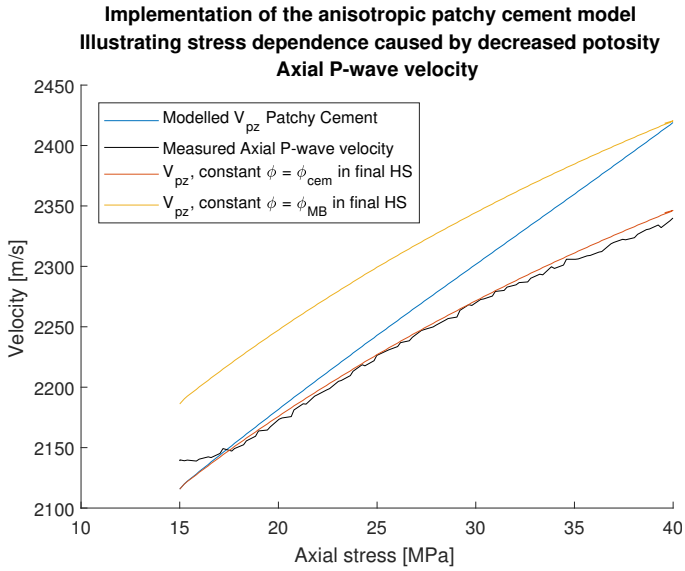

Figure 10.3: Axial P-wave velocity modelled from the anisotropic patchy cement model (APC) with different porosities used in the final Hashin-Shtrikman iteration. The estimated porosities from the experimental data create the blue curve. Using a constant porosity, with the one at the start of burial after compaction yields the red curve. The yellow curve is created by using a constant porosity, with the one at max "burial". This figure illustrates the stress dependence created by the changing porosity. It also demonstrates how the APC with only the stress dependence from the granular media model seems to provide a better match to the experimental data than when incorporating porosity changes after cementation into the stiffness considerations. This is an interesting empirical observation. The cement volume is still 1.6%

The cementation interval is one where the experimental procedure deviates from that likely observed in natural rocks. This is because in a real field case the cementation would happen at the same time as any potential compaction of the pore space, as opposed to being finished prior to the loading. In fact, models such as that of Walderhaug (1996) assume that mechanical compaction ceases at the onset of cementation, and that subsequent porosity loss is only due to the infill of pores by cement. Implementation of this methodology on a field case, in combination with the model of Walderhaug (1996) would thus not consider any porosity loss due to other factors than cementation, and any porosity loss, such as is estimated in the experimental data would subsequently not be included.

The estimated porosity loss comes from the measured change in axial strain over the course of the loading after cementation. This strain was given in figure 3.4. It is observed how during the first few increments of loading there is very little strain, before there is a "kink" in the stress strain curve, and the strain (and thus porosity loss) accelerates. One possible reason for this "kink" is that cement bonds start breaking due to shear. This reduces the strength of the rock, and allows for the development of increased strain. If the cementation was continued during the loading, it could be that this strain would be hindered by the increased stiffness of the rock due to continued cementation, limiting the porosity loss due to other factors than cementation.

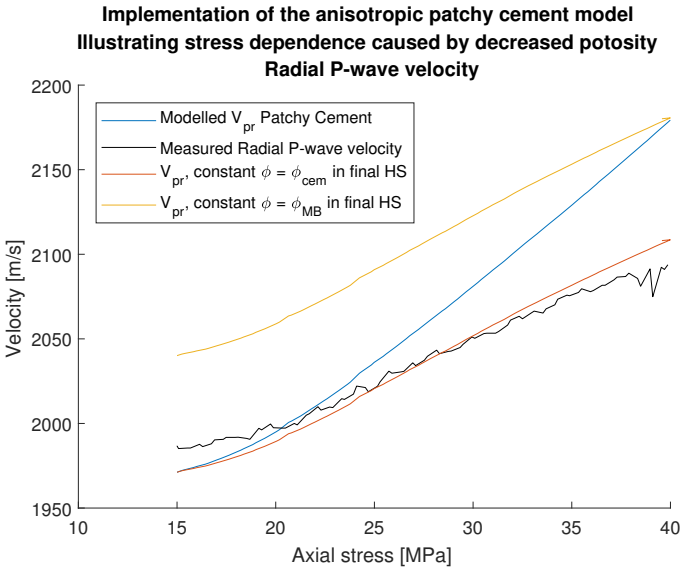

Figure 10.4: Radial P-wave velocity modelled from the anisotropic patchy cement model (APC) with different porosities used in the final Hashin-Shtrikman iteration. The estimated porosities from the experimental data create the blue curve. Using a constant porosity, with the one at the start of burial after compaction yields the red curve. The yellow curve is created by using a constant porosity, with the one at max "burial". This figure illustrates the stress dependence created by the changing porosity. It also demonstrates how the APC with only the stress dependence from the granular media model seems to provide a better match to the experimental data than when incorporating porosity changes after cementation into the stiffness considerations. This is an interesting empirical observation. The cement volume is still 1.6%

Assuming that the increased strain is indeed caused by deformation of cement bonds, it can then be understood why this methodology overpredicts the stress dependence. The rock would likely obtain a higher velocity due to reduced porosity, but the reduced stiffness due to the breakage of cement bonds would cause a decrease in velocity. As only the porosity effect is incorporated into the model as it stands, the velocities are overpredicted.

The quality of the porosity estimation is of course also in question. At the stress level where the cementation occurs the cement volume and porosity are factors that scale the observed results, and so an erroneous porosity at that point would in this implementation be compensated by a different cement volume.

Thus, based on the observations, it is assumed that the stress dependence on the stiffness after cementation in the experimental data is caused only by the stress dependence contained in the granular media model. The consequence of this is that the last iteration of Hashin Shtrikman in the anisotropic patchy cement implementation uses the estimated porosity at the start of loading after cementation over the entire interval. One positive note is that the same cement volume predicts both the axial and radial P-wave velocities simultaneously to an OK extent.

10.4 Summarising Remarks

As a summarising statement, the stress sensitivity predicted by the patchy cement model is relatively good if the effect of mechanical reduction in porosity on the stiffnesses are ignored. In such a setting, the only factors increasing stiffness is the cement volume and increased stress on grain contacts.

It is clear that this interval introduces uncertainty in the full-scale modelling, as the processes happening in the laboratory and the field might be crucially different. Preserving the P-wave anisotropy, requires a great deal of "tweaking". Both arguments regarding the development of the no-slip/slip relationship, and the availability of the cement as a free fitting parameter pose problems for extension to a forward-modelling sequence.

As the model used for porosity prediction with depth (Walderhaug, 1996) consider cementation as the only porosity reducing factor after the onset of cement, applications to full-scale burial histories would produce the curves that show a decent fit. These will be used for further modelling. This is done with a conscious awareness that the APC model implemented directly as presented in Avseth et al. (2016) would overpredict the stress sensitivity in the laboratory data.

The anisotropic patchy cement model might thus not be the most appropriate model for describing the experimental observations. In fact, the crack model might then be more appropriate to describe the processes in the laboratory. Implementation of the crack model in this interval is discussed in the extended discussion in part VI, but as the anisotropic patchy cement model still seems most applicable in the context of modelling real burial histories it will be utilised in those scenarios.

Part V

Combination to a Full “Burial History”

Chapter 11

Modelling Uplift in the Experimental Data

11.1 Introduction to the Uplift Modelling Procedure

As described in Part II, the crack model in Fjær (2006) was investigated as a potential way to model the effect of the simulated uplift on the velocities. The preceding two parts have attempted to formulate models capable of modelling the experimental data down to the start of the simulated uplift.

In this chapter, necessary modifications to the crack model to enhance its applicability are considered. This means that in this chapter, the stiffnesses at max burial are given by the measured velocity and estimated density, as opposed to results from modelling.

In the next chapter, the modified crack model from Fjær (2006) is appended to the results from the previous parts in order to create a full burial history. As has been thoroughly pointed out, the modelling down to this "max burial" point is not straightforward. Particularly the modelling of the P-wave anisotropy requires "tweaking" in order to match the observed experimental data. This is likely a testament to the multitude of assumptions that are concocted together in the formulation of the physical models at the base of the derivations.

11.2 Necessary Modifications to the Crack Model

The crack model was described in part II. It uses strain as an input, which is generally problematic in a field setting. As a pragmatic solution, it is assumed that for small enough changes in stress, Hooke's law can be used to estimate the corresponding small changes in strain.

The experiment conducts the unloading under uniaxial strain, which allows the axial strain increment to be calculated according to Hooke's law as[1]

$$\Delta\epsilon_z = \frac{\Delta\sigma_z}{C_{33}} \tag{11.1}$$

[1]The problem in extending the discussion to non-uniaxial strain during unloading is considered in the next chapter.

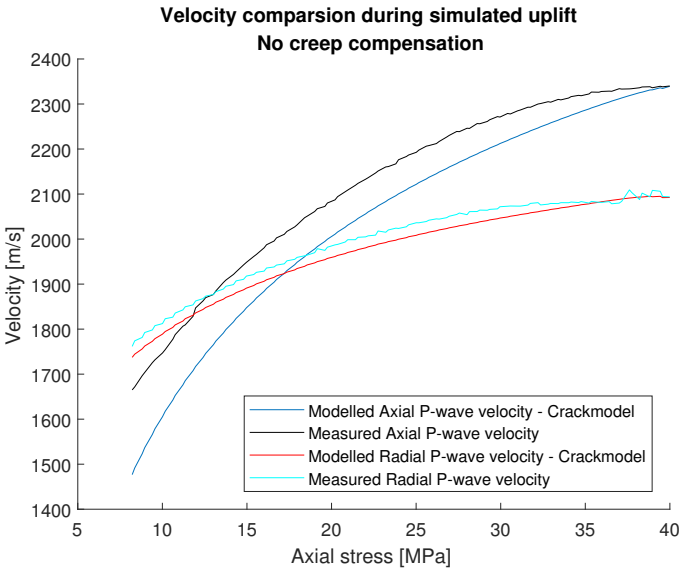

Figure 11.1: Modelled and measured P-wave velocities for the simulated uplift interval. The modelled velocities were created using an iterative combination of the crack model and Hooke's law. The velocities are underpredicted throughout the simulated uplift. This is a result of the fact that the iterative methodology does not take into account the creep that is observed in the experimental data.

This change in strain can then be used to define the strain value inputted into the crack model, and thus the change in stiffness over the small change in stress can be estimated. This can then be run in an iterative loop over the unloading interval.

11.3 Results of the Modified Crack Model

Figure 11.1 shows the modelled axial and radial P-wave velocities obtained by implementing the suggested modification to the crack model. The results might at first glance appear somewhat underwhelming, with the velocities being underestimated. The late stage trends are however captured to some extent.

The strain as a function of stress was given in figure 3.4, showing some creep at the start of the simulated uplift. Positive

strain in the crack model would yield an increase in the velocity. Implementing the iterative Hooke's law methodology would naturally predict a negative change in strain from the onset of unloading.

Therefore, to some extent it is encouraging that the velocities are as they are in figure 11.1. It makes sense that the crack model without the creep would predict lower velocities than observed in the sample.

11.4 Compensating for the Creep

Although the observed velocities in figure 11.1 make sense it is of interest to see whether the creep can be compensated for in the modelling. Three methods are tested

- Creep compensation by initial shifting
- Creep compensation by changing the reference point
- Creep compensation by adding delayed strain

11.4.1 Initial Shifting

This proposal is based on the observation that the trends at later stages of uplift were captured quite well. A way to consider this is that if the effects of creep were allowed to happen at the maximum stress, the velocity would increase, and subsequent unloading would produce a trend similar to that observed in figure 11.1. The result of shifting the starting velocities up by an appropriate amount is seen in figure 11.2, and can be seen to provide a better fit. The shift is based on eye-measurement, but it is noted that a similar synthetic sandstone, with less cement, was left to settle at 40MPa, and displays a shift of roughly the same magnitude (see figure C.4).

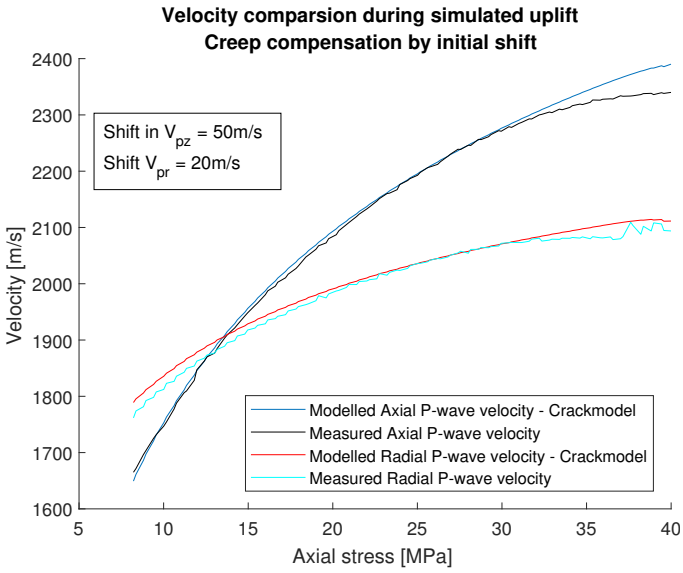

Figure 11.2: Modelled P-wave velocities from the crack model, where the creep has been compensated by shifting the starting point up by an appropriate amount. The assumption behind this correction is that if there is no creep after stress reversal, the shape of the graph should be similar to that of the modelled velocities in figure 11.1. If the creep had been allowed then to run to completion prior to stress reversal, this would lead to a velocity increase at the maximum "burial depth". The shift in this figure is based on fitting the observed data at large "uplift" values, but in a similar experiment on a synthetic sandstone that had undergone the same process (but with less cement) there was a period at max burial to allow for the creep effects. This is displayed in figure C.4 in appendix C, and shows a shift of similar magnitude to that implemented in this figure.

11.4.2 New Reference Point

This proposal is based on starting the modelling at a stress level where any delayed strain does not act to cause strain in the opposite direction to that predicted by the stress release. The results of this can be seen in figure 11.3, and an improved fit is observed. The amount that the reference needs to be shifted is based on the strain development in figure 3.4. At some point the delayed strain will start to act in the same direction as the incremental strain change. When any delayed information is acting in the same direction as the strain caused by subsequent stress changes, it can be argued that the delayed strain which occurs at a given stress level compensates for any deformation that is delayed in the current change in stress (Fjær et al., 2011).

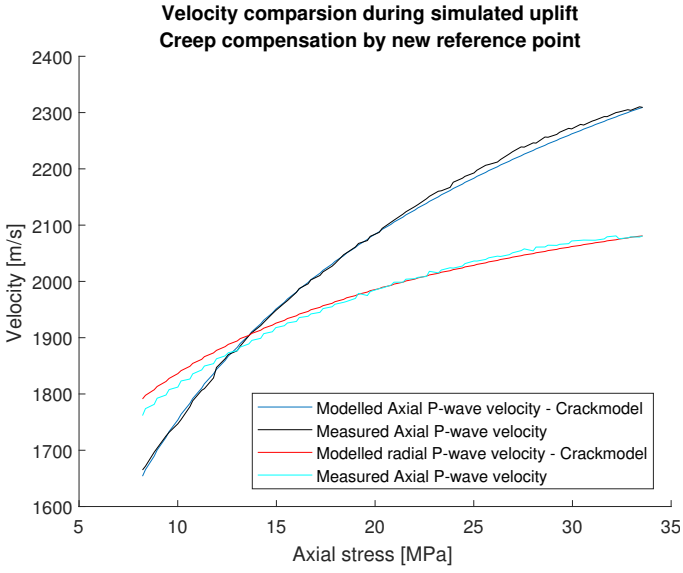

Figure 11.3: Modelled P-wave velocities from the crack model, where the creep is dealt with by starting the modelling from a stress along the "uplift" curve. The argument for doing this is that in a situation that any delayed strain has the same direction as the current strain direction, the strains estimated by Hooke's law in the iteration loop should be appropriate. This is in part based on arguments in Fjær (2006). The amount of shifting is based on the reversal of the strain trend in figure 3.4.

11.4.3 Delayed Strain

This proposal is based on adding a pragmatic delayed strain, such that the strain profile looks similar to that observed in figure 3.4. The results are shown in figure 11.4. The amount of

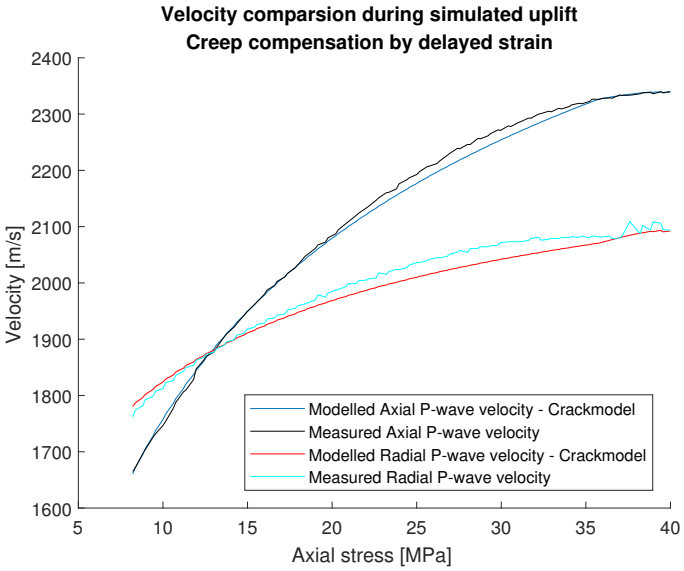

Figure 11.4: Modelled P-wave velocities from the crack model, where the creep is compensated by altering the input strain in the crack model by some amount to make a strain profile with a similar shape to that seen in figure 3.4.

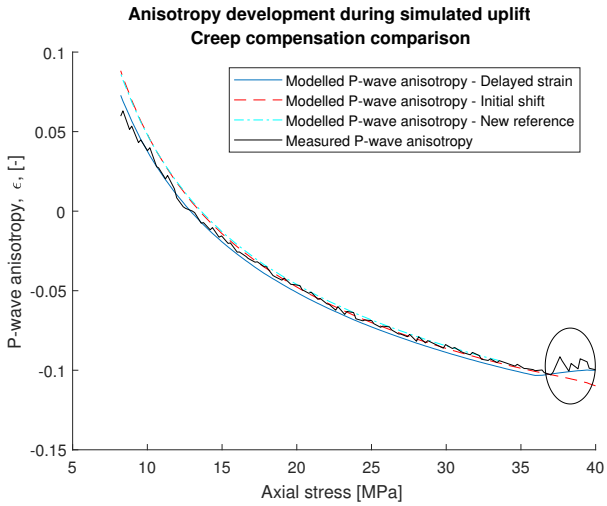

Figure 11.5: Comparison of the P-wave anisotropies of the three different methods of compensating for the creep. Observe how the slight decrease in P-wave anisotropy at the start of the simulated uplift is captured by the method of adding some delayed strain.

delayed strain is again based on observations. The strain is defined as

$$\epsilon_{cc} = \begin{cases} |\sum_{i=1}^{n} \Delta\epsilon|, & |\sum_{i=1}^{n} \Delta\epsilon| < c \\ 2c + \sum_{i=1}^{n} \Delta\epsilon, & |\sum_{i=1}^{n} \Delta\epsilon| \geq c \end{cases} \tag{11.2}$$

In this equation, c is some parameter describing the amount of delayed strain. ϵ_{cc} is the creep compensated strain inputted into the crack model, and $\Delta\epsilon$ is the incremental strain changes at each stress increment predicted by the iteration method.

The change in strain predicted by Hooke's law will, for negative changes in stress be negative. If the magnitude of the cumulative strain estimated by the iteration method is smaller than the predefined value of c, then the strain put into the crack model is the absolute value, i.e., it will increase until c is reached. Once the cutoff is reached, the input strain starts decreasing. Continuity is maintained since in the limit of

$$|\sum_{i=1}^{n} \Delta\epsilon| \rightarrow c = c \tag{11.3}$$

for both equations.

11.5 Summarising Remarks

The effect of the creep might be another factor that separates the laboratory measurements from the field case. Compensating for it as done above is possible, yet pragmatic. If the creep is not as prevalent in the field scenario, something more like figure 11.1 might very well be expected.

It is also important to remember that in these figures, the input parameters of the crack model are changed as to facilitate that the curves fit. The value for η was taken from the Levendberg-Marquart results presented in part II. In the < 10 milliStrain domain, which is the case for the uplift, the results are relatively independent on the η parameter, due to the term with ϵ^2 becoming very small, unless of course η is brought to a correspondingly high level. Thus most of the curve fitting by altering the crack model parameters was done by altering the value of n and β. The main argument for why the crack model seems appropriate, even given the availability for altering of the parameters, is that the *same* parameters simultaneously provide good predictions of both P-wave velocities over the entire unloading interval.

In terms of which creep compensation methodology to implement, the delayed strain is the one that will be used. This is based on a small detail regarding the anisotropy predictions. The anisotropy predictions given by the three models are compared in figure 11.5. All are quite good, after the compensation and fitting has been done, which is of no surprise. The delayed strain method can be seen to actually capture the small decrease in P-wave anisotropy during the first few MPa's of unloading.

Chapter 12

Modelling the Entire "Burial History"

In the previous chapter, the implementation of the crack model in an iterative loop with Hooke's law was investigated. The starting stiffnesses of those models were however chosen based on the measured velocities and estimated densities, rather than the modelled velocities from granular media and cement models.

In this chapter, a full "burial history" is created for the observed experimental data, before an implementation with cement estimation, i.e. combination with the model from Walderhaug (1996) is created.

12.1 Combining All Modelling Intervals

The final modelling results for the axial and radial P-wave velocities in comparison to the measured data are shown in figures 12.1 and 12.2. The models can be observed to create a relatively decent fit to the observed velocities.

A key aspect of this work has been to investigate the possibility of using the P-wave anisotropy in burial and uplift modelling, and the final result can be seen in figure 12.3, where the model can be seen to recreate the measured anisotropy to a decent extent.

Throughout this work it has been made clear that each of the three intervals that are to be modelled have a set of input parameters that can be altered in order to fit the observed data to an as best as possible extent. The ability of the model to fit the data over the entire "burial history" should therefore not be taken as a complete validation that the model is true.

The full range of utilised parameters are summarised in table 12.1, and a short note on their selection is warranted.

12.1.1 Grain Parameters

These were mainly selected based on the work done in part III. The exact values of these parameters are subject to some debate, and different references could be chosen to justify a range of values. The coordination number is by several sources (see figure 8.4) modelled to be porosity dependent. The argument made in part III is that a potential porosity dependence of the coordination number can be modelled, together with other factors, by the no-slip/slip fractions. This is limited by the scenario where the coordination number changes so much that the observed values venture above the predefined no-slip limit.

One solution to this would be to let the coordination number be anisotropic and stress dependent, in addition to the already anisotropic, stress dependent no-slip/slip fractions. This would simply give the model *even more* freedom. Another modification could be to let the coordination number "do the job" that the no-slip/slip fractions are doing in the current model. That is, *instead of* having anisotropic, stress dependent no-slip/slip fractions, the coordination number is made anisotropic and stress dependent.

12.1.2 No-slip Fractions

For the pre-cementation interval, values are chosen exclusively based on the work done in part III. For the cement interval, they are identical to that used in part IV. The reason for keeping the value for C_{11} constant during the cement interval was based on the observation that the curve was seen to stabilise between the no-slip/slip limits toward the maximum values of loading prior to cementation, as well as the lack of correlation between the minimum and maximum values. The values for the no-slip/slip fractions for C_{33} is increased slightly over the cementation interval based on the observation that there still appears to be some increase in the value towards the maximum loading value prior to cementation. Furthermore, there was a strong positive correlation between the start value and end value in the accepted solutions, suggesting that the [min max] relationships have a larger role in defining the accepted solutions for C_{33}, and so a further rise might be expected upon increased stress.

12.1.3 Cement Parameters

For the cement interval, the isotropic limit was defined at 6%. This is lower than the 10% suggested in Avseth et al. (2016). The reason for the lower value is the observation that the rock loses about half of the anisotropy during cementation, but there

is known to be only small amounts of cement. To need 10% to achieve isotropy therefore seemed a bit excessive, but it is noted that this is an argument based purely on observation. The cement volume that then fit the curves is seen to be 1.6%, which seems plausible. It is noted that the cement volume and isotropic limit can be altered together to define several combinations that yield acceptable fits.

Another aspect of the cement interval is the choice to exclude the effects of porosity decrease on the stiffness in the anisotropic patchy cement model through the final Hashin-Shtrikman iteration. This was discussed in part IV and the assumption originates from potential differences in the behaviour of rocks in the laboratory due to the experimental procedure. The exclusion of this porosity change on the stiffness was seen to significantly improve the stress dependence predicted by the model.

12.1.4 Crack Model Parameters

The grain parameters are kept constant throughout the modelling sequence, which means that shear wave modelling is excluded from the crack model (see part II). The creep compensation method utilised was that of delayed strain, and so the n and β parameters utilised are from that fitting. The η parameter was from the Levenberg-Marquardt fitting done in Torset (2017), and is not changed due to the low dependence on the η parameter in the < 10 mStrain domain.

Table 12.1: Key factors used in the creation of the modelled P-wave velocities and P-wave anisotropy seen in figures 12.1, 12.2 and 12.3. The elastic properties of the quartz cement are assumed to be equal to those of the quartz grains.

Grain parameters	
Poisson's ratio	0.08
Shear Modulus	42 GPa
Coordination number	9
Granular media no-slip fractions [Start, Cementation stress, Max Burial]	
C_{11}	[0.25, 0.35, 0.35]
C_{33}	[0.2, 0.5, 0.7]
Cement interval parameters	
Volume of cement	1.6%
Isotropic cement limit	6%
Crack model parameters	
n_{cm}	0.055
β	2.3
η	182
"Delayed strain" for equation (11.2)	0.35 mStrain

12.2 Incorporation of Cement Estimation

In the field scenario, quartz cementation would likely be continuous over loading and unloading within a defined temperature interval, so the model would look somewhat different. The developed models can be combined with a model to estimate the cement volume to depict how this would influence the properties of the sediment and rock.

This methodology is the same as when creating the figures used in the conceptual illustration (see figure 1.2), but with the updated models honouring anisotropic stress fields used in place of the isotropic models. A discussion on what parameters are used is of interest, and the values are found in table 12.2.

12.2.1 Burial History and Stress Field

The burial history utilised is identical to that used in the creation of the updated conceptual model in figure 4.8. Instead of an isotropic stress, the stress is taken to be $\sigma_z = 2\sigma_r$. The choice of this stress level is not rooted in anything particular, other than a desire for it to be anisotropic.

12.2.2 Grain Parameters and Porosity

The shear modulus, Poisson's ratio and coordination number are the same values as used in the modelling of the experimental data. The coordination number is kept constant in this implementation, as for the implementation on the experimental data, although it could have been modelled as porosity dependent.

The stiffnesses of the granular media will be calculated at 36% porosity, and subsequently extrapolated using the anisotropic friable sand model. The depositional porosity is set to 36%, and the porosity as a function of overburden stress is calculated based on Lander and Walderhaug (1999). The β parameter in this model is set to 0.06, which was also used in the introductory conceptual example, and is taken from Lander and Walderhaug (1999).

12.2.3 No-slip fractions

One problem in forward modelling, which to some extent already has been discussed, is the choice of the values of the [min max] values for the different elastic stiffnesses. The anisotropic, stress dependent fractions were implemented in order to account for potentially several factors in the simplest possible way. This implementation however requires sufficient amount of data in order to be properly determined, as was done when modelling the experimental results.

Thus, instead of choosing a [min max] relationship, the following implementation is done using the no-slip and slip limits. These are then assumed to act as a form of bounds. If measure-

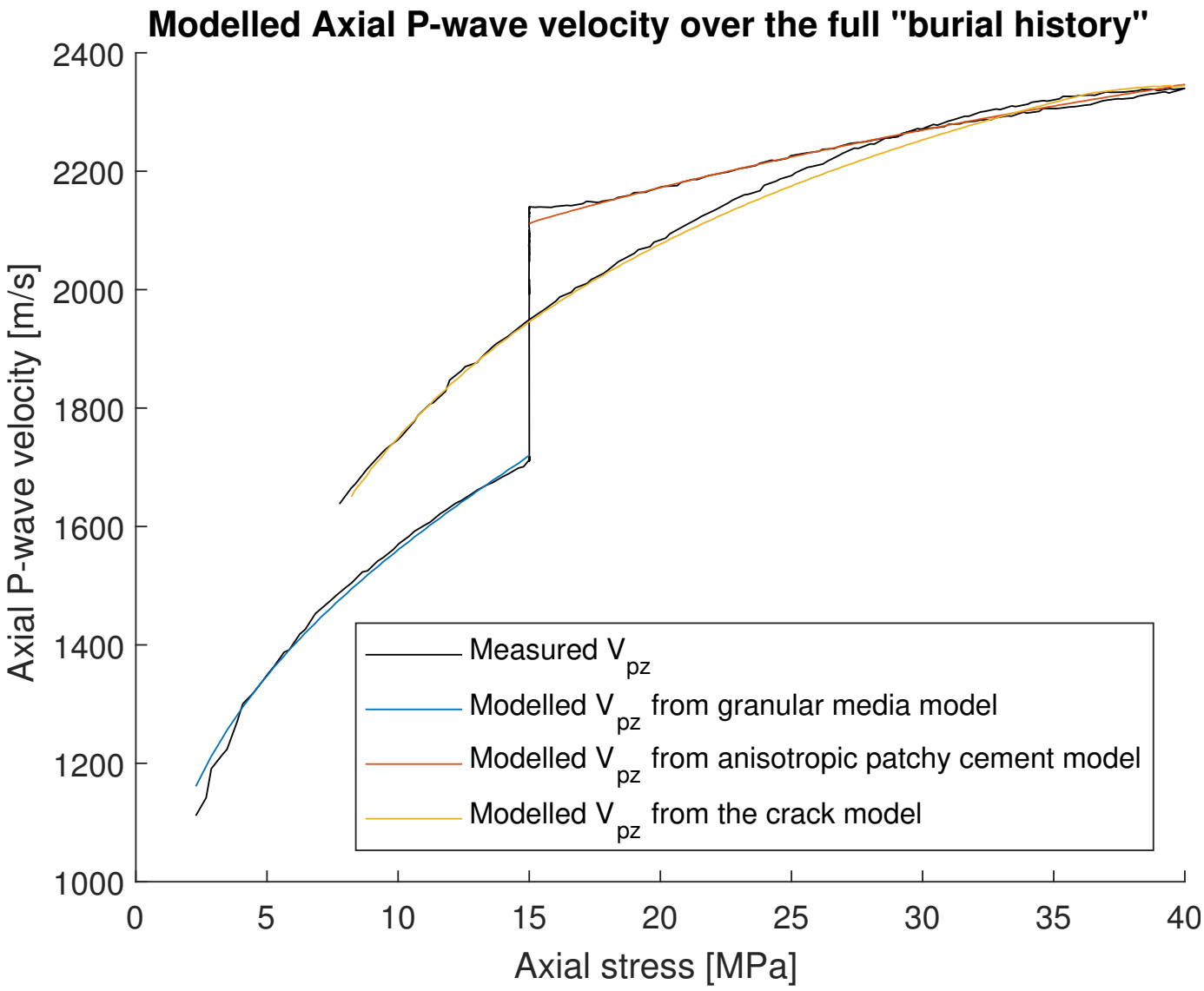

Figure 12.1: Modelled axial P-wave velocity over the full "burial history" of the synthetic sandstone. The parameters inputted to create these curves are displayed in table 12.1. The model can be seen to have the ability to conform with the measured velocities quite well, it is however important to remember that the parameters in table 12.1 are chosen on the basis of creating the best fit.

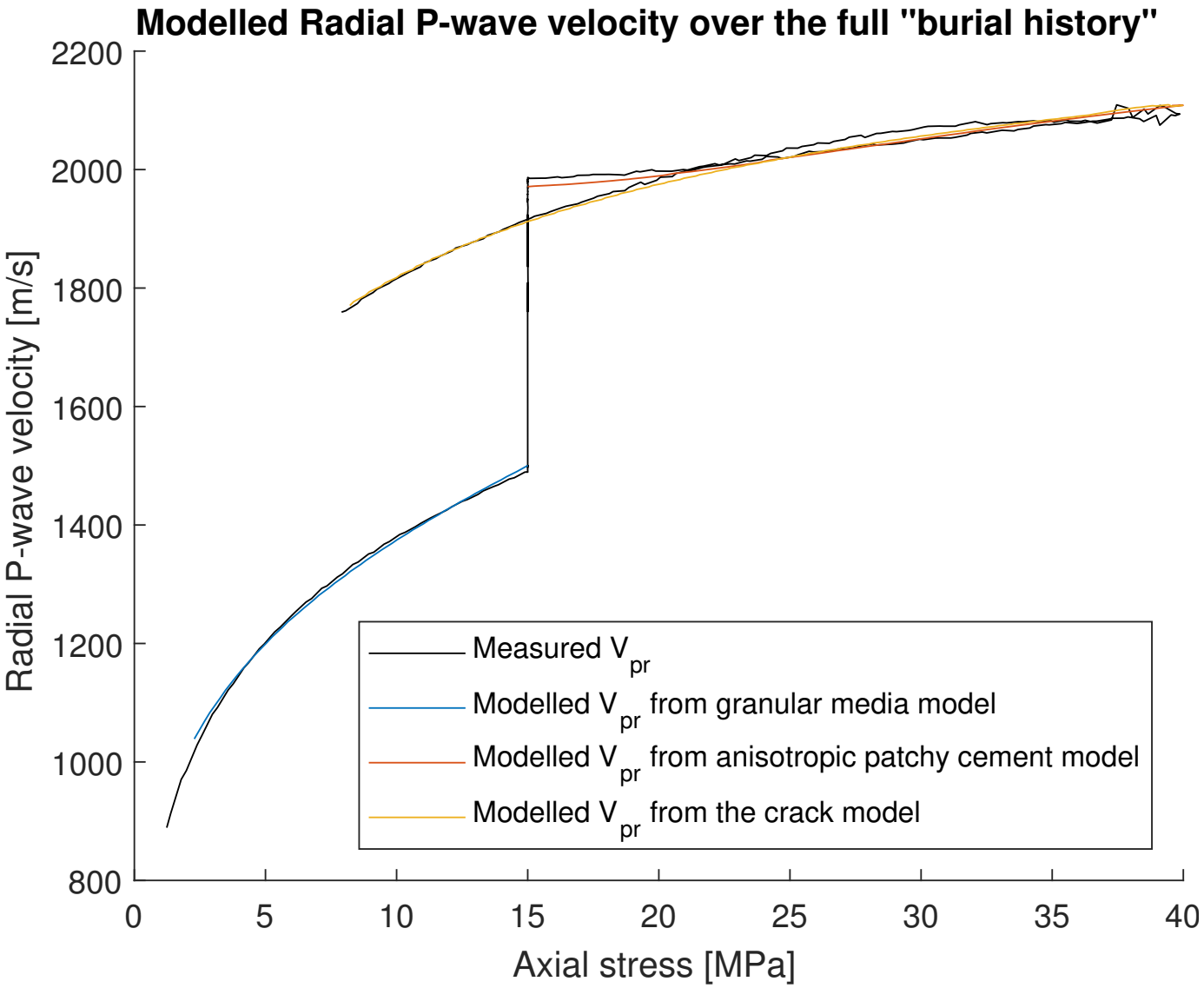

Figure 12.2: Modelled radial P-wave velocity over the full “burial history” of the synthetic sandstone. The parameters inputted to create these curves are displayed in table 12.1. The model can be seen to have the ability to conform with the measured velocities quite well, it is however important to remember that the parameters in table 12.1 are chosen on the basis of creating the best fit.

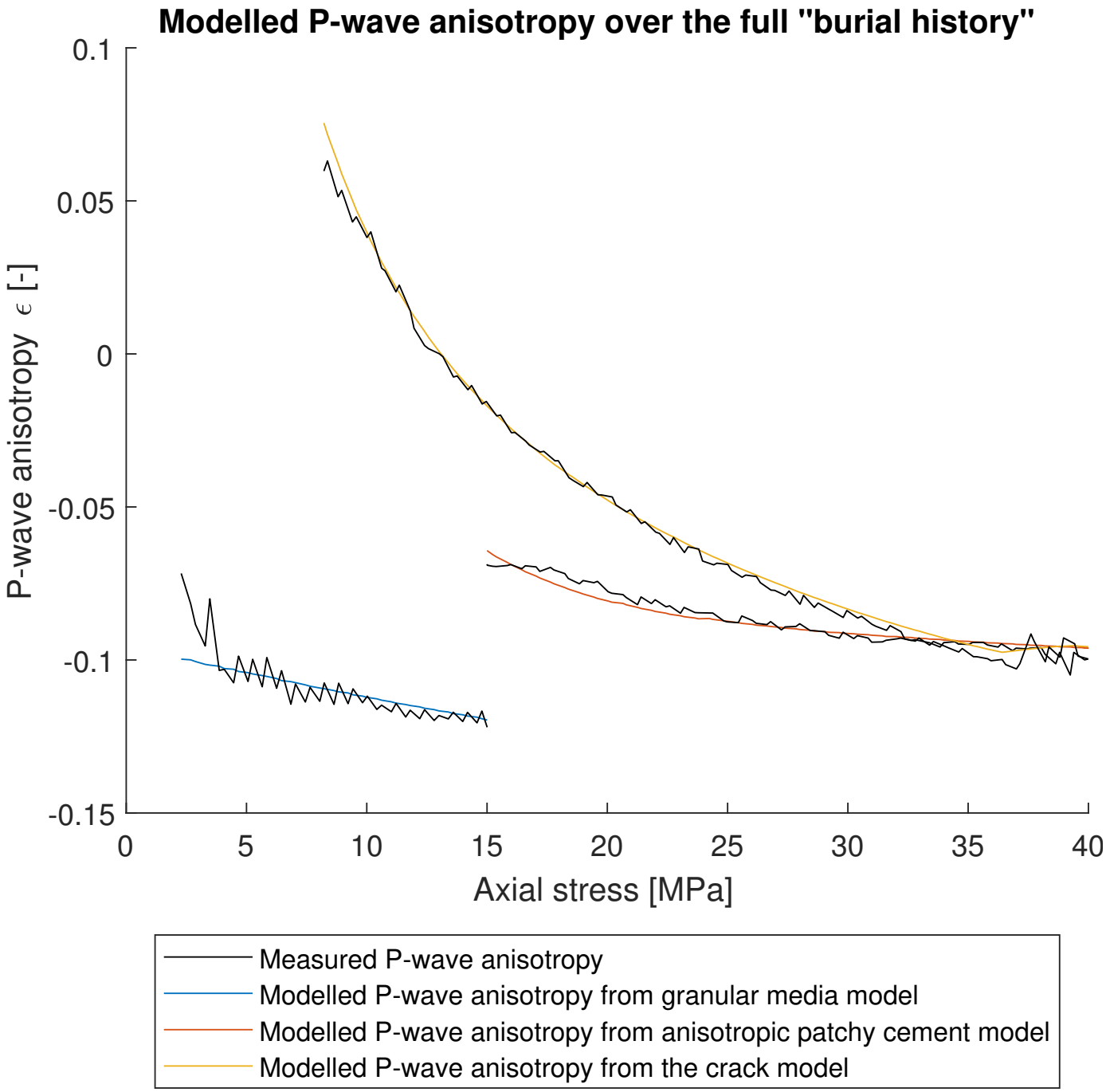

Figure 12.3: Modelled P-wave anisotropy over the full "burial history" of the synthetic sandstone. The parameters inputted to create these curves are displayed in table 12.1. The model can be seen to have the ability to conform with the measured P-wave anisotropy quite well, it is however important to remember that the parameters in table 12.1 are chosen on the basis of creating the best fit.

ments at different stress levels are available, an idea of a potential no-slip/slip fraction might be inferred from these bounds. It is noted that these bounds are of course dependent on the choice of grain parameters and the coordination number, taken to be constant in this modelling.

12.2.4 Cement Parameters

The key difference in the current implementation and that in the previous section is the incorporation of cement estimation through Walderhaug (1996), instead of setting a cement volume. Furthermore, the cementation will now naturally occur over a larger range of stress. It is assumed by Walderhaug (1996) that there is no porosity loss due to mechanical compaction after the onset of cement. This assumption will be carried into the modelling, and so porosity loss at increased depths after the onset of cement will come from the cement volume.

The limit of isotropy is in this case reverted back to the value used in Avseth et al. (2016) of 10%. The values of the a and b parameters are taken from Walderhaug (1996) with $a = 6.247 \cdot 10^{-9} \frac{moles}{cm^2 \cdot m.yr}$, $b = 0.022 \frac{1}{^\circ C}$. A grain size is needed, and this is set to have a diameter of $D = 0.03cm$. The molar mass of quartz is $M = 60.09 \frac{g}{mole}$.

12.2.5 Crack Model Parameters

The estimation of radial strain from Hooke's law requires the knowledge of C_{12} and C_{13} (see equation (2.2)). Whilst it is certainly possible to utilise the values predicted for C_{13} and C_{12} together with C_{11} and C_{33} in the iteration loop of Hooke's law and the crack model to estimate and utilise radial strain, the current implementation will be limited to uniaxial strain. This is because the experimental data allow for no indication of the quality of C_{12} and C_{13} produced from the modelling.

Furthermore, the axial shear wave velocity was seen to need an alteration in the grain parameters (Poisson's ratio) in order to be modelled by the crack model. Similar problems might arise for the modelled values of C_{12} and C_{13}. These problems would then be manifested in the estimated strain values, derailing the model. Limiting the uplift modelling to uniaxial strain means that only C_{33} is needed in the strain estimation.

In this modelling it is also assumed that there is a negligible effect of creep on the rock as burial changes to uplift. The extensional deformation is assumed to happen on the onset of uplift, meaning that no creep compensation methods are implemented.

The crack model is integrated with the patchy cement model, in the interval where there is both cementation and uplift. This is similar to the methodology used when creating the updated conceptual model in figure 4.8, except now it is the patchy cement, rather than contact cement model that is superposed with the crack model. As before, the effects are assumed to be superpositionable, in that they can simply be added. This is likely a simplification of the processes occurring in the subsurface. The consequence of using the patchy cement model during the unloading interval is that the granular media model is also present during unloading. The granular media model as formulated in part III produces stiffnesses defined by the stress level and not stress history, which means that the granular media model will predict the same stiffness for a given stress level during loading and unloading. This is not investigated in any detail in this work, but it is noted that as the cement volume increases, the effect of a deviation in the granular media model is decreased, as it constitutes a smaller part of the overall stiffness.

12.2.6 Results of Integrating Cement Estimation in the Rock Physics Model

The modelled axial P-wave velocity is shown in figure 12.4. The same trends as was seen for the updated conceptual model in figure 4.8 can be observed, with a decrease in P-wave velocity as the rock is subjected to unloading. The key difference is that the P-wave anisotropy is now also modelled, and this is shown in figure 12.5.

During the loading prior to cementation, the P-wave anisotropy can be seen to become slightly less negative for both the no-slip and slip limits. Based on equation (7.30), for a constant σ_z/σ_r relationship the solution of E_r should be unchanged. From (7.23) and (7.24), the P-wave anisotropy should thus remain constant, according to the granular media theory. It should be constant because E_{33} will cancel from all the expressions (see equations (7.1) to (7.4)), leaving only E_r and the grain parameters. The slight change in P-wave anisotropy still observed is due to the anisotropic friable sand model affecting C_{11} and C_{33} in a manner that causes the observed change.

It can be seen how increasing the fraction of no-slip contacts (uniformly) would act to move the P-wave anisotropy toward the no-slip limit, i.e. towards isotropy. This point was discussed earlier, in relation to figure 8.8. This formed some of the argumentation for making this fraction anisotropic, in addition to stress dependent, as the experimental data when subjected to loading shows a move towards stronger anisotropy.

The cementation starts at 2000m, and here the velocity increase accelerates. As the cement volume increases, the rock also moves towards isotropy, as more and more of the assemblage consists of the isotropic cemented media. As the sample gradually consists of smaller amounts of the granular media, the distance between the slip and no-slip limits is also reduced. Once uplift begins the effects of the crack model and the anisotropic patchy cement model are superposed. Initially, there is an increase in velocity, before, as temperature drops and cementation slows down, the velocity increases is flattened out, before it starts decreasing. As uplift continues, the anisotropy is brought towards isotropy, before a reversal of the anisotropy occurs, as for the experimental data.

Table 12.2: Key factors used in the creation of the modelled axial P-wave velocity and P-wave anisotropy whilst incorporating cement estimation seen in figures 12.4 and 12.5. The elastic properties of the quartz cement are assumed to be equal to those of the quartz grains. Parameters marked (WH) are those used in the Walderhaug model.

Burial history	
Burial rate	$50 \frac{m}{m.yr}$
Uplift rate	$100 \frac{m}{m.yr}$
Geothermal gradient	$35 \frac{^\circ C}{km}$
Maximum burial	$3200m$
β	0.06
Grain parameters	
Poisson's ratio	0.08
Shear Modulus	42 GPa
Coordination number	9
Density	$2.650 \frac{g}{cm^3}$
Cement interval parameters	
Isotropic cement limit	10%
a (WH)	$6.247 * 10^{-9} \frac{moles}{cm^2 \cdot m.yr}$
b (WH)	$0.022 \frac{1}{^\circ C}$
D (WH)	$0.03cm$
M (WH)	$60.09 \frac{g}{mole}$
Crack model parameters	
n_{cm}	0.07
β_{cm}	2.77
η_{cm}	182

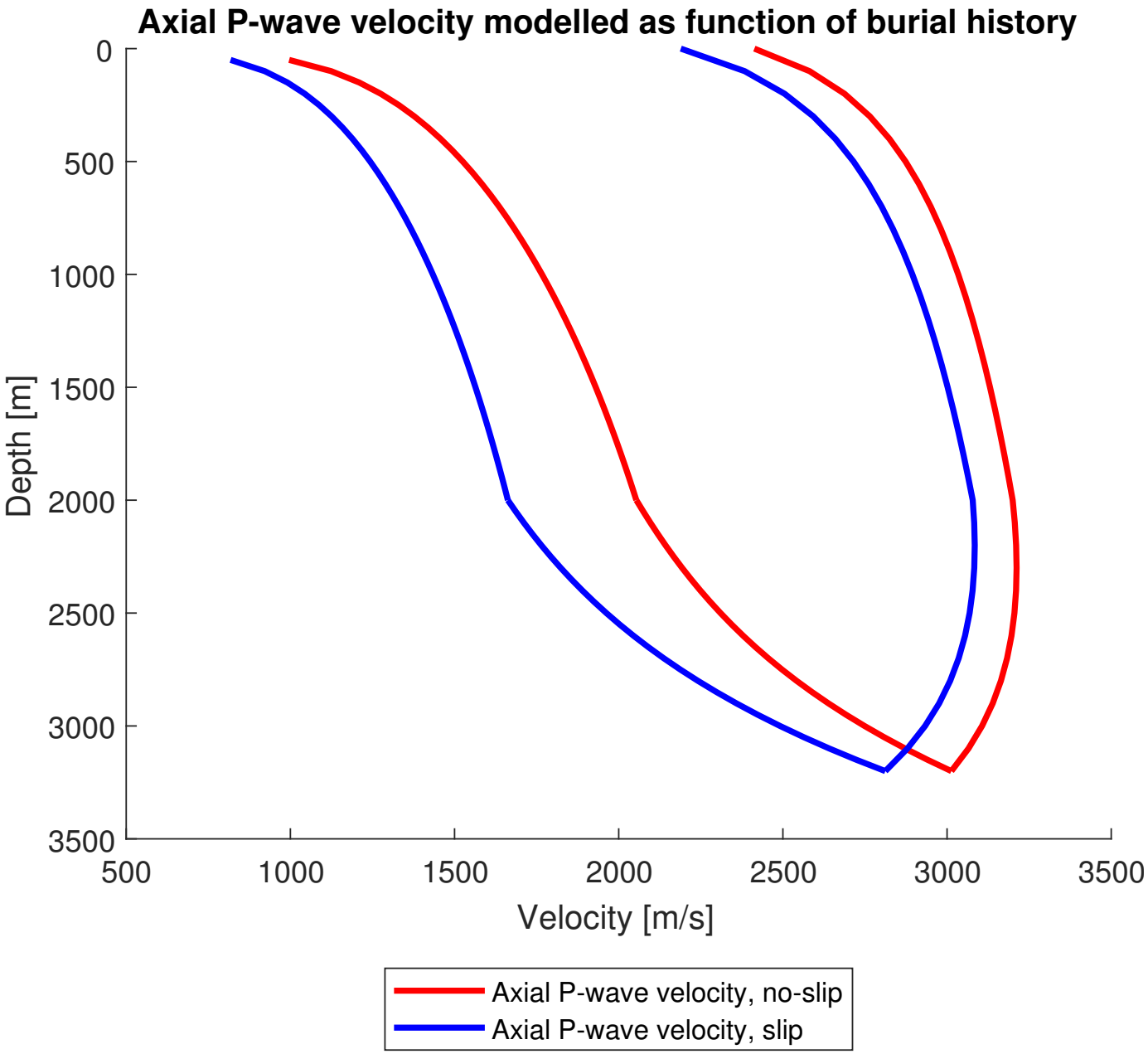

Figure 12.4: Modelled axial P-wave velocity over the same burial history that was used to create the updated conceptual model in figure 4.8. The radial stress is assumed to always be half of the estimated vertical stress. During the pre-cementation loading, the granular media model based on Walton (1987), presented in part III is utilised. The porosity loss is modelled after Lander and Walderhaug (1999). After the onset of cement, the volume of cement is estimated using the model of Walderhaug (1996), and the cement volume is assumed to be the only porosity reducing factor. The stiffnesses during burial after the onset of cement are modelled using the anisotropic patchy cement model (APC). The APC model is based on the work done in Avseth et al. (2016), and is presented in part IV. During uplift whilst in the cementation domain, the changes in stiffnesses are taken to be the superposed effects of the APC model and those predicted by the crack model presented in Fjær (2006). The crack model is used in an iteration loop with Hooke’s law assuming uniaxial compaction, to avoid the problem of lack of information regarding C_{12} and C_{13}.

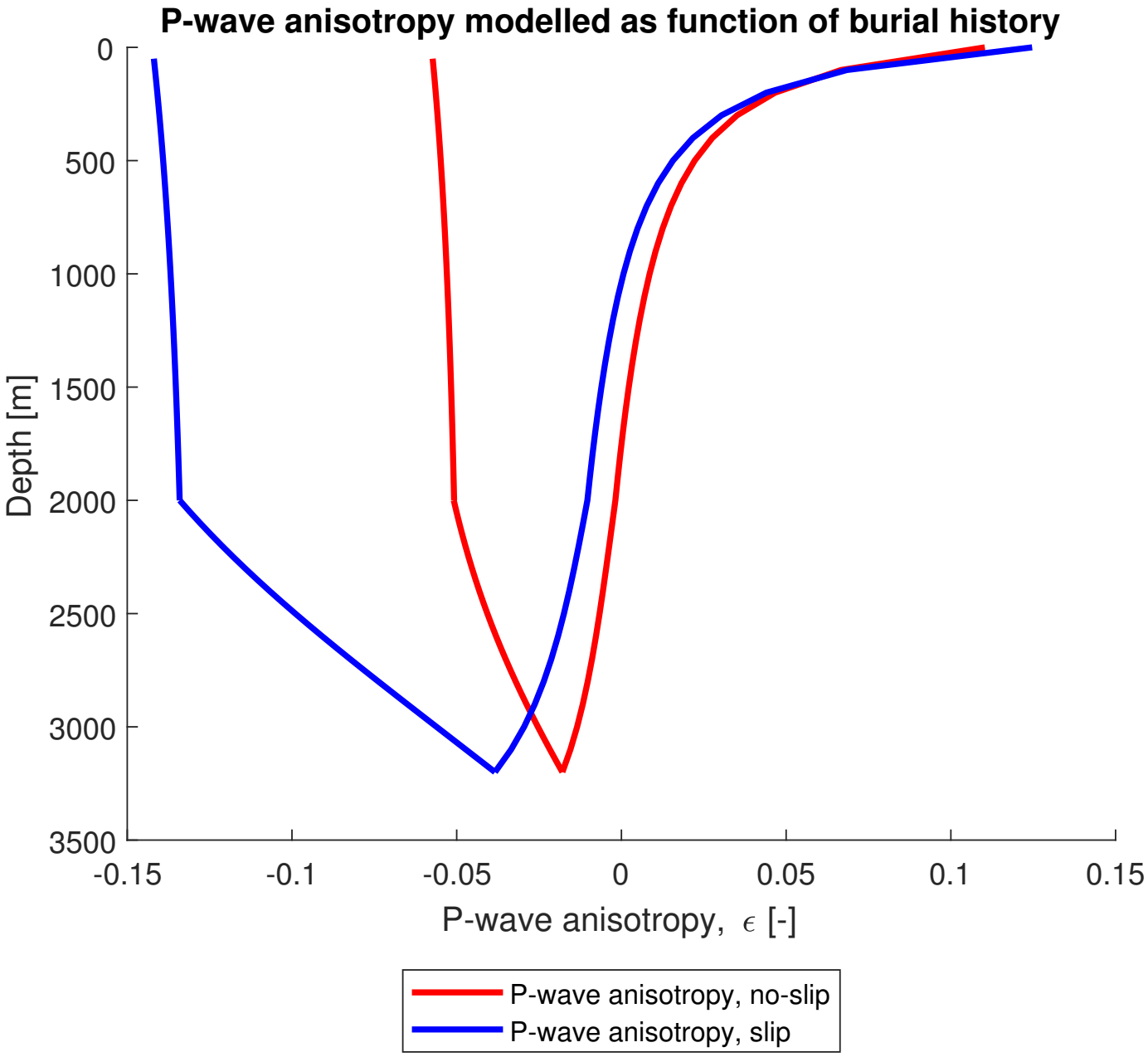

Figure 12.5: Modelled P-wave anisotropy over the same burial history that was used to create the updated conceptual model in figure 4.8. The radial stress is assumed to always be half of the estimated vertical stress. During the pre-cementation loading, the granular media model based on Walton (1987), presented in part III is utilised. The porosity loss is modelled after Lander and Walderhaug (1999). After the onset of cement, assumed to happen at 2km, the volume of cement is estimated using the model of Walderhaug (1996), and the cement volume is assumed to be the only porosity reducing factor. The stiffnesses during burial after the onset of cement are modelled using the anisotropic patchy cement (APC) model. The APC model is based on the work done in Avseth et al. (2016), and is presented in part IV. During uplift whilst in the cementation domain, the changes in stiffnesses are taken to be the superposed effects of the APC model and those predicted by the crack model presented in Fjær (2006). The crack model is used in an iteration loop with Hooke's law assuming uniaxial compaction, to avoid the problem of lack of information regarding C_{12} and C_{13}.

Part VI

Discussion, Limitations and Conclusion

Chapter 13

Extended Discussion

13.1 Chapter Introduction

The end product of the previous part is a rock physics model that sows together granular media models, cementation models, and the crack model. This is a model capable of modelling the development of P-wave velocities and subsequently P-wave anisotropy in sediments subjected to a triaxial stress during loading[1], and uniaxial strain during uplift.

The model was able to reproduce the observed experimental data quite well, but as pointed out, the model contains weaknesses. In this chapter, these weaknesses will be reviewed and elaborated, in an attempt to provide an overview of the limitations present in the modelling results.

The chapter will first consider each of the modelling intervals individually, effectively summarising the results of parts III, IV and V. Following this, the representability of laboratory data in relation to the field is discussed. In light of the limitations and representability, the qualitative and quantitative nature of the model can be established. Following this, additional laboratory will shed some light on the effect of cement volume and stress path, before the role of fluids in the pore space is briefly discussed.

13.2 Granular Media Model

To be able to model the experimental data, a granular media model capable of handling a triaxial stress state, with a confining stress and axial stress, was required. Starting from the work in Walton (1987) and Bandyopadhyay (2009) such a model was created and tested in part III.

The manufactured model was able to recreate the axially propagating P and S-wave velocities, as well as the radial P-wave velocity, but only after a pragmatic implementation of anisotropic and stress dependent fractions of no-slip and slip limits.

In Walton (1987) it is assumed that no contacts are created or lost. Furthermore, all spheres are assumed to be spherical and of equal size. The idea that no contacts are created or lost is equivalent to having a constant coordination number as the stress is increased. As previously discussed the coordination number might be stress dependent, but in the modelling it is kept constant. The potential for non-spherical grains and non-perfect sorting would also mean that the slip and no-slip limits are not perfect representations of what the actual slip and no-slip limits would look like.

In a sense therefore, the binary mixing model, where slip and no-slip contacts from Walton (1987) are mixed, is the pragmatic mixing of non-perfect limits to describe factors not covered by the model. These factors have been discussed previously, and include things such as force chain networks, and increased friction on grain contacts.

The fact that the model is able to fit the observed P-wave velocities, using anisotropic stress dependent fractions of slip and no-slip contacts, is not necessarily a testament to the models validity. It simply means that the model, with the pragmatic alterations, has the freedom of parameters to account for natural deviations compared to the assumptions in Walton (1987).

In addition to the uncertainties in the granular media model, there is the question of extrapolation to other porosities than the 36% of a random dense packing of spherical grain. The friable sand model is used. This is, as previously described, at its core simply a form of interpolation between the 36% and 0% porosity points.

The porosities were throughout the experimental data estimated, but never measured. This introduces a further uncertainty in the modelling results. It is however likely that the pragmatic modifications to fit the experimental data would be able to counteract potential errors introduced by using the wrong porosity (and subsequently density) by altering other parameters.

13.3 Cementation Model

In the model used to recreate the experimental data a cement volume was chosen on the basis that it was not measured. The only knowledge was that the there was not a lot of cement. The effect of cement volume on the uplift mechanisms is discussed

[1] But in the current formulation limited to scenarios where the horizontal stresses are equal.

in more detail later.

The contact cement model with its extensions (constant cement and increasing cement) (Dvorkin et al. (1991), Dvorkin et al. (1994), Dvorkin and Nur (1996), Avseth et al. (2010)) was used to describe the stiffness of cemented media with sufficient amounts such that a granular assemblage is isotropic and stress independent. The problem of creating a continuous velocity as function of burial history when combining true application of granular media models and the model in Dvorkin and Nur (1996) was discussed in part IV. The primary issue is that the model in Dvorkin and Nur (1996) is based on unstressed cement contacts at the start of cementation. In a scenario where the rock has been subjected to several km's of burial this condition is not met. Furthermore, the model in Dvorkin and Nur (1996) creates a rock that is stress insensitive, and isotropic.

The patchy cement model with an anisotropic granular media as the lower bound was used to describe both the stress dependence and anisotropy of the assemblage after cementation. The cement volume was used as a free fitting parameter giving the model significant freedom in regard to the magnitude of the velocities. One cement volume did however simultaneously provide reasonable estimations for the magnitude of both the radial and axial P-wave velocities.

When the estimated porosity loss after cementation was included in the final Hashin-Shtrikman iteration it was observed that the stress dependence of the velocities was overpredicted. The stress dependence of the underlying granular media seemed to conform better with the observed stress dependence. This led to the implementation of the patchy cement model without incorporating the stress sensitivity created by the loss of porosity due to mechanical compaction after cementation.

The strain causing the porosity loss was theorised to occur due to deformation caused by the loading. This deformation would act to reduce the velocity, but would not be incorporated in the anisotropic patchy cement model. One way to potentially model this in the experimental data would have been to incorporate the crack model from the onset of loading after cementation, instead of the anisotropic patchy cement model. This is because in the crack model, the effects on stiffness of both the reduced porosity and the formation of cracks can be incorporated. The results of a Levenberg-Marquardt fit of the loading interval after cementation for the axial P-wave velocity and P-wave anisotropy are shown in figures 13.1 and 13.2.

In the field however, the cementation at one stress level followed by loading with no more cementation is not realistic. Instead, cementation is continuous, and upon further cementation the rock will become stiffer, and so the strain causing the porosity loss in the experimental data upon loading after cementation might not be seen in the field. Therefore, instead of incorporating the crack model earlier, the extra apparent stress dependence predicted by the patchy cement model due to the porosity loss during loading after cementation was ignored. This provides a better fit with the observed experimental data,

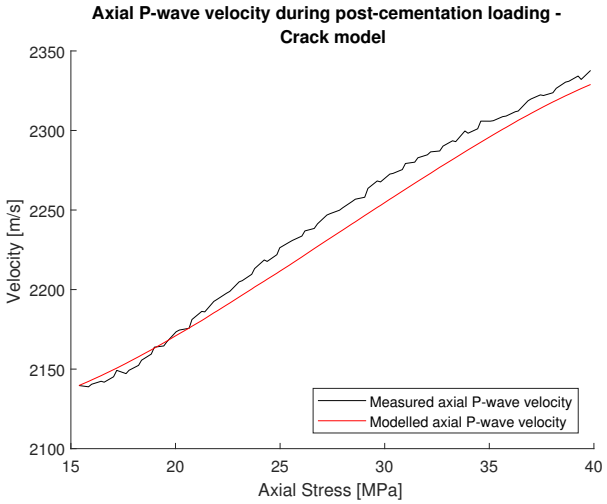

Figure 13.1: Modelling the axial P-wave velocity during the loading after cementation with a Levenberg-Marquardt fit of the crack model, as opposed to the APC model. This was done on the basis of the accelerating strain, which could be an indicator of crack formation (broken cement bonds) softening the rock as a whole. The crack model is also seen to be able to produce reasonable fits of the observed data, and might in fact be a more appropriate approach to the physical processes *in the experimental data*. In a scenario where the cementation is continuous over the cementation interval (as in the field), it is however possible that the APC model will be more appropriate in describing the effects than the crack model.

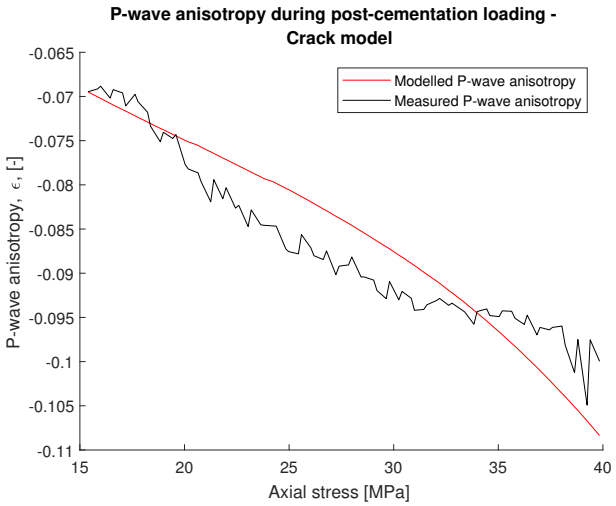

Figure 13.2: Modelling the P-wave anisotropy during the loading after cementation with a Levenberg-Marquardt fit of the crack model, as opposed to the APC model. This was done on the basis of the accelerating strain, which could be an indicator of crack formation (broken cement bonds) softening the rock as a whole. The crack model is seen to be able to produce reasonable fits of the observed data (although the trends seem somewhat better in the modified APC model i.e., where the stress dependence due to porosity decrease during loading was ignored), and might in fact be a more appropriate approach to the physical processes *in the experimental data*. In a scenario where the cementation is continuous over the cementation interval (as in the field), it is however possible that the APC model will be more appropriate in describing the effects than the crack model.

and might be more representative of the field scenario. In fact, as the model in Walderhaug (1996) assumes no mechanical compaction after cementation, there will be no porosity loss due to increased stress in the model incorporating cement estimation. By "more representative" is meant that the only porosity loss considered is that caused by cementation. The porosity vs stress curves will in general be quite different for the field and laboratory scenario due to this continuous cementation.

In the application of the cement models in the field, the final product of the patchy cement model is dependent on both the parameters in the underlying granular media, as well as those chosen in the cementation models. This gives a wide degree of freedom to model observed data, especially in the event of the cement volume being unknown.

13.4 The Crack Model

In Torset (2017) the formation of microcracks as a result of failing cement contacts during uplift is used as an argument for implementation of the crack model. This was based on the observations of the experimental data and the work done in Holt et al. (1997) and Holt et al. (2004).

In Holt et al. (1997) coring damage is investigated, and a synthetic sandstone similar to that described in this work is unloaded after formation. Holt et al. (1997) state that during unloading, "microcracks, that may well be associated with grain bond breakage are opened". These microcracks cause a decrease in velocities and increase in stress dependence.

In Holt et al. (2004), numerical simulation are conducted that show that uplift can cause the breaking of cement bonds. This can be done through both tension and shear. In the numerical simulations, the cementation is done at peak stress, rather than a lower stress level such that the methodology is somewhat different from that in the experimental data. This might however be more representative of the field case, where more cement is formed at higher stress.

The claim that the cement bonds breaking are the main cause of the increased stress dependence in the sample described in part II is not justified further, and has not in this work been "proven" by observation, by for example creation of thin sections. The problem of making thin sections of the cores in the laboratory and from the field is that it requires unloading all the way to atmospheric conditions. This might give an unrepresentative view of the deformation mechanisms over the unloading intervals considered in this work.

One weakness of the model as formulated was the limitation of uniaxial strain, as discussed in the previous part. This was because the desire to exclude strain from the modelling involved an iterative combination of the crack model and Hooke's law. This is based on the assumption that over small changes in stress and strain the relations in the generalised Hooke's law are valid. The estimation of the strains in the generalised Hooke's law for an arbitrary strain state requires the moduli C_{12} and C_{13} in addition to C_{11} and C_{33}. In the case of uniaxial strain, only C_{33} is needed. C_{12} is related to the horizontally propagating shear wave modulus C_{66}. There is no information regarding how well the moduli C_{12} and C_{13} are modelled up to the onset of uplift. Utilising these stiffnesses in the iteration loop with the crack model is therefore uncertain, and as pointed out in part V might derail the model. The results in this work are therefore limited to describing uniaxial strain during uplift. The methodology should *in theory* be valid for non-uniaxial strain during uplift.

The sensitivity of the axial shear wave velocity with regard to the Poisson's ratio was discussed in part II, and with a value close to that used in the previous modelling intervals, i.e., $\nu_s \approx 0.08$, the axial shear wave velocity was poorly modelled. If the assumption that the P-wave anisotropy should be calibrated in the reference point, a similar consideration to that done in part II can be undertaken, revealing that the radial S-wave would also fall in the "domain with no physical meaning (similar to figure 4.6)". The choice of $\nu_s = 0.08$ came from the desire of keeping the quartz parameters constant. A material corresponding to 0 porosity and 0 crack density is in this work considered as a solid block of quartz, and therefore expected to have the same parameters as the quartz grains. However, in the implementational strategy in Fjær (2006), the Poisson's ratio "typical for rock constituting solids" is set at a fixed value of 0.2, and is allowed to vary independently of the H^0 and G^0. Therefore, it is within the limits of the model in Fjær (2006) to change the Poisson's ratio during uplift, to facilitate the incorporation of modelling of the axial shear wave velocity, and possibly better prediction of the remaining parameters.

13.5 The Choice of Models

There exists several models that attempt to depict the processes occurring in sediments as they are subjected to various burial histories.

In the granular media domain for example, another triaxial strain model in the no-slip limit is that presented in Johnson et al. (1998). Appendix D briefly discusses this model, and shows how in the no-slip limit, the results from Walton (1987) and one particular strain history[2] in Johnson et al. (1998) are equal. The desire to derive general expressions directly from Walton (1987), instead of using the results of Johnson et al. (1998) originates from the fact that the derivations produced both slip and no-slip limits, facilitating the use of the binary mixing model.

In terms of cement volume, work by Oelkers et al. (1996) shows that at greater depths the cement distribution is uneven where stylolite spacing is sparse. Thus, the assumption that the precipitation is rate determining is dependent on the maximum depth of burial not being too high, if the stylolite spacing is

[2]Corresponding to where both the radial and axial strain are increased simultaneously, with the axial strain being increased faster, as was the case in the experimental data.

sparse. In Oelkers et al. (1996), a sample at 3750m of burial depth shows a relatively even distribution of porosity with irregular stylolite spacing, indicating that diffusion is not rate controlling, and so the model in Walderhaug (1996) might be appropriate. As no greater depths are investigated in this work, the implementational simplicity of the model in Walderhaug (1996) was preferred. A model incorporating stylolite spacing can be found in Bjørkum et al. (1998).

Regardless of the cementation model chosen, the volume of cement is dependent on the parameters entered into the models. These include grain sizes, geothermal gradient, burial rate and the presence of inhibiting coatings such as chlorite (Walderhaug, 1996). Such information might be available through geological constraints and core samples. These parameters thus define the amount of the cemented media that enter into the patchy cement model.

The stiffness of the cemented rock was modelled with an anisotropic modification of the patchy cement model Avseth et al. (2016). Although other extensions to the contact cement theory presented in Dvorkin and Nur (1996) exist (see for example Dvorkin et al. (1999)) the patchy cement model allows for incorporating of both stress dependence and anisotropy relatively easily. This feature makes the patchy cement model attractive, although it is not without its weaknesses, as previously discussed.

Two additional models to the crack model were tested on the experimental data in the uplift domain in Torset (2017). These were the models presented in Prioul et al. (2004) and Ciz and Shapiro (2008) which attempt to describe the dependence of stiffnesses in terms of the observed stress (Ciz and Shapiro (2008)) or strain (Prioul et al. (2004)). It was in the previous work suggested that out of the three models the crack model was most appropriate.

Other methods to model reduction in velocities as rocks are exhumed also exist. One such example is found in Bredesen (2017), in response to the diagenetic sandstone modelling overpredicting velocities in the Kobbe sandstone Formation in the Barents Sea. Microcrack formation during uplift is also used as an interpretation in Bredesen (2017) for the lack of fit between the modelled and observed data. Bredesen (2017) uses a methodology from Avseth et al. (2014a) which combines the contact cement model with "Differential Elastic Media", which can incorporate crack-like pore-geometries in low-porosity sandstones. A key aspect of the present work was the P-wave anisotropy observed during uplift, which is readily obtained from the crack model. The work presented in Avseth et al. (2014a) is concerned with bulk and shear moduli, and so is limited to isotropy. The possibility of extending the model from Avseth et al. (2014a) to anisotropy is not investigated in this work.

As a final note, the main problem in the choice of models was to find models that allow for the incorporation of P-wave anisotropy. The desire to include anisotropy modelling came from the reversal of the P-wave anisotropy seen in the experimental data. Models that allowed for incorporation of anisotropy either directly or with some modification were therefore preferred.

13.6 The Advantage of Laboratory Data

Using laboratory data means that the assemblage of grains can be controlled, such that other burial diagenetic features than compaction and quartz cementation can be neglected. Some examples of such reactions were discussed in part I. These reactions may act to alter the stiffness of the detrital assemblages at many stages during burial (Worden and Burley, 2003). This is not to say that well sorted, quartz rich sediments do not occur in nature, but in the laboratory it can be guaranteed.

The laboratory therefore provides an arena where the observed changes in the velocities can with a greater degree of certainty be ascribed to the processes considered by the multitude of models used in this work.

13.7 From Laboratory to Field

Although processes can to some extent be controlled in the laboratory, the extension of the validity of the result to the field is not trivial.

13.7.1 Lithology

The laboratory data in this work is limited to quartz assemblages. Holt et al. (2000) presented four criteria as a "measure of representativeness", which were discussed in part II. The quartz grains used to create the synthetic sandstones are from real sediments, and so is a fair representation of a certain composition of sandstones. The event of mineralogical variations, in other words not purely quartz would introduce uncertainty in terms of the validity of the experimental data as representative.

The experiments could of course be conducted for a greater variety of feldspathic and lithic sandstone assemblages, to establish a "catalogue of parameters", but regardless the variety of mineral assemblages found in nature will likely also vary somewhat from that tested in the lab. Alternate mineralogies might also introduce grains that have preferred orientations. This will impact the observed anisotropies (Fjær et al., 2008).

The silicate cement formed is indicated by Holt et al. (2000) to be less brittle than that formed naturally. This might mean that more deformation can occur before the cement contacts break. This artificial cement is also not ruled out as "at least a partial source of creep" (Holt et al., 2014).

This work has been exclusively concerned with sandstones, and models to describe the effects of burial history on sandstones. Sandstones however make up only about 20-25% of the sedimentary column (Boggs Jr, 2006). This limits the availabil-

ity of sandstone velocity and stress measurements to calibrate the necessary parameters.

13.7.2 Time and Temperature

In addition to the wide range of compositional variety in natural sedimentary deposits, there is the question of the rate at which these processes occur. Burial and uplift of rocks happen over millions of years, whereas the experiment is done in a couple of hours.

The cementation in the experiment also deviates from that seen in natural rocks. In the sediment the synthetic quartz cement is precipitated over a constant stress interval, whereas in natural rocks, it is expected to be cemented over a range of stresses. In the laboratory, this has been thought to create an overexaggerated porosity loss due to subsequent loading, as the stiffness of the rock is reduced through the breakage of cement bonds. The effect of increased stiffness due to porosity is incorporated into the final Hashin-Shtrikman bound in the anisotropic patchy cement model, but the effect of decreased stiffness due to crack formation would not be seen in this model. This led to the observation that the velocities seemed overly dependent on stress during loading after cementation.

Even though natural quartz cement might be more brittle than that formed in the laboratory, for a given confining pressure an increase in temperature and decreased strain rate will in general lead to more ductile behaviour (Gudmundsson, 2011).

The differences means that the parameters determined in the previous sections are not likely to be general for all burial histories. The hope is however, that the fact that the model is able to fit the data for a certain parameters is an indicator that the physical processes described by the models can to some extent be seen as responsible for the changes. If this is the case, then other assemblages of grains might be attained by altering the parameters used in the models.

13.7.3 Measurements from Seismic and Well data

One of the uncertainties in seismic is that vertical velocities in offshore surveys are typically estimated, rather than directly measured. This arises from the distance between source and receiver in the offshore seismic surveys. The methodology of creating velocity profiles from seismic and well data is not discussed in any further detail in this work. An illustration of velocity estimation as function of offset can be found in for example Simm and Bacon (2014). Frequency is another aspect of the comparison to the field case. The sample in the laboratory is considered dry, and so dispersion effects due to the presence of fluids are not present. Using Biot-Gassmann fluid substitution (see appendix B) to model the effects of fluids produces the low frequency result if the equations of the form of (2.6) are used. This might be sufficient in the seismic frequency range, but in wells where the frequency can be in the kHz range, dispersion due to fluids in the pore space might become a factor.

13.8 All Models Are Wrong, but Some Are Useful

The timeless words of statistician George Box (Box, 1979) are certainly applicable to the work done in this thesis. As described throughout the thesis, the underlying models contain assumptions and limitations aplenty. In the knowledge that the final model designed through part III to part V is likely inadequate to exactly describe all physical processes in a natural rock, the question remains, is it useful?

13.8.1 The Qualitative Nature

The qualitative nature refers to the ability to describe the characteristics, or trends, rather than exact values. In this regard, the full burial and uplift history might indeed provide some useful insights.

The incorporation of the crack model commingled with the cementation model is definitely able to capture the observed trend of decreased velocity and increased stress sensitivity upon uplift. Furthermore, the trend of the anisotropy to become reversed upon uplift is also captured when applying the crack model in combination with Hooke's law. This implies that the model can give an indication of qualitatively the effect of burial and uplift compared to a reference area.

13.8.2 The Quantitative Nature

By quantitative nature, the ability of the model to predict numerically a value for the uplift is in question.

In the introductory conceptual example it was claimed that the current methodology of assuming no uplift would underestimate the uplift by 400m. By the end of this thesis, the reader should hopefully have been convinced that this is wholly dependent of the choice of parameters through the entire modelling history.

In the "inverse" case where data is available at all stress levels, parameters that fit the data well can be determined, as seen in figures 12.1 to 12.3. In this scenario, the uplift is however already known, and used to estimate the parameters needed. As has been already addressed, due to differences between the field and the laboratory, it is unlikely that the same set of parameters will be appropriate in a general case.

This means that the forward application of this model to quantitatively establish a value for the uplift is uncertain. This caveat is however not unique for this model, but true for any model using rock physics to quantitatively determine uplift.

Some degree of quantitative determination of the uplift would require plentiful data to calibrate the parameters. This is

where the model runs into another problem, because although vertically travelling P-wave velocities are measured in wells and estimated from seismic data, accurate determination of the radial P-wave velocity and P-wave anisotropy are less available.

This is troublesome for the pragmatic alteration of the granular media models, as these had stress dependent and anisotropic values for the no-slip/slip fractions. Having anisotropic no-slip fractions means that determination of the appropriate relation for the axially propagating P-wave does not necessarily give any information on the radially propagating P-wave.

There does exist a way to compensate for the same effects as the anisotropic, stress dependent values of the no-slip/slip ratio, although it is slightly less intuitive. The δ parameter in the anisotropic Hashin-Shtrikhman (see Parnell and Calvo-Jurado (2015)) describes the shape and distribution (as $\epsilon = \delta$)[3] of the phases that enter into the calculation of the bounds. So far this has been set to 1. Setting it to 1 means that mixing of two isotropic phases should yield an isotropic result, identical to the isotropic Hashin-Shtrikhman bound, as was demonstrated in part I.

By letting $\delta \neq 1$ the friable sand model can be used to alter the observed P-wave anisotropy. This means that the $\delta(= \epsilon)$ parameter is capable of incorporating the possible deviations from the granular media model in the friable sand model.

Figures 13.3 and 13.4 show the axial P-wave velocity and P-wave anisotropy in a scenario where the no-slip/slip ratio is kept constant at 0.4, but the δ parameter in the anisotropic Hashin-Shtrikman formulation is allowed to vary from 0.9 to 1.55 over the course of the loading.

The modelling can be seen to fit the measured data quite well, where the same set of parameters can be used to model both the axial and radial P-wave velocities. This does of course not fix the issue of this being a pragmatic way to account for potentially complex processes occurring in the grain assemblage. It is noted that the axial shear wave velocity is still overpredicted as long as the same fraction if no-slip and slip contacts are used as for the P-wave velocities.

Thus, even though the P-wave anisotropy modelling can be done without the anisotropic no-slip/slip relationships, the solution is less intuitive and still pragmatic.

In the crack model interval, calibrating the model to give a decent fit to the axial P-wave velocity simultaneously provided a decent fit to the radial P-wave velocity, which is the ideal scenario.

If there is sufficient data available regarding stress history, some of the parameters might be inferred in a semi-quantitative nature, but as is apparent, exact uplift determination is difficult.

[3] As confusing as the variable notation used is, this is now the ϵ, δ from the Anisotropic Hashin-Shtrikman paper of Parnell and Calvo-Jurado (2015) and not the anisotropy parameters from Thomsen (1986).

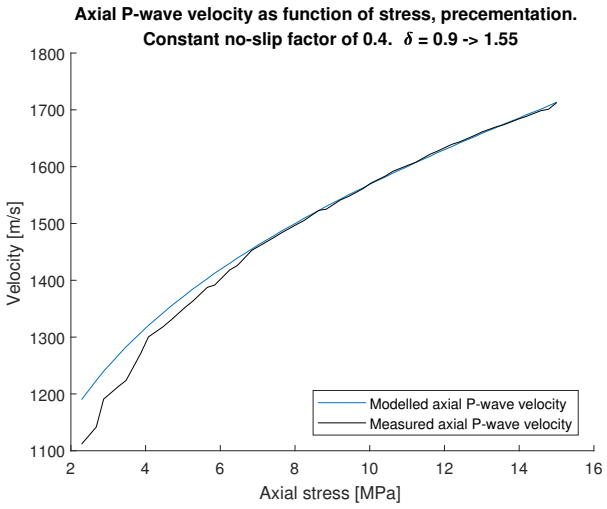

Figure 13.3: Modelled axial P-wave velocity based on the equations derived in part III. The difference between this modelling and the modelling done in part III is that instead of letting the no-slip/slip fraction be anisotropic and stress dependent, the δ parameter in the anisotropic Hashin-Shtrikman formulation is allowed to be stress dependent. The no/slip slip fraction is constant and uniform (i.e., the same for C_{11} and C_{33}).

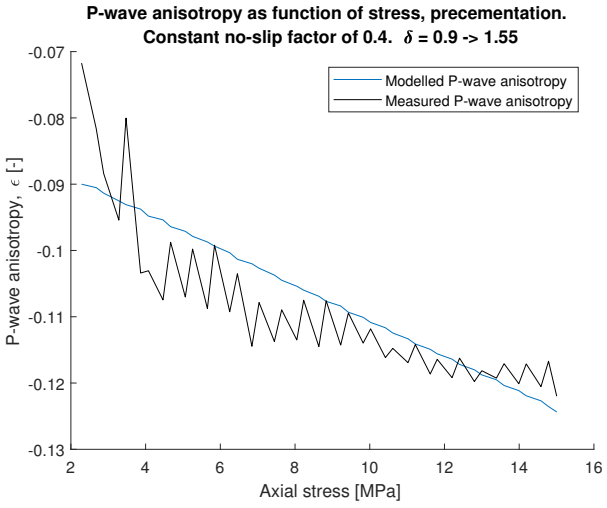

Figure 13.4: Modelled P-wave anisotropy based on the equations derived in part III. The difference between this modelling and the modelling done in part III is that instead of letting the no-slip/slip fraction be anisotropic and stress dependent, the δ parameter in the anisotropic Hashin-Shtrikman formulation is allowed to be stress dependent. The no/slip slip fraction is constant and uniform (i.e., the same for C_{11} and C_{33}).

This also casts a shadow of doubt on all attempts to model uplift from velocity measurements, and is as mentioned not unique to this work. This is because previous modelling attempts also make assumptions regarding the stress history (most commonly that it is isotropic) and the no-slip/slip relationships. An example is that the use of Hertz-Mindlin will imply an isotropic stress state, and unless a reduced shear factor is mentioned, a no-slip fraction of 1. In a sense then, the model in this work is not *less* quantitative than existing diagenetic sandstone models for predicting uplift, whose uplift estimates also depend on the choice of parameters.

The cement volume, if it can be estimated can be used to legitimise the time that a rock has been subjected to time and temperature conditions suitable for cementation. Estimation methods could be point counting in thin section, or a combination of cathodoluminescence data with backscatter electron images (McBride (1989), Oelkers et al. (1996)). It is clear however, that if using the model in Walderhaug (1996) that a cement volume is not unique to one burial history, and thus the velocity development with depth and time is also not unique. What is meant by this is that several burial histories can produce the same volume of cement.

As an example, consider the two burial histories in figures 13.5 and 13.6. Burial history 1 enters the cementation domain and stays there for 36 million years, with a burial rate of $\frac{50m}{m.yr}$, an uplift rate of $100\frac{m}{m.yr}$ and a geothermal gradient of $35\frac{^\circ C}{km}$. In burial history 2, after reaching a depth of 2500m, the rock is static for 66 million years, before being uplifted. The rates of burial and uplift are identical to burial history 1.

The amount of cement produced by the two burial histories are indicated in figure 13.7. The two burial histories produce the same amount of cement over different time-scales.

The subsequent velocities are shown in figure 13.8. The pre-cementation interval is modelled using Hertz-Mindlin (as it is not of immediate interest), with the effect of cement modelled with the patchy cement model. As the velocities are at larger cement volumes primarily a function of the cement volume, the velocities at 2000m are extremely similar, although the burial histories are different.

Other geological factors could, if available, be used to constrain the possible burial history, as discussed in part I. The results in figure 13.8 are simply an illustration of the fact that using cement volume as a legitimisation for a burial history is uncertain. In addition, the final estimated cement volume is as ever dependent on the parameters fed into the model in Walderhaug (1996).

This section was an attempt to justify the usefulness of the model. The quantitative nature of using the modelled velocities, or for that matter P-wave anisotropy is uncertain. Using the slip and no-slip limits as boundaries provides a qualitative illustration of the trends, although these limits are also subject to grain parameters, stress history, burial rate, geothermal gradient

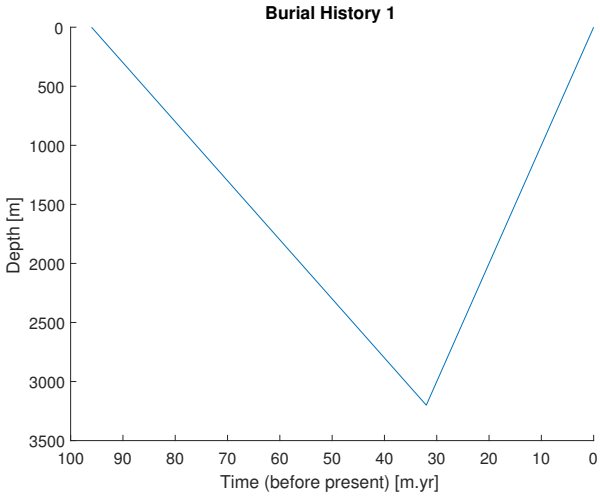

Figure 13.5: The first burial history (Burial History 1) used for comparison of the development of the volume of cement, and subsequently velocity, as function of time and temperature (depth) in figures 13.7 and 13.8.

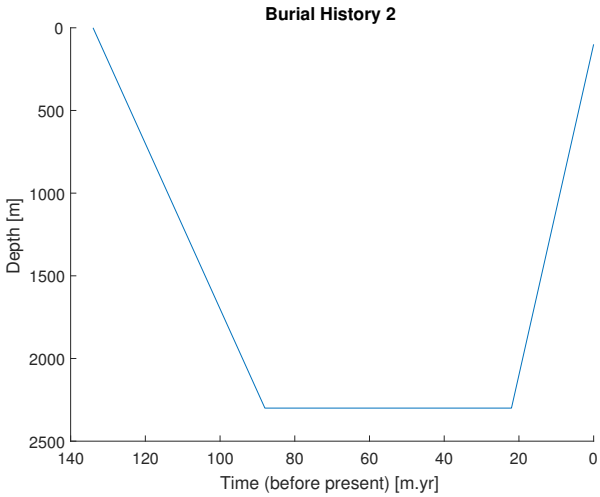

Figure 13.6: The second burial history (Burial History 2) used for comparison of the development of the volume of cement, and subsequently velocity, as function of time and temperature (depth) in figures 13.7 and 13.8.

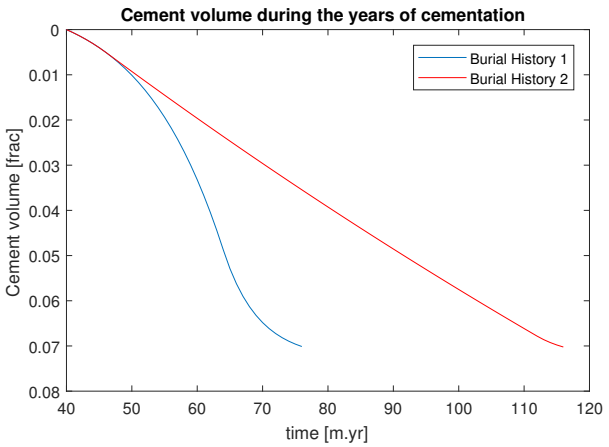

Figure 13.7: Cement volume estimated from the burial histories in figure 13.5 and 13.6. Note how the final cement volume estimated by the two burial histories is identical, although the development with time is vastly different. This is a natural result of the lower temperatures in Burial history 2

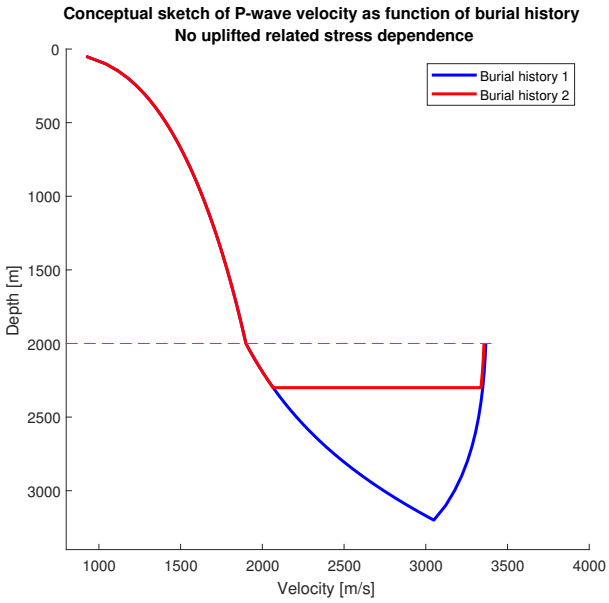

Figure 13.8: Velocities as a function of depth for the two burial histories in figures 13.5 and 13.6. The pre-cementation velocities are estimated using Hertz-Mindlin, and the velocities in the cement domain are modelled using the patchy cement model. No uplift-related velocity changes are added in this particular modelling. Note how the velocities end up at the same velocity after being subjected to two different burial histories. This is because the cement volume is essentially the same. This is a rather extreme comparison, but serves as an example as to how using cement volume to legitimise modelled velocities, in the lack of other constraining geological information, could introduce errors.

etc. A semi-quantitative inference might be made in the event that sufficient data, and other constraining geological factors are available and under conditions where the effects interpreted in the laboratory might be expected to have occurred in the field.

13.9 The Effect of Cement Volume

The calibration of experimental data has been focused around one particular sample, and thusly one cement volume. Similar experiments have however been conducted with variable amounts of cement.

13.9.1 Very Little Cement - “Soft”.

The velocity as function of axial stress for the case of very little cement is shown in figure 13.9. The P-wave anisotropy is shown in figure 13.10. There are a couple of things that stand out.

Firstly, the anisotropy prior to cementation would be expected to be equal, it is not. This is because the radial strain measured in this experiment is only about half that measured in the laboratory data described in part II, leading to lower radial velocities. The lower radial velocities would be predicted by the equations in part III given lower radial strain, but why the radial strain is lower for an apparently identical assemblage for identical loading conditions is unknown. It goes to show that the laboratory procedures are not perfect either.

Secondly, the P-wave anisotropy becomes stronger upon cementation. This is possible even though both velocities increase according to equation (9.26b).

There are two notable deviations from the experimental procedure in part II. The creep period over which the P-wave velocity keeps increasing at max burial, as well as the fact that the unloading is only conducted down to a value of 15MPa axial stress.

The qualitative observations that were made in part II regarding the uplift interval are also observed in the experimental data presented in figures 13.9 and 13.10. Upon unloading, the P-wave velocity shows a greater degree of stress dependence than during burial after cementation, and the P-wave anisotropy shows a distinct move towards less negative values, although it is not reversed in the softer sample. This is an attribute of the fact that the P-wave anisotropy is stronger to begin with, and that the stress is not reduced to the same extent as in the sample in part II.

The stress dependence of the axial P-wave velocity during loading after cementation is greater for the sample with less cement. This is in accordance with the patchy cement model, as the stress-dependent granular media contacts will play a more dominant role in the overall mixture. The difference between the loading after cementation and unloading interval in the sample with less cement is less prominent than for the

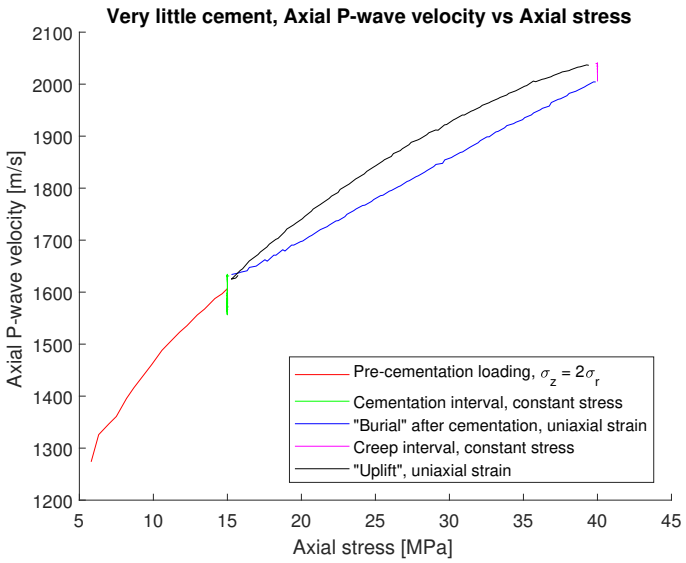

Figure 13.9: Measured P-wave velocity on a similar synthetic sandstone as that described in part II, but with smaller amounts of synthetic quartz cement. The key differences in the experimental procedure are that the sample in this figure is left at 40MPa, which allows for the viewing of the previously described creep effects. Note also how upon unloading, the velocity decrease is more immediate than for the sample in part II, also a likely testament to the fact that the creep has been allowed to occur. The second difference in experimental procedure is that this sample is only unloaded until 15MPa axial stress. In terms of interpretation, there is less cement in this sample, leading to a smaller increase in velocity upon cementation. There is an increased stress dependence upon unloading, as was described for the stiffer sample in part II, but the difference between loading and unloading after cementation is smaller.

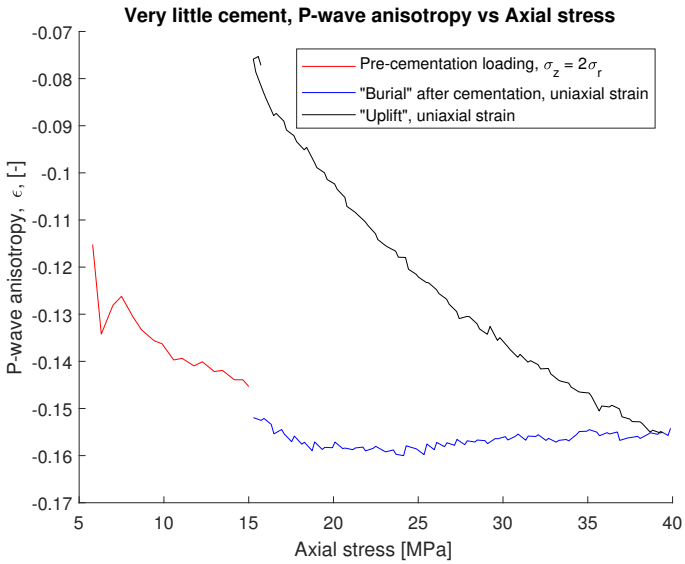

Figure 13.10: Measured P-wave anisotropy on a similar synthetic sandstone as that described in part II, but with smaller amounts of quartz cement. The P-wave anisotropy prior to cementation deviates from that in part II. This seems to be due to a lower observed radial strain. A lower radial strain would according to the granular media theory presented in part III provide a lower radial P-wave velocity. Why the radial strain is lower for the same stress state and similar granular assemblage is not investigated further. Upon cementation the P-wave anisotropy becomes stronger, in that it deviates more from isotropy. Upon unloading, the same trend, with progressively less negative P-wave anisotropy is observed.

sample with more cement. An interesting observation is that the additional decrease during unloading exactly matches the increase during the creep period, such that the velocity is the same at 15MPa before loading, and after simulated uplift.

13.9.2 EPOX-stone - Stiffer

The other end of the spectra are samples that contain more "cement" than that in part II. This sample is however created with epoxy rather than synthetic quartz cement, and so the composition varies in other terms than just the amount of cement. The experimental procedure is no longer identical, which can be seen by loading to 30MPa prior to cementation and subsequent loading to 90MPa. There is also a temperature aspect of the experimental procedure in this sample, but this will not be discussed in any detail.

The axial P-wave velocity and P-wave anisotropy for this sample is shown in figures 13.11 and 13.12. The effect of cementation is to increase the velocity significantly and bring the rock close to isotropy. Upon loading after cementation there is a very small increase in the P-wave velocity, but more importantly, the P-wave anisotropy does not behave as the previous samples, and is seemingly unaffected.

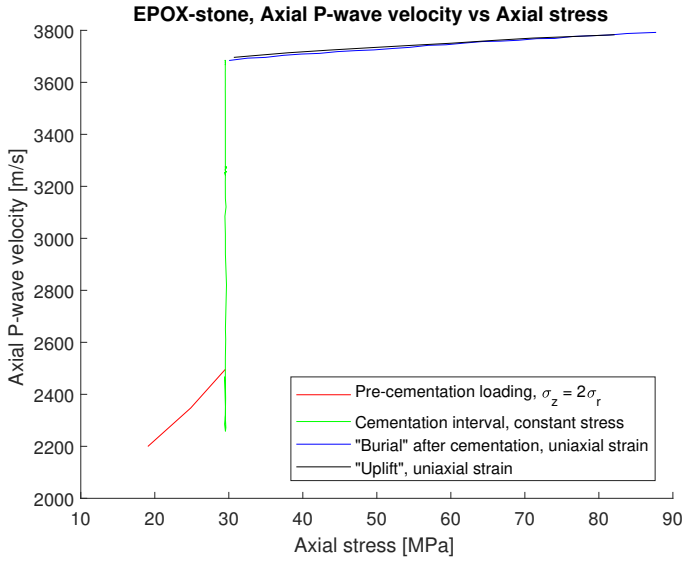

Figure 13.11: Axial P-wave velocity plotted against axial stress for a sample with epoxy which significantly stiffens the sample. Note that the grain assemblage and experimental procedure is not identical to the previous samples. In this sample it can be observed how the stress dependence after cementation is extremely minor, and that upon unloading, the velocities are pretty much identical to that seen whilst loading for a given stress level

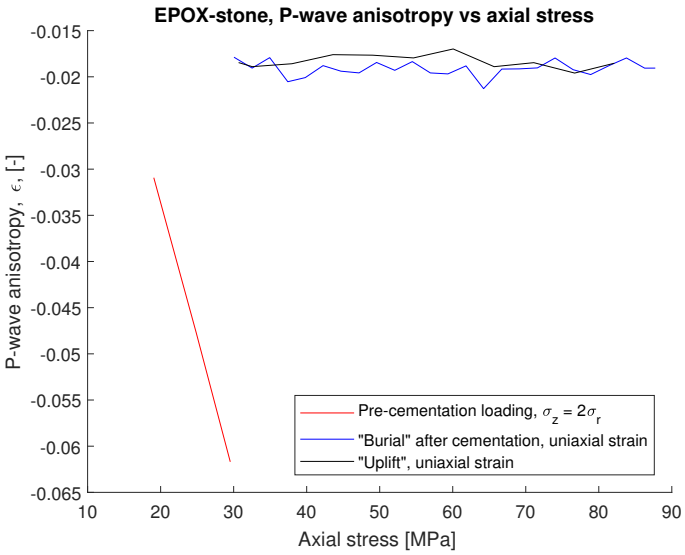

Figure 13.12: P-wave anisotropy plotted against axial stress for a sample with epoxy. Note that the grain assemblage and experimental procedure is not identical to the previous samples. In this sample it can be observed how the anisotropy after cementation approaches isotropy. Furthermore, in contrast to the previous samples, upon unloading the P-wave anisotropy behaves identically as during loading after cementation.

13.9.3 Interpretation of Observations Regarding Cement Volume

The implementation of the crack model in Torset (2017) was as mentioned done on the basis of the increased stress dependence being caused by broken and failing cement bonds acting as microcracks. In the case of a sample with a lot of cement/epoxy, an argument could be that the breaking of a given number of cement bonds has a smaller effect on the rock as a whole, thus muting the effects of uplift.

The stress unloading in the simulated uplift of the EPOX-stone is over 50 MPa, but the extensional strain is only 2 mStrain (see figure C.8 in Appendix C). The sample in part II showed an extension of 8 mStrain over an unloading of about 30MPa. This means that extensional tension on grain contacts is smaller in the stiffest sample, such that the epoxy might not undergo brittle deformation. During loading of the epoxy sample, there is 4 mStrain of compaction, significantly smaller than the other samples. This means that less deformation happened during loading, reducing the chance of reactivation of microcracks during uplift.

In the sample with the least cement, there is 5mStrain of extensional strain, but direct comparison is difficult due to the creep period. Although microcrack formation might be happening in this sample as well, it was observed that the increase in stress dependence during uplift was less prominent. This might be a pointer to cement bonds breaking being a factor in the microcrack formation, as less cement means that the potential for brittle deformation to increase the stress dependence is smaller.

The results of variable cement volume indicate that the effects seen during uplift in part II might be limited by extensive amounts of cement. In the epoxy case, a methodology of assuming that the velocity and porosity remains constant after cementation has ceased (Avseth et al. (2014b), Avseth and Lehocki (2016)) could thus prove quite accurate.

13.10 Unloading After Cementation - Simulated Coring

The stress paths considered so far involve loading after cementation prior to unloading. In a different set of stress paths, coring was simulated by unloading right after cementation. The "coring" stress path (B2) is given in figure 13.13. Note that the unloading in this scenario is not limited to uniaxial strain. Figure 13.14 shows the axial P-wave development as a function of axial stress for this stress path[4]. The orange curve represents the "coring" interval and shows a decrease in velocity from the onset of unloading[5]. The decrease in velocity in this sample suggests that the assumption of no change during unloading would be inadequate also in the scenario where the cement is not loaded after cementation prior to unloading.

The P-wave anisotropy during coring is shown in figure 13.15, together with the anisotropy in the relevant stress interval from the sample discussed in part II. The trends are observed to be quite similar. For the "cored" sample the development in P-wave anisotropy correspond well with a potential stress dependence in the sample. As the axial stress is brought towards the radial stress, the anisotropy decreases, as the axial P-wave velocity approaches the radial P-wave velocity.
Figure 13.16 compares the stress dependence during loading after cementation, unloading following loading after cementation and simulated coring. The "stress dependence" is quantified through absolute change in axial P-wave velocity per 10MPa. This is plotted against the axial P-wave velocity after cementation, which is an indicator of the amount of cement, and therefore the stiffness of the cemented rocks. The small difference in stress dependence between the loading and unloading of the samples with little cement and the very stiff sample discussed earlier is observed. Furthermore it is observed that the samples subjected to simulated coring show an even greater degree of stress dependence ("uplift after cementation").

[4] In appendix C, the effects of reloading and unloading after "coring" are also included.

[5] Velocity data is not available below 8MPa.

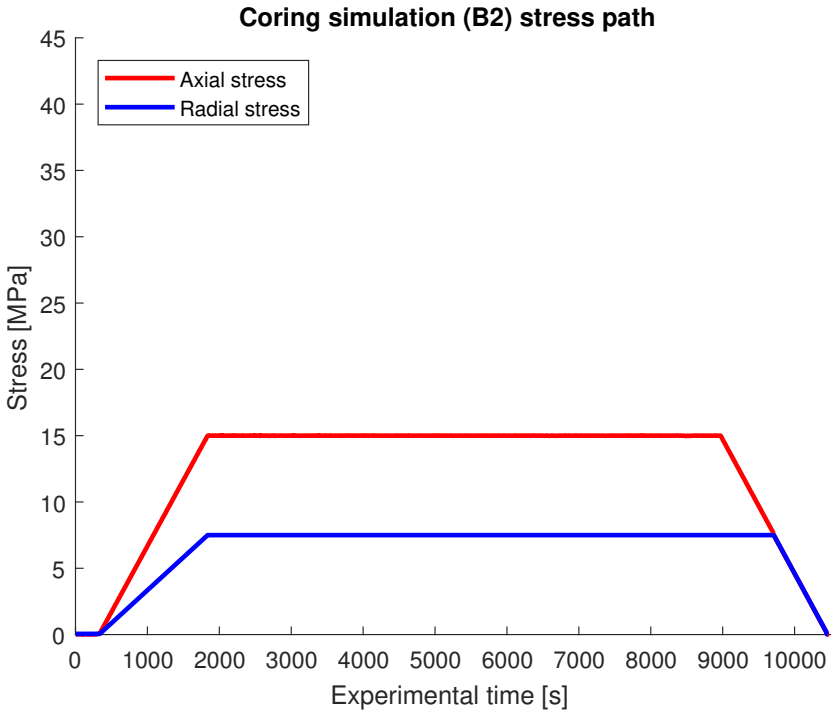

Figure 13.13: Stress path for the stress history referred to as "B2" up to the end of the simulated coring. During loading prior to cementation the stress is identical to that in the sample in part II ($\sigma_z = 2\sigma_r$). The difference is that instead of further loading the sample is brought back to 0 stress. First, the axial stress is reduced whilst the radial stress is kept constant. When the axial stress has reached the level of the radial stress they are brought down equally.

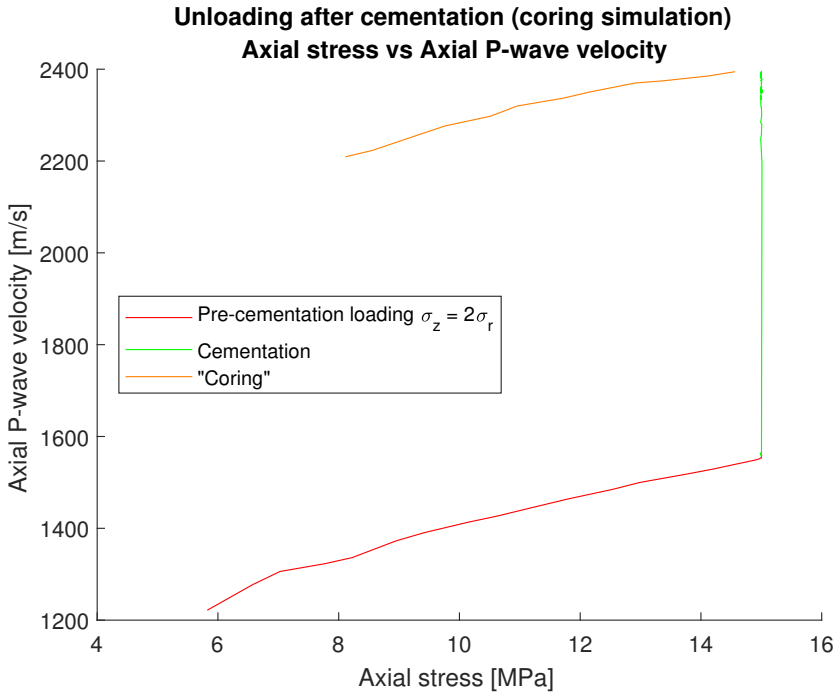

Figure 13.14: Axial P-wave velocity during pre-cementation loading, cementation and simulated coring for the sample subjected to stress history "B2". Upon unloading the velocity decreases, and this decrease is larger at lower stress level indicating a degree of increased stress dependence during unloading. The axial P-wave velocity data is limited to unloading down to 8MPa of axial stress.

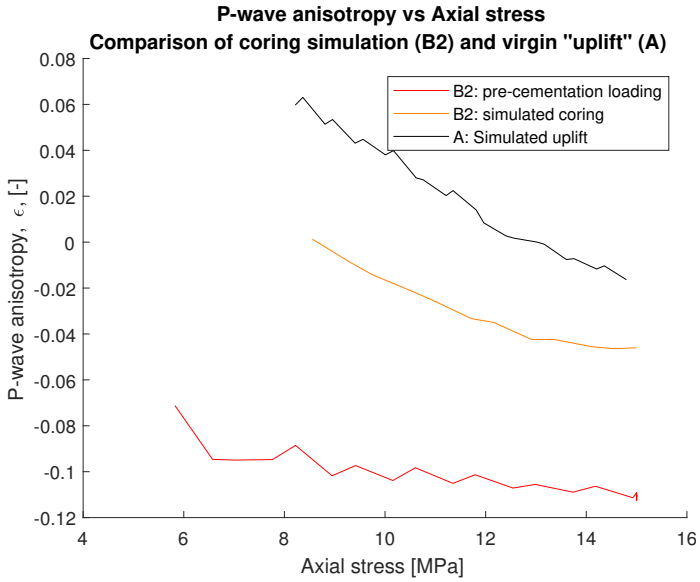

Figure 13.15: P-wave anisotropy for the sample subjected to simulated coring according to the "B2" stress path. For comparison, the P-wave anisotropy of the relevant stress interval from the sample form part II is also included. During the unloading where velocity data is available, the axial stress is decreased whilst the radial stress is kept constant. During simulated coring the strain is not limited to be uniaxial. The observed results make sense in regard to stress sensitivity. As the axial stress approaches the radial stress, the axial P-wave velocity approaches the radial P-wave velocity, which acts to bring the rock towards isotropy.

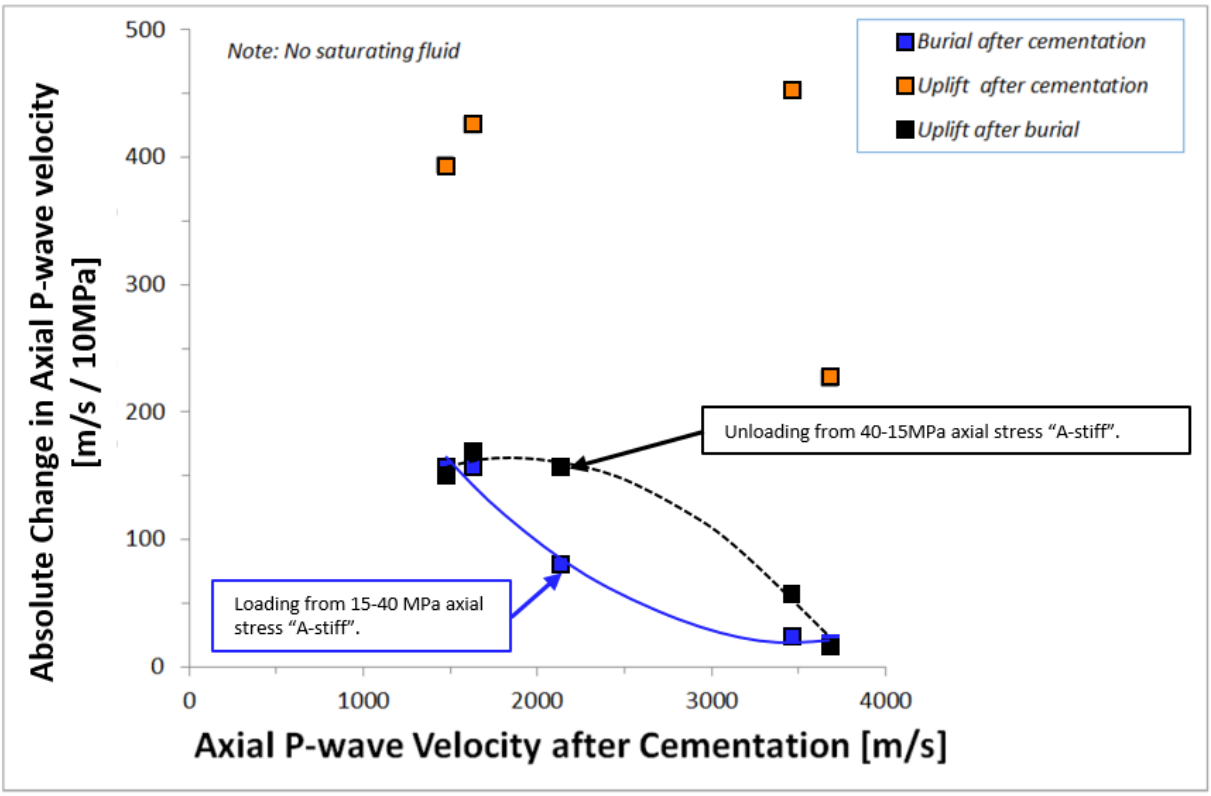

Figure 13.16: Illustration of the stress sensitivity for samples with varying amounts of cement. The measure of stress sensitivity is a relatively simplistic methodology of normalising the change in P-wave velocity to 10 MPa. "Burial after cementation" refers to the interval of loading after cementation present in the "A" paths. "Uplift after burial" refers to the simulated uplift in the "A" paths, and "uplift after cementation" are samples subjected to simulated coring. The cement volume is represented by the Axial P-wave velocity after cementation. Samples with more cement have higher velocities after cementation. The effect of small differences between the stress sensitivity of the loading and unloading after cementation of the samples with small amounts of cement and the EPOX-stone are observed at the end of the black and blue curves. The arrows point to the values obtained when the normalisation procedure is applied to the sample from part II ("A-stiff"). Modified from Torset et al. (2018).

13.11 Testing the Crack Model on the "Soft" Sample

In part V the modified crack model was implemented on the "main" sample that has been used throughout this work. The fact that the soft sample has been left to creep means that implementation of the crack model might yield decent results without requiring any form of compensation, and thus testing the modified crack model[6] on this sample as well is of interest.

Figure 13.17 shows the modelled P-wave velocities, and figure 13.18 shows the modelled P-wave anisotropy. In this modelling, the starting stiffnesses are taken based on the estimated density and measured velocity. The grain parameters are identical to those used previously. The crack model inputs are $n = 0.04$, $\beta = 1.5$, $\eta = 100$, and these are obtained based on observation, and a Levenberg-Marquardt fit similar to that used in part II. The stress dependence on both the P-wave velocities (and subsequently the P-wave anisotropy) can now be modelled with the iterative combination of Hooke's law and the crack model without any form of creep compensation. This is an encouraging result for the possibility of using the crack model to model the effects of uplift.

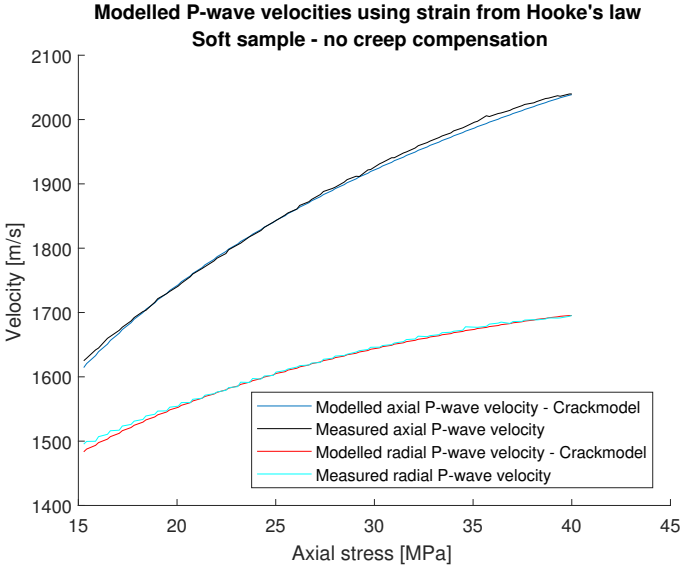

Figure 13.17: Modelled P-wave velocities using the crack model together with Hooke's law for the sample denoted "soft". Starting stiffnesses were based on measured velocities and estimated density. Note how the model is able to fit the data well without the need for creep compensation, which was required for the sample denoted "stiff" (see part V).

13.12 The Effect of Fluids

Throughout this work, all velocities considered have been dry velocities, that is, there are assumed to be no stiffness contributions from fluids. A brief discussion on the concept of

[6] I.e., using strains from Hooke's law instead of measured experimental strain.

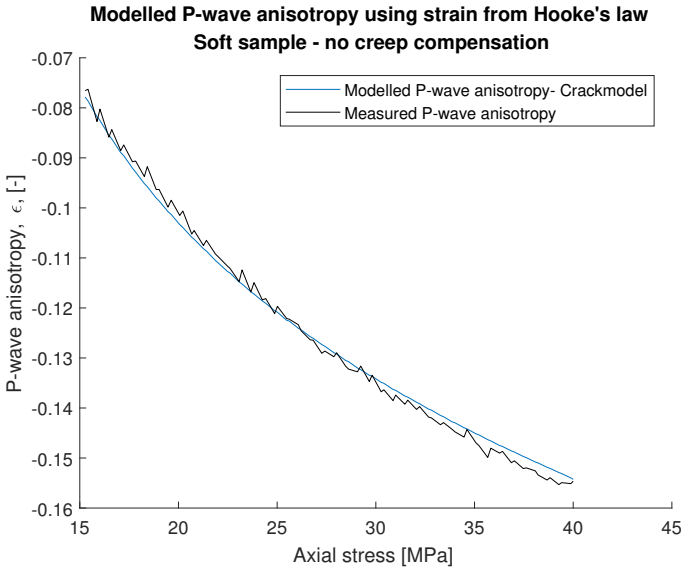

Figure 13.18: Modelled P-wave anisotropy using the crack model together with Hooke's law for the sample denoted "soft". Starting stiffnesses were based on measured velocities and estimated density. Note how the model is able to fit the data well without the need for creep compensation, which was required for the sample denoted "stiff" (see part V).

poroelasticity is given in appendix B.

Gassmann (1951) derived equations for poroelasticity in anisotropic media. The problem with these equations (see Appendix B) is however that all moduli are needed. The experimental data carry no information regarding C_{66} or C_{13} and so it is not possible to investigate the degree to which these are satisfactorily modelled.

In Torset (2017) experimental data from Lo et al. (1986) was used to investigate the error introduced by using the isotropic Biot-Gassmann fluid substitution and found that there was less than 2% error for the axial P-wave velocity and around 2.5% error for the radial P-wave velocity. The isotropic fluid substitution in both cases underpredicted the velocity. Based on this, and the fact that anisotropy in the sample from part II is relatively weak, it is assumed that the error imposed by using the isotropic Gassmann substitution would be small (Torset et al., 2018). In a general case, this would of course depend on the rock.

The effect of introducing the pore fluid through the isotropic Gassmann substitution in the measured data for the axial P-wave velocity and P-wave anisotropy is shown in figure 13.19 and 13.20 respectively.

The fluid, assumed to be water with a density of $1000\frac{kg}{m^3}$ and bulk modulus of $2.2GPa$ can be shown to increase the axial P-wave velocity. The extent to which the anisotropy is affected by the simulated uplift is also reduced, but the reversal of the P-wave anisotropy is still present.

The presence of a fluid has other effects than just altering the velocities. The pressure of the pore fluid is part of the definition

of effective stress, and so knowledge of overpressured zones, both in space and time, is part of an accurate stress history. Furthermore, the presence of the fluid might facilitate chemical reactions in more unstable mineral assemblages than that used in the laboratory. This is also dependent on the composition of the fluid (Carter et al. (1990), Worden and Burley (2003)).

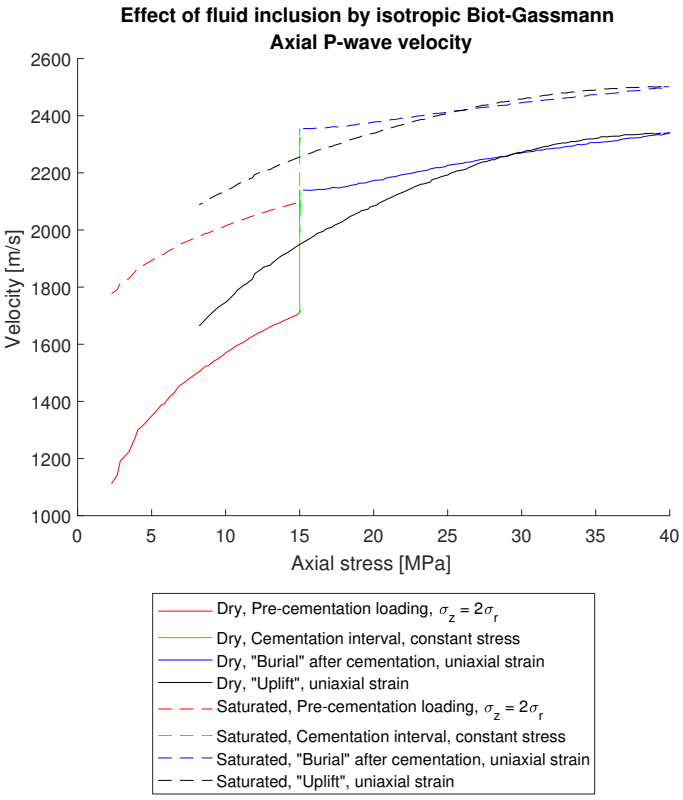

Figure 13.19: Axial P-wave velocity obtained by implementing the isotropic Biot-Gassmann fluid substitution on the measured experimental data. The fluid was taken to have density of 1000 kg/m^3 with a bulk modulus of $2.2GPa$. The velocities can be seen to increase, with the effect of the fluid inclusion being most significant prior to cementation. The effect of increased stress dependence during simulated uplift is still visible, but somewhat reduced.

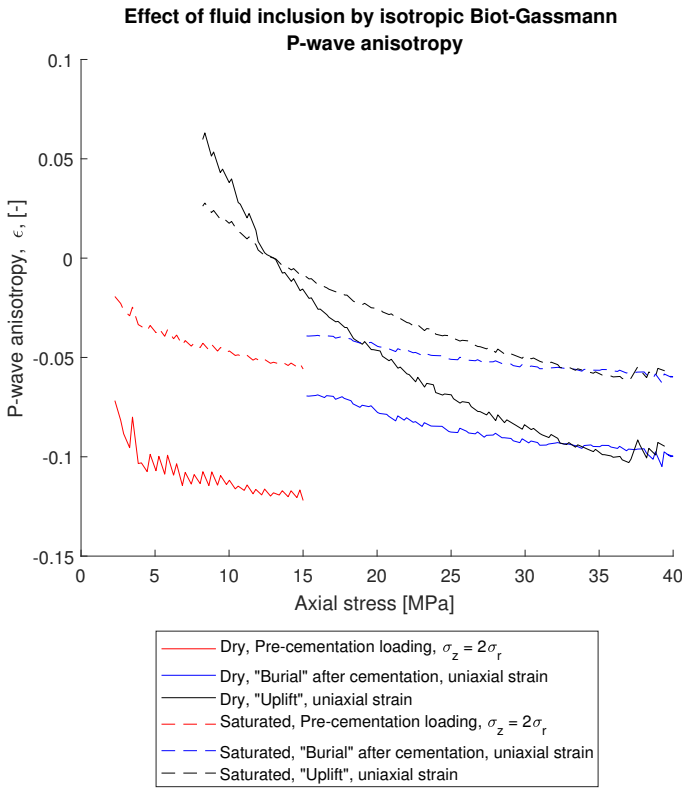

Figure 13.20: P-wave anisotropy obtained by implementing the isotropic Biot-Gassmann fluid substitution on the measured experimental data. The fluid was taken to have density of 1000 kg/m^3 with a bulk modulus of $2.2GPa$. The P-wave anisotropy can be seen to move closer to isotropy as the velocities are increased. The effect of anisotropy reversal during simulated uplift is still observed, but the the absolute value of the change in anisotropy over the unloading interval is reduced.

Chapter 14

Conclusion and Suggestions for Future Work

14.1 Conclusion

The aim of this work has been to develop a rock physics model that predicts the axial and radial P-wave velocities (and subsequently P-wave anisotropy) as function of burial history, in order to incorporate observations made in the laboratory of a synthetic sandstone subjected to loading and unloading. By combining this rock physics model with a model for cement estimation, an updated diagenetic sandstone model for characterising the effects of uplift on the properties of sandstones has been created. The necessity for such a modification came from the observation in the laboratory that simulated uplift created a significant increase in stress dependence on the synthetic sandstone. This observation casted doubt on the assumption often implemented in the modelling of sandstones, that once cementation ceases, the properties of the rock are preserved through uplift. Whilst this assumption proved reasonable for the porosity, it was clearly inadequate for the velocity of the synthetic sandstone during simulated uplift under uniaxial strain.

Another observation that the model attempts to recreate was the reversal of the P-wave anisotropy that was seen in the experimental data. If processes in the laboratory are taken as representative for that seen in the field, the P-wave anisotropy provides an interesting potential attribute for uplift characterisation. Being able to model how it develops through the simulated burial history was therefore needed.

The modelling of the experimental data was done in three "domains"

- Loading prior to cementation
- Loading after cementation
- Unloading

Loading prior to cementation was done under the stress condition $\sigma_z = 2\sigma_r$, and so a granular media model describing a triaxial strain state was needed. In addition to this, it was of interest to incorporate the idea of binary mixing of so-called rough and smooth contacts. To accomplish this, the general expressions given in Walton (1987) were solved for a scenario of triaxial strain, where the horizontal strains are equal, taken as the radial strain. The notation and derivation strategy was adopted from Bandyopadhyay (2009), but the equations derived in this work were however not limited to a small strain anisotropy. This means that they are valid over a wider range of strain states, and reduce to the explicit limits presented in Walton (1987) at uniaxial compaction.

During further loading after cementation, the synthetic sandstone retained both stress dependence and anisotropy. To model both of these effects, an anisotropic modification to the patchy cement model presented in Avseth et al. (2016) was utilised. It was observed that the porosity loss during compaction after cementation caused the model to overpredict the stress sensitivity, due to the last Hashin-Shtrikman iteration in the patchy cement model. The representability of the experimental procedure in relation to the field case in this interval was brought into question, as the cementation in the field will likely be more continuous over the loading history. The processes seen in the laboratory in this interval might therefore not be exactly analogous of those that would be observed in real rocks. The fact that the anisotropic patchy cement model is able to fit the data reasonably well is therefore an observation that should be treated with care.

Uplift was modelled using the crack model from Fjær (2006). The implementational strategy was modified slightly from Fjær (2006), because instead of using the observed strain, the strain was estimated using Hooke's law for small stress variations, and this change in strain together with the change in stress is used to update the stiffness. This was run in an iterative loop until the end of the simulated uplift. After pragmatically compensating for observed creep in the experimental data, the crack model was able to recreate the P-wave anisotropy trends observed during the simulated uplift for the sample presented in part II[1]. For a sample that had been left to creep, the crack model was able to recreate the velocities well, without the requirement of creep compensation.
The experimental data were limited to uniaxial strain during uplift. Although the cementation model and crack model *in theory* are able to model strain states that are not uniaxial, some problems regarding the crack model have been identified

[1] The sample that formed the basis for the model development.

in relation to the value of Poisson's ratio. Furthermore, implementation of a non-uniaxial strain required estimation of C_{12} and C_{13}. The experimental data contained no information on these parameters, and so the quality of the modelling of these parameters down to the onset of uplift has not been investigated. The results in this work are therefore limited to providing adequate modelling of P-wave velocities under uniaxial strain.

Both the effect of cement volume and the presence of fluids in the pore space have an effect of the observed results. Based on experimental results from a very stiff sample, it appears as if the increase in stress dependence could be muted by a significant amount of cement. The effect of fluids were modelled using the isotropic Biot-Gassmann equation and the results were a less prominent increase in stress dependence, and a smaller absolute change in the P-wave anisotropy during simulated uplift. In other words, the trends were still there, but weaker.

The quantitative nature of the results in terms of uplift estimation is uncertain. The uplift estimate is dependent on the parameters entered into the model, and is also a victim of the intrinsic assumptions in the models that are altered and sown together. In the presence of abundant data however, the limits of no-slip and slip might provide a qualitative to semi-quantitative illustration of how the velocities and P-wave anisotropy has developed through time.

14.2 Suggestions for Future Work

The rock physics model developed in this work has only been thoroughly tested in its entirety on one burial history of one specific synthetic sandstone. Future work should expand this to include a more diverse selection of lithologies, stress histories and cement volumes. Furthermore, the link to seismic and well data needs to be established. Several factors that could create deviations between that seen in the laboratory and in the field were described in part VI.

In addition to expanding the experimental result "catalogue" for the burial history as a whole for synthetic sandstones, work should also be done to test the underlying modelling intervals i.e., loading prior to cementation, the effects of cementation and microcrack formation during uplift. True for all of these intervals is that measurements that would enable the determination of C_{12} and C_{13} would yield further insight into the capabilities of the model.

For the granular media, a set of experiments with spherical glass beads could be conducted, which is more in line with the assumptions in Walton (1987). Such experiments do exist for isotropic loading, but in this work, equations for a particular triaxial strain state have been derived. Additional experiments to investigate how these equations compare to experimental results for such a loading state would provide further insight into the modelling procedure as a whole. These experiments would not only provide useful information for the work in relation to uplift, but for work with loading of granular media as a whole.

The cementation interval has been pointed at a potential source of significant variability in the processes occurring in the laboratory in comparison to the field scenario. This arises from the methodology of cementing at constant stress prior to subsequent loading, which is not likely to provide a realistic recreation of the sequence of events in the field. Experiments with incremental cementation over the loading interval might provide better insight into whether the anisotropic patchy cement model is an adequate solution to preserve stress dependence and anisotropy. Ideally, the cement volume should be increased according to a predicted stress-volume relationship from for example Walderhaug (1996). The volume is related in the field to time and temperature, but through the burial history, these factors can be related to the stress. By such a methodology, the simulated uplift can then be initiated at variable stress levels, corresponding to different volumes of cement. This would provide further insight into the comments regarding the possibility of the increased stress dependence being effectively muted by a sufficient amount of cement. Exact control of the cement volume in the laboratory in relation to stress is likely to be a difficult task, but a wide distribution of cement volumes and stress levels at the onset of simulated uplift should be achievable.

The crack model from Fjær (2006) proved promising in modelling the effects of the simulated uplift in the experimental data. This observation is however limited to implementation on two synthetic sandstones, under uniaxial compaction. The problems of extending the Hooke's law iteration methodology to non-uniaxial strain are not reiterated, but designing experiments to investigate the applicability of the crack model under more general strain states would be fruitful. This would yield information into the weakness of the crack model relating to the Poisson's ratio, and also provide insight into how dependent the observations are on the strain state during simulated uplift. In other words, how limited are the observations in this work by restriction of uniaxial strain during the simulated uplift?

Creating thin sections after the simulated uplift might also further the understanding of the processes happening, as the interpretation of the formation of microcracks can be investigated. Furthermore, the nature of the origin of these microcracks can be established (i.e., is the interpretation of broken cement bonds valid?). The problem of this would be that it is hard to characterise at which stress levels deformation occurred, but it would serve as an analogy to rocks uplifted to the surface in terms of stress level.

Future work should therefore focus on both testing the validity of the rock physics model in the laboratory, and investigating the representativeness of observations in the laboratory to observations made in the field. This would ascertain the applicability (or lack thereof) of the model presented in this thesis.

Bibliography

Abid, I. A., Hesse, R., Harper, J. D., 2004. Variations in mixed-layer illite/smectite diagenesis in the rift and post-rift sediments of the jeanne d'arc basin, grand banks offshore newfoundland, canada. Canadian Journal of Earth Sciences 41 (4), 401–429.

Adams, R. A., Essex, C., 2009. Calculus: A Complete Course, 7th Edition. Pearson.

Allen, P. A., Allen, J. R., 2013. Basin analysis: Principles and application to petroleum play assessment. John Wiley & Sons.

Almon, W. R., Davies, D. K., 1981. Formation damage and the crystal chemistry of clays. Clays and the Resource Geologist. Mineralogical Association of Canada, Short Course Handbook 7, 81–103.

Avseth, P., Johansen, T. A., Bakhorji, A., Mustafa, H. M., 2014a. Rock-physics modeling guided by depositional and burial history in low-to-intermediate-porosity sandstones. Geophysics 79 (2), D115–D121.

Avseth, P., Lehocki, I., 2016. Combining burial history and rock-physics modeling to constrain avo analysis during exploration. The Leading Edge 35 (6), 528–534.

Avseth, P., Mukerji, T., Mavko, G., 2010. Quantitative seismic interpretation: Applying rock physics tools to reduce interpretation risk. Cambridge university press.

Avseth, P., Skjei, N., Mavko, G., 2016. Rock-physics modeling of stress sensitivity and 4d time shifts in patchy cemented sandstonesapplication to the visund field, north sea. The Leading Edge 35 (10), 868–878.

Avseth, P., Veggeland, T., Lehocki, I., 2014b. Combined burial history and rock physics modeling of quartz-rich sandstones–norwegian shelf demonstrations. In: SEG Technical Program Expanded Abstracts 2014. Society of Exploration Geophysicists, pp. 2809–2813.

Bachrach, R., Avseth, P., 2008. Rock physics modeling of unconsolidated sands: Accounting for nonuniform contacts and heterogeneous stress fields in the effective media approximation with applications to hydrocarbon exploration. Geophysics 73 (6), E197–E209.

Bandyopadhyay, K., 2009. Seismic anisotropy: Geological causes and its implications to reservoir geophysics. Stanford University.

Berryman, J. G., 1995. Mixture theories for rock properties. Rock physics & phase relations: A handbook of physical constants, 205–228.

Biot, M. A., 1962. Mechanics of deformation and acoustic propagation in porous media. Journal of applied physics 33 (4), 1482–1498.

Bjørkum, P. A., 1996. How important is pressure in causing dissolution of quartz in sandstones? Journal of Sedimentary Research 66 (1).

Bjørkum, P. A., Oelkers, E. H., Nadeau, P. H., Walderhaug, O., Murphy, W. M., 1998. Porosity prediction in quartzose sandstones as a function of time, temperature, depth, stylolite frequency, and hydrocarbon saturation. AAPG bulletin 82 (4), 637–648.

Bjørlykke, K., 2010. Introduction to petroleum geology. In: Petroleum Geoscience. Springer, pp. 1–26.

Bjørlykke, K., Egeberg, P., 1993. Quartz cementation in sedimentary basins. AAPG bulletin 77 (9), 1538–1548.

Bjørlykke, K., Høeg, K., Mondol, N. H., 2015. Introduction to geomechanics: stress and strain in sedimentary basins. In: Petroleum Geoscience. Springer, pp. 301–318.

Bjørlykke, K., Jahren, J., 2010. Sandstones and sandstone reservoirs. In: Petroleum Geoscience. Springer, pp. 113–140.

Boggs Jr, S., 2006. Sedimentology and stratigraphy. Pearson Education.

Box, G. E., 1979. Robustness in the strategy of scientific model building. Robustness in statistics 1, 201–236.

Bredesen, K., 2017. On integration of rock physics in quantitative seismic interpretation.

Cardott, B. J., 2012. Introduction to vitrinite reflectance as a thermal maturity indicator. In: Adapted from an Oral Presentation at Tulsa Geological Society Luncheon, May 8, 2012. American Association of Petroleum Geologists Search and Discovery.

Carter, N., Kronenberg, A., Ross, J., Wiltschko, D., 1990. Control of fluids on deformation of rocks. Geological Society, London, Special Publications 54 (1), 1–13.

Cheng, A. H.-D., Detournay, E., 2014. Fundamentals of poroelasticity. Analysis and Design Methods: Comprehensive Rock Engineering: Principles, Practice and Projects 2, 113.

Ciz, R., Shapiro, S. A., 2008. Stress-dependent anisotropy in transversely isotropic rocks: Comparison between theory and laboratory experiment on shale. Geophysics 74 (1), D7–D12.

Digby, P., 1981. The effective elastic moduli of porous granular rocks. Journal of Applied Mechanics 48 (4), 803–808.

Dillen, M. W., Cruts, H. M., Groenenboom, J., Fokkema, J. T., Duijndam, A. J., 1999. Ultrasonic velocity and shear-wave splitting behavior of a colton sandstone under a changing triaxial stress. Geophysics 64 (5), 1603–1607.

Duffaut, K., 2011. Stress sensitivity of elastic wave velocities in granular media.

Duffaut, K., Landrø, M., Sollie, R., 2010. Using mindlin theory to model friction-dependent shear modulus in granular media. Geophysics 75 (3), E143–E152.

Dvorkin, J., Berryman, J., Nur, A., 1999. Elastic moduli of cemented sphere packs. Mechanics of materials 31 (7), 461–469.

Dvorkin, J., Gutierrez, M. A., et al., 2002. Grain sorting, porosity, and elasticity. Petrophysics 43 (03).

Dvorkin, J., Mavko, G., Nur, A., 1991. The effect of cementation on the elastic properties of granular material. Mechanics of Materials 12 (3-4), 207–217.

Dvorkin, J., Nur, A., 1996. Elasticity of high-porosity sandstones: Theory for two north sea data sets. Geophysics 61 (5), 1363–1370.

Dvorkin, J., Nur, A., Yin, H., 1994. Effective properties of cemented granular materials. Mechanics of materials 18 (4), 351–366.

England, P., Molnar, P., 1990. Surface uplift, uplift of rocks, and exhumation of rocks. Geology 18 (12), 1173–1177.

Eslinger, E., Pevear, D. R., 1988. Clay minerals for petroleum geologists and engineers. Society of Economic Paleontologists and Mineralogis ts.

Fjær, E., 2006. Modeling the stress dependence of elastic wave velocities in soft rocks. In: Golden Rocks 2006, The 41st US Symposium on Rock Mechanics (USRMS). American Rock Mechanics Association.

Fjær, E., Holt, R., Nes, O., Stenebraten, J., et al., 2011. The transition from elastic to non-elastic behavior. In: 45th US Rock Mechanics/Geomechanics Symposium. American Rock Mechanics Association.

Fjær, E., Holt, R. M., Raaen, A., Risnes, R., Horsrud, P., 2008. Petroleum related rock mechanics. Vol. 53. Elsevier.

Fjær, E., Stroisz, A., Holt, R., et al., 2015. Static versus dynamic moduli: Another piece in the puzzle. In: 49th US Rock Mechanics/Geomechanics Symposium. American Rock Mechanics Association.

García, X., Medina, E. A., 2006. Hysteresis effects studied by numerical simulations: Cyclic loading-unloading of a realistic sand model. Geophysics 71 (2), F13–F20.

Gassmann, F., 1951. Elasticity of porous media. Vierteljahrsschrder Naturforschenden Gesselschaft 96, 1–23.

Gavin, H., 2011. The levenberg-marquardt method for nonlinear least squares curve-fitting problems. Department of Civil and Environmental Engineering, Duke University, 1–15.

Gudmundsson, A., 2011. Rock fractures in geological processes. Cambridge University Press.

Holt, R., Brignoli, M., Kenter, C., 2000. Core quality: quantification of coring-induced rock alteration. International Journal of Rock Mechanics and Mining Sciences 37 (6), 889–907.

Holt, R., Furre, A.-K., Horsrud, P., 1997. Stress dependent wave velocities in sedimentary rock cores: Why and why not? International Journal of Rock Mechanics and Mining Sciences 34 (3-4), 128–e1.

Holt, R., Kenter, C., Verboom, B., Doornhof, D., 2004. Influence of stress history on in situ and core compaction. In: Numerical Modeling in Micromechanics via Particle Methods-2004: Proceedings of the 2nd International PFC Symposium, Kyoto, Japan, 28-29 October 2004. CRC Press, p. 391.

Holt, R., Larsen, I., Stenebrten, F., 2013. Core damage effects on compaction of soft sandstone, sintef report (confidential).

Holt, R., Li, L., Stenebråten, J., 2007. Compaction behavior of unbonded granular media: Discrete particle vs. experimental vs. analytical modelling. In: Proceedings of the First Canada-US Rock Mechanics Symposium. pp. 393–401.

Holt, R., Stenebråten, J., Brignoli, M., et al., 2014. Effects of cementation on in situ and core compaction of soft sandstone. In: 48th US Rock Mechanics/Geomechanics Symposium. American Rock Mechanics Association.

Japsen, P., Bidstrup, T., 1999. Quantification of late cenozoic erosion in denmark based on sonic data and basin modelling. Bulletin of the Geological Society of Denmark 46, 79–99.

Jenkins, J., Johnson, D., La Ragione, L., Makse, H., 2005. Fluctuations and the effective moduli of an isotropic, random aggregate of identical, frictionless spheres. Journal of the Mechanics and Physics of Solids 53 (1), 197–225.

Johnson, D., Schwartz, L., Elata, D., Berryman, J., Hornby, B., Norris, A., 1998. Linear and nonlinear elasticity of granular media: Stress-induced anisotropy of a random sphere pack. Journal of Applied Mechanics 65 (2), 380–388.

Kiesel, R., van Oene, H., 1982. Dehydrated sodium silicate bound core sand for aluminum casting. ACS Publications.

Kreyszig, E., 2010. Advanced engineering mathematics. John Wiley & Sons.

Lander, R. H., Walderhaug, O., 1999. Predicting porosity through simulating sandstone compaction and quartz cementation. AAPG bulletin 83 (3), 433–449.

Lo, T.-w., Coyner, K. B., Toksöz, M. N., 1986. Experimental determination of elastic anisotropy of berea sandstone, chicopee shale, and chelmsford granite. Geophysics 51 (1), 164–171.

Majmudar, T. S., Behringer, R. P., 2005. Contact force measurements and stress-induced anisotropy in granular materials. Nature 435 (7045), 1079.

Manegold, E., von Engelhardt, W., 1933. Über kapillarsysteme, xii (2). die berechnung des stoffgehaltes homogener gerüststrukturen. Kolloid-Zeitschrift 62 (3), 285–294.

Marcussen, Ø., Thyberg, B. I., Peltonen, C., Jahren, J., Bjørlykke, K., Faleide, J. I., 2009. Physical properties of cenozoic mudstones from the northern north sea: Impact of clay mineralogy on compaction trends. AAPG Bulletin 93 (1), 127–150.

Mavko, G., Mukerji, T., Dvorkin, J., 2009. The rock physics handbook: Tools for seismic analysis of porous media. Cambridge university press.

McBride, E. F., 1989. Quartz cement in sandstones: a review. Earth-Science Reviews 26 (1-3), 69–112.

Mindlin, R., 1949. Compliance of elastic bodies in contact. J. Appl. Mech. Trans. ASME 16, 259–268.

Molnar, P., England, P., 1990. Late cenozoic uplift of mountain ranges and global climate change: chicken or egg? Nature 346 (6279), 29–34.

Murphy, W. F., 1982. Effects of microstructure and pore fluids on the acoustic properties of granular sedimentary materials. Ph. D. dissertation, Stanford University.

Norris, A., Johnson, D., 1997. Nonlinear elasticity of granular media. Journal of Applied Mechanics 64 (1), 39–49.

Oelkers, E. H., Bjørkum, P., Murphy, W. M., 1996. A petrographic and computational investigation of quartz cementation and porosity reduction in north sea sandstones. American Journal of Science 296 (4), 420–452.

Osborne, M. J., Swarbrick, R. E., 1997. Mechanisms for generating overpressure in sedimentary basins: a reevaluation. AAPG bulletin 81 (6), 1023–1041.

Parnell, W. J., Calvo-Jurado, C., 2015. On the computation of the hashin–shtrikman bounds for transversely isotropic two-phase linear elastic fibre-reinforced composites. Journal of Engineering Mathematics 95 (1), 295–323.

Prioul, R., Bakulin, A., Bakulin, V., 2004. Nonlinear rock physics model for estimation of 3d subsurface stress in anisotropic formations: Theory and laboratory verification. Geophysics 69 (2), 415–425.

Richardsen, G., Vorren, T. O., Tørudbakken, B. O., 1993. Post-early cretaceous uplift and erosion in the southern barents sea: a discussion based on analysis of seismic interval velocities. Norsk Geologisk Tidsskrift 73 (1), 3–20.

Rottmann, K., 1960. Matematisk formelsamling (original title mathematische formelsammlung). Bibliographisches Institut-Hochschultaschenbuecher, Mannheim: Bibliographisches Institut,— c1960, 2. Auflage, edited by Rottmann, Karl.

Sathar, S., Jones, S., 2016. Fluid overpressure as a control on sandstone reservoir quality in a mechanical compaction dominated setting: Magnolia field, gulf of mexico. Terra Nova 28 (3), 155–162.

Shearer, P. M., 2009. Introduction to seismology. Cambridge University Press.

Sheldon, H. A., Wheeler, J., Worden, R. H., Cheadle, M. J., 2003. An analysis of the roles of stress, temperature, and ph in chemical compaction of sandstones. Journal of Sedimentary Research 73 (1), 64–71.

Simm, R., Bacon, M., 2014. Seismic Amplitude: An interpreter's handbook. Cambridge University Press.

Smith, W., Foote, P. D., Busang, P., 1929. Packing of homogeneous spheres. Physical Review 34 (9), 1271.

Thomsen, L., 1986. Weak elastic anisotropy. Geophysics 51 (10), 1954–1966.

Torset, S., 2017. Investigating the effects of simulated uplift on synthetic sandstones (unpublished).

Torset, S., Duffaut, K., Holt, R., 2018. Contribution of rock physics laboratory tests and modelling to improving uplift estimates. In: 80th EAGE Conference and Exhibition 2018.

Voigt, W., 1910. Lehrbuch der kristallphysik: (mit ausschluss der kristalloptik). B.G. Teubners Sammlung von Lehrbüchern auf dem Gebiete der mathematischen Wissenschaften ; Bd. XXXIV. B.G. Teubner.
URL https://books.google.no/books?id=SvPPAAAAMAAJ

Walderhaug, O., 1994. Precipitation rates for quartz cement in sandstones determined by fluid-inclusion microthermometry and temperature-history modeling. Journal of Sedimentary Research 64 (2).

Walderhaug, O., 1996. Kinetic modeling of quartz cementation and porosity loss in deeply buried sandstone reservoirs. AAPG bulletin 80 (5), 731–745.

Walderhaug, O., Lander, R., Bjørkum, P., Oelkers, E., Bjørlykke, K., Nadeau, P., Worden, R., Morad, S., 2000. Modelling quartz cementation and porosity in reservoir sandstones: examples from the norwegian continental shelf. Quartz cementation in sandstones 29, 39–49.

Walderhaug, O., Oelkers, E. H., Bjørkum, P. A., 2004. An analysis of the roles of stress, temperature, and ph in chemical compaction of sandstones: discussion. Journal of Sedimentary Research 74 (3), 447–449.

Walton, K., 1987. The effective elastic moduli of a random packing of spheres. Journal of the Mechanics and Physics of Solids 35 (2), 213–226.

Waples, D. W., 1980. Time and temperature in petroleum formation: application of lopatin's method to petroleum exploration. AAPG bulletin 64 (6), 916–926.

Winkler, K. W., 1985. Dispersion analysis of velocity and attenuation in berea sandstone. Journal of Geophysical Research: Solid Earth 90 (B8), 6793–6800.

Wood, D. M., 1990. Soil behaviour and critical state soil mechanics. Cambridge university press.

Worden, R., Burley, S., 2003. Sandstone diagenesis: the evolution of sand to stone. Sandstone Diagenesis: Recent and Ancient 4, 3–44.

Part VII

Appendix

Appendix A

Proofs

A.1 Loading of Granular Media

A.1.1 Integral Equations

This subsection will go through the derivation of the integral equation to produce I_9 in equation (7.9). The other integrals can be obtained using similar considerations, and are omitted due to the similarity. The software used throughout this project is *maple*.

Recall that

$$I_9 = \langle (E_{pq} n_p n_q)^{1.5} n_1^2 \rangle \tag{A.1a}$$
$$n_1 = sin(\theta) cos(\phi) \tag{A.1b}$$
$$\langle x \rangle = \frac{1}{4\pi} \int_0^{2\pi} \int_0^{\pi} x \sin(\theta) d\theta d\phi \tag{A.1c}$$

Introducing the strain condition where the horizontal strains are equal

$$E_{ij} = E_{11}\delta_{i1}\delta_{j1} + E_{11}\delta_{i2}\delta_{j2} + E_{33}\delta_{i3}\delta_{j3} \tag{A.2}$$

Where δ is the Kronecker delta.
Implementation of Einstein's summation convention yields

$$(E_{pq} n_q n_p) = (E_{11} n_1^2 + E_{11} n_2^2 + E_{33} n_3^2) \tag{A.3}$$

Following the derivations done in part II

$$(E_{11} sin^2(\theta)(\sin^2(\phi) + \cos^2(\phi)) + E_{33}\cos^2(\theta))^{1.5} = \tag{A.4a}$$
$$(E_{11}\sin^2(\theta) + E_{33}\cos^2(\theta))^{1.5} = \tag{A.4b}$$
$$E_{33}^{3/2}\Big(\frac{E_{11}}{E_{33}}\sin^2(\theta) + \cos^2(\theta)\Big)^{1.5} = \tag{A.4c}$$
$$E_{33}^{3/2}\Big(\frac{E_{11}}{E_{33}}\sin^2(\theta) + \frac{E_{33}}{E_{33}}(1 - \sin^2(\theta))\Big)^{1.5} = \tag{A.4d}$$
$$E_{33}^{3/2}\Big(1 + \frac{E_{11} - E_{33}}{E_{33}}\sin^2(\theta)\Big)^{1.5} = \tag{A.4e}$$
$$E_{33}^{3/2}\Big(1 + 2E_r \sin^2(\theta)\Big)^{1.5} \tag{A.4f}$$

After inserting equations (A.4f) and (A.1b) into equation (A.1a), followed by insertion into equation (A.1c), (A.1c) can be solved in *maple*. The result of this is

$$\begin{aligned} I_9 = \frac{5\,{E_{33}}^{3/2}}{64\,{E_r}^{3/2}}\Big(&2\sqrt{2}(E_r - \frac{1}{10})(E_r + \frac{1}{2})^2 R + \\ &i(E_r + \frac{1}{2})^2(E_r - \frac{1}{10})\sqrt{2}S - \\ &i(E_r + \frac{1}{2})^2(E_r - \frac{1}{10})\sqrt{2}T + \\ &\frac{1}{5}\sqrt{E_r} + \frac{44\,{E_r}^{3/2}}{15} + 4\,{E_r}^{5/2}\Big) \end{aligned} \tag{A.5}$$

Where

$$R = \arctan\left(\frac{1}{4}\frac{\sqrt{2}\,(2\,E_r - 1)}{\sqrt{E_r}}\right) \tag{A.6a}$$
$$S = \ln\left(\frac{-i\sqrt{2\,E_r + 1}}{\sqrt{E_r}}\right) \tag{A.6b}$$
$$T = \ln\left(\frac{i\sqrt{2\,E_r + 1}}{\sqrt{E_r}}\right) \tag{A.6c}$$

From Rottmann (1960)[1]

$$arctan(x) = \frac{-i}{2}\ln\frac{1 + ix}{1 - ix} \tag{A.7}$$

From Theorem 2, Chapter 3.3 Adams and Essex (2009) and from Equation 2 & Example 1 in chapter 13 Kreyszig (2010)

$$\begin{aligned} &\ln(a \cdot b) = \ln a + \ln b \\ &\ln(\frac{a}{b}) = \ln(a) - \ln(b) \\ &\ln(-i) = \frac{-\pi i}{2} \\ &\frac{1}{i} = -i \end{aligned} \tag{A.8}$$

Utilising equation (A.7) and (A.8) with

$$x = \frac{1}{4}\frac{\sqrt{2}(2E_r - 1)}{\sqrt{E_r}}$$

[1] The reference is to the original published by Karl Rottmann, but it is in fact taken from the Norwegian translation "Matematisk Formelsamling". In the Norwegian translation (13th edition,2013) it is found on page 91

yields

$$\begin{aligned} arctan\left(\frac{1}{4}\frac{\sqrt{2}(2E_r-1)}{\sqrt{E_r}}\right) = \\ \frac{1}{2}i\cdot ln\left(1-\frac{(0.25\sqrt{2}i)(2E_r-1)}{\sqrt{E_r}}\right)- \\ \frac{1}{2}i\cdot ln\left(1+\frac{(0.25\sqrt{2}i)(2E_r-1)}{\sqrt{E_r}}\right) \end{aligned} \tag{A.9}$$

The expression within the first natural logarithm can be manipulated as

$$\begin{aligned} \frac{\sqrt{E_r}}{\sqrt{E_r}}-\frac{(0.25\sqrt{2}i)(2E_r-1)}{\sqrt{E_r}} = \\ \frac{4\sqrt{E_r}-2\sqrt{2}iE_r+\sqrt{2}i}{4\sqrt{E_r}} = \\ \frac{-i}{4\sqrt{E_r}}(2\sqrt{2}E_r+4i\sqrt{E_r}-\sqrt{2}) \end{aligned} \tag{A.10}$$

Similarly for the expression within the second natural logarithm:

$$\begin{aligned} \frac{\sqrt{E_r}}{\sqrt{E_r}}+\frac{(0.25\sqrt{2}i)(2E_r-1)}{\sqrt{E_r}} = \\ \frac{i}{4\sqrt{E_r}}(2\sqrt{2}E_r-4i\sqrt{E_r}-\sqrt{2}) \end{aligned} \tag{A.11}$$

The first natural logarithm term in (A.9) can then be expanded as

$$\begin{aligned} \frac{1}{2}i\cdot\ln\left(1-\frac{(0.25\sqrt{2}i)(2E_r-1)}{\sqrt{E_r}}\right) = \\ \frac{1}{2}i\cdot\ln\left(\frac{-i}{4\sqrt{E_r}}(2\sqrt{2}E_r+4i\sqrt{E_r}-\sqrt{2})\right) = \\ \frac{1}{2}i\cdot\left(\ln\left(\frac{-i}{4\sqrt{E_r}}\right)+\ln(2\sqrt{2}E_r+4i\sqrt{E_r}-\sqrt{2})\right) = \\ \frac{1}{2}i\cdot\left(\ln(-i)-\ln(4\cdot\sqrt{E_r})+\ln(2\sqrt{2}E_r+4i\sqrt{E_r}-\sqrt{2})\right) = \\ \frac{1}{2}i\cdot\left(\frac{-i\pi}{2}-\ln(4\cdot\sqrt{E_r})+\ln(2\sqrt{2}E_r+4i\sqrt{E_r}-\sqrt{2})\right) \end{aligned} \tag{A.12}$$

Similarly for the second natural logarithm term in equation (A.9)

$$\begin{aligned} \frac{1}{2}i\cdot\ln\left(1+\frac{(0.25\sqrt{2}i)(2E_r-1)}{\sqrt{E_r}}\right) = \\ \frac{1}{2}i\cdot\ln\left(\frac{i}{4\sqrt{E_r}}(2\sqrt{2}E_r-4i\sqrt{E_r}-\sqrt{2})\right) = \\ \frac{1}{2}i\cdot\left(\ln\left(\frac{i}{4\sqrt{E_r}}\right)+\ln(2\sqrt{2}E_r-4i\sqrt{E_r}-\sqrt{2})\right) = \\ \frac{1}{2}i\cdot\left(\ln(i)-\ln(4\cdot\sqrt{E_r})+\ln(2\sqrt{2}E_r-4i\sqrt{E_r}-\sqrt{2})\right) = \\ \frac{1}{2}i\cdot\left(\frac{i\pi}{2}-\ln(4\cdot\sqrt{E_r})+\ln(2\sqrt{2}E_r-4i\sqrt{E_r}-\sqrt{2})\right) \end{aligned} \tag{A.13}$$

Thus

$$\begin{aligned} \arctan\left(\frac{1}{4}\frac{\sqrt{2}(2E_r-1)}{\sqrt{E_r}}\right) = \\ \frac{1}{2}i\cdot\left(\frac{-i\pi}{2}-\ln(4\cdot\sqrt{E_r})+\ln(2\sqrt{2}E_r+4i\sqrt{E_r}-\sqrt{2})\right)- \\ \frac{1}{2}i\cdot\left(\frac{i\pi}{2}-\ln(4\cdot\sqrt{E_r})+\ln(2\sqrt{2}E_r-4i\sqrt{E_r}-\sqrt{2})\right) = \\ \frac{\pi}{2}+0.5i\big(\ln(2\sqrt{2}E_r+4i\sqrt{E_r}-\sqrt{2})- \\ \ln(2\sqrt{2}E_r-4i\sqrt{E_r}-\sqrt{2})\big) = \\ \frac{\pi}{2}+0.5i\ln\frac{(2\sqrt{2}E_r+4i\sqrt{E_r}-\sqrt{2})}{(2\sqrt{2}E_r-4i\sqrt{E_r}-\sqrt{2})} = \\ \frac{\pi}{2}+0.5i\ln\frac{(2E_r+2i\sqrt{E_r}\sqrt{2}-1)}{(\sqrt{2}\sqrt{E_r}-i)^2} \end{aligned} \tag{A.14}$$

Now the ln terms (S and T) will be considered.

$$\begin{aligned} \ln\left(\frac{i\sqrt{2E_r+1}}{\sqrt{E_r}}\right) = \\ \ln\left(\frac{i\sqrt{2E_r+1}}{i\sqrt{-E_r}}\right) = \\ \ln\left(\frac{\sqrt{2E_r+1}}{\sqrt{-E_r}}\right) = \\ \ln\sqrt{2E_r+1}-\ln\sqrt{-E_r} = \\ \frac{1}{2}\ln(2E_r+1)-\frac{1}{2}\ln(-E_r) \end{aligned} \tag{A.15}$$

where the last equality follows from the fact that $\ln(a^b) = b\ln(a)$. This expression is real due to the range of E_r

Similarly

$$\begin{aligned} \ln\left(\frac{-i\sqrt{2E_r+1}}{\sqrt{E_r}}\right) = \\ \ln\left(\frac{-i\sqrt{2E_r+1}}{i\sqrt{-E_r}}\right) = \\ \ln\left(\frac{-\sqrt{2E_r+1}}{\sqrt{-E_r}}\right) = \\ \ln(-1)+\ln(\sqrt{2E_r+1})-\ln(\sqrt{-E_r}) = \\ \pi i+\frac{1}{2}\ln(2E_r+1)-\frac{1}{2}\ln(-E_r) \end{aligned} \tag{A.16}$$

Thus[2]

$$\begin{aligned} a\cdot i\ln\left(\frac{-i\sqrt{2E_r+1}}{\sqrt{E_r}}\right)-a\cdot i\ln\left(\frac{i\sqrt{2E_r+1}}{\sqrt{E_r}}\right) = \\ -a\cdot\pi \end{aligned} \tag{A.17}$$

Using equations (A.14) and (A.17) it can then be shown that

[2] This means that for the ln terms of equation (A.5) the lack of definition in the limits is seemingly not of great concern.

$$
\begin{aligned}
&2a\arctan\left(\frac{1}{4}\frac{\sqrt{2}(2E_r-1)}{\sqrt{E_r}}\right)+\\
&ai\ln\left(\frac{-i\sqrt{2E_r+1}}{\sqrt{E_r}}\right)-ai\ln\left(\frac{i\sqrt{2E_r+1}}{\sqrt{E_r}}\right)=\\
&a\pi+ai\ln\frac{(2E_r+2i\sqrt{E_r}\sqrt{2}-1)}{(\sqrt{2}\sqrt{E_r}-i)^2}-a\pi=\\
&ai\ln\frac{(2E_r+2i\sqrt{E_r}\sqrt{2}-1)}{(\sqrt{2}\sqrt{E_r}-i)^2}
\end{aligned}
\tag{A.18}
$$

It is of interest to remove the imaginary terms in the remaining logarithm

$$W=ia\ln\left(\frac{2E_r+2i\sqrt{E_r}\sqrt{2}-1}{(\sqrt{2}\sqrt{E_r}-i)^2}\right) \tag{A.19a}$$

$$W=ia\ln\left(\frac{(\sqrt{2}\sqrt{E_r}+i)^2}{(\sqrt{2}\sqrt{E_r}-i)^2}\right) \tag{A.19b}$$

$$W=ia\ln\left(\frac{(i\sqrt{2}\sqrt{-E_r}+i)^2}{(i\sqrt{2}\sqrt{-E_r}-i)^2}\right) \tag{A.19c}$$

$$W=ia\ln\left(\frac{(i(\sqrt{2}\sqrt{-E_r}+1))^2}{(i(\sqrt{2}\sqrt{-E_r}-1))^2}\right) \tag{A.19d}$$

$$W=ia\ln\left(\frac{i^2(\sqrt{2}\sqrt{-E_r}+1)^2}{i^2(\sqrt{2}\sqrt{-E_r}-1)^2}\right) \tag{A.19e}$$

$$W=ia\ln\left(\frac{(\sqrt{2}\sqrt{-E_r}+1)^2}{(\sqrt{2}\sqrt{-E_r}-1)^2}\right) \tag{A.19f}$$

$$W=2\cdot ia\ln\left(-\frac{\sqrt{2}\sqrt{-E_r}+1}{\sqrt{2}\sqrt{-E_r}-1}\right) \tag{A.19g}$$

$$W=2\cdot ia\ln\left(\frac{\sqrt{2}\sqrt{-E_r}+1}{-\sqrt{2}\sqrt{-E_r}+1}\right) \tag{A.19h}$$

The equality from (A.19f) to (A.19g) follows from $\ln(a^b)=b\ln(a)$ but the minus sign inside the $\ln$ expression in (A.19g) needs further explanation. $\sqrt{x^2}=\pm x$. The overall expression within the $\ln$ is clearly positive from (A.19f) (as all the i's are removed, the squares will produce positive numbers). The denominator in equation (A.19g) is however negative for all E_r in $-0.5<E_r<0$. Thus, for the equality to hold, there has to a minus sign in front.

Equation (A.5) can now be expressed using equation (A.18) with $a=\sqrt{2}(E_r-\frac{1}{10})(E_r+0.5)^2$ and equation (A.19h) (note that the terms in a have been expanded)

$$
\begin{aligned}
&I_9=\frac{5E_{33}^{3/2}}{64E_r^{3/2}}\Bigg[2\sqrt{2}iV({E_r}^3+\frac{9\,{E_r}^2}{10}+\frac{3\,E_r}{20}-\frac{1}{40})+\\
&\frac{\sqrt{E_r}}{5}+\frac{44E_r^{3/2}}{15}+4E_r^{5/2}\Bigg]
\end{aligned}
\tag{A.20}
$$

Where

$$V=\ln\left(\frac{1+\sqrt{2}\sqrt{-E_r}}{1-\sqrt{2}\sqrt{-E_r}}\right) \tag{A.21}$$

It is of further interest to remove the imaginary unit, as it is not obvious that the final result is real from equation (A.20).

To get rid of the imaginary unit, recall that $E_r\leq 0$, which means that $\sqrt{-E_r}$ is real. Further

$$\sqrt{E_r}=\sqrt{-1\cdot -E_r}=\sqrt{-1}\sqrt{-E_r}=i\sqrt{-E_r} \tag{A.22}$$

$$
\begin{aligned}
&(E_r)^{3/2}=E_r\sqrt{E_r}=i\sqrt{-E_r}E_r=\\
&-i\sqrt{-E_r}(-E_r)=-i(-E_r)^{3/2}
\end{aligned}
\tag{A.23}
$$

$$E_r^{5/2}=\sqrt{E_r}E_r^2=i\sqrt{-E_r}(-E_r)^2=i(-E_r)^{5/2} \tag{A.24}$$

(A.25)

This can then be used in equation (A.20), together with the last equation in equation (A.8)

$$
\begin{aligned}
&I_9=\frac{i5E_{33}^{3/2}}{64(-E_r)^{3/2}}\Bigg[2\sqrt{2}iV({E_r}^3+\frac{9\,{E_r}^2}{10}+\frac{3\,E_r}{20}-\frac{1}{40})+\\
&\frac{i\sqrt{-E_r}}{5}-i\frac{44(-E_r)^{3/2}}{15}+i4(-E_r)^{5/2}\Bigg]
\end{aligned}
\tag{A.26}
$$

$$
\begin{aligned}
&I_9=\frac{-5E_{33}^{3/2}}{64(-E_r)^{3/2}}\Bigg[2\sqrt{2}V({E_r}^3+\frac{9\,{E_r}^2}{10}+\frac{3\,E_r}{20}-\frac{1}{40})+\\
&\frac{\sqrt{-E_r}}{5}-\frac{44(-E_r)^{3/2}}{15}+4(-E_r)^{5/2}\Bigg]
\end{aligned}
\tag{A.27}
$$

$$
\begin{aligned}
&I_9=\\
&\frac{-E_{33}^{3/2}}{1536(-E_r)^{3/2}}\Bigg[V(240\sqrt{2}{E_r}^3+216\sqrt{2}E_r^2+36\sqrt{2}E_r-6\sqrt{2})\\
&+24\sqrt{-E_r}-352(-E_r)^{3/2}+480(-E_r)^{5/2}\Bigg]
\end{aligned}
\tag{A.28}
$$

The final representation is obtained by simply scaling the terms to remove some of the fractions. As an example $\frac{5}{64}\cdot\frac{44}{15}=\frac{1}{1536}\cdot 352$. The expression in (A.28) is recognised as the expression given in equation (7.9). The methodology to obtain the other 9 integral equations is identical, and thus it is not deemed necessary to run through the full calculations one more time.

A.1.2 The Limits of Isotropic and Uniaxial Compaction

Again, this will be demonstrated for I_9. This derivation could probably have been carried out directly on equation (A.5), but as this is equal to the final expression for I_9 given in equation (A.28), this is used to ease the process (as derivatives are implemented).

A.1.2.1 Isotropic Compaction

From equation (A.28) it is clear that $E_r=0$ incites a division by 0. Further

$$\lim_{E_r\to 0}(V)=ln(1)=0 \tag{A.29}$$

L'hôpital's rule, described in theorem 3, chapter 4.3 in Adams and Essex (2009) (see also example 2 in the same chapter) states

that in the case of

$$lim_{x\to a} g(x) = lim_{x\to a} f(x) = 0 \tag{A.30}$$

$$lim_{x\to a} \frac{g'(x)}{f'(x)} = L \to \tag{A.31}$$

$$lim_{x\to a} \frac{g(x)}{f(x)} = L \tag{A.32}$$

If

$$lim_{x\to a} g'(x) = lim_{x\to a} f'(x) = 0 \tag{A.33}$$

it can be used several times, until a limit L might be reached.

Letting

$$g(E_r) = V(240\sqrt{2}{E_r}^3 + 216\sqrt{2}E_r^2 + 36\sqrt{2}E_r - 6\sqrt{2}) + 24\sqrt{-E_r} - 352(-E_r)^{3/2} + 480(-E_r)^{5/2} \tag{A.34a}$$

$$f(E_r) = (-E_r)^{3/2} \tag{A.34b}$$

It is clear that both f and g approach 0 as $E_r \to 0$. The factor $\frac{-E_{33}^{3/2}}{1536}$ is left out for the time being for ease of notation, it will simply be multiplied onto the final product.

Differentiating $g(E_r)$ and $f(E_r)$ yields

$$g'(E_r) = \frac{-1440}{\sqrt{-E_r}}\left[{E_r}^2 + \frac{13\,E_r}{30} - \frac{-\sqrt{2}}{40}\ln\left(\frac{1+\sqrt{2}\sqrt{-E_r}}{1-\sqrt{2}\sqrt{-E_r}}\right)\cdot (\sqrt{-E_r} - 12\,(-E_r)^{3/2} + 20\,(-E_r)^{5/2})\right] \tag{A.35a}$$

$$f'(E_r) = -\frac{3\sqrt{-E_r}}{2} \tag{A.35b}$$

The limit of $g'(E_r)$ as $E_r \to 0$ is still 0. As the logarithm term goes to infinity, and the denominator $\sqrt{-E_r}$ can be multiplied into the higher exponent terms. It should be clear that also $f'(E_r) \to 0$ as $E_r \to 0$. Thus, the differentiation is conducted a second time

$$g''(E_r) = \frac{-2880}{\sqrt{-E_r}}\left[E_r + \frac{2}{15} - \frac{-3}{20}\ln\left(\frac{1+\sqrt{2}\sqrt{-E_r}}{1-\sqrt{2}\sqrt{-E_r}}\right)\cdot (\sqrt{-E_r} - 12\,\frac{3(-E_r)^{3/2}}{10})\right] \tag{A.36a}$$

$$f''(E_r) = \frac{3}{4\sqrt{-E_r}} \tag{A.36b}$$

Dividing the two double derivatives yields

$$\frac{g''(E_r)}{f''(E_r)} = 576\,(\sqrt{-E_r} - 10/3\,(-E_r)^{3/2})\sqrt{2}\ln\left(\frac{1+\sqrt{2}\sqrt{-E_r}}{1-\sqrt{2}\sqrt{-E_r}}\right) - 3840\,E_r - 512 \tag{A.37a}$$

$$\lim_{E_r\to 0}\frac{g''(E_r)}{f''(E_r)} = -512 \tag{A.37b}$$

Thus

$$I_9(E_r \to 0) = -\frac{E_{33}^{3/2}}{1536}\cdot -512 = \frac{E_{33}^{3/2}}{3} \tag{A.38}$$

A.1.2.2 Uniaxial Compaction

In this limit, the expression for the limit is split in two

$$I_9(E_r \to -0.5) = \frac{-E_{33}^{3/2}(24\sqrt{0.5} - 352(0.5)^{3/2} + 480(0.5)^{5/2}}{1536(0.5)^{3/2}} + \frac{E_{33}^{3/2}V(E_r\to -0.5)(240\sqrt{2}{E_r}^3 + 216\sqrt{2}E_r^2 + 36\sqrt{2}E_r - 6\sqrt{2})}{1536(-E_r)^{3/2}} \tag{A.39}$$

The reason for this is that the first term is a well defined limit. The second term is of the form $\infty \cdot 0$. This is because as $E_r \to -0.5$ the argument of the logarithm in V goes to 0. This follows from

$$\ln(\frac{1+\sqrt{2}\sqrt{-E_r}}{1-\sqrt{2}\sqrt{-E_r}}) \to \ln\frac{2}{0^+} \to \ln\infty \to \infty \tag{A.40}$$

The positive superscript on the zero indicates that the limit is approached from "the right" (i.e., from the positive side). The multiplication by 0 comes from the fact that

$$(240\sqrt{2}(-0.5)^3 + 216\sqrt{2}(-0.5)^2 + 36\sqrt{2}(-0.5) - 6\sqrt{2}) = 0 \tag{A.41}$$

Further, define

$$X = (240\sqrt{2}(E_r)^3 + 216\sqrt{2}(E_r)^2 + 36\sqrt{2}(E_r) - 6\sqrt{2}) \le 0,\quad -0.5 \le E_r \le 0 \tag{A.42}$$

$$Y = \ln(\frac{1+\sqrt{2}\sqrt{-E_r}}{1-\sqrt{2}\sqrt{-E_r}}) \ge 0,\quad -0.5 \le E_r \le 0 \tag{A.43}$$

$$\tag{A.44}$$

This means that $X \cdot Y \le 0$.

Following this, define

$$Z = e^Y = \frac{1+\sqrt{2}\sqrt{-E_r}}{1-\sqrt{2}\sqrt{-E_r}} > Y \tag{A.45}$$

such that $X \cdot Z \le X \cdot Y \le 0$. The "smaller than" comes from the fact that $|Z| > |Y|,\ \ X \le 0$

In $X \cdot Z$ a $\frac{0}{0}$ is obtained as both the numerator and denominator approach zero. L'hôpital's is utilised to yield

$$\frac{f'(E_r)}{g'(E_r)} = 6\,(1+2\,E_r)\left(140\,{E_r}^2 + 20\,E_r + 60\,(-E_r)^{3/2}\sqrt{2} - 6\sqrt{2}\sqrt{-E_r} - 1\right)\sqrt{2} \tag{A.46}$$

The limit of this as $E_r \to -0.5$ is 0, as can be seen from the first bracket $(1 - 2\cdot 0.5 = 0)$.

Thus $X \cdot Z \to 0 \le X \cdot Y \le 0$. It is therefore concluded that

$$\lim_{E_r\to -0.5}\frac{E_{33}^{3/2}V(240\sqrt{2}{E_r}^3 + 216\sqrt{2}E_r^2 + 36\sqrt{2}E_r - 6\sqrt{2})}{1536(-E_r)^{3/2}} = 0 \tag{A.47}$$

Such that

$$I_9(E_r \to -0.5) = \frac{-E_{33}^{3/2}(24\sqrt{0.5} - 352(0.5)^{3/2} + 480(0.5)^{5/2}}{1536(0.5)^{3/2}} = \frac{E_{33}^{3/2}}{24} \tag{A.48}$$

A.1.3 Expression for Strain in Terms of Stress from Bandyopadhyay (2009)

Bandyopadhyay (2009) presents equations for strain in terms of stress, as a means of not having to estimate strain values in the field. The strain and stress form a system of two equations and two unknowns. The solutions for strain anisotropy and axial strain suggested by Bandyopadhyay (2009) were given in equations (6.11) and (6.13). To check whether a solution to such a system is correct, one can back substitute, and check that one ends up where one started. This is done in *maple* for the equations suggested in Bandyopadhyay (2009) for a set of grain parameters, and the implementation sequence is shown below. It can be seen that the stresses from the estimated strains when back-substituted in the original equations do not produce the starting values, as would be expected., in fact, the value of the strain anisotropy obtained by these equations fall outside the allowable range of the parameter if the limits are taken at uniaxial and hydrostatic strain.

$\sigma_{11} := -10^7$

-10000000 **(1)**

$\sigma_{33} := -1.05 \cdot 10^7$

$-1.050000000\ 10^7$ **(2)**

$S_1 := \sigma_{11}^{\ 2} - 4 \cdot \sigma_{11} \cdot \sigma_{33} + 4 \cdot \sigma_{33}^{\ 2}$

$1.210000000\ 10^{14}$ **(3)**

$S_2 := 3 \cdot \sigma_{11}^{\ 2} - 7 \cdot \sigma_{11} \cdot \sigma_{33} + 22 \cdot \sigma_{33}^{\ 2}$

$1.990500000\ 10^{15}$ **(4)**

$S_3 := \sigma_{11}^{\ 2} + 26 \cdot \sigma_{11} \cdot \sigma_{33} + 9 \cdot \sigma_{33}^{\ 2}$

$3.822250000\ 10^{15}$ **(5)**

$\mu_s := 41 \cdot 10^9$

41000000000 **(6)**

$\nu_s := 0.076$

0.076 **(7)**

$$\text{lambda} := \frac{2 \cdot \mu_s \cdot \nu_s}{1 - 2 \cdot \nu_s}$$

$7.349056604\ 10^9$ **(8)**

$$B := \frac{1}{4 \cdot \text{Pi}} \cdot \left(\frac{1}{\mu_s} + \frac{1}{\mu_s + \text{lambda}} \right)$$

$3.586808960\ 10^{-12}$ **(9)**

$$C := \frac{1}{4 \cdot \text{Pi}} \cdot \left(\frac{1}{\mu_s} - \frac{1}{\mu_s + \text{lambda}} \right)$$

$2.950189185\ 10^{-13}$ **(10)**

$P := 9 \cdot C^2 \cdot S_1 + 4 \cdot B \cdot C \cdot S_2 + 4 \cdot B^2 \cdot S_3$

$2.052160038\ 10^{-7}$ **(11)**

$\text{phi} := 0.36$

0.36 **(12)**

$N := 9$

9 **(13)**

$$Z := \frac{(1 - \text{phi}) \cdot N}{\pi^2 \cdot B \cdot (2 \cdot B + C)}$$

$2.178578180\ 10^{22}$ **(14)**

$$E_r := \frac{1}{16 \cdot B \cdot \sigma_{33}} \left(\sigma_{11} \cdot (2 \cdot \text{B} + 3 \cdot \text{C}) - 2 \cdot \sigma_{33} \cdot (7\ B + 3\ C) - P \right)$$

$$-0.7717682831 \tag{15}$$

$$E_{33} := \left(\frac{1}{2 \cdot Z \cdot \left(9 \cdot C^3 + 40 \cdot C^2 \cdot B + 28 \cdot C \cdot B^2 - 32 \cdot B^3\right)} \left(12 \cdot B^2 \cdot \left(\sigma_{11} + 13 \cdot \sigma_{33}\right) + 27 \cdot C^2 \left(\sigma_{11} - 2 \cdot \sigma_{33}\right) + (9 \cdot C + 6 \cdot B) \cdot P + 6 \cdot B \cdot C \cdot \left(6 \cdot \sigma_{11} - 7 \cdot \sigma_{33}\right)\right)^{\frac{2}{3}} \right)$$

$$0.004169879330\ 2^{1/3} \tag{16}$$

$$\sigma_{33} := \frac{-Z}{15} \cdot E_{33}^{\frac{3}{2}} \cdot \left(5\ C + 10\ B + (6\ C + 8\ B) \cdot E_r\right)$$

$$-5.409274575\ 10^6 \sqrt{2} \tag{17}$$

$$-7.649869465\ 10^6 \tag{18}$$

$$\sigma_{11} := \frac{-Z}{15} \cdot E_{33}^{\frac{3}{2}} \cdot \left(5\ C + 10\ B + 16\ B \cdot E_r^{\,2} + 12\ C \cdot E_r + 28\ B \cdot E_r\right)$$

$$3.408617741\ 10^6 \sqrt{2} \tag{19}$$

$$\overset{\text{simplify}}{=}$$

$$4.820513437\ 10^6 \tag{20}$$

A.2 Anisotropic Hashin Shtrikhman - Supplementary Material

It was claimed that

$$I_{11}^{\delta=1,iso} = I_{13}^{\delta=1,iso} = I_{33}^{\delta=1,iso} = \frac{4\pi}{5} \tag{A.49}$$

The expressions for I_{13}, I_{11}, I_{33} before insertion of δ with $\nu_1 = \nu_2 = \nu_3 = 1$ can be given as

$$I_{11} = \frac{\pi\,\delta\,\left(\delta^3 - 5/2\,\delta + 1.5\,\arccos\left(\delta\right)\left(-\delta^2+1\right)^{-0.5}\right)}{\left(\delta^2-1\right)^2} \tag{A.50}$$

$$I_{13} = \frac{\pi\,\delta^2\left(-6.0\,\delta\,\arccos\left(\delta\right)\left(-\delta^2+1\right)^{-0.5} + 2\,\delta^2 + 4\right)}{\left(\delta^2-1\right)^2} \tag{A.51}$$

$$I_{33} = \frac{\pi\,\left(-16/3\,\delta^2 + 4/3 + 4.0\,\delta^3\,\arccos\left(\delta\right)\left(-\delta^2+1\right)^{-0.5}\right)}{\left(\delta^2-1\right)^2} \tag{A.52}$$

for $\delta < 1$ and

$$I_{11} = \frac{\pi\,\delta\,\left(\delta^3 - 5/2\,\delta + 1.5\,\mathrm{arccosh}\left(\delta\right)\left(\delta^2-1\right)^{-0.5}\right)}{\left(\delta^2-1\right)^2} \tag{A.53}$$

$$I_{13}\frac{\delta^2\pi\,\left(-6.0\,\delta\,\mathrm{arccosh}\left(\delta\right)\left(\delta^2-1\right)^{-0.5} + 2\,\delta^2 + 4\right)}{\left(\delta^2-1\right)^2} \tag{A.54}$$

$$I_{33} = \frac{\pi\,\left(-16/3\,\delta^2 + 4/3 + 4.0\,\delta^3\mathrm{arccosh}\left(\delta\right)\left(\delta^2-1\right)^{-0.5}\right)}{\left(\delta^2-1\right)^2} \tag{A.55}$$

for $\delta > 1$ Plotting these expressions against δ is done in figure A.1 and they can be seen to converge to the proposed limit of $\frac{4\pi}{5}$

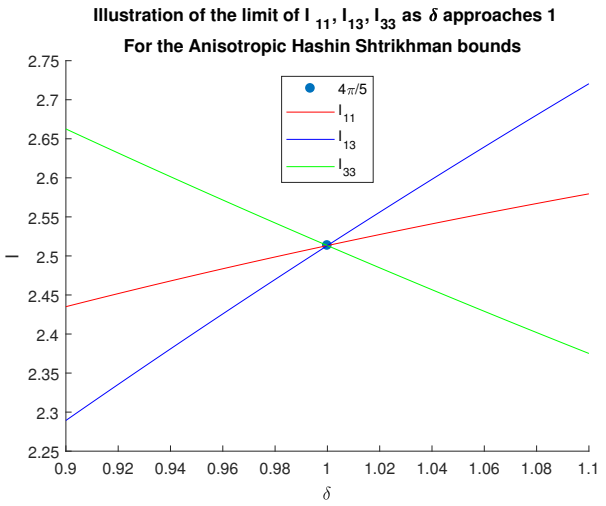

Figure A.1: Visualisation of I_{13}, I_{11} and I_{33} used in the anisotropic Hashin-Shtrikman bounds. The expressions are undefined in $\delta = 1$, but the limit can be visualised as $\frac{4\pi}{5}$

Appendix B

Poroelasticity and Pore Pressure

This is a short theory section on poroelasticity taken from previous work (Torset, 2017), deemed excessive for the main manuscript.

B.1 Isotropic Media

In subsurface rocks, fluids are generally present in the pores space. This acts to modify the mechanical response of the rock. Poroelasticity describes the interplay between deformation of a volume element attached to the solid and the movement of the fluid, relative to the movement of the solid (Cheng and Detournay, 2014).

When a rock is compressed due to an external load, it will seek to compact. If it contains a fluid in the pore space that is unable to escape, the pore pressure will increase, which causes an expansionary mechanism (Cheng and Detournay, 2014). Therefore, the necessary steps are to relate two stresses, the elements of the stress tensor and the pore pressure, to the strain parameters ϵ_{vol} and ζ (Fjær et al., 2008, Chapter 1). ζ represents the relative displacement of the fluid compared to that of the solid and is referred to as the "increment of fluid content" (Biot, 1962).

In Biot (1962) the stresses and strains are related through a set of equations[1]. The medium is porous and permeable, linearly elastic and in this formulation isotropic[2]

$$\sigma_x = 2G\epsilon_x + \lambda\epsilon_{vol} - C\zeta \tag{B.1a}$$
$$\sigma_y = 2G\epsilon_y + \lambda\epsilon_{vol} - C\zeta \tag{B.1b}$$
$$\sigma_z = 2G\epsilon_z + \lambda\epsilon_{vol} - C\zeta \tag{B.1c}$$
$$p_f = C\epsilon_{vol} - M\zeta \tag{B.1d}$$

C and M are additional elastic moduli required to characterise the two phase system. Adding equations (B.1a), (B.1b) and (B.1c) yields

$$\sigma_x + \sigma_y + \sigma_z = 3(\frac{2G}{3}(\epsilon_x + \epsilon_y + \epsilon_z) + \lambda\epsilon_{vol} - C\zeta) \rightarrow$$
$$\bar{\sigma} = \epsilon_{vol}(\frac{2G}{3} + \lambda) - C\zeta \tag{B.2}$$

The relations for mean stress, $\bar{\sigma} = \frac{\sigma_x+\sigma_y+\sigma_z}{3}$ and volumetric strain, $\epsilon_{vol} = \epsilon_x + \epsilon_y + \epsilon_z$ have been applied (Fjær et al., 2008, Chapter 1).
One of the aforementioned relationships between the elastic moduli is that $K = \frac{2G}{3} + \lambda$ (Fjær et al., 2008, Chapter 1), thus equation B.2 can be written as

$$\bar{\sigma} = K\epsilon_{vol} - C\zeta \tag{B.3}$$

Three specific scenarios can then be implemented to derive useful relationships: If the fluid does not move relative to the solid, then $\zeta = 0$, and the system is said to be undrained (Fjær et al., 2008, Chapter 1). Utilising this in equation (B.3), it can be inferred that K is the bulk modulus of the undrained system.

By having an "open" system, the pore fluid is allowed to escape when stress is applied, such that the change in pore pressure is zero (Biot, 1962). From equation (B.1d) it then follows that $\frac{C}{M}\epsilon_{vol} = \zeta$. Inserting this in equation (B.2), when the rock is subjected to an external hydrostatic pressure σ_{hs} it is obtained that.

$$\sigma_{hs} = \epsilon_{vol}(K - \frac{C^2}{M}) \rightarrow \frac{\sigma_{hs}}{\epsilon_{vol}} = K - \frac{C^2}{M} \tag{B.4}$$

This can be identified as the bulk modulus of the solid framework, since the fluid in this case is escaping rather than carrying any load, such that the framework is carrying the entire load (Fjær et al., 2008, Chapter 1).

Finally, the porous and permeable medium is placed within a container of fluid, such that the pore pressure is equal to the

[1] Notation modified slightly
[2] An anisotropic version exists and shall be discussed later

hydrostatic pressure in the fluid, that is $p_f = \sigma_{hs}$.

$$\begin{aligned}
&\zeta = \frac{C}{M}\epsilon_{vol} - \frac{p_f}{M} \rightarrow \\
&\sigma_{hs} = \epsilon_{vol}(K - \frac{C^2}{M}) + \frac{C \cdot_f}{M} \rightarrow \\
&\frac{\sigma_{hs}}{\epsilon_{vol}}(1 - \frac{C}{M}) = K_{fr} \rightarrow \\
&\frac{\sigma_{hs}}{\epsilon_{vol}} = \frac{K_{fr}}{1 - \frac{C}{M}}
\end{aligned} \tag{B.5}$$

The fact that $p_f = \sigma_{hs}$ means that there is uniform stress in the sample. This further implies that the rock framework deforms uniformly (Fjær et al., 2008, Chapter 1). In other words

$$\frac{\Delta V_{tot}}{V_{tot}} = \frac{\Delta V_p}{V_p} = \frac{\Delta V_s}{V_s} \tag{B.6}$$

where V_{tot} refers to the total volume, V_p refers to the pore volume, and V_s refers to the solid volume. Thus

$$\frac{\Delta V_s}{V_s} = -\epsilon_{vol} = -\frac{p_f}{K_s} \tag{B.7}$$

Correlating equations (B.5) and (B.7) it is clear that

$$K_s = \frac{K_{fr}}{1 - \frac{C}{M}} \tag{B.8}$$

These results, together with the definition of ζ can be combined to form the "Biot-Gassmann" equation, relating the bulk moduli of the solid, fluid and framework together with the porosity to the bulk modulus of the undrained system (Fjær et al., 2008).

$$K = K_{fr} + \frac{K_f}{\phi}\frac{(1 - \frac{K_{fr}}{K_s})^2}{1 + \frac{K_f}{K_s\phi}(1 - \phi - \frac{K_{fr}}{K_s})} \tag{B.9}$$

The considerations above were done based on the work of Biot (1962), but Gassmann (1951) derived the same result.

It was demonstrated earlier that the bulk modulus of a porous, undrained material is related to the bulk moduli of the framework, fluid and solid as well as the porosity. According to the theory derived by Biot, there is also a frequency dependence introduced by the presence of a viscous fluid (Biot, 1962).

The low frequency limit for poroelastic media was given in (2.6) (Fjær et al., 2008, Chapter 5).. In other words

$$v_p(\omega \rightarrow 0) = \sqrt{\frac{K + \frac{4G_{fr}}{3}}{\rho}} \tag{B.10}$$

K is given by equation (B.9), and the argument for why $G = G_{fr}$ is that there aren't shear forces associated with the fluid (Fjær et al., 2008, Chapter 1). The density of the system is given by the density of the solid material and the density of the fluid through $\rho = (1-\phi)\rho_s + \phi\rho_f$ where ϕ is the porosity.

The dispersion mechanisms suggested by Biot are generally not sufficient to explain the dispersion seen in real, saturated rocks. The dispersion suggested by the Biot mechanism is generally on the scale of 1-3%, whereas dispersion observed in real rocks may be higher than this (Fjær et al., 2008, Chapter 5). Other mechanisms involve so called "local flow" where the compliance of thin, compliant pores "cracks" is determined by the frequency. In the low frequency limit, the pore fluid in these cracks is able to flow into adjacent, stiffer pores, making the crack more compliant. At higher frequencies, the pores are essentially isolated due to the rapidly oscilating motion, i.e., the pore fluid remains in the thin pores. This means that the pores are less compliant, and the effective stiffness is thus increased (Fjær et al., 2008, Chapter 5).

Recall that linear elasticity was assumed for (B.9) and thus also implied in equation (B.10). It has been mentioned that rocks might very well not behave elastically under significant stress application, but for the case of small enough stress variations, such as those brought about by a propagating wave, the concept of differential elasticity is thought to apply (Gassmann, 1951).

The mechanisms suggested above for dispersion relate mainly to the presence of a fluid. By then assuming that for dry rocks, the velocity is independent of frequency, experimental data in the ultrasonic range can be applied to the field case (Winkler, 1985). For application to field data from seismic (low frequency) range, the method is to calculate the expected velocity through equations (B.9) and (2.6) (Winkler, 1985).

B.2 Anisotropic Media

The poroelasticity consideration previously made were done under isotropic assumptions. Gassmann (1951) however extends the discussion to porous systems with an anisotropic frame. Keeping with the notation used so far, the elastic stiffness parameters of the bulk material c, can be be expressed in terms of the elastic stiffness parameters of the anisotropic frame c_{fr}, bulk modulus of the solid and fluid K_s, K_f and the porosity ϕ through the equation (Gassmann, 1951)

$$c_{ij} = c_{fr,ij} + \frac{\alpha}{D^*}b_i b_j, \qquad i,j = 1,2...6 \tag{B.11}$$

Where

$$b_i = \epsilon_i - \frac{c_{fr,1i} + c_{fr,2i} + c_{fr,3i}}{3 * K_s} \quad i = 1,2...6$$

$$\epsilon_i = \begin{cases} 1 & \text{if} \quad i = 1,2,3 \\ 0 & \text{if} \quad i = 4,5,6 \end{cases}$$

$$D^* = 1 + \frac{\alpha}{3 \cdot K_s}(b_1 + b_2 + b_3)$$

$$\frac{1}{\alpha} = \phi\Big(\frac{1}{K_f} - \frac{1}{K_s}\Big)$$

B.3 Pore Pressure

The hydrostatic pressure gradient is defined by Osborne and Swarbrick (1997) as the "pressure that would be exerted by

a continuous column of static fluid". If the pressure exceeds that which would be expected from the hydrostatic pressure gradient at a certain depth, the fluid is said to be overpressured. Osborne and Swarbrick (1997) present several mechanisms by which such overpressure can be generated. The most prominent is disequilibrium compaction. When sediments are originally deposited, they can have very high porosities, 40% for sandstone, and even higher for shales. As sediments are buried, the pore space compacts, which forces the fluid to escape. If the permeability of the sediment is very low, or the sediment is encapsulated in a low permeability rock, such that the fluid is unable to escape quickly enough in response to the decrease in pore space, the fluid becomes overpressured. This mechanism is called disequilibrium compaction (Osborne and Swarbrick, 1997).

The pore pressure controls the effective stress, as was demonstrated earlier, and it is the effective stress which has the primary control on compaction mechanisms, in areas where little cementation has occurred (Bjørlykke et al., 2015). Thus, overpressured rocks might have higher porosities at a specified depth than expected, as compaction (pore space reduction) is slowed down. Furthermore, in areas where pressure solution is the dominant process for the diagenetic setting, the overpressure will reduce the effective stress, which will act to preserve porosity (Sathar and Jones, 2016).

In the situation where the rock is dry, as for the laboratory tests in this project, the stress values represent the effective stress. It is the magnitude of the effective stress components that failure and slip properties in granular and porous media are primarily dependent on (Biot, 1962).

Appendix C

Additional Discussion of the Experimental Data

This chapter provides some additional experimental results than that given in the main text. This is to provide a better insight into the range of experimental data available. The purpose of including additional experimental data is to reinforce the interpretation of microcrack formation as a cause of stress dependence. The main focus of the thesis was to develop a rock physics model to describe the entire burial history, which is calibrated to one set of cement volume and stress history. To that extent, only the experimental data needed in part II were critical which is why the remainder of the experimental data were put in the extended discussion or the appendix.

In the subsequent the distinction "stiff" and "soft" are used. The "stiff" sample is still quite soft, it is simply "stiff" in relation to the "soft" sample. The reason for this terminology is because it is this what is adopted by SINTEF when they conducted the experiments (Holt et al., 2014). The "stiff" sample is the sample that was introduced in part II.

C.1 "Stiff"

The axial P-wave velocity, P-wave anisotropy and axial strain have have all been given previously. Additional figures given in this section include a comparison of the P-wave velocities as functions of axial stress, figure C.1. The radial P-wave velocity as function of radial stress is given in figure C.2 and finally the radial stress as function of axial stress is given in figure C.3.

The display of the P-wave velocities in figure C.1 gives a further insight into the P-wave anisotropy. Observe how the P-wave velocities cross at around 12MPa, corresponding to reversal of P-wave anisotropy discussed at length in the main text. Note that when compared to the axial stress, the radial P-wave velocity remains above the velocity it had during loading down to around 20MPa of unloading.

It has been shown that according to the crack model, in terms of stress, the axial P-wave velocity will be mainly dependent on the axial stress and the radial P-wave velocity will be mainly dependent on the radial stress. When the radial P-wave velocity is viewed as a function of radial stress, as done in figure C.2, it can be seen that the velocity drops below the value during loading quite quickly.

The key lies in the plot of radial stress versus axial stress given in figure C.3. It can be seen that under the conditions of uniaxial compaction and extension, the radial stress behaves differently during unloading and loading. During unloading, the radial stress is consistently higher than that observed during loading, for a given axial stress. Eventually the radial P-wave velocity also falls below that seen during loading when plotted against axial stress as well, due to an increase in stress dependence during simulated uplift.

C.2 "Soft"

The axial strain compared to axial stress is shown in figure C.4 for the sample with less cement. The notable difference is the creep period at max "burial". After this creep period, the strain starts decreasing on the onset of unloading, in contrast to the "stiff" sample. In the "stiff" sample, the strain (given in figure 3.4) increased slightly during the first few MPa's of unloading. During loading after cementation, two distinct gradients can be observed, with a "bend" observable at around 23 MPa of axial stress. After this bend the relationship between the axial stress and strain is quite linear upon subsequent loading. It is further observed that the degree of axial strain in this sample is significantly larger after cementation than for the "stiff" sample, reflecting the lower amount of cement. For the "stiff" sample, there were about 15 mStrain of compaction during loading after cementation, whereas in the "soft" sample the value is close to 40.

During unloading, the decrease in axial strain is somewhat difficult to compare due to variable treatment of creep. The "soft" sample during unloading to 15MPa axial stress can be seen to show a smaller decrease in strain than the increase during creep. In other words, the sample contracted more over the creep period than it expanded during unloading. Whether the creep was finished or not, or whether this is an attribute to further delayed information is not investigated in further detail. In the "stiff" sample the unloading down to 15MPa's produces a combined expansion due to stress unloading and compaction due to creep response that has the sample expand compared to

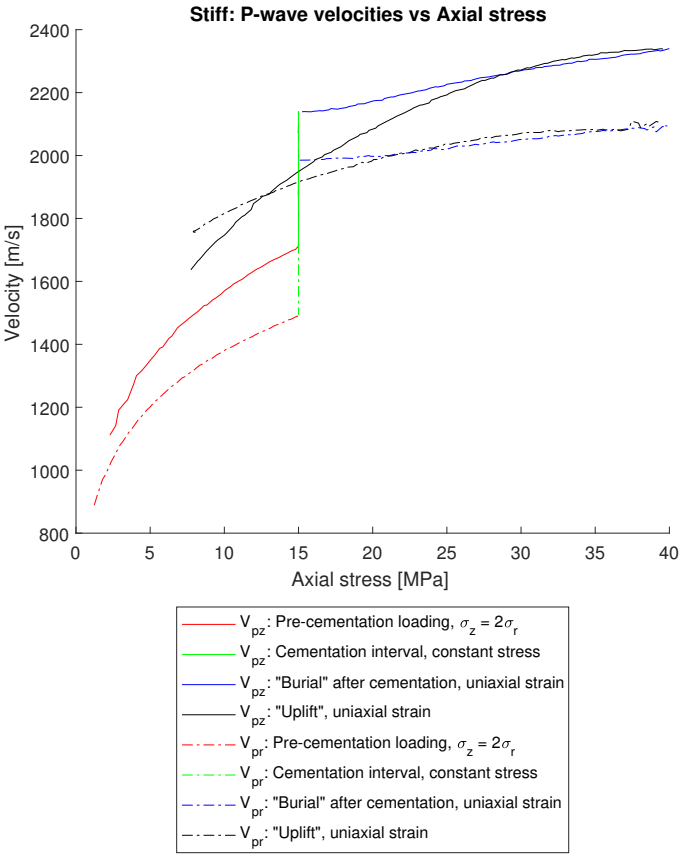

Figure C.1: Axial and Radial P-wave velocities plotted against axial stress for the sample termed "stiff". The reversal of P-wave anisotropy is observed as the axial P-wave velocity drops below that of the radial P-wave velocity. The initial higher axial P-wave velocity during unloading can be linked to axial compaction due to creep during the first few MPa's of unloading. The observations that the radial P-wave velocity remains higher during the first 20MPa's of axial stress unloading is considered in figures C.2 and C.3

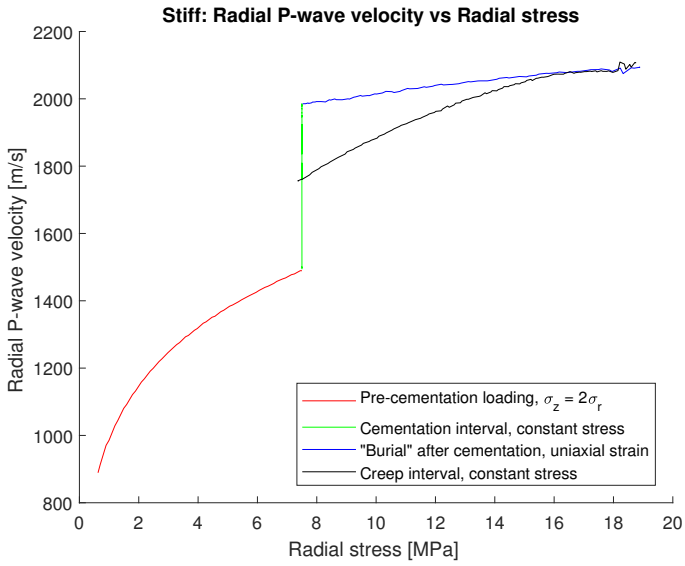

Figure C.2: Radial P-wave velocity plotted against radial stress for the sample termed "stiff". It is noted in figure C.1 that the radial P-wave velocity when plotted against axial stress remains above its value during loading down to about 20MPa during unloading. Note however that when plotted against radial stress it drops below quite quickly. The two observations are connected by the observations in figure C.3.

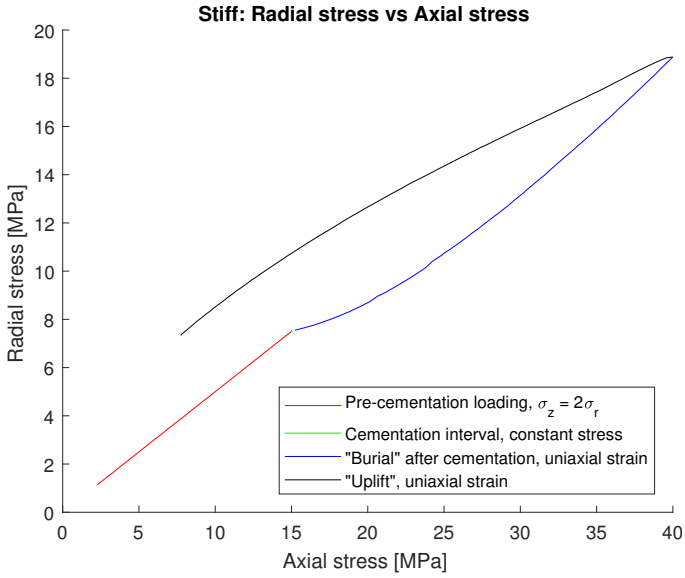

Figure C.3: Radial stress plotted against axial stress for the sample termed "stiff". The radial stress can be seen to be higher for a given axial stress during unloading compared to loading. This can be linked to the observation that the radial P-wave velocity when plotted against axial stress remains higher during unloading compared to loading for around 20MPa of unloading. When the radial P-wave velocity is compared to radial stress however, the velocity drops below after a few MPa's of unloading

the maximum “burial” stress. This might be an indication that the effect of uplift is greater in the stiffer sample, that is, the stress unloading has a bigger effect on expansion than in the “soft” sample. The different creep conditions however make this interpretation uncertain. Holt et al. (2014) provides some discussion on the creep effects in these experiments.

The P-wave velocities are shown in figure C.5. No reversal of the P-wave anisotropy is observed in this sample, but the unloading only occurs down to 15MPa axial stress, in contrast to the “stiff” sample. If the trends of the axial and radial P-wave velocities are extrapolated, it is not unlikely that a reversal of the P-wave anisotropy would occur also in this sample. During the creep both the axial and radial P-wave velocities increase. The increase in the axial P-wave velocity is about 40 m/s, and for the radial P-wave velocity it is about 30 m/s.

The trend for the P-wave velocities when comparing loading and unloading is that the effect of the simulated uplift is smaller in the “soft” sample than in the “stiff” sample. Consider the radial P-wave velocity plotted against radial stress for the “soft” sample given in figure C.6. Over the unloading the change in velocity over the unloading interval is close to identical to that seen during the same stress levels during loading. The reason for the unloading interval only extending down to about 12MPa radial stress is the aforementioned deviation in the extent of unloading, compared to the stress path in the “stiff” sample (cf. figure 3.1). The increased stress dependence has been attributed to the opening of microcracks. If the increase in stress dependence is smaller in the “soft” sample this means that the opening of microcracks should have a smaller impact on the rock as a whole. Since the cement volume is smaller in the “soft” sample, this could be a pointer to cement bonds breaking being the cause of the microcrack formation. Since there are more potential cement bonds that could be breaking in the “stiff” sample, due to more cement, the effect would be larger. The axial strain was also interpreted to be extensional to a larger degree in the “stiff” sample, although the creep somewhat complicates the interpretation. This might accelerate the breaking of cement bonds. Since the cement bonds are not likely oriented exactly in the radial and axial direction there will be some effect in the radial direction as well.

Another interesting observation is made by comparing the radial P-wave velocity as function of axial stress in figure C.5 and the plot of radial stress against axial stress in figure C.7. The shape of the two curves during loading after cementation and unloading is strikingly similar, further reinforcing the idea of the radial P-wave velocity being primarily dependent on the radial stress. A further consequence of this is that it reinforces that the increase in stress dependence for the radial P-wave velocity over the unloading interval is smaller than that observed in the stiff sample. If the stress dependence increased considerably, the radial P-wave velocity would decrease to a larger extent during unloading (compared figure C.5 and C.7 to figure C.1 and C.3).

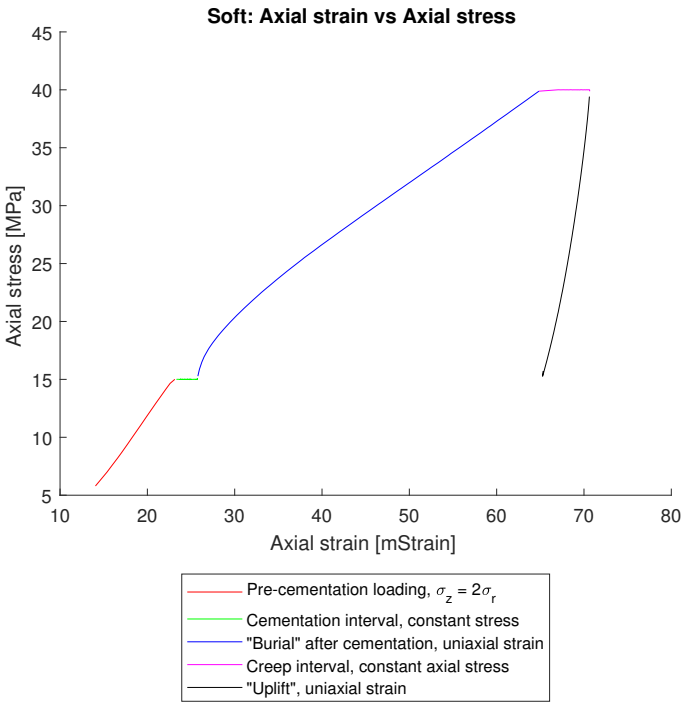

Figure C.4: Axial strain plotted against axial stress for the sample termed “soft”. A key thing to note is the creep period at maximum “burial” where the strain continues to increase even as the axial stress is kept constant. Upon the onset of unloading, the axial strain starts to decrease at once, in contrast to what was observed for the stiff sample (cf. figure 3.4). As for the “stiff” sample an accelerated strain can be seen after the first few MPa’s of loading. From around 23 to 40 MPa’s of loading, the behaviour between the axial stress and axial strain behaves quite linearly.

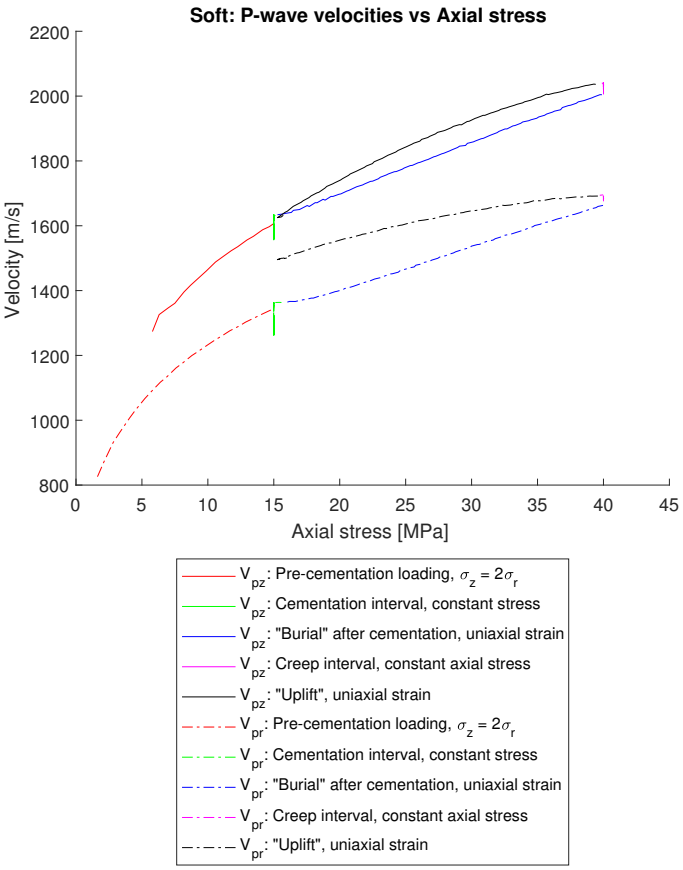

Figure C.5: Comparison of the P-wave velocities plotted against axial stress for the sample termed "soft". The effect of simulated uplift to 15MPa axial stress can be seen to have a more muted effect on the velocities in this sample compared to the "stiff" sample. When plotted against axial stress, it can be seen how the change in radial P-wave velocity during unloading is smaller than during loading. This is due to radial stress considerations, discussed in more detail in relation to figures C.6 and C.7. In the stiff sample, over the same axial unloading interval, the change in the radial P-wave velocity was bigger during unloading compared to loading. The creep period increases the axial P-wave velocity by roughly 40 m/s and the radial P-wave velocity by roughly 30 m/s

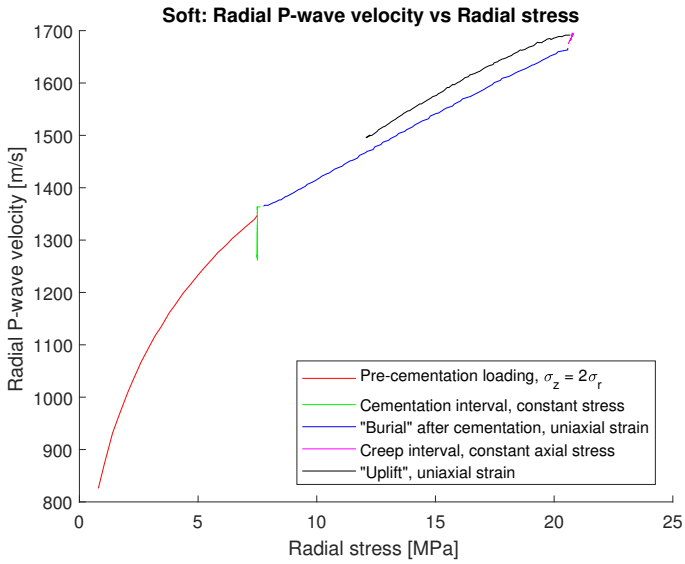

Figure C.6: Radial P-wave velocity visualised against radial stress for the sample termed "soft". Over the unloading interval, the axial stress is only unloaded to the value at the start value of the post-cementation loading, which, with reference to figure C.7 causes the radial velocity to be limited to unloading down to 12MPa. Over this unloading interval, the radial P-wave velocity can be seen to have a very similar velocity change compared to the velocity change observed over the same radial stress interval during loading. This is in contrast to the stiff sample, and is indicative of the increase in stress dependence being less prominent in the "soft" sample. In terms of the interpretation of the increased stress dependence being related to the formation of microcracks in the sample, this might then be an indication of fewer microcracks being formed. Further, since the cement volume is smaller this might point to the microcracks being formed due to failing cement bonds

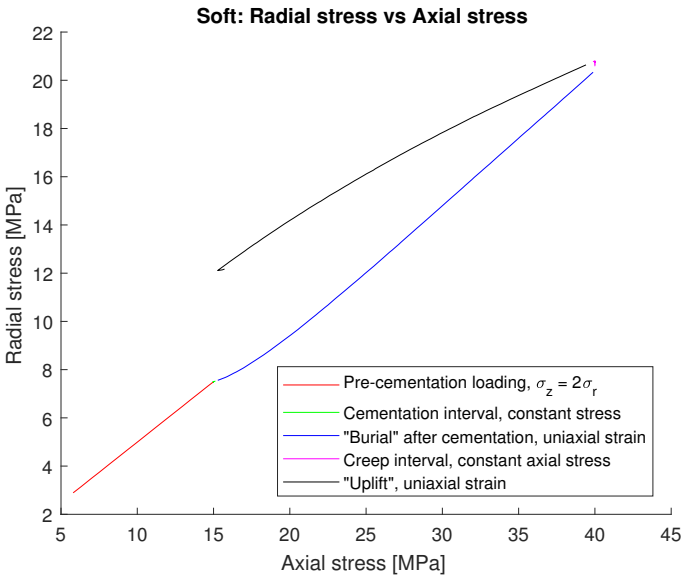

Figure C.7: Radial stress plotted against axial stress for the sample termed "soft". The radial stress during unloading remains higher than during loading for all axial stress levels. The axial stress is only unloaded down to 15MPa in the "soft" sample, which is in contrast to that observed in the sample termed "stiff" (cf. figure C.3). The shape of the radial vs axial stress in this curve is very similar to the radial velocity plotted against radial stress during the loading after cementation and unloading intervals. This is an indication that the increase in stress dependence for the radial P-wave velocity is smaller for the "soft" sample than for the stiff sample. If microcracks are responsible for the stress formation, this the means that the opening of microcracks has a less prominent effect on the "soft" sample than the stiff sample.

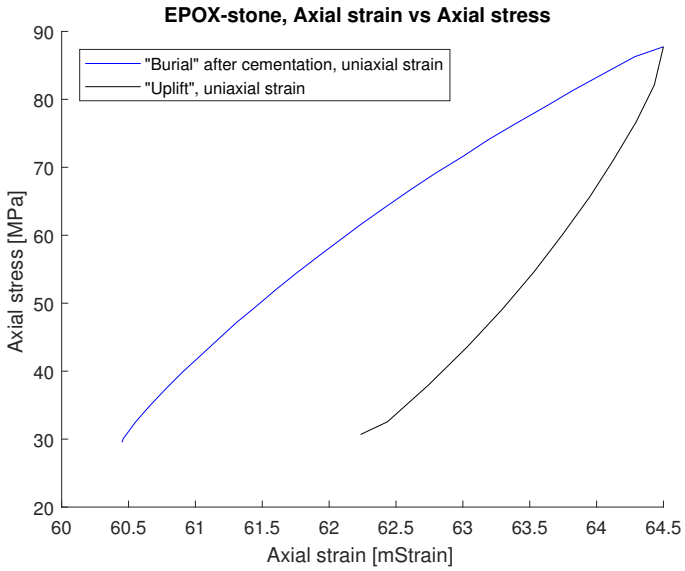

Figure C.8: Axial stress vs axial strain for the EPOX-stone over the intervals of loading after cementation and simulated uplift. During the loading interval, the change in strain is larger than during unloading, but the values in both intervals are smaller than that observed for the two other samples considered in this work (see figure 3.4 and figure C.4).

C.3 EPOX-stone

The stress vs strain is given for the EPOX-stone in figure C.8 during the loading after "cementation" and simulated uplift. Note how there is nearly no change in strain during either of these intervals, when compared to the main sample used in this work (figure 3.4) and the softer sample (figure C.4). During loading there is a change in strain of less than 4 mStrain over a stress increase of 60MPa (compared to around 18mStrain in the sample from part II and more than 35mStrain in the "soft" sample over an axial stress increase of 25MPa). There is no defined kink in the strain curve either, suggesting that the epoxy does not mimic the potential breakage of cement bonds interpreted for the other samples. During unloading there is only 2mStrain of extension. This indicates that any deformation mechanisms are less active in this sample than in the other samples. Crack formation during uplift and reactivation of previously formed microcracks were interpreted as the main cause of the increased stress dependence in the other samples, and since this is not present in any significant quantity in the EPOX-stone, the stress sensitivity does not change during uplift.

C.4 Simulated Coring

Figure C.9 shows an extension of the stress history of the sample subjected to simulated coring (see figure13.13). During loading (from 15 to 40MPa) and unloading after coring, the samples were limited to uniaxial compaction. The resulting velocities are shown in figure C.10. The coring interval is discussed in part VI. During the loading after coring the velocity increase is 75% larger than that seen during loading

after cementation in the sample not subjected to coring over the same stress interval. The simulated coring is therefore seen to suggest that cores are not representative for measuring the stress dependence of in-situ rocks, which was the original motivation for conducting the experiments (Holt et al., 2014). The reason for this could be the formation of microcracks during the simulated coring. These microcracks act to increase the stress dependence of the core. During reloading, cracks formed during coring could be closing, meaning that the stress dependence decreases with increased loading. After a small creep period, the sample is unloaded along a uniaxial strain path. The velocity change during unloading is very similar to that seen during the loading over the same stress interval. This observation is similar to that made regarding the softer sample. This might be a further indicator of cement-bonds breaking during the simulated coring. As cement bonds cannot heal in the experimental setup, those that are broken during the coring cannot break again. This limits the potential for a further increase in stress dependence during the unloading after reloading of the sample.

The P-wave anisotropy is shown in figure C.11. Contrary to the sample from part II ("stiff") and the "soft" sample, there is not a significant difference between the loading from 15-40 MPa and the unloading back to 15MPa. The "soft" sample and the "cored" sample therefore have similar observations regarding how the stress dependence of the velocity varies from loading to unloading, but differ in how the anisotropy develops. This is likely a testament to the cause of the stress dependence in the samples. In the "soft" sample the stress dependence during loading comes from the lack of cement, so that the granular media, with its stress dependent contacts, is dominant. In the "cored" sample, the stress dependence during loading comes from the deformation caused by the simulated coring, which due to the initial anisotropic stress field during "coring" is anisotropic. A small increase in the stress dependence in the cored sample is observed during unloading after reloading, which could indicate some additional microcrack formation occurring during this stress interval.

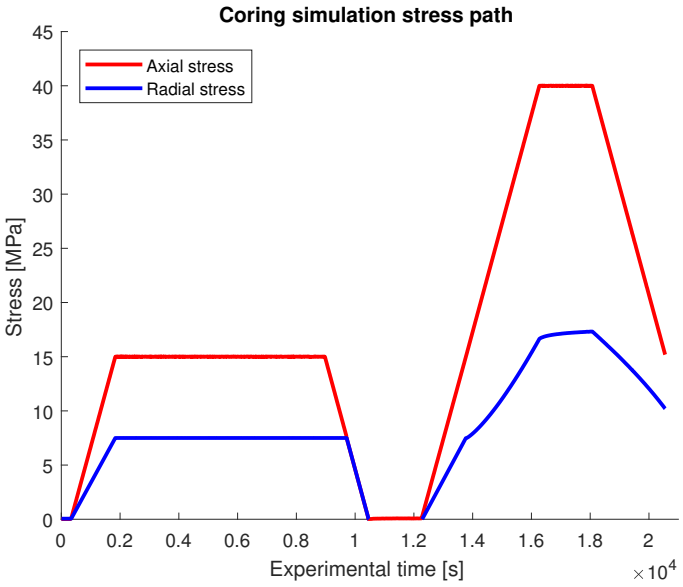

Figure C.9: Continuation of the stress path after coring. Subsequent loading up to 40MPa of axial stress. From 15 MPa during reloading the sample was restricted to uniaxial strain.

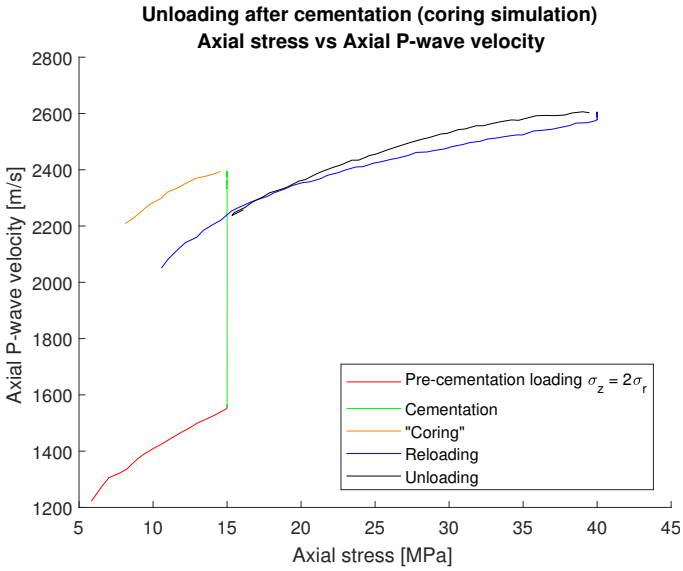

Figure C.10: Velocities of the cored sample including reloading and subsequent unloading. The stress dependence of the sample during loading from 15MPa-40MPa axial stress is larger than for the samples not subjected to simulated coring. This is likely a testament to deformation that occurred during the simulated coring interval. Upon unloading, the stress sensitivity of the velocity increases, but only slightly, and shows a similar trend of returning to the velocity value at 15MPa as was seen in the sample with less cement (see part VI). This can be put into context of broken cement bonds as microcracks, as cement bonds that are broken during coring are not healed in the experimental setup. This means that new deformation during unloading after reloading happens to a smaller extent than that which was seen in the sample with similar amounts of cement with no coring simulation (the sample presented in part II).

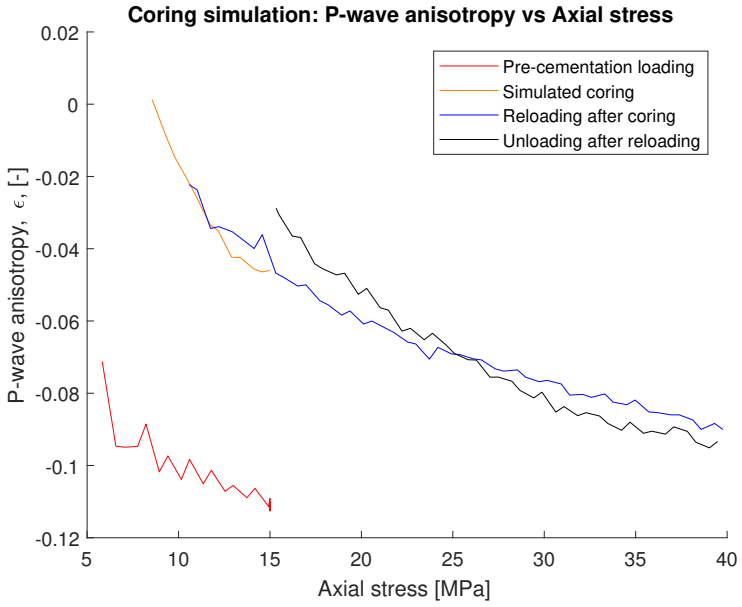

Figure C.11: P-wave anisotropy of the sample subjected to coring simulation, including reloading and unloading. There is less difference in the anisotropy trends during reloading and unloading in this sample than in the same stress intervals of the samples that had not been subjected to the coring simulation. The anisotropy is slightly more stress dependent during the unloading, but the apparent increase in stress dependence during simulated uplift compared to loading after cementation is smaller than that observed in the other samples. This is interpreted as a result of microcrack formation during the simulated coring, such that the closing of those microcracks enter into the definition of the stress dependence of the velocities during reloading after coring. During the unloading, there might be some additional microcrack formation, adding to the re-opening of those closed during the reloading.

Appendix D

Alternate Strain Formulation (Johnson 1998)

In part III expressions for a particular triaxial strain and stress state are derived for the no-slip and slip limit from Walton (1987). A similar triaxial strain is considered in Johnson et al. (1998) for the no-slip case. It is of interest to see how the equations derived in part III compare with those of Johnson et al. (1998) for the loading of the granular media prior to cementation. This is to provide further insight and validation for the derivations.

D.1 The Model in Johnson (1998)

Johnson et al. (1998) considers a transversely isotropic strain as a combination of a hydrostatic and uniaxial strain:

$$\epsilon_{ij} = \epsilon\delta_{ij} + \epsilon_3\delta_{i3}\delta_{j3} \tag{D.1}$$

The rough limit (no slip) is considered, and yields the following moduli (Johnson et al., 1998):

$$C^r_{11} = \frac{\gamma}{\alpha}\left\{2B_w[I_0(\alpha) - I_2(\alpha)] + \frac{3C_w}{4}[I_0(\alpha) - 2I_2(\alpha) + I_4(\alpha)]\right\} \tag{D.2a}$$

$$C^r_{33} = \frac{\gamma}{\alpha}\{4B_w I_2(\alpha) + 2C_w I_4(\alpha)\} \tag{D.2b}$$

$$C^r_{13} = \frac{\gamma}{\alpha}C_w[I_2(\alpha) - I_4(\alpha)] \tag{D.2c}$$

$$C^r_{44} = \frac{\gamma}{\alpha}\left\{\frac{B_w}{2}[I_0(\alpha) + I_2(\alpha)] + C_w[I_2(\alpha) - I_4(\alpha)]\right\} \tag{D.2d}$$

$$C^r_{66} = \frac{\gamma}{\alpha}\left\{B_w[I_0(\alpha) - I_2(\alpha)] + \frac{C_w}{4}[I_0(\alpha) - 2I_2(\alpha) + I_4(\alpha)]\right\} \tag{D.2e}$$

The remaining factors needed are

$$C_n = \frac{4\mu_s}{1-\nu_s} \tag{D.3}$$

$$C_t = \frac{8\mu_s}{2-\nu_s} \tag{D.4}$$

$$B_w = \frac{2}{\pi C_n} \tag{D.5}$$

$$C_w = \frac{4}{\pi}\left[\frac{1}{C_t} - \frac{1}{C_n}\right] \tag{D.6}$$

$$\gamma = \frac{3}{32}C_n C_t n(1-\phi)\sqrt{\epsilon} \tag{D.7}$$

$$\alpha = \sqrt{\frac{\epsilon}{\epsilon_3}} \tag{D.8}$$

$$I_n(\alpha) = \int_0^1 x^n\sqrt{\alpha^2 + x^2}dx \tag{D.9}$$

The integrals can, according to Johnson et al. (1998) be solved analytically to give

$$I_0(\alpha) = \frac{1}{2}\left[\sqrt{1+\alpha^2} + \alpha^2 ln\big(\frac{1+\sqrt{1+\alpha^2}}{\alpha}\big)\right] \tag{D.10}$$

$$I_{2n+2} = \frac{1}{2n+4}[(1+\alpha^2)^{3/2} - (2n+1)\alpha^2 I_{2n}(\alpha)] \tag{D.11}$$

The method of modelling velocities will be the same as that in part III: Estimate the strains based on the measured stress and use this estimated strain in the stiffness equations. The additional applicability of the model in Johnson et al. (1998) is that the strain path is also considered. This is not explored in detail in this work, due to the availability of experimental data, but it is noted that three explicit sets of stress equations is given in Johnson et al. (1998), together with a general, path dependent expression.

The path utilised here corresponds to a situation where ϵ and ϵ_3 are increased together. This coincides with the experimental data presented earlier, where the radial and axial strain both increase, with the axial strain increasing faster. The radial strain is given by ϵ, whereas the axial strain is $\epsilon_z = \epsilon + \epsilon_3$. The stress equations are then given as (Johnson et al., 1998):

A: Expression set equal to 0

$$\left(2\left(C_t\left(0.0833333333\left(\alpha^2+1\right)^{1.5}-0.25\,\alpha^2\left(0.5\sqrt{\alpha^2+1}+0.5\,\alpha^2\ln\left(\frac{1+\sqrt{\alpha^2+1}}{\alpha}\right)\right)\right)+\frac{1}{2}\alpha^2\left(0.25\left(\alpha^2+1\right)^{1.5}-0.25\,\alpha^2\left(0.5\sqrt{\alpha^2+1}+0.5\,\alpha^2\ln\left(\frac{1+\sqrt{\alpha^2+1}}{\alpha}\right)\right)\right)\right)+C_n\left(\frac{1}{2}\alpha^2\left(0.25\left(\alpha^2+1\right)^{1.5}-0.25\,\alpha^2\left(0.5\sqrt{\alpha^2+1}+0.5\,\alpha^2\ln\left(\frac{1+\sqrt{\alpha^2+1}}{\alpha}\right)\right)\right)+\frac{1}{6}\left(\alpha^2+1\right)^{1.5}\right)\right)\Bigg/\left(-C_t\left(0.0833333333\left(\alpha^2+1\right)^{1.5}-0.25\,\alpha^2\left(0.5\sqrt{\alpha^2+1}+0.5\,\alpha^2\ln\left(\frac{1+\sqrt{\alpha^2+1}}{\alpha}\right)\right)\right)+\frac{1}{2}\alpha^2\left(0.25\left(\alpha^2+1\right)^{1.5}-0.25\,\alpha^2\left(0.5\sqrt{\alpha^2+1}+0.5\,\alpha^2\ln\left(\frac{1+\sqrt{\alpha^2+1}}{\alpha}\right)\right)\right)\right)+C_n\left(\alpha^2\left(0.5\sqrt{\alpha^2+1}+0.5\,\alpha^2\ln\left(\frac{1+\sqrt{\alpha^2+1}}{\alpha}\right)\right)+\left(-\alpha^2+1\right)\left(0.25\left(\alpha^2+1\right)^{1.5}-0.25\,\alpha^2\left(0.5\sqrt{\alpha^2+1}+0.5\,\alpha^2\ln\left(\frac{1+\sqrt{\alpha^2+1}}{\alpha}\right)\right)\right)-\frac{1}{6}\left(\alpha^2+1\right)^{1.5}+\frac{1}{2}\alpha^2\left(0.25\left(\alpha^2+1\right)^{1.5}-0.25\,\alpha^2\left(0.5\sqrt{\alpha^2+1}+0.5\,\alpha^2\ln\left(\frac{1+\sqrt{\alpha^2+1}}{\alpha}\right)\right)\right)\right)\right)-\frac{\sigma_{33}}{\sigma_{11}}$$

B: Derivative

$$-\Bigg(24.000\Bigg(\left(\left(1.0000\,C_t\,C_n+1.0000\,C_n^2\right)\alpha^8\sqrt{\alpha^2+1.}+\left(1.0000\,C_t\,C_n+1.0000\,C_n^2\right)\alpha^{10}+\left(1.0000\,C_t\,C_n+1.0000\,C_n^2\right)\alpha^8\right)\ln\left(\frac{1.+\sqrt{\alpha^2+1.}}{\alpha}\right)^2+\left(\left(\left(4.0000\,C_t\,C_n+4.0000\,C_n^2\right)\alpha^8+\left(13.333\,C_t\,C_n+13.333\,C_n^2\right)\alpha^6+\left(14.667\,C_t\,C_n+14.667\,C_n^2\right)\alpha^4+\left(5.3333\,C_t\,C_n+5.3333\,C_n^2\right)\alpha^2\right)\sqrt{\alpha^2+1.}+\left(\left(-2.0000\,C_t\,C_n-2.0000\,C_n^2\right)\alpha^8+\left(-6.0000\,C_t\,C_n-6.0000\,C_n^2\right)\alpha^6+\left(-4.0000\,C_t\,C_n-4.0000\,C_n^2\right)\alpha^4\right)\sqrt{\alpha^2+1.}+\left(2.0000\,C_n^2-1.0667\,10^{-10}C_t^2+2.0000\,C_t\,C_n\right)\alpha^8+\left(-1.0667\,10^{-10}C_t^2+7.3333\,C_n^2+7.3333\,C_t\,C_n\right)\alpha^6+\left(10.667\,C_n^2+10.667\,C_t\,C_n\right)\alpha^4+\left(5.3333\,C_t\,C_n+5.3333\,C_n^2\right)\alpha^2\right)\ln\left(\frac{1.+\sqrt{\alpha^2+1.}}{\alpha}\right)+\left(\left(1.0667\,10^{-9}C_n^2+1.0667\,10^{-9}C_t\,C_n\right)\alpha^6+\left(1.3333\,C_n^2+2.1333\,10^{-10}C_t^2+1.3333\,C_t\,C_n\right)\alpha^4+\left(2.6667\,C_n^2+3.2000\,10^{-10}C_t^2+2.6667\,C_t\,C_n\right)\alpha^2+1.3333\,C_t\,C_n+1.3333\,C_n^2+1.0667\,10^{-10}C_t^2\right)\sqrt{\alpha^2+1.}+\left(\left(-1.0667\,10^{-10}C_t^2-3.0000\,C_n^2-3.0000\,C_t\,C_n\right)\alpha^6+\left(-7.0000\,C_n^2-1.0667\,10^{-10}C_t^2-7.0000\,C_t\,C_n\right)\alpha^4+\left(-4.0000\,C_t\,C_n-4.0000\,C_n^2\right)\alpha^2\right)\sqrt{\alpha^2+1.}+\left(-3.0000\,C_t\,C_n-3.0000\,C_n^2\right)\alpha^8+\left(-8.6667\,C_t\,C_n-8.6667\,C_n^2+2.1333\,10^{-10}C_t^2\right)\alpha^6+\left(-7.0000\,C_t\,C_n+5.3333\,10^{-10}C_t^2-7.0000\,C_n^2\right)\alpha^4+\left(-2.1333\,10^{-9}C_t\,C_n+4.2667\,10^{-10}C_t^2+4.2667\,10^{-9}C_n^2\right)\alpha^2+1.3333\,C_t\,C_n+1.3333\,C_n^2+1.0667\,10^{-10}C_t^2\right)\alpha\Bigg)\Bigg/\Bigg(\sqrt{\alpha^2+1.}\left(\sqrt{\alpha^2+1.}+1.0000\right)\Bigg(\left(\left(1.0000\,C_t+1.0000\,C_n\right)\alpha^6+\left(2.0000\,C_t+6.0000\,C_n\right)\alpha^4\right)\ln\left(\frac{1.+\sqrt{\alpha^2+1.}}{\alpha}\right)+\left(\left(-1.0000\,C_t-1.0000\,C_n\right)\alpha^4+\left(-1.3333\,C_t+5.3333\,C_n\right)\alpha^2-1.3333\,C_t+1.3333\,C_n\right)\sqrt{\alpha^2+1.}\Bigg)^2\Bigg)$$

Figure D.1: A: The expression that is set equal to zero to solve α numerically using Newton's method. **B:** The derivative of the expression in A with respect to α, needed in the implementation of Newton's method

$$\sigma_{11} = -\frac{Q\left(C_t\ (I_2 - I_4) + C_n\ \left(\alpha^2 I_0 + \left(1-\alpha^2\right) I_2 - I_4\right)\right)}{4} \tag{D.12}$$

$$\sigma_{33} = -\frac{Q\left(C_t\ (I_2 - I_4) + C_n\ \left(\alpha^2 I_2 + I_4\right)\right)}{2} \tag{D.13}$$

where

$$Q = \frac{\epsilon^{3/2}\left(1-\phi\right)n}{\pi\,\alpha^3} \tag{D.14}$$

Note that in this formulation strain is positive in compaction, whilst stress is negative in compression, consistent with the derivations in part III, based on that used in Bandyopadhyay (2009).

Due to the nested logarithm expressions created by I_0, obtaining explicit expressions for the strains in terms of stresses is difficult. Instead, the methodology of using Newton's method is implemented, which is the same as was done in part III. Dividing σ_{33} by σ_{11} creates an expression where the only strain parameter is α. This expression can then be differentiated, and fed into *matlab*. The expression to be set equal to zero is shown in figure D.1A, and the derivative is given in figure D.1B.

The results of implementing this for the axial and radial P-wave velocities is shown in figures D.2 and D.3 respectively. The similarity to that obtained in part III (denoted "Walton Rough") is not unexpected, as Johnson et al. (1998) states "Note that the limit $\epsilon_3 \to 0$ leads to the result for hydrostatic pressure (Eq. (3.19) of Walton (1987)) and that in the opposite limit of purely uniaxial compression, $\epsilon \to 0$, the above equations all reduce to Eqs. (3.24) of Walton (1987)". Therefore, the fact that they coincide is unsurprising. The advantage of using the equations derived in part III over the result from Johnson et al. (1998) is that the slip limit in Walton (1987) can be used in the binary mixing model. It might be that the equations Johnson et al. (1998) can be modified to recognise the equations for the rough limit in part III, by relating α to E_r etc, but this possibility is not investigated further.

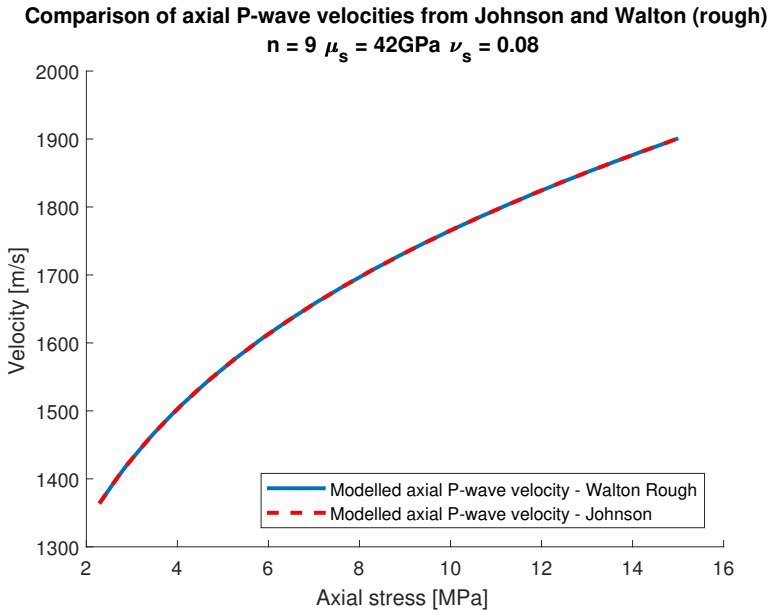

Figure D.2: Comparison of the axial P-wave velocity in the rough limit from the equations derived from Walton (1987) and the results from Johnson et al. (1998) with a strain path where the hydrostatic and uniaxial parts of the strains in Johnson et al. (1998) are increased simultaneously. Note that the results are indistinguishable. The stress state corresponds to that in the pre-cementation loading in the experimental data, with $\sigma_z = 2\sigma_r$.

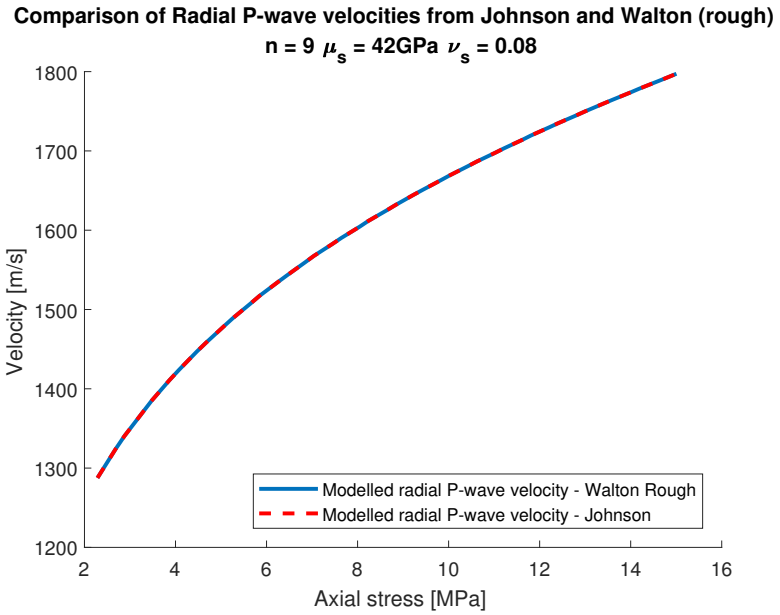

Figure D.3: Comparison of the radial P-wave velocity in the rough limit from the equations derived from Walton (1987) and the results from Johnson et al. (1998) with a strain path where the hydrostatic and uniaxial parts of the strains in Johnson et al. (1998) are increased simultaneously. Note that the results are indistinguishable. The stress state corresponds to that in the pre-cementation loading in the experimental data, with $\sigma_z = 2\sigma_r$.